Efficient generation of atomic chlorine by a low-temperature plasma and application to atmospheric chemistry

Joshua George Boothroyd

Doctor of Philosophy

University of York

Physics

September 2020

Abstract

Short-lived reactive species, such as hydroxyl (OH) and atomic chlorine (Cl) radicals, play a crucial role in atmospheric self-regulation and low temperature plasma applications. The oxidative removal of volatile organic compounds (VOC) in the atmosphere depend critically upon the local density of these reactive species. Direct measurements of radical concentration and reactivity (loss rate) are challenging in the atmosphere. Indirect techniques have been shown to be of value, notably for OH reactivity measurements. Low-temperature plasmas have potential as efficient sources of radicals at atmospheric pressure for use in these indirect techniques.

In this work, atomic chlorine generated by a capacitively coupled, radio-frequency driven plasma was applied to a competitive reactivity method for measuring the reactivity of atomic chlorine in a gas sample. Argon with a small admixture (0.04–0.096%) of molecular chlorine was used as the plasma feed gas. The main production and destruction mechanisms of Cl_2 in the plasma were investigated by a zero-dimensional global model. Optical emission spectroscopy of the plasma identified humid air impurities through OH and N_2 rotational band emission. Proton transfer reaction mass spectrometry (PTR-MS) was used to indirectly quantify the reactive species downstream of the plasma through adding VOC to the plasma effluent and monitoring the resulting mixture. Despite efforts to remove impurities in the argon gas line, $\sim 8\times10^{11}$ cm^{-3} OH was scrubbed from the plasma effluent using benzene. Additionally, $(6-13)\times10^{11}$ cm^{-3} radical fragments were observed as Cl_2 was added to the plasma. The loss rate of atomic chlorine in a mixture of toluene/isoprene, using diethyl-ether as the reference was also attempted for the first time.

Contents

List of Tables

List of Figures

Acknowledgements

First and foremost I would like to thank Timo Gans for the opportunity to work on atmospheric pressure plasmas throughout the last few years. With his support I have been able to develop my own independent work and participate in the wider plasma science community. Many thanks also to Terry Dillon for his patience, motivation and guidance through the field of atmospheric chemistry and for the introduction to the Wolfson Atmospheric Chemistry Laboratory (WACL). Whilst working at WACL, I would like to thank Jacob Shaw and Fiona Whitting for their chemistry knowledge and support whilst studying for their own PhDs.

I feel privileged to have been a member of the York Plasma Institute, and to have taken part in something so unique. Special thanks to those in the low temperature plasma group past and present. Thanks to Alex Foote, Andy West and David Blackman for help settling into the YPI. Thanks to Sandra Schröter for the COMSOL modelling and Andrew Gibson for his advice on the chlorine data review and the model. For their sense of humour I would like to thank Dave Meehan, Scott Doyle and David Shaw. Thanks to Helen Davies, Michael Mo and Fred Riedel for making the office a brilliant place to work, it has been a pleasure. Even in the strange circumstances that I am writing this, it is good to know that you're all out there.

Of course no physical science PhD would be possible without the help of the technical staff. It is no exaggeration that my work would not be possible without the creativity and true craft of the scientific glassblower Abigail Mortimer. Thanks to both Richard Armitage and Kari Niemi for their sage advice and support. Sincere thanks to Marvin Shaw, Stephen Andrews and Stuart Young for their time and hands-on field experience with mass spec-

trometers & electronics. I would also like to thank the administration staff at the YPI; Ruth Lowman, Kathryn Harvey & Hillary Marshall are all worth their weight in gold!

Alongside my PhD, I would like to thank Erasmus du Toit for introducing me to the graduate football team, as well as Matthew Thomas and Alasdair Wynn for their banter and career advice. My thanks go out to my family; Virginia, David, Thomas, Eleanor and Isobel with my final thanks to Montana. I would not have seriously considered doing a PhD without you all. Thank you dearly for your love and support over the past few years.

Declaration

I declare that this thesis is a presentation of original work and I am the sole author. This work has not previously been presented for an award at this, or any other, University. All sources are acknowledged as References.

The modelling of the gas reactor in section 2.1.3 was carried out by Dr Sandra Schröter with the subsequent interpretation and analysis by myself. The design and production of the plasma source used in this project (section 2.1.1) was a product of collaborative work by Dr James Dedrick, Dr Alex Foote, Dr Jérôme Bredin and myself. The gas reactor used in this work was produced by Abigail Mortimer with the design chosen by Dr Terry Dillon and myself.

Chapter 1

Introduction

1.1 Aims & objectives

Low temperature plasmas are used everyday to create chemically reactive species for a wide variety of different cases. These vary from biomedical applications for sterilisation and physical therapy to semiconductor manufacture and the etching of silicon wafers to produce computer chips [1]. Substantial quantities of short-lived reactive species at ambient pressure and temperature are possible using a plasma source, using relatively simple and inexpensive equipment. By taking advantage of this, they have shown to be effective sources of short-lived radical species [2, 3].

Common to both plasma physics and atmospheric chemistry, atomic chlorine (Cl) is considered not just an important radical in terms of the fabrication of nano-processors and in excimer lasers [4, 5] but also due to the potential of Cl to affect atmospheric oxidative cycles [6]. The reaction rate of Cl with many organic compounds is typically faster than with hydroxyl radicals (OH) [7–9]. Due to this typically high reaction rate and relatively unknown emission rate, the concentration of atomic chlorine in the atmosphere has been estimated to be around $10^4 - 10^5$ radicals cm^{-3} [10–12]. Alongside this, the strong spatial variation of [Cl] makes modelling the role of Cl in the atmosphere an arduous task. Still under active investigation, atomic chlorine has been shown to have a much wider spatial distribution in the troposphere and may also have negative impacts on air quality [13, 14].

A recurrent theme in atmospheric chemistry has been in adapting well established laboratory analysis methods to long experimental campaigns and field measurements. The "Comparative Reactivity Method" (CRM) by Sinha et al. [15] is currently used to measure OH reactivity (the inverse lifetime of OH, $1/\tau_{OH}$) in the field. Unlike other techniques that measure OH reactivity, the CRM does not rely on an optical technique (laser induced fluorescence or long-path absorption) to detect OH radicals directly. Rather, the reactivity of a sample is deduced by the relative change in the concentration of an artificially added reference compound, $[x]$; in essence, a relative rate experiment. The OH reactivity of a gas sample (R_{sample}), is measured using the scheme shown in fig. 1.1 and eq. (1.1);

$$R_{sample} = \left(\frac{[x]_C - [x]_B}{[x]_A - [x]_C} \right) k_x \cdot [x]_A \tag{1.1}$$

where k_x is the measured reaction rate of the reference compound x with OH.

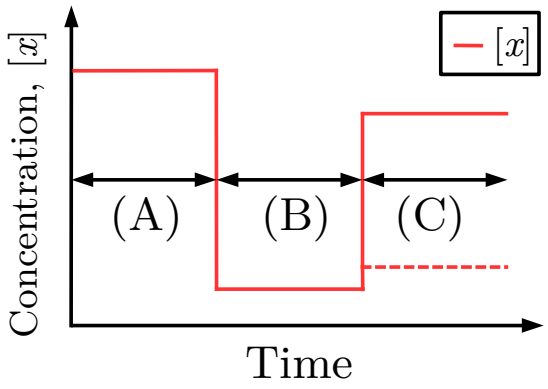

Figure 1.1: Figure showing the concept behind the comparative reactivity method (see section 1.3.4). Cases (A), (B) & (C) relate to the different operational conditions. (A): reference compound in purified (zero) air, (B): reference compound in zero air depleted by OH radicals, (C): reference compound diluted in the gas sample depleted by OH - the chemical components present in the sample compete with the reference compound for the available OH radicals, leading to recovery of the reference compound. The solid and dashed lines at (C) correspond to the high and low reactivity cases respectively.

In case (A), the chosen reference compound x, diluted in only zero air, (also known as

blank or purified air/nitrogen, well characterised and chosen for very low, approx. ≤ 0.1 ppm, total hydrocarbons) is monitored on leaving a flow tube kept at atmospheric pressure. Once a baseline concentration is established, some constant amount of OH is also introduced into the vessel, thus depleting some of the reference compound, giving case (B). After sometime, the zero air diluting x is replaced with the gas sample under investigation, case (C). Depending upon the sample composition, the measured concentration of x will then lie between the baseline, $[x]_A$ or the OH radicals and zero air case, $[x]_B$.

In other words, a gas mixture with low OH reactivity will result in $[x]_C$ being relatively close to $[x]_B$, with most/all of the available OH depleting x. For the case of high reactivity, the unknown compounds in the sample will compete with the reference for the available OH radicals, resulting in recovery of the reference compound. Similar to other techniques that measure OH-VOC reaction coefficients, a UV lamp (185 nm from Hg emission) is used to generate OH in a flow of humidified nitrogen [16].

Through repeating (A) $\rightarrow$ (B) $\rightarrow$ (C), measurements of OH reactivity are made during a field campaign. Techniques regularly used to directly measure ambient OH concentrations and reactivity around the globe are discussed in sections 1.3.3 and 1.3.4 respectively. These techniques have allowed for better constraint of the atmospheric OH budget and have identified "missing reactivity", probably due to unmeasured VOC. Benefits of the CRM compared with other techniques are twofold; the sample need not be completely characterised and no direct optical measurement of OH is needed to measure reactivity.

The production of radicals in a chemistry laboratory setting usually includes the use of flash lamps, lasers and microwave cavities. There is also a wide range of different chemical precursors used, thus there is a good selection of literature on the reactions of radicals with different volatile organic compounds, at ranging temperatures and pressures [8, 9].

From a plasma science viewpoint, molecular chlorine gas has been used extensively as a component in the typical gas mixtures used for semiconductor processing (see section 3.3.4). Thus the gas has been subject to modelling and experimental investigation by several research groups in low pressure inductively coupled plasmas (ICPs) [17–22]. With high enough concentrations, two photon absorption laser induced fluorescence (TALIF) has been used to

measure absolute atomic chlorine densities directly [23–26]. Studies have also shown that ICPs using attaching gases have been subject to instabilities as they transition between capacitive (E) and inductive (H) modes [27–31]. Unfortunately, due to the difficulty of handling chlorine at atmospheric pressure, there is an absence of literature on the use of molecular chlorine gas in atmospheric pressure plasmas.

This thesis aims to explain the investigation of an atmospheric pressure plasma source for the production of atomic chlorine and application to a novel method for measuring the reactivity of atomic chlorine in an air sample, based on the work by Sinha et al. [15]. The new aspects of this work was in the characterisation and use of a chlorine-containing low temperature plasma at atmospheric pressure. Volatile organic compounds were used to probe the short-lived radicals in the plasma effluent, with the resulting mixture sampled using proton transfer reaction mass spectrometry. Optical emission spectroscopy was also used to identify some of the species present within the plasma.

Due to the interdisciplinary nature of the thesis, both the background plasma science and atmospheric chemistry are discussed. Firstly, the fundamental plasma science is described, with detail about the relevant processes that occur with the presence of free electrons and the importance of the electron energy distribution function.

Secondly, the background atmospheric chemistry is introduced, with previous work investigating the role of OH in the atmosphere. The motivation for measuring reactivity and investigating Cl specifically is discussed.

1.2 Plasma science background

1.2.1 Plasma fundamentals

Plasma, often referred to as the fourth state of matter [32], is a mixture of unbound electrons, ions and often neutral particles in which the long-range electromagnetic force dominates (over thermal effects). Excited particles and electromagnetic fields are required to sustain plasma through a process called ionisation. This occurs when an excited particle (usually an electron or another charged species) collides with an atom or molecule, freeing another electron. Typically, external electromagnetic fields are used to transfer energy to the charged particles, inducing ionisation. Found both in nature and the lab, plasma is considered to be the state in which the majority of ordinary matter in the observable universe exists. For example, the polar aurorae and lightning are naturally occurring terrestrial plasma. Extending this beyond the Earth, both the interstellar medium and every living star are regarded as plasma.

Spread over vast temperature and density scales (see fig. 1.2), plasma is influenced and manipulated by electromagnetic fields. Because of the long-range electromagnetic force, plasma exhibits complex, collective behaviour such as oscillations, charge shielding and filamentation. Through taking advantage of these properties, artificially produced plasma is used for a wide range of applications; from energy production in inertial confinement fusion (ICF) and magnetic confinement fusion (MCF) to etching and deposition for the fabrication of integrated circuits.

Electrical charge screening is an important plasma characteristic. To demonstrate this concept, assume a positively charged point source is lowered into a plasma where the ions and electrons have the same magnitude and opposite charge. The charged species will all experience the same electrostatic force from the point source ($\mathbf{F} = q\mathbf{E}$). Because of their lower mass, the electrons start to accelerate towards the sphere more than the positive ions are repelled away ($\mathbf{F} = m\mathbf{a}$). For simplicity, we assume the ions are stationary compared to the electrons - due to their higher mass, the ions react much slower to the external electrostatic force from the point source. A cloud of electrons (with a few slow/stationary

ions) thus gathers around the positively charged sphere. Once a steady state is reached, there will be a point in space beyond which the electrostatic influence of the charged sphere into the rest of the plasma is cancelled out, and no more electrons are accelerated towards the sphere. The distance to this point from the sphere is called the Debye length (λ_{De}) and is defined as

$$\lambda_{De} = \left(\frac{\varepsilon_0 k_B T_e}{n_e e^2} \right)^{1/2}$$

where ε_0, k_B, T_e, n_e and e is the permittivity of free space, Boltzmann constant and electron temperature, density and charge respectively. As we assume the ions are stationary compared to the electrons, we only consider the electron temperature and density.

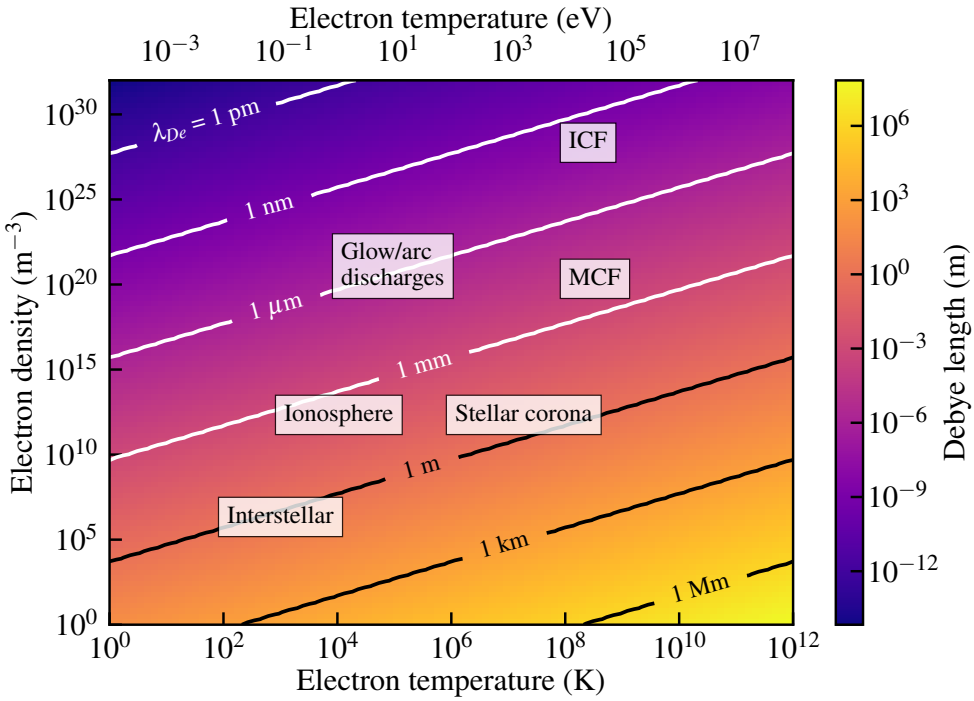

Figure 1.2: Electron density versus electron temperature, showing contours of constant Debye length, λ_{De} and examples of artificial and naturally occurring plasmas [33].

For an ionised gas to truly be a plasma, the size of the discharge must be greater than the Debye length. This is related to the property of quasi-neutrality, where the positive and

negative species densities are equal to one another on the macroscopic scale. This property breaks down when looking at microscopic volumes of plasma, considering external sources of electrons or within the plasma sheath (fig. 1.4) for example.

Related to the Debye length, the Debye number (N_{De}) is the number of electrons within a sphere of radius λ_{De} (also known as the Debye sphere).

$$N_{De} = \frac{4}{3}\pi\lambda_{De}^3 \times n_e$$

The Debye number should be sufficiently high to screen charges from outside the Debye sphere. The final criterion used to define a plasma is the electron plasma frequency. If the electrons in a slab of plasma are displaced by a distance δx (fig. 1.3) an electric field in the x-direction is generated to oppose the change. Similar to a damped mass on a spring, this results in the characteristic frequency, ω_{pe};

$$\omega_{pe} = \sqrt{\frac{e^2 n_e}{\varepsilon_0 m_e}} \tag{1.2}$$

which could be considered as the natural frequency of the plasma. For electrostatic interactions to dominate over ordinary gas kinetics, the electron plasma frequency (ω_{pe}) has to be greater than the electron-neutral collision frequency (ν_m).

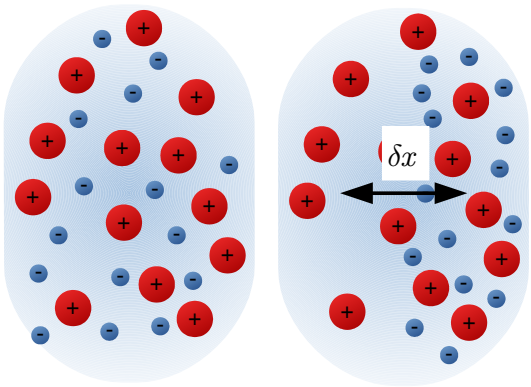

Figure 1.3: Before and after the perturbation of electrons in a plasma slab by some distance δx.

In the case of argon at atmospheric pressure (as is used in this work), the electron-neutral collision frequency is of the order 4.028×10^{12} s^{-1} [34]. Using equation eq. (1.2), and substituting in this electron-neutral collision frequency for the plasma frequency ω_{pe}, the theoretical minimum electron density needed to sustain an atmospheric pressure argon plasma would be $\sim5.1\times10^{21}$ m^{-3}. For radio-frequency driven, atmospheric pressure plasmas, the typical electron density is found to be roughly 1×10^{17} m^{-3} [35,36].

The reason for the experimentally measured value being lower than the theoretical minimum is due to the rate of collisions that occur at atmospheric pressure. Because of the high rate of collisions, the oscillatory motion of the electrons is lost and an average drift velocity (v_d) is assumed;

$$v_d = \mu_e E = \frac{eE}{m_e \nu_m}$$

where μ_e is the electron mobility and E is the applied electric field. Due to the electron mobility being at least two orders of magnitude greater than the ion mobility, the displacement of the ions is commonly neglected [34]. Thus the ions are generally governed by the gas kinetics and the electrons by the applied electric field.

Related to charge shielding, figure 1.4 shows the variation in ion and electron density and electric potential from a floating wall to the middle of a plasma. Due to the higher mobility of electrons than ions, the electrons are able to reach the surface first and transfer charge. The relative abundance of negative charge on the surface repels any further incoming electrons and accelerates ions that exit the plasma bulk. This leaves a net positive charge at the edge of the plasma bulk and is referred to as a sheath.

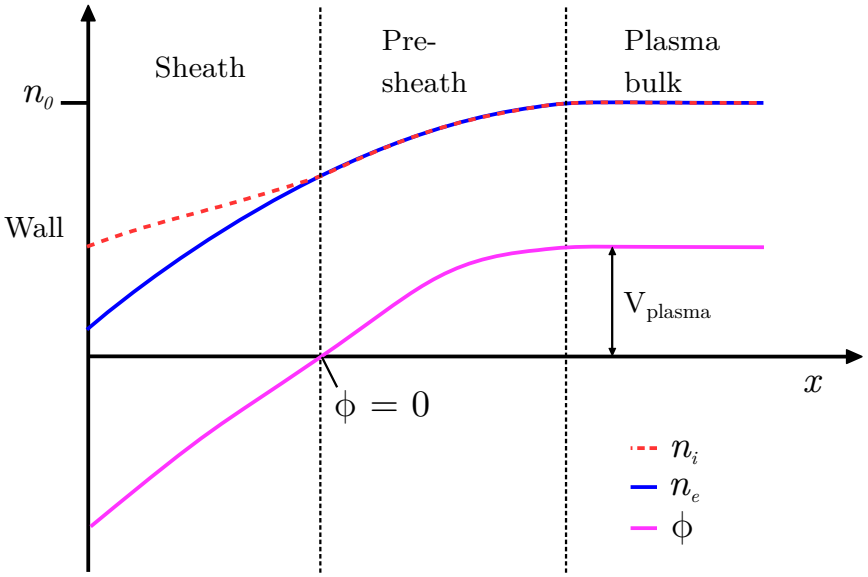

Figure 1.4: Example of the ion and electron density and potential across the sheath between the wall and plasma bulk.

In general, electromagnetic fields are used to sustain plasmas through the transfer of energy to the charged species. Physical properties such as the surface/volume ratio of the container, gas pressure, ionisation energy, molecular mass and degrees of freedom all effect the amount of energy that is required to sustain a plasma. This is best illustrated when considering varying the voltage between two parallel plates (separated by a distance d) with a chosen gas of pressure p between the plates. The voltage at which the gas breaks down and switches to being conductive is recorded, for varying p and d. Known as the Paschen curve (fig. 1.5), this breakdown voltage is plotted versus the pressure-distance product (pd).

For monatomic gases such as helium, argon and krypton for example, the minimum required breakdown voltage (V_{min}) is lower than that of molecular gases such as oxygen or nitrogen. As the extra degrees of freedom in molecular gases act to store energy, more energy (and thus higher voltage) is required to breakdown molecular gases. Noble gases with much lower degrees of freedom require a lower voltage to breakdown.

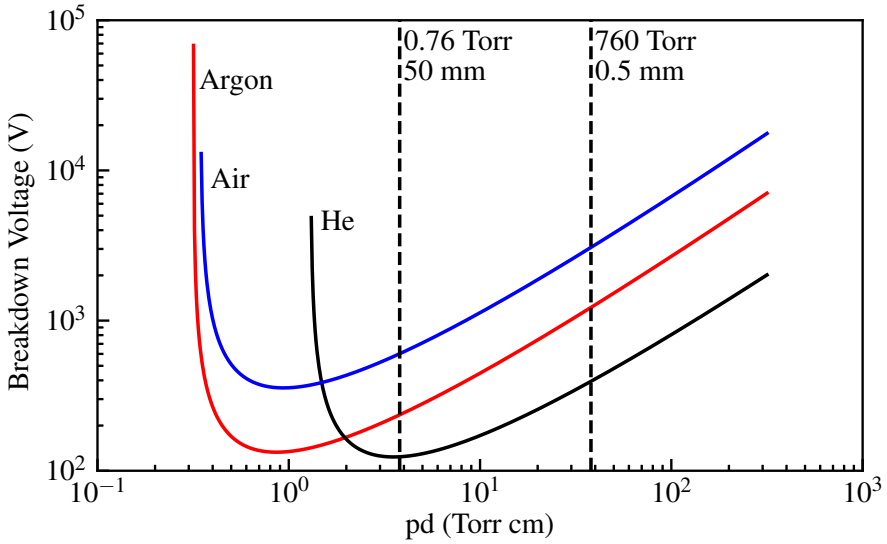

Figure 1.5: Paschen curves of air, argon and helium [37]. Breakdown voltage is plotted versus the pressure-length product.

The shape of the curves in fig. 1.5 can be explained by considering the electron mean free path and consequently, the frequency of ionisation events. At very low pd, ionisation events are rare, either because the region between the plates is close to being at vacuum or otherwise due to d being much smaller than the electron mean free path. As pd increases, the sudden drop in the breakdown voltage results from more frequent ionisation events (as the electrons already gain enough energy from the field to cause ionisation) until an optimum is reached. The pd of the minimum voltage (pd_{min}) will depend upon the collision cross section of the gas (which is proportional to its mass). From fig. 1.5, the average molecular mass of air and argon are relatively similar, thus they have a similar pd_{min}. The mass of helium is much less, thus a higher pressure is required to achieve the same optimum electron mean free path in helium. If the pd is increased further, collisions not resulting in ionisation start occurring more frequently, as electron energy is lost in collisions with the gas. The electrons simply do not have enough time to pick up energy from the applied field to cause ionisation.

1.2.2 Low temperature plasmas

In the case of atmospheric pressure, low temperature plasmas, the typical energy density and residence time mean that the system does not reach thermal equilibrium. Characterised by low ionisation degree and non-thermal equilibrium between electrons and heavier particles (atoms/molecules/ions), the proportion of heavy particles that exist as charged ions is heavily outweighed by those that are neutral. The electron energy distribution is generally not Maxwellian and strongly depends on the nature (pressure, power deposition, gas composition) of the discharge.

The electron temperature is typically a few thousand Kelvin (∼3 eV), while the neutral and ion population are close to room temperature. For inelastic processes such as electron impact dissociation (reaction 1.3) and excitation (reaction 1.4) there is an associated process-dependant threshold energy. Therefore, because of the electron energy distribution, there is a population of electrons with sufficient energy to enable processes such as dissociation (reaction 1.3, ∼3 eV threshold) and electronic excitation (reaction 1.4, ∼6 eV threshold):

$$AB + e^- \rightarrow A + B + e^- \tag{1.3}$$

$$AB + e^- \rightarrow AB^* + e^- \tag{1.4}$$

Other inelastic collisions such as ionisation (reaction 1.5, ∼10 eV threshold) or attachment (reaction 1.6, typically a very low ∼0 eV threshold) changes the electron energy distribution from being Maxwellian, through changing the number of electrons,

$$AB + e^- \rightarrow AB^+ + 2e^- \tag{1.5}$$

$$AB + e^- \rightarrow AB^- \tag{1.6}$$

Thus to model and investigate the plasma dynamics, the electron energy distribution function needs to be determined.

To calculate the electron energy distribution function (EEDF), the Boltzmann equation, eq. (1.7) can be solved using numerical techniques [38],

$$\frac{\partial f}{\partial t} + \boldsymbol{v} \cdot \nabla f - \frac{e}{m_e} \boldsymbol{E} \cdot \nabla_{\mathbf{v}} f = C[f] \tag{1.7}$$

where f is the electron distribution in six dimensional phase space, $\boldsymbol{v}$ is the velocity vector (v_x, v_y, v_z), e and m_e is the electron charge and mass respectively, $\boldsymbol{E}$ is the electric field, $\nabla_{\mathbf{v}}$ is the velocity-gradient operator and C represents the rate of change in f due to collisions. To solve the equation for f, spherical coordinates in velocity space are used to drastically simplify the system. An isotropic electric field and collision probabilities on the scale of the electron mean free path are imposed [38]. This method can be computationally complex and take some time to complete. Another way of determining the EEDF is by using the much more simplified technique of Gudmundsson [39], where the EEDF is defined by the equation

$$f(\varepsilon) = c_1 \varepsilon^{1/2} exp(-c_2 \varepsilon^x) \tag{1.8}$$

where

$$c_1 = \frac{x}{\langle\varepsilon\rangle^{3/2}} \frac{[\Gamma(\xi_2)]^{3/2}}{[\Gamma(\xi_1)]^{5/2}}, \quad c_2 = \frac{1}{\langle\varepsilon\rangle^x} \left[\frac{\Gamma(\xi_2)}{\Gamma(\xi_1)}\right]^x, \quad \xi_1 = 3/(2x), \quad \xi_2 = 5/(2x)$$

and $\Gamma(\xi)$ is the gamma function. The mean electron energy, $\langle\varepsilon\rangle = (3/2)T_{eff}$, where T_{eff} is the effective electron temperature. For Maxwellian and Druyvestyn distributions, $x = 1$ and $x = 2$ respectively (see fig. 1.6a). A concave energy distribution, highly populated at low energies with a pronounced high energy tail is also shown for comparison (using $x = 0.5$). The $x = 0.5$ case may be a loose approximation to those in low pressure systems. Druyvestyn distributions are typical for low ionisation degree, high pressure plasmas.

As mentioned earlier, many different productive and destructive processes occur due to the presence of free electrons. These include dissociation and electronic, vibrational and rotational excitation, depending on the gas(-es) used. The rates of these reactions depend on the electron energy distribution, itself a function of the gas mixture and externally supplied electromagnetic field. For example, a neutral chlorine molecule can undergo electron impact

ionisation, resulting in a molecular chlorine cation and an unbound electron. The rate of this process depends upon the mean electron energy and ionisation cross section.

The rate coefficient can be calculated using eq. (1.9),

$$k(T_{eff}) = \left(\frac{2e}{m_e}\right)^{1/2} \int_0^\infty \sigma(\varepsilon)\varepsilon^{1/2} f(\varepsilon) d\varepsilon \tag{1.9}$$

As shown in fig. 1.6, the EEDF has a significant impact on the resulting rate coefficients [40]. The cross section for each process is unique to each atom, molecule and vibrational/electronic/rotational excited state. The cross section for ionisation and attachment are relatively easier to measure, as they produce charged products. Cross sections for other processes, such as vibrational and electronic excitation sometimes require ab initio calculations to determine the cross section.

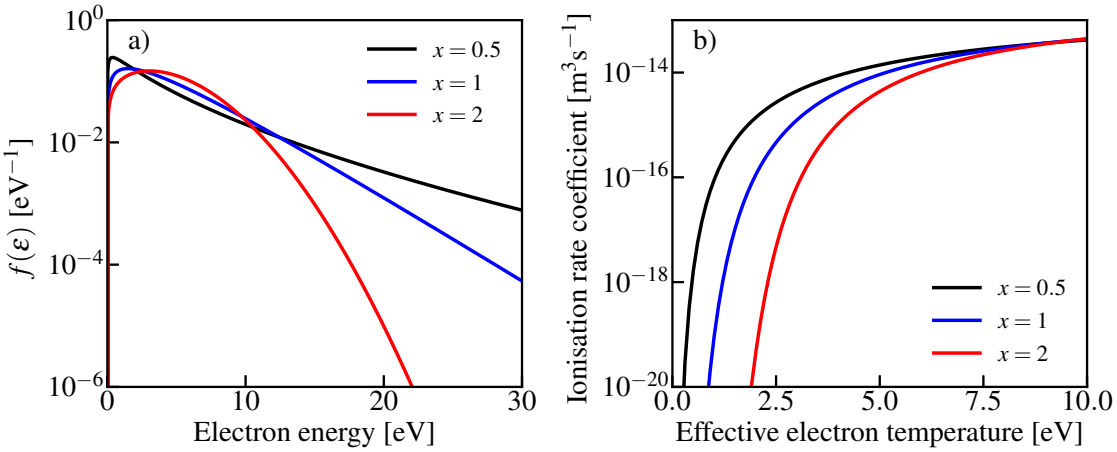

Figure 1.6: a) Electron energy distribution function for an effective electron temperature of 3 eV, calculated using eq. (1.8) with variation of x. b) Calculated single ionisation rate coefficient using the Cl_2 cross section from Basner and Becker [41](section 3.3.1) and the EEDFs in a) using eq. (1.9).

Depending on the gas, the plasma may also contain electro-negative species, altering the dynamics of the plasma bulk. This can complicate the plasma chemistry due to the unique spatial structure of the discharge. The dynamics of the plasma are also manipulated by the

power deposition profile, whether the plasma is an ICP or CCP (see fig. 1.7), the driving frequency, and waveform shape amongst other factors.

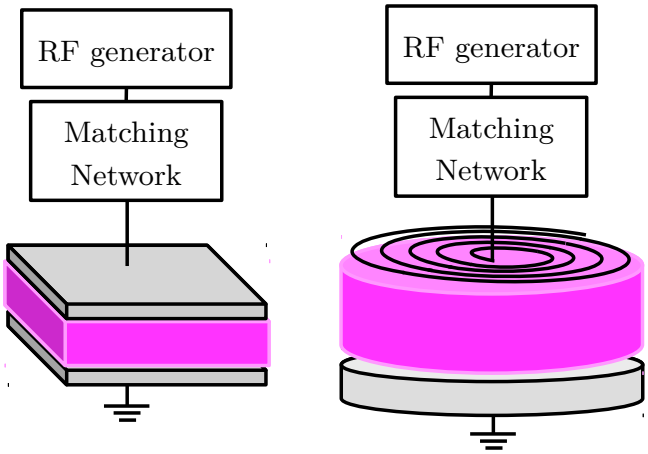

Figure 1.7: Typical configuration of plasma power delivery. Left: capacitively coupled plasma (CCP), right: inductively coupled plasma (ICP).

In radio-frequency driven, atmospheric pressure plasmas, 13.56 MHz or higher harmonics of it are used to couple energy into the charged plasma species. The reason 13.56 MHz is specifically chosen is to adhere with the band defined as for industrial, scientific or medical applications by the International Telecommunication Union. Due to the high mobility of the electrons, they are much more able to respond on the timescale of the changing electric field, thus most of the energy supplied ends up with the electrons, thus the rate coefficients for all the electron-driven processes are critical.

1.2.3 Swarm parameters

Swarm parameters is a term used for a collection of electron transport properties, such as drift velocity and the Townsend ionisation and attachment coefficients. These measured properties emerge from the unique electron-impact cross section for a given gas. Thus they are sometimes used to provide evidence if a cross section is close or not to the true, unique cross section. They are usually plotted versus reduced electric field (electric field E/ total

gas density N) with experiments done at several different pressures and gas mixtures [42].

1.2.4 Optical emission spectroscopy

As mentioned previously, there are several processes that cause excitation of the plasma species. Once these species are in a higher excited state, they can spontaneously decay to a lower state and emit a photon of equivalent energy to the difference between higher and lower states. Optical emission spectroscopy (OES) is a passive diagnostic technique that can identify the different species in the plasma through collecting these photons. It is also possible to use the emission to measure the temperature of some molecular species [43].

The reason it is called a passive spectroscopy technique is because it only collects plasma emission. Unlike active methods such as laser induced fluorescence or Thomson scattering that use a laser to probe for a specific plasma process that then results in characteristic emission.

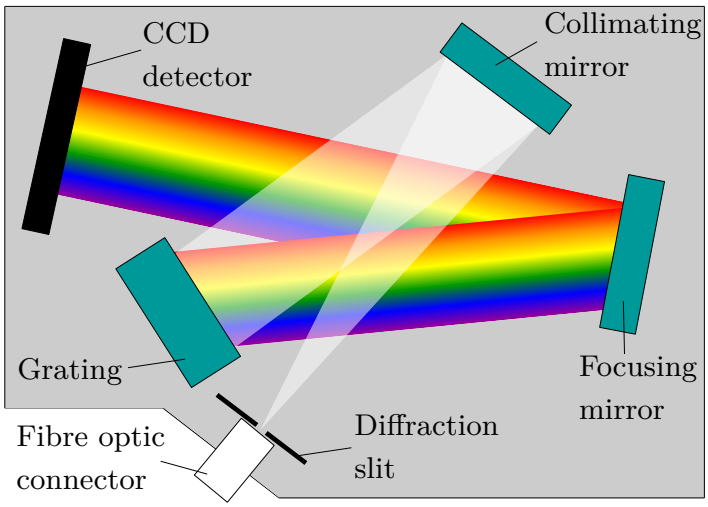

Figure 1.8: Schematic of a spectrometer similar to the ones used in this work.

In this work, two different spectrometers were used. One was used for broadband light (196.03–1119.76 nm) and another at higher resolution for considering UVA and UVB bands (294.44–393.78 nm). Both use the same operational layout as shown in fig. 1.8. Light is collected using a fibre optic and is passed into the spectrometer where it first passes through

a diffraction slit. This light is then collimated using a mirror onto a diffraction grating. The resolution and wavelength range of the spectrometer depend upon the groove density of the grating. A focussing mirror is then used to focus the light onto the CCD, which can then be processed. In this work, emission from OH radicals, N_2 molecular rotational bands and oxygen and argon atoms are the most relevant.

1.3 Atmospheric chemistry background

1.3.1 The atmosphere

The Earth's atmosphere is a partially closed photochemical reactor, with a continuous flux of matter that is emitted, transported and converted [44]. Numerous different mechanisms and catalytic cycles exist due to the vast array of possible chemistry and the physical scale of the atmosphere. Laboratory studies, field measurements and modelling are used synergistically to help develop our understanding of the atmosphere. For example, field measurements taken from different parts of the globe (i.e. data collected by satellites or planes, by weather stations on land and sea) are used to inform 3-D models of the atmosphere. To investigate the predictions of these models, small-scale field measurements are conducted, helping to highlight areas of significant scientific interest. Alongside this, carefully controlled laboratory experiments and simulations are used to investigate reaction kinetics and inform the input and assumptions of the models further. Through development of these parallel laboratory studies, new measurement techniques can be suggested for use in the field [45].

In general, chemical sources in the atmosphere can be split into three categories: biogenic, anthropogenic and radiogenic emissions. Respiration of flora and fauna is a biogenic source of carbon dioxide and water into the troposphere. Paddy fields and ruminant livestock are major anthropogenic sources of atmospheric methane. The α decay of radium-226 is an example of a radiogenic source of radon-222. Biogenic emissions of non-methane hydrocarbons (NMHC) is also of particular relevance, having great range of variety and quantity across the globe.

Once emitted, species transport and chemistry occur. Powered by temperature and

pressure gradients in the atmosphere (fig. 1.9), vertical and horizontal mixing of air currents promote the transportation of moderate and long-lived species across the globe (fig. 1.12).

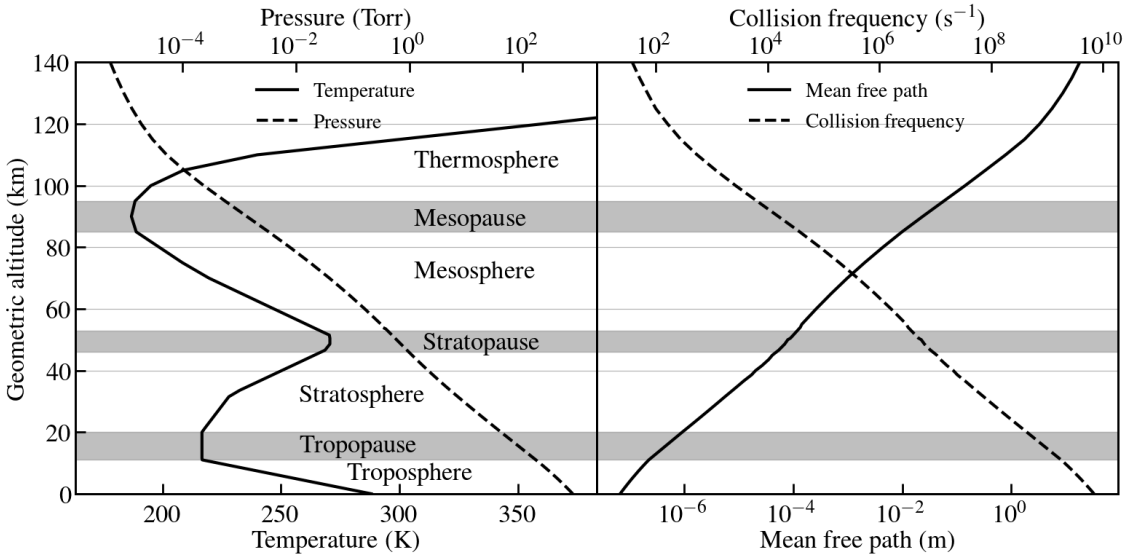

Figure 1.9: Structure of the atmosphere using US standard atmosphere data [46].

In the case of short-lived species, i.e. hydroxyl or nitrate radicals, transport is generally neglected and local processes are assumed to dominate. In other words, if the chemical lifetime is short compared with the transportation timescale, only direct, local conditions are considered. In the scope of this thesis, the troposphere is only treated, with the chemistry of the stratosphere and above being considerably different (see figure 1.9). At the end of the species lifetime, destruction mechanisms such as wet (relevant for water soluble compounds), dry deposition and escape from the atmosphere into space occur, depending upon the species. In the case of the short-lived species considered here, gas phase chemical reactions are the main sink.

1.3.2 Radical-initiated chemistry

Defined as an atom, molecule or ion with an unpaired valence electron, radicals are an integral part of chemistry [47]. The main source of radicals in the atmosphere comes from photolysis

of chemical bonds via sunlight. Paired electron bonds are broken leading to unpaired radical products. Thus there is strong temporal variability in ambient radical concentrations.

Short lived free radicals such as hydroxyl (OH) play an important role in the oxidative capacity of the atmosphere. The initiation and rate limiting step of the oxidation of volatile organic compounds (VOCs) in the troposphere depend upon these highly reactive, intermittent species. The breakdown and removal of VOCs in the atmosphere depend on the local ambient radical-mediated reactivity (or loss rate in s^{-1}). Other important atmospheric oxidants include hydroperoxyl (HO_2), nitrate (NO_3) and alkyl peroxide radicals (RO_2) as well as ozone (O_3). In the troposphere, radicals generally have short lifetimes, low time-averaged ambient concentrations and high spatio-temporal variability because of the availability of VOC (fig. 1.12). Above the troposphere, the general availability of VOC reduces, (and mean free path increases, see fig. 1.9) thus the lifetime of radicals generally gets longer.

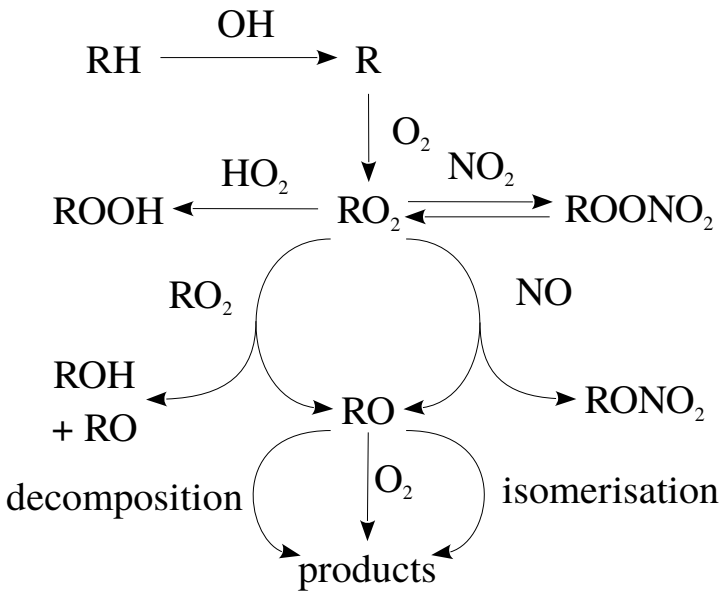

Figure 1.10: Breakdown of alkanes in the atmosphere, based from figure in [48].

Volatile organic compounds include but are not excluded to: aliphatic, aromatic and oxygenated hydrocarbons, diols, and halocarbons. A general oxidation and removal scheme

of these species is shown in fig. 1.10. For example, terpenes, a range of VOCs produced by plants, can be attacked by OH, NO_3 or O_3 and oxidised. This is shown in fig. 1.11 in the oxidation of d-limonene (a terpene that smells of oranges) initiated by OH. Firstly, an OH radical adds itself to the carbon-carbon double bond in the cyclohexene ring. Due to the abundance of molecular oxygen in air, O_2 rapidly adds itself to the other end of the double bond, forming a peroxy radical [fig. 1.11b)]. The RO_2 radical then reacts with NO to form NO_2 and an RO radical [fig. 1.11c)]. This RO radical eventually terminates, after reaction with O_2 leaving fig. 1.11d).

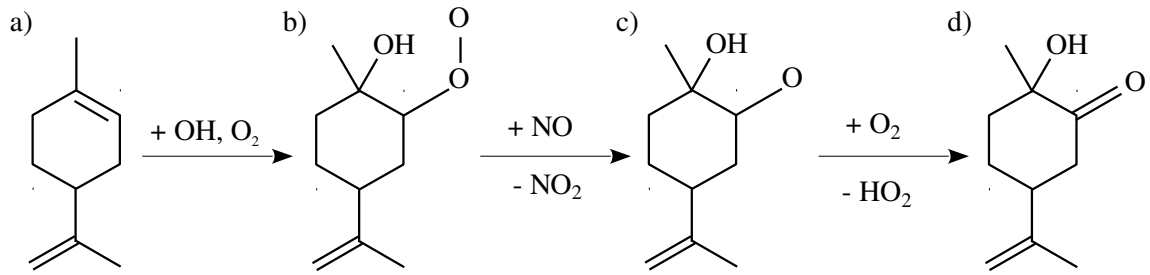

Figure 1.11: Oxidation of d-limonene to one of many different stable products. The smallest number of oxidation events until the original d-limonene is reduced to CO_2 and H_2O is approx 20/30 [49, 50]. The detailed pathway is to some extent dependent on environmental factors, notably pressure, temperature and the availability of OH, NO and NO_2.

Transient species concentrations can either be measured directly or calculated using the relevant destruction and production rates. For example, methane has several emission sources that are highly uncertain and variable, with many relying on the climate [52]. The main destruction mechanism of methane is reaction with OH to form water and a methyl radical. This reaction is highly dependent upon temperature (see fig. 1.13).

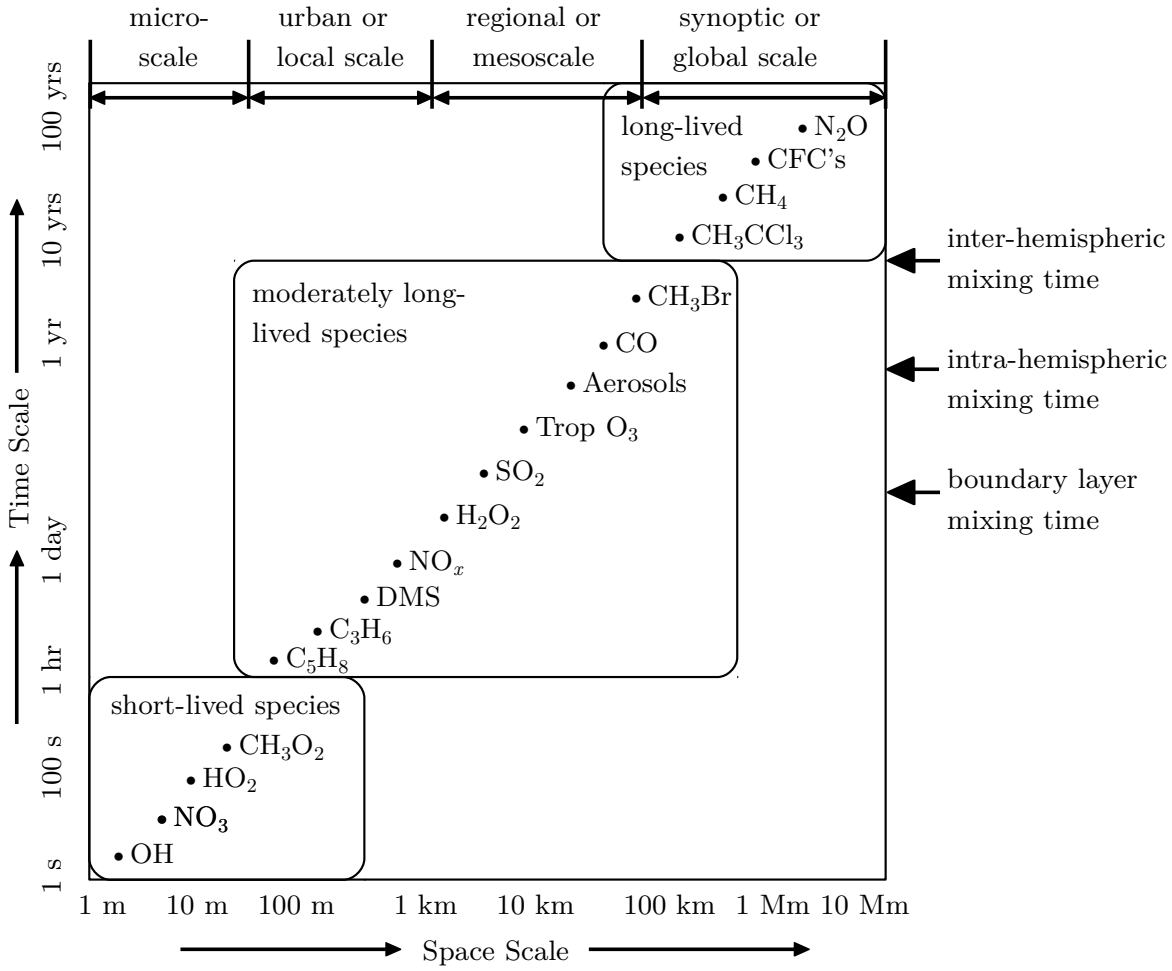

Figure 1.12: Spatio-temporal scale for many relevant atmospheric species. OH = hydroxyl radical; NO_3 = nitrogen trioxide; CH_3O_2 = methyl peroxy radical; C_5H_8 = isoprene; C_3H_6 = propene; DMS = dimethyl sulfide; CH_3CCl_3 = methyl chloroform; CH_3Br = methyl bromide. Based on a figure from [51].

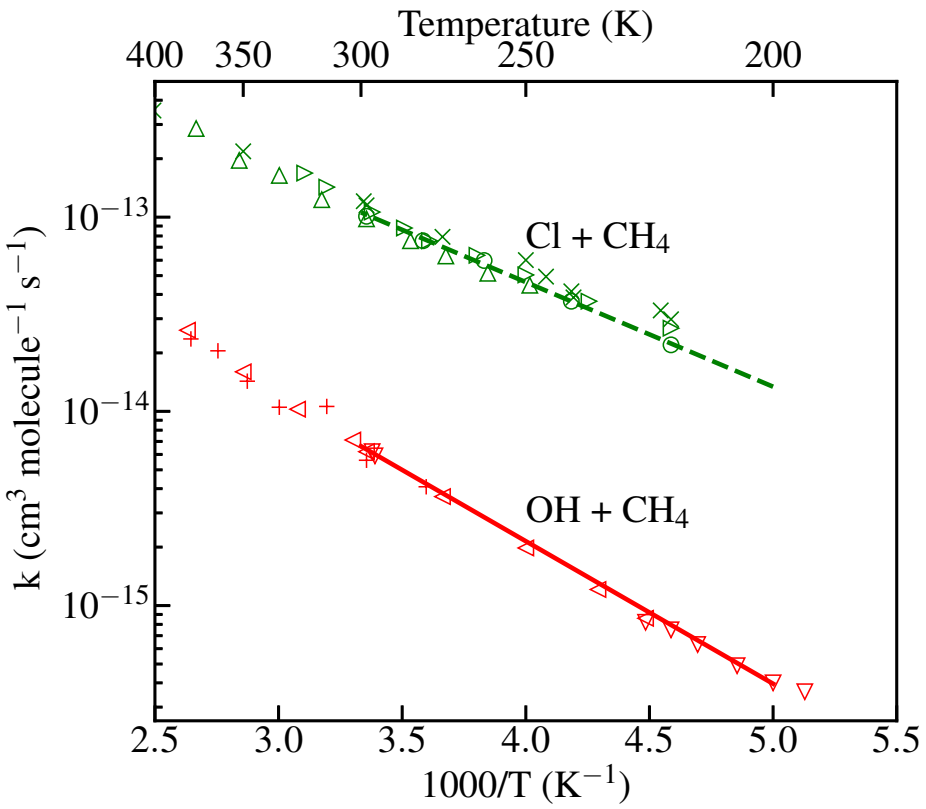

Figure 1.13: Arrhenius plot of the Cl + CH_4 and OH + CH_4 reactions, (–) IUPAC recommended k(T). For the Cl + CH_4 reactions: (×) Watson et al. [53], (△) Ravishankara and Wine [54], (▷) Manning and Kurylo [55], (◯) Wang and Keyser [56]. For OH + CH_4 reactions: (◁) Vaghjiani and Ravishankara [57], (+) Finlayson-Pitts et al. [58], (▽) Gierczak et al. [59].

The spatio-temporal concentration of OH around the globe also varies. The main production of OH is through the photodissociation of ozone by ultraviolet sunlight [60],

$$O_3 + h\nu(\lambda < 330 \text{ nm}) \rightarrow O(^1D) + O_2$$

and then subsequent reaction with water vapour,

$$O(^1D) + H_2O \rightarrow 2OH$$

Thus the lifetime of methane ranges from a few years over tropical rainforests (typically high [OH] and temperature) to a few thousand years over polar regions.

On the other hand, compounds such as nitryl chloride ($ClNO_2$) and formaldehyde (CH_2O) are photolysed in the atmosphere. Formaldehyde for example, is quickly photolysed into hydrogen and carbon monoxide or oxidises into formic acid in the order of a few hours. Molecular hydrogen and carbon monoxide then have lifetimes of a few years and months respectively. To understand the relative concentration and role of the various atmospheric species, their kinetics, i.e. rate coefficients with reactive species must be investigated.

1.3.3 Hydroxyl measurements

For measuring the rate coefficients of short-lived atmospheric species with volatile organic compounds, several different techniques have been used. These include discharge flow resonance fluorescence [56, 61–63], flash photolysis resonance fluorescence [55], pulsed laser photolysis resonance fluorescence [54, 64], pulsed laser photolysis laser induced fluorescence [65] and relative rate [66]. All of these studies have added to the collection of reaction rates used in atmospheric chemistry models [67].

In several of these cases, microwave cavities have been used to produce the short-lived species under investigation. For example, in the measurement of the CH_4 + Cl reaction by Wang and Keyser [56] a 2.45 GHz microwave cavity at 1 Torr using a mixture of Cl_2 and He is used to produce atomic chlorine. The stated dissociation "efficiency" was around 55%, producing up to 4.1×10^{11} atoms/cm^3.

The detection methods of these techniques have been adapted so that field measurements are possible. For example, "Differential Optical Absorption Spectroscopy" (DOAS) [68] has been used as a method to measure the concentration of OH and many other radicals [68, 69]. In this technique, the Lambert-Beer law,

$$T = \frac{I_T}{I_0} = \exp(-A), \quad A = \sigma(\lambda) \int_0^L n_{\mathrm{OH}} dl \tag{1.10}$$

is used to measure the line integrated absolute density of OH ($\int_0^L n_{\mathrm{OH}} dl$). In equation 1.10, T is the transmission, A is the absorption of a specific line, I_T is the measured light

intensity at the line centre (λ_0) of an absorption transition, I_0 is the measured light intensity at the same wavelength without absorber, $\sigma(\lambda)$ is the effective absorption cross section at λ, L is the total path length of the light through the absorber. The accuracy of the technique is limited by the error of the effective absorption cross section σ and signal-to-noise ratio. The benefit of this technique is that it gives absolute densities without the need for calibration. The drawback is that a very large (approx. 5 km) path length is required, thus the spatial resolution is poor. For example, if the concentration of OH is required at a specific location to verify other measurements, using DOAS would not be viable. The sensitivity of the technique is also dependent on the path length, compounding this issue.

Another direct analytical technique, called "Fluorescence Assay by Gas Expansion" (FAGE) [70–73], uses laser induced fluorescence to measure [OH]. As is mentioned in the review by Heard [71], there are several quite severe issues with measuring ambient OH density in the atmosphere. These include the typically very short OH lifetime (less than a second) with concentrations of around 0.1 part per trillion by volume (pptv). With the removal rate of OH depending on the concentration of pollutants or surfaces, and the production rate depending mainly on sunlight intensity, the resulting spatial OH density can vary dramatically, making the design of any instrumentation troublesome.

In FAGE, ambient air is continuously sampled, drawn through a small 1 mm ID nozzle into a large volume vessel that expands the gas to low pressure. Laser-induced fluorescence is used to detect OH. The gas sample is primarily reduced to low pressure to reduce the amount of collisional quenching of the upper excited state, leading to a longer-lived observed signal. The low pressure environment also reduces Rayleigh, Raman and Mie scattering. The measured signal used to infer the OH density for FAGE is from the 308 nm $A^2\Sigma^+ \rightarrow X^2\Pi_i$ transition.

To calibrate this technique, a series of different methods have been used [74]. The two main methods are: the production of OH from UV-photolysis of water vapour or the production of OH from the steady-state reaction of ozone with alkenes.

As well as the techniques already mentioned here, there are several direct mass spectrometry methods that measure the compounds in air that are reactive to OH. For example, chem-

ical ionization mass spectrometry (CIMS) [75] has branched out into many different mass spectrometry methods, such as proton transfer reaction mass spectrometry (PTR-MS) [76], thermal- desorption proton-transfer-reaction mass spectrometry (TD-PTR-MS) [77], proton transfer reaction time-of-flight mass spectrometry (PTR-TOF-MS) [78] and selected ion flow tube mass spectrometry (SIFT-MS) [79].

To get a sense of the extensive use of PTR-MS/PTR-TOF in the field, it has been used in such broad applications as in the monitoring of VOC from a burning barn full of hay and straw [80], human emissions during a football game [81] and by a cinema audience [82]. It has also been used in long-term atmospheric measurements along the eastern U.S. coast [83], in the amazon [84] and northern India [85]. The review by Ellis et al. [86] includes many other examples of the application of PTR-MS, such as in plant studies, food science and medical applications.

To help understand the role of OH, the measured data from several different field experiments have been compared to models [84, 87–89]. There are several large-scale models that are used to simulate and predict atmospheric composition, such as GEOS-chem [90] and Logan et al. [91].

1.3.4 Reactivity measurements

Combining the knowledge of the known reaction rates and measured concentrations, the loss rate of OH can be calculated. Also known as the reactivity of OH, it is equivalent to the sum of the compound concentration multiplied by the compound rate coefficient with OH for all the compounds in the sampled air mass,

$$\begin{aligned} R_{\mathrm{OH}} = \tau_{\mathrm{OH}}^{-1} = k_{\mathrm{OH+CH_4}}[\mathrm{CH_4}] + k_{\mathrm{OH+CO}}[\mathrm{CO}] + k_{\mathrm{OH+OVOC}}[\mathrm{OVOC}] + \ldots \\ \ldots + k_{\mathrm{OH+NO_2}}[\mathrm{NO_2}] + k_{\mathrm{OH+NMHC}}[\mathrm{NMHC}] + \ldots \end{aligned} \tag{1.11}$$

where OVOC and NMHC are oxygenated volatile organic compounds and non methane hydrocarbons respectively. Radical propagation of OH leads to atmospheric oxidation with a significant number of direct observational studies of OH concentrations and reactivity already. These include studies by V. Sinha et al. [15, 85, 92–94], D. Heard et al. [71, 95], F.L.

Eisele et al. [75], A. Hofzumahaus et al. [96], P.S. Stevens et al. [74, 97, 98] and reviews by R. Atkinson et al. [99–101].

As mentioned previously, the reactivity of OH with ambient air has been measured using the comparative reactivity method (CRM), itself a variant on more traditional relative rate experiments [15, 92–94, 102]. Although this technique requires high radical concentrations, careful selection of a reference compound is used to infer the OH reactivity of the sampled air. This method assumes that only the single radical species investigated reacts with the selected reference compound, x and the chemical components of the sampled ambient air (not at all with the zero air). Another assumption is that no secondary chemistry occurs between the product of OH + x and OH and that the reference compound concentration is higher than the radical concentration, i.e. $[x] > [\mathrm{OH}]$. This is so that the radicals are completely titrated by the reference compound.

To be suitable, the reference compound x should meet the following criteria:

1. must be volatile so that it can be made into a good bottled standard;
2. well established rate coefficient with OH;
3. competitive rate coefficient with OH, comparable with other reactive species in ambient air;
4. be easily detectable using a suitable technique;
5. not be present at comparable concentrations in ambient air, as not to interfere with the detection method.

At the beginning, the VOC reference compound x is introduced into a glass reaction vessel diluted with zero air, and its concentration ($[x]_A$) kept constant. After some time, artificially created OH radicals are introduced into the reactor, and through reactions with x, the radicals are completely titrated. This gives concentration $[x]_B$. The zero air diluting the reference compound is then stopped and replaced with actual ambient air or a pre-made gas standard for calibration. The concentration of reference compound and artificially created [OH] radicals entering the reactor stays the same. The artificially produced OH radicals

then react with the VOCs and other compounds in the ambient air, which means that the concentration of the reference compound changes to $[x]_C$ due to competition.

Assuming $[x] > [\mathrm{OH}]$, the first order loss rate coefficients of OH in its reactions with $[x]$ and air are given by $R_x = k_x[x]$ and $R_{air} = k_{air}[air]$. The two following equations describe the sinks of OH radicals:

$$\mathrm{OH} + [x] \rightarrow products$$

$$\mathrm{OH} + air \rightarrow products$$

The corresponding rate equation for the concentration of OH in the reactor with the reference VOC and air is thus:

$$-\frac{d[\mathrm{OH}]}{dt} = k_{\mathrm{OH}+x}[\mathrm{OH}][x] + k_{\mathrm{OH}+air}[\mathrm{OH}][air]$$

If all the OH is lost through reactions with x and air, the relative loss of OH by R_x and R_{air}, i.e. between $[x]_A$ and $[x]_C$ is given by:

$$[x]_A - [x]_C = \frac{R_x}{R_x + R_{air}}[\mathrm{OH}]$$

We know however, that the concentration of OH is equal to $[x]_A$ - $[x]_B$ as it is titrated using the reference VOC:

$$[x]_A - [x]_C = \frac{R_x}{R_x + R_{air}}([x]_A - [x]_B)$$

After rearranging this equation, we get:

$$R_{air} = \left(\frac{[x]_A - [x]_B}{[x]_A - [x]_C} - 1\right) R_x$$

however we know that $R_x = k_x \cdot [x]_A$ so therefore:

$$R_{sample} = \left(\frac{[x]_A - [x]_B}{[x]_A - [x]_C} - 1\right) k_x \cdot [x]_A$$

after rearranging,

$$R_{sample} = \left(\frac{[x]_C - [x]_B}{[x]_A - [x]_C} \right) k_x \cdot [x]_A$$

The limit of the inequality, $[x] >$ [OH] is governed by the instrumental limit of quantification. For example, given a value of $[x]/[\mathrm{OH}] = 10$, with a typical value of [OH] $\simeq 1 \times 10^{12}$ molecules cm^{-3}, assuming $k_{OH} = 1.20 \times 10^{-10}$ cm^3 molecule^{-1} s^{-1} and true OH reactivity of 5 s^{-1}, the difference between $[x]_B$ and $[x]_C$ would be ~0.2 ppb. With the baseline $[x]_A$ being 3 orders of magnitude greater (400 ppb) it would not be possible to distinguish $[x]_B$ and $[x]_C$ from noise. For example, in the work by Sinha et al. [15] a value of $[x]/[\mathrm{OH}] = 1.22$ was used, using proton transfer reaction mass spectrometry to measure $[x]$. Similarly, in this work $[x]$ will be measured using PTR-MS [76] (see chapter 2).

Studies comparing the CRM measured total OH reactivity with the OH reactivity calculated using eq. (1.11) has shown there is a large OH-reactive component that is not accounted for (in eq. (1.11)). The resulting 'missing' OH reactivity (see figure 1.14) is likely due to unmeasured NMHC, OVOC and perhaps SO_2 for example. This has also been shown in several different studies [92, 103].

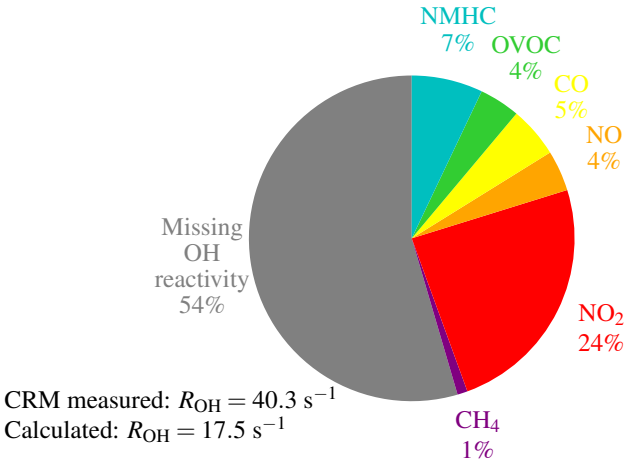

Figure 1.14: Figure showing the discrepancy between CRM-measured and calculated (using eq. (1.11)) OH reactivity (R_{OH}) in Paris [92]. NMHC = non-methane hydrocarbons, OVOC = oxygenated volatile organic compounds.

What this could mean is that there is incomplete knowledge of the sinks of OH, or of the rate coefficients of the OH + VOC reactions. Another possibility is that we currently underestimate the effect of short-lived radicals upon the reactivity of OH in ambient air.

To take advantage of the CRM, we could consider replacing OH in this method with Cl to measure the reactivity to Cl of the sample. This could give us new information on atomic chlorine radical reactions in the atmosphere.

1.3.5 Atomic chlorine chemistry

Historically, atomic chlorine in the atmosphere was originally studied for its impact in the stratosphere, specifically on ozone layer depletion in the 1970/80s [104]. Due to the long lifetime of CFCs and HCFCs, they would be able to reach the stratosphere, where they would be photolysed by solar UV radiation. The atomic chlorine produced would then take part in the catalytic destruction of ozone.

Following on from this, tropospheric chlorine has also been studied. Through mixing of sea salt aerosol with humid air it is known to be a source of chemically active chlorine compounds for a number of years [105–109]. The main source of active chlorine atom precursors was thought to be from sea spray, as ionic chlorine in sea salt is thrown into the air which then reacts with water or OH, possibly also in aerosol surface reactions - see reactions 1.12, 1.13 and 1.15.

Similar to hydroxyl, atomic chlorine radicals in the atmosphere are thought to play an important role in the oxidative budget of the atmosphere. Recent studies suggest that chlorine atoms are important in daytime oxidation, have larger concentrations and are more geographically extensive than previously thought [6, 13, 110]. The sources of atomic chlorine are still much more uncertain however, with various different pathways considered, such as the photolytic breakdown of $ClNO_2$. Starting with the acid displacement reactions,

$$HNO_{3(g)} + NaCl_{(aq)} \rightarrow HCl_{(g)} + NaNO_{3(aq)} \tag{1.12}$$

$$H_2SO_{4(g)} + 2NaCl_{(aq)} \rightarrow 2HCl_{(g)} + Na_2SO_{4(aq)} \tag{1.13}$$

HCl is produced which then goes on to react with other compounds in the air. These include hydrocarbon radicals, nitrogen oxides, hydroxyl radicals etc:

$$N_2O_{5(g)} + HCl_{(aq)} \rightarrow ClNO_{2(g)} + HNO_{3(aq)} \tag{1.14}$$

$$OH_{(g)} + HCl_{(g)} \rightarrow H_2O_{(l)} + Cl_{(g)} \tag{1.15}$$

Reaction 1.14 occurs between NO_x ($N_2O_5 \rightleftharpoons [NO_2^+][NO_3^-]$) in the air and Cl^- from moisture. After this, the photolytic breakdown of $ClNO_2$ releases active chlorine radicals:

$$ClNO_2 + h\nu \rightarrow Cl + NO_2 \tag{1.16}$$

What this succession of reactions can tell us is the source of Cl atoms. If there is a correlation between $ClNO_2$ and N_2O_5 then that would suggest that the original source of Cl is from anthopogenic sources as nitrogen oxides have very low concentrations in the marine boundary layer (MBL). If they do not correlate and other evidence suggests that OH is important, then this would suggest air from the MBL.

In Thornton et al., a different source of active Cl was inferred from measuring the concentration of nitrogen oxides during February 2009 [13]. The concentration of $ClNO_2$ and N_2O_5 was measured over the course of 14 days in Boulder, Colorado. The air masses that entered this location were from adjoining cities (urban plume) and from the Rocky Mountain region (cleaner air), no marine plumes were expected to be observed, as Boulder is far away from the nearest sea. The results of the study showed that a large amount of the tropospheric Cl source was anthropogenic and confined to polluted regions. It also showed that the concentration of Cl was highest in the morning, due to reaction 1.16.

Unfortunately direct absolute atomic chlorine concentration measurements are not feasible in the field, due to the complexity and absorption of VUV photons by H_2O and O_2. Laser methods such as FAGE and DOAS are not feasible as the wavelength absorbed by Cl-atoms (133–138 nm) [111] is also absorbed by several common atmospheric gases, notably O_2 and H_2O. Therefore an alternative method must be used. As mentioned earlier, it may

be possible to infer [Cl] by measuring production (P_{Cl}) and loss rates [44], assuming steady state of Cl;

$$\frac{d[\mathrm{Cl}]}{dt} = P_{\mathrm{Cl}} - k[\mathrm{Cl}] = 0$$

where k is the first order decay constant. However, given the problems with using VUV absorption, it would be difficult to use direct (e.g. FAGE) detection of Cl even at the elevated levels used in a reactivity instrument. Therefore an instrument using the same methodology as the competitive reactivity method may be more successful.

Due to the absence of a reliable source of chlorine radicals, there are few direct atmospheric observations of the Cl reactivity of air. This hinders the power of various chemical models and stops us from fully understanding how much Cl atoms contribute to the oxidation potential of the atmosphere. As elucidated in Simpson et al., there is a need for further measurements of reactive halogens in the troposphere as well as for better instrumentation and alternative measurement techniques [112].

1.4 Thesis outline

Chapter 2 describes the proton transfer reaction mass spectrometer that was used in the characterisation and investigation of the plasma effluent. The experimental setup and validation of the mass spectrometry measurements using prepared gas standards and calibrated mass flow controllers is given.

Chapter 3 explains the plasma model used to simulate the plasma. The currently published data for modelling chlorine-containing plasmas is reviewed in light of the plasma model used. Pathway analysis and results of the simulation are given.

Chapter 4 presents the results from the optical emission spectroscopy of the plasma, with mass spectroscopy results with using benzene mixed into the plasma effluent. The choice of reference compound is explained with variation of chlorine admixture in the plasma. The use

of a isoprene and toluene mixture polluted air proxy in a series of reactivity measurements.

Chapter 5 gives the conclusions of the thesis and suggestions of some areas of improvement for the experimental setup. The potential of using CRM over direct techniques and future work to develop a Cl-CRM is discussed.

Chapter 2

Reactor characterization by proton transfer reaction mass spectrometry

This chapter describes the experimental setup and proton transfer reaction mass spectrometer used for gas sampling. Verification of measurements taken using the PTR-MS is given with description of the calibration technique with prepared gas standards. The production of the gas standards and calibration of the mass flow controllers is also described.

2.1 Experimental setup

Chlorine radicals have been produced using a variety of different techniques. At atmospheric pressure, UV lamps with a specific chemical precursor are commonly used to produce atomic chlorine. Unfortunately, due to the low photo-dissociation rate of these lamps, chemical interference from the precursor is possible. This can happen due to the precursor reacting with atomic chlorine, ambient air, the VOC under investigation and/or the detector itself. To minimise this effect, a more efficient process can be used for generating atomic chlorine, requiring less chemical precursor. A more chemically stable and safe precursor can also be

chosen. Another difficulty with using chlorine is the possibility of atomic chlorine recombining with itself in the gas phase and at the container walls, shortly after being dissociated. For simplicity and ability to more closely model the resulting plasma, molecular chlorine gas was chosen as the precursor.

The overarching experimental design should optimise the conversion of molecular chlorine. To do this, the plasma source takes advantage of low lying electron impact dissociative processes such as dissociative attachment and electronic excitation to anti-bonding levels (see chapter 3). Additionally it has been shown for similar plasma sources that using 40.68 MHz driving frequency results in greater dissipated plasma power than for lower harmonics of 13.56 MHz with the same input voltage [113]. This allows for greater input power while avoiding arcing. As the electron density is dependent upon the input power, assuming the same applied voltage, the dissociation of molecular oxygen, nitrogen and carbon dioxide has been shown to be greater for the higher harmonics of 13.56 MHz [113, 114]. The chosen reactor and plasma vessel walls are glass to ensure surface reactions are kept to a minimum. As shown in [114], when argon was used as the feed gas for the same plasma source as used in this work, the conversion of CO_2 into CO was greater than when helium was used. Possible reasons for this could have been a higher electron density and temperature due to the lower ionisation energy of argon. Thus the rate of direct electron impact dissociation would've been higher for argon than for helium.

As described in section 1.3.4, the comparative reactivity method uses a small glass vessel to mix the gas-phase reactants and allow them to interact. A similar vessel used in this work is described in section 2.1.2. The proton transfer reaction mass spectrometer used to sample the gas leaving this reactor is described in section 2.2. An atmospheric pressure plasma source is used to produce the radical species, unlike the UV mercury lamp used by Sinha et al. [15], the plasma source is described in section 2.1.1.

Figure 2.1 shows the orientation of the plasma source and gas reactor. A closeup of the plasma source and the reactor vessel is given in figs. 2.2 and 2.3. All the experiments carried out used the same plasma source and gas reactor.

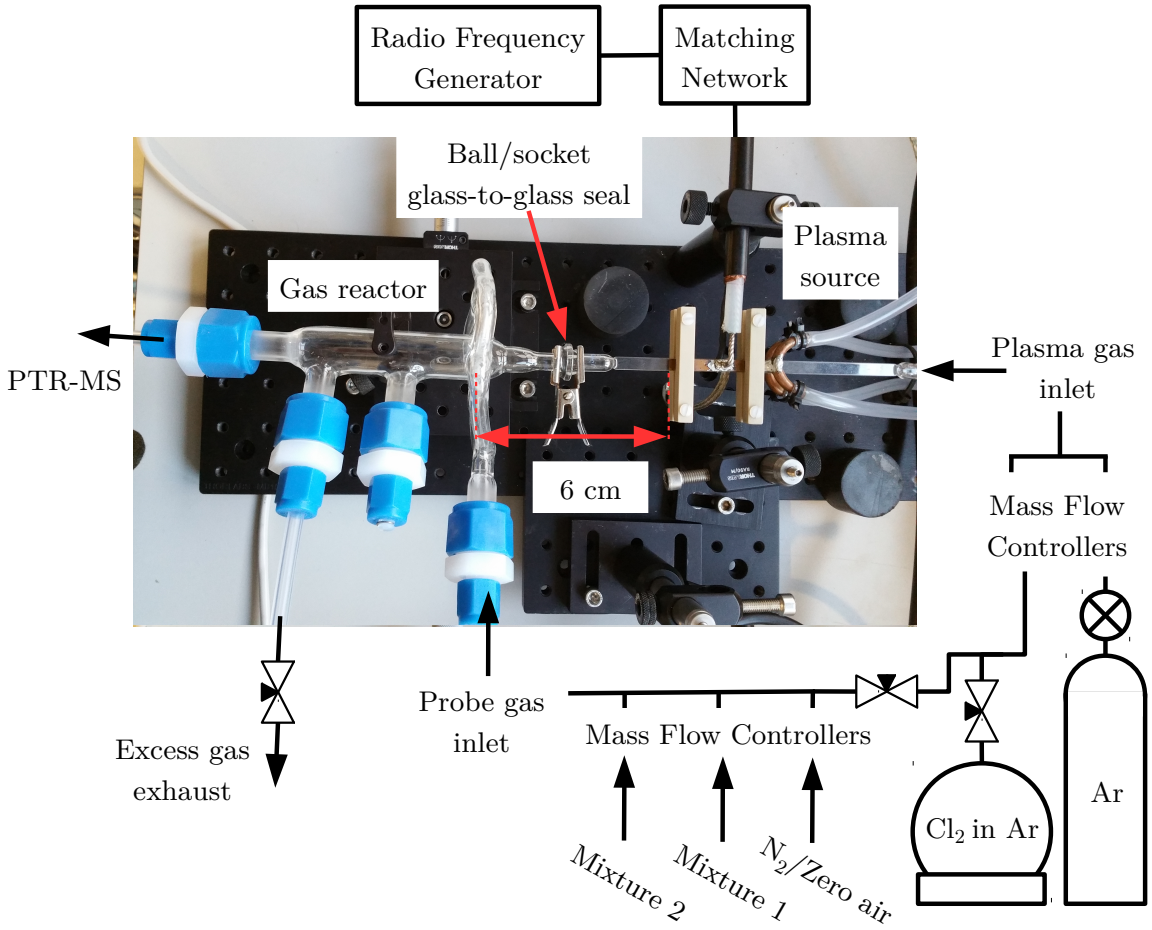

Figure 2.1: Overview of the experimental setup. The plasma source and gas reactor have further detail in figs. 2.2 and 2.3. In general, two flow controllers regulate the Ar/Cl_2 gas mixture into the plasma source. The resulting effluent then enters the gas reactor through a glass-to-glass ball and socket joint. The distance between the end of the plasma source and the probe gas inlet is ∼6 cm. Three mass flow controllers then regulate the flow into the mixing ring of the reactor, with the outflow ports connected to the PTR-MS and the lab exhaust.

2.1.1 Plasma source

The plasma source used in this work is a symmetric planar volume dielectric barrier discharge with an effective electrode-electrode gap distance of 1.2 mm, similar to the COST reference plasma jet [114–117].

The plasma is contained within a large aspect-ratio rectangular (5 × 0.5 mm ±10 % ID) borosilicate capillary (VitroCom) with 0.350 mm (±20 %) thick walls (see fig. 2.2). Two 50 × 5 × 1 mm planar copper electrodes are held either side of the capillary using two clamps made from low thermal conductivity polyether ether ketone (PEEK) to provide the required power to sustain the plasma. PEEK is chosen to minimise thermal conduction & expansion that else could crush the capillary.

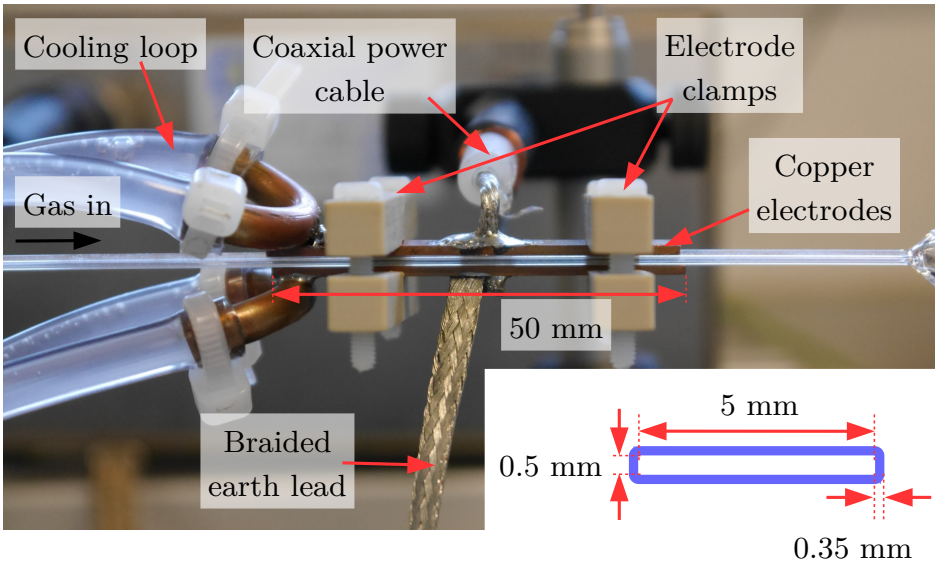

Figure 2.2: Photograph of the capacitively coupled RF plasma source, inset is the cross section of the borosilicate capillary. Gas enters the glass capillary from the left. Both electrodes (50 × 5 × 1 mm, copper) are held to the capillary using two clamps and water cooled using two copper tubes. The core of the coaxial cable is soldered to the top planar electrode, while the lower electrode is soldered to the outer mesh of the coaxial cable (not shown) and to the braided earth lead.

The powered electrode is soldered to the core of a short (<20 cm) coaxial cable that is connected in series to a 40.680 MHz Advanced Energy Cesar 403 RF power supply through a Coaxial Power Systems MMN 150-40.68 manual L-type matching network. The matching network and power supply are also separately connected to the laboratory ground through a 150 × 600 × 12.7 mm anodized aluminium optical breadboard. The anodized layer of the breadboard is abraded away at these grounding points to ensure a full electrical connection. In this work, the effective forward power of the generator is quoted, not the true power deposited in the plasma.

The ground electrode is soldered to a braided steel earth cable and outer shielding mesh of the powered coaxial cable. For cooling the solder and electrodes during operation, a bent copper tube is soldered to each electrode which water is pumped through. The water is then fed through a fan-cooled radiator as part of a closed cooling loop. An aluminium box connected to the breadboard by a short braided earth lead is placed over the plasma source during operation to shield the emitted RF radiation.

The plasma source capillary is connected to the input gas lines using a fused glass to 1/4" stainless steel swagelok seal. To minimise the potential for permeation of water vapour into the input gas lines, stainless steel lines were used [118] and designed to have the absolute minimum number of connections. The capillary exit is connected to the gas reactor by a glass-to-glass ball and socket joint. BOC N6.0 grade argon (99.9999% purity) at typically 420-500 sccm (standard cubic centimetre per minute) with 0-80 sccm of ∼0.6-2% Cl_2 in argon was used as the input gas mixture to the plasma. The concentration of Cl_2 into the plasma could then be varied between 0-0.32%. With a plasma volume of (5 × 0.5 × 0.05 cm) 0.125 cm^3 and typical flow rate 500 sccm, the resulting residence time is 15 ms.

Because of safety considerations around the handling of chlorine gas, a small 6 litre Restek SilcoCan is used to store the chlorine (∼1.6%) in argon mixtures in the lab. As seen in fig. 2.1, the mass flow controller connected to this canister is flushed with dry N_2. The distance between the plasma source and the gas reactor is ∼6 cm, with a similar cross section once the effluent leaves the glass capillary. With a volume of (6 × 0.5 × 0.05 cm) 0.15 cm and flow rate of 500 sccm, the time taken to get from the plasma to the reactor is 18 ms.

Because of the very high mobility of gases, the recombination of atomic chlorine produced by the plasma will be reaction limited, rather than diffusion limited. This can be shown if we compare the collision frequency ($\sim 2.5\times10^{10}$ s^{-1}) with the experimentally measured reaction rate ($\sim 7.5\times10^{6}$ s^{-1}) assuming 1 bar of Cl atoms with the recombination rate coefficient 1.28×10^{-32} cm^6 s^{-1} [208].

The Reynolds number (Re) is a dimensionless value that helps to predict laminar or turbulent flow. Majority laminar flow is predicted at low values, i.e. $Re < 2300$, switching to dominant turbulent flows at $Re > 2900$. For calculating the Reynolds number the following equation can be used,

$$Re = \frac{\rho u L}{\mu}$$

where ρ is the fluid density (kg m^{-3}), u is the flow speed (m s^{-1}), L is known as the hydraulic diameter (m) and μ is the dynamic viscosity of the fluid (Pa·s). For the rectangular cross section of flow here, L is calculated using

$$L = \frac{2ab}{a+b}$$

where a and b are the lengths of the sides. For the 500 sccm ($u = 3.33$ m s^{-1}) predominantly argon flow ($\rho = 1.784$ kg m^{-3}, $\mu = 2.23 \times 10^{-5}$ Pa·s) through the plasma source ($L = 9 \times 10^{-4}$ m), $Re \simeq 240$ suggesting strongly laminar flow.

2.1.2 Gas reactor

The gas reactor was a 8 cm long, 2 cm diameter cylindrical glass vessel with 4× 1/2" ports and an axial glass-to-glass ball/socket seal (see fig. 2.3). Because of the fragility of the plasma source capillary, the gas reactor and plasma source capillary were made into two separate pieces of glassware. To mitigate any leaks during operation, a compression seal (ball/socket with clamp) was used to connect the two. 1/2" to 1/4" Swagelok PFA reducing unions and short (<1 m) PTFE tubing were used to connect the glassware to the input gas flow controllers, PTR-MS and laboratory gas outlet. In total, there were 5 mass flow

controllers used. Two for controlling the argon/chlorine gas mixture through the plasma source. Three others were used for regulating the gas mixture into the reactor. For a total volume of 25.1 cm^3 and typical total input flow rate of 1000 sccm, the mean residence time was 1.5 s.

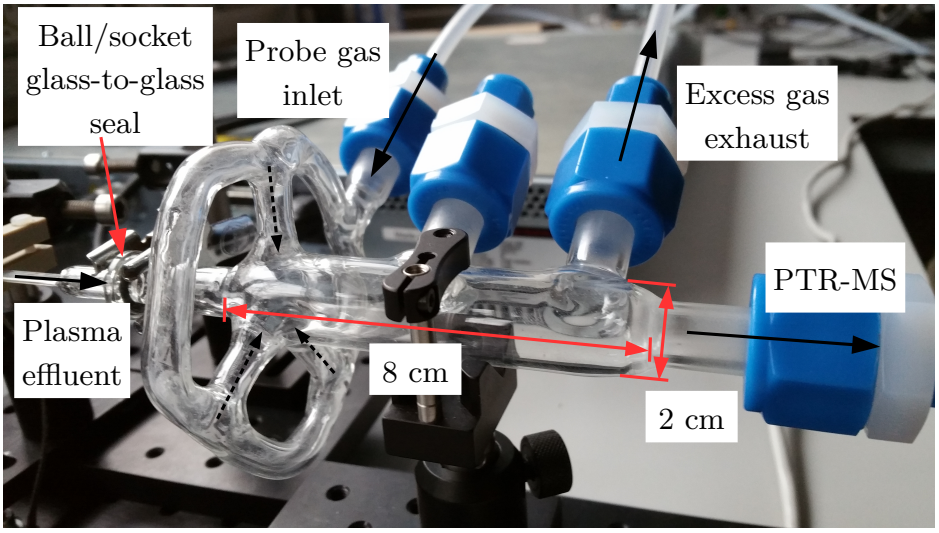

Figure 2.3: Photograph of the gas reactor, black arrows indicate gas flow. Plasma effluent enters the reactor through a ball & socket glass-glass seal from the left and mixes with the flow from internal gas ports that are all fed from the probe gas inlet. The two gas outlets lead to the PTR-MS and an excess gas exhaust.

Assuming a total flow rate of 1 slm, with 2:1 air/argon ($\rho = 1.466$ kg m^{-3}, $\mu = 1.95 \times 10^{-5}$ Pa·s) through the 2 cm ($L = 2$ cm) diameter reactor, $Re \simeq 80$ suggesting laminar flow.

2.1.3 COMSOL modelling

To investigate the impact varying the flow rates has on the amount of mixing inside the reactor, a series of simulations by Dr Sandra Schröter using COMSOL multiphysics were undertaken. A high and low flow case were modelled, assuming the same concentration of atomic chlorine and VOC entered the reactor. The spatial distribution of atomic chlorine and VOC density in the reactor are shown in figs. 2.4 and 2.5 respectively.

As is shown in the work by Hansen et al. [119], the total gas flow rate through the reactor

currently used for the comparative reactivity method is ∼500 sccm. In the work here, the total flow rate used was 750 sccm; 500 sccm from the plasma source and 250 sccm from the mixing port. To mitigate the possibility of the plasma overheating and damaging the glassware, a minimum flow rate of 500 sccm through the plasma source was used. Looking at figs. 2.4 and 2.5 a flow rate of 0.2 slm from the plasma could cause overheating, the modelling results are included here only for comparison.

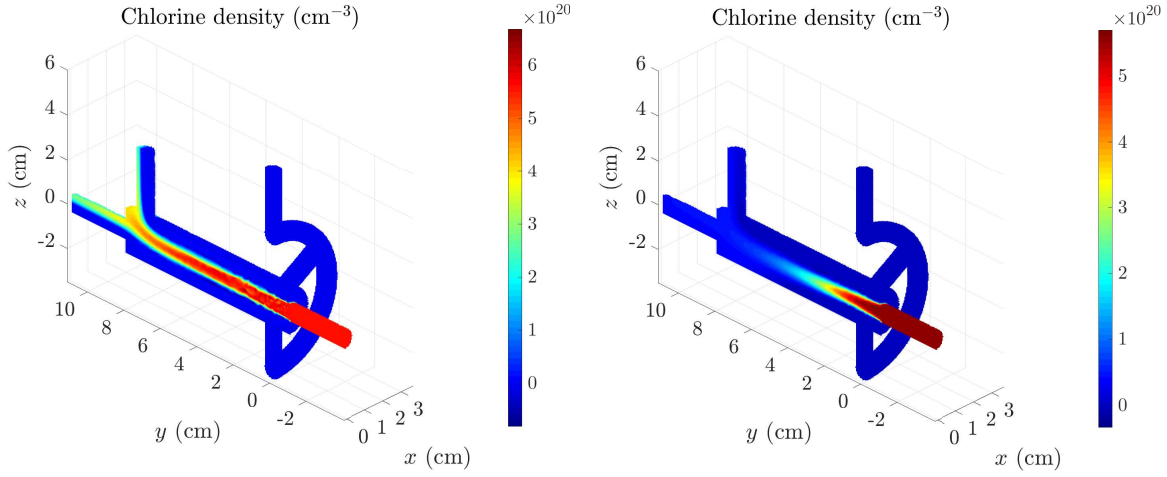

Figure 2.4: COMSOL modelling of the reactor showing atomic chlorine density. Left: 1 slm argon with 24 ppm Cl, 0.5 slm N_2 with 50 ppm VOC marker. Right: 0.2 slm argon with 24 ppm Cl, 0.1 slm N_2 with 50 ppm VOC marker. The low flow case is only included for comparison, such a low flow through the plasma may cause overheating and potential arcing.

With lower flow rates the heat loss from the plasma may be decreased, possibly resulting in a slightly higher overall gas temperature. The increased gas temperature thus may increase the conversion of Cl_2 to Cl as the rate coefficient for heavy-heavy reactions may increase. With a lower flow rate however, the transport time from the plasma source to the reactor would increase, resulting in more chlorine atom recombination (see section 3.6 for further discussion).

With comparison to figure 2.4, it is clear that with a total flow rate of 1.5 slm there is insufficient mixing of the plasma flow with the mixed-in N_2, with some of the plasma effluent

leaving the reactor. For a flow rate of 0.2 slm, there is much more sufficient mixing.

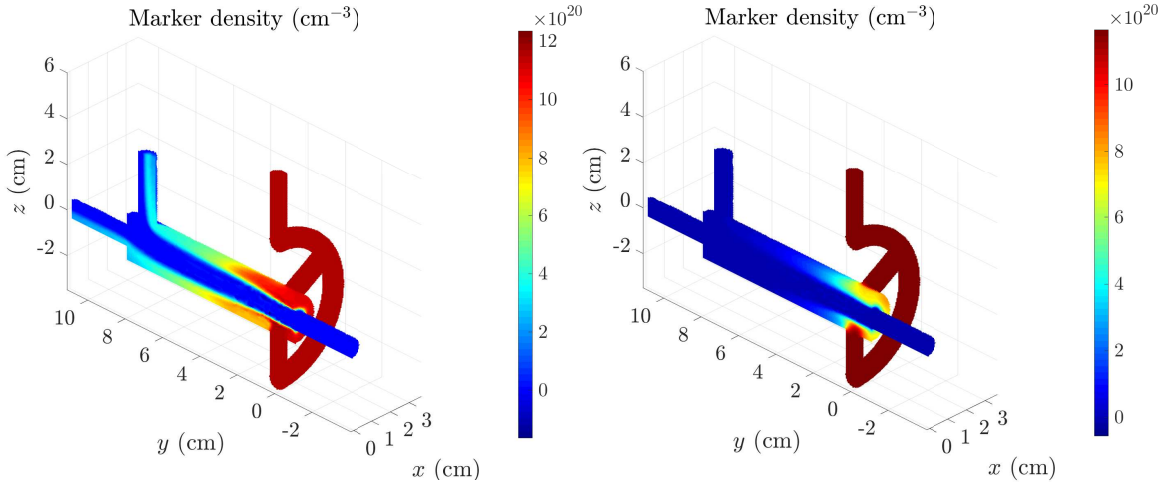

Figure 2.5: COMSOL modelling of the reactor showing VOC density. Left: 1 slm argon with 24 ppm Cl, 0.5 slm N_2 with 50 ppm VOC marker. Right: 0.2 slm argon with 24 ppm Cl, 0.1 slm N_2 with 50 ppm VOC marker. The low flow case is included for comparison, such a low flow through the plasma may cause overheating and potential arcing.

2.1.4 Gas flows

The gas flow into the plasma source and the reactor was controlled using a series of mass flow controllers. The mass flow controllers themselves were controlled using a in-house built system, consisting of 2× Lab Jack U3's and the suitable electrical connectors and cables. The mass flow controllers themselves were all calibrated using a Gilian Gilibrator-2 NIOSH Primary Standard Air Flow Calibrator (Sensidyne) using the appropriate gas, i.e. compressed air for the MFCs regulating zero air and mixtures 1 and 2, with argon used for the argon and argon/chlorine mixture MFCs. This gave the added benefit that MFCs originally calibrated for different gases could be re-calibrated and re-purposed. Figure 2.6 shows the most recent calibration of the 5 MFCs that were used (they were calibrated 3 times total throughout the project).

After applying these calibration factors, the flow rate was again checked with the Gili-

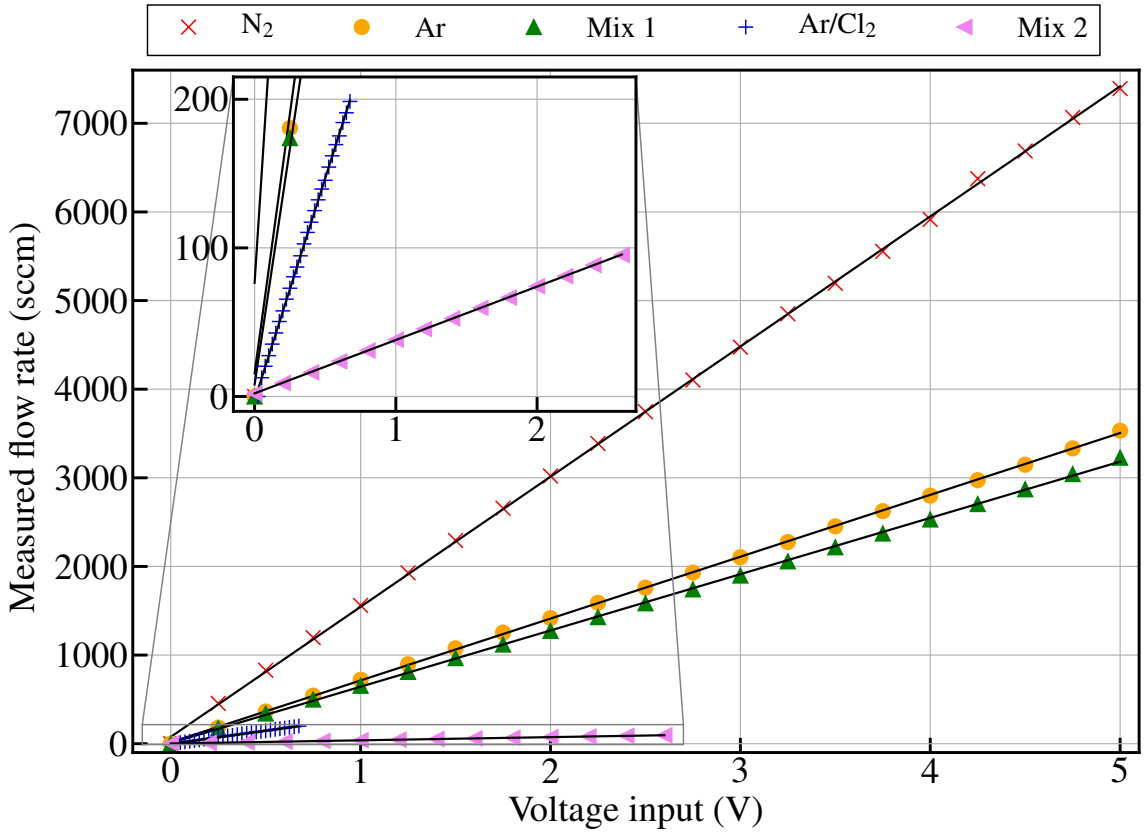

Figure 2.6: Calibration of the 5 mass flow controllers used in this work.

brator and the maximum error between the set point and measured flow rate was ±5 %.

2.1.5 Mixtures

The volatile organic compound mixtures used in this project were made up using a Schlenk line. The Schlenk line used in this project was a manifold consisting of a 1 in diameter glass tube with several connecting arms branching off, each arm sealed by a J Youngs greaseless tap. One end of the manifold is closed, while the other end is connected to a rotary vane vacuum pump via a liquid nitrogen cold trap. Two Baratron capacitance (10 and 1000 Torr) and a Pirani pressure gauge were connected to arms of the manifold to monitor the pressure. A J Young greaseless tap between the cold trap and main manifold allowed for precise control of the pressure in the system.

Table 2.1: Values of the linear fits used in fig. 2.6.

Gas	Calibration equation	r^2
N_2	$y = 1468x + 76$	0.999
Mix 1	$y = 634.9x + 8.092$	0.999
Mix 2	$y = 35.94x + 2.087$	0.999
Ar	$y = 698x + 15$	0.999
Ar/Cl_2	$y = 298.8x - 2.555$	0.999

To prepare a gas standard, glass Schlenk tube(s) containing the concentrated volatile compound(s) (in liquid form) and the canister were connected to separate arms of the line. The canister was then cleaned and flushed; while on the line, the canister was placed under vacuum and the outside heated with a heat gun to agitate and encourage adsorbed compounds to leave the inside surface of the canister. The canister was then filled with N_2 and evacuated, then heated again. This process was repeated at least 3/4 times to ensure the canister was properly flushed.

The volatile compound(s) were then degassed and purified using a freeze-pump-thaw-degassing procedure. To remove any dissolved gases or other impurities that could otherwise affect the partial pressure of the desired compound in the finished canister, the compound was frozen using a small flask of liquid nitrogen (77 K). The whole manifold and frozen compound was then placed under vacuum and the compound was allowed to thaw using a tepid water bath. Allowing the impurities to effervesce, this freeze-pump-thaw process was repeated until no more effervescence was observed. The cleaned canister was opened onto the manifold and the volatile compound was then used to flush the manifold and canister several times. The desired partial pressure of the compound in the canister was then reached using the tap between the cold trap and manifold. This could then be repeated for the other volatile compounds required in the gas standard. The canister was then filled with N_2 and diluted as many times as necessary. The concentration of the compounds in the canister was thus known by the relevant partial pressures (and any subsequent dilution).

2.2 Proton transfer reaction mass spectrometry

The proton transfer reaction mass spectrometer (PTR-MS) takes advantage of the proton affinity of water to measure the concentration of trace volatile compounds in a gas sample [120]. Trace compounds are discriminated against the main constituents of ambient air, i.e. N_2, O_2 and CO_2 without sample concentration or preparation. Simultaneous online monitoring of various volatile organics such as terpenes, alcohols and halogen-containing compounds down to ppbv levels is possible. Developed at the Institut für Ionenphysik at the Leopold-Franzens University in Innsbruck [120], PTR-MS has been utilised on many field campaigns for the measurement of a suite of volatile organic compounds worldwide [80, 83, 84, 121]. The PTR-MS instrument used in this work was a commercial instrument, including integrated quadrupole mass spectrometer.

The instrument is designed so that critical components are spatially separated from one another, ensuring total control and measurement stability over long experimental campaigns and field measurements. These components include: hydronium source (section 2.2.1), inlet system and reaction drift tube (section 2.2.2) and ion detection system (quadrupole mass filter and secondary electron multiplier, section 2.2.3).

In brief, a continuous stream of hydronium ions (H_3O^+, also known as primary ions) are used to chemically ionise the sample (R) in a drift tube by the following reaction;

$$H_3O^+ + R \xrightarrow{k} H_2O + RH^+ \tag{2.1}$$

assuming $[R] \ll [H_3O^+]$. Because proton transfer is a soft chemical ionisation process, fragmentation of the resulting ions is kept low. The product ions (RH^+) enter a quadrupole mass filter, are separated by their mass/charge ratio (m/z) and detected by an secondary electron multiplier. The sensitivity, response time and detection limit depend upon several factors, including but not restricted to; the pressure and temperature of the drift tube, the voltage across the drift tube and the time allocated by the quadrupole mass filter to detect each selected mass/charge ratio (also known as dwell time). The minimum response time is ∼0.2 s (then increases depending upon the number of different m/z and their cor-

responding dwell times), with the instrumental sensitivity and detection limit varying from 6–50 ncps/ppbv and 34–820 pptv respectively, varying for different compounds [83,121–124].

2.2.1 Hydronium source

The PTR-MS uses a DC hollow cathode with a venturi-like exit orifice plate to produce a highly pure stream of H_3O^+ ions into the drift tube (see fig. 2.7). The ion source itself is the product of years of development at Innsbruck University, so only the most relevant details are given here [125–127].

A reservoir of doubly distilled water is used to supply the ion source with water vapour. A flow controller is used to control the flow of humidified air into the end-cap of the ion source (typical operating flow rate is 5–7 sccm). The flow is regulated to avoid an over-production of H_3O^+ ion – neutral water molecule clusters (usually <5% $H_3O^+ \cdot nH_2O$ is chosen), too little flow can cause the ion source to become unstable and supply an insufficient number of H_3O^+ ions. In most measurements, a flow rate of 5.5 sccm was used, unless stated.

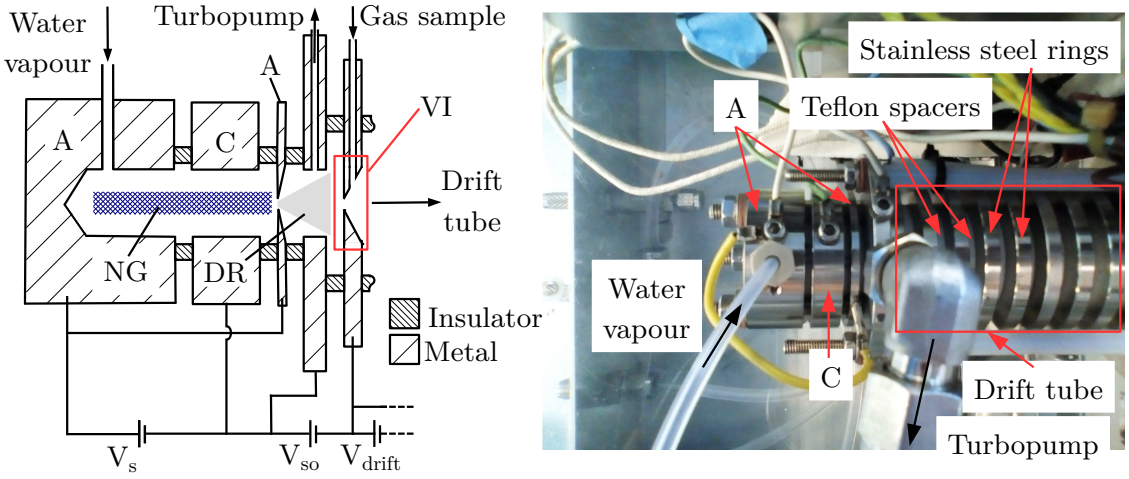

Figure 2.7: Ion source schematic and photo: A, anode; C, cathode; NG, negative glow; DR, drift region; VI, venturi-like inlet [123, 124].

The main production of H_3O^+ ions is initiated through electron impact reactions with H_2O creating H_2O^+, OH^+, H_2^+, O^+ and H^+ ions (reactions 2.2–2.5).

$$e^- + H_2O \rightarrow H_2O^+ + 2e^- \tag{2.2}$$

$$e^- + H_2O \rightarrow H_2^+ + O + 2e^- \tag{2.3}$$

$$e^- + H_2O \rightarrow H^+ + OH + 2e^- \tag{2.4}$$

$$e^- + H_2O \rightarrow O^+ + H_2 + 2e^- \tag{2.5}$$

This collection of ions are accelerated towards the cathode (see fig. 2.7) and cause the creation of secondary electrons from the inner surface. These secondary electrons are then accelerated towards the anode causing further ionisation. The original ions ultimately produce H_3O^+ through the reactions

$$O^+ + H_2O \rightarrow H_2O^+ + O \tag{2.6}$$

$$H^+ + H_2O \rightarrow H_2O^+ + H \tag{2.7}$$

$$H_2^+ + H_2O \rightarrow H_3O^+ + H \tag{2.8}$$

$$\rightarrow H_2O^+ + H_2 \tag{2.9}$$

$$OH^+ + H_2O \rightarrow H_3O^+ + O \tag{2.10}$$

$$\rightarrow H_2O^+ + OH \tag{2.11}$$

$$H_2O^+ + H_2O \rightarrow H_3O^+ + OH \tag{2.12}$$

A short drift region between the anode plate and drift tube allows the initial ions to react with H_2O, eventually producing H_3O^+. To influence these reactions, the pressure in the drift region can be changed using a needle valve placed in-between one of the turbopumps and the drift region (fig. 2.9). Because of the reaction scheme and ion source design, the ions that leave the ion source are 99.5% H_3O^+ [76, 120]. During operation, secondary ions (NO^+ and O_2^+) are also produced by the ion source, causing oxidation of the walls. This leads to a reduction in the production of secondary electrons from the surface and thus gradual degradation of primary ion (H_3O^+) production. After sufficient loss of primary ion production, the inner surfaces of the ion source was cleaned. The ion source (and drift tube)

is constructed from a series of alternating stainless steel and insulating teflon-PTFE rings which are compressed together to create an air-tight seal (fig. 2.7). The pressure in the ion source and drift tube is assumed to be similar, i.e. ∼2 mbar (1.5 Torr). The density of anions in the source is approximately 10^{10}–10^{11} cm^{-3} [120].

To optimise the primary ion count, the potential between the anode and cathode (V_S), and the potential between the drift region and first ring of the drift tube can be altered (V_{SO}, see figs. 2.7 and 2.8). As previously mentioned, the effective pressure in the drift region can also be changed. By increasing the voltage and/or decreasing the pressure, ions undergo more energetic collisions, causing breakup of water clusters and creating more O_2^+ and NO^+ secondary ions. The typical values of V_S, V_{SO} and source current are 110 V, 80 V and 5 mA, typically chosen to ensure the O_2^+ is less than 3% of the H_3O^+ counts (see fig. 2.8).

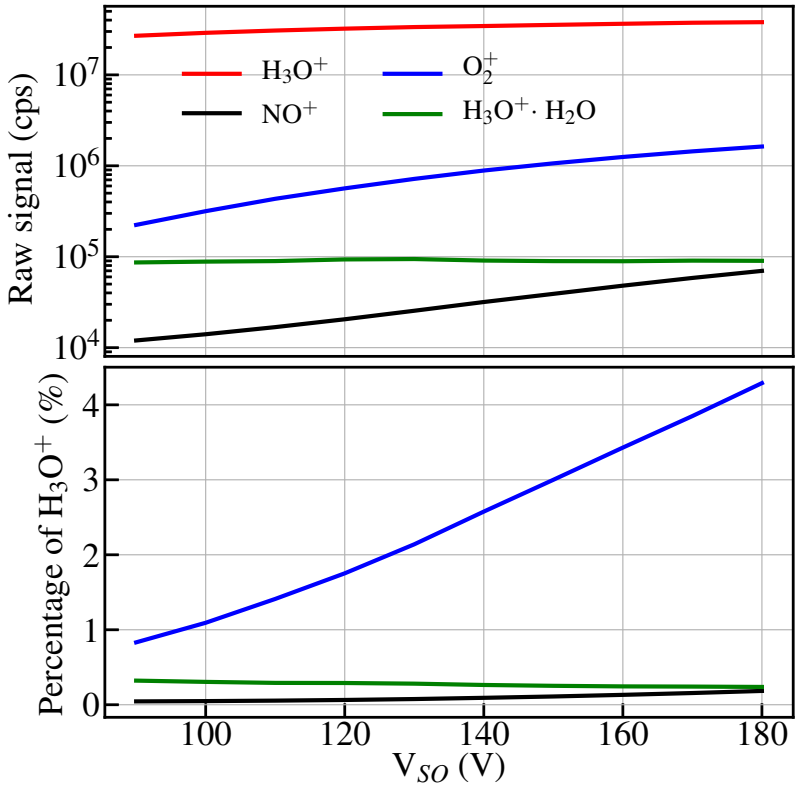

Figure 2.8: Measured raw counts per second on m/z 21, ($H_3{}^{18}O^+$), 30 (NO^+), 32 (O_2^+) and 37 ($H_3O^+ \cdot H_2O$) and their corresponding percentage of the primary ion signal under variation of the ion source output voltage (V_{SO}). To prolong the life of the SEM, H_3O^+ is measured using m/z 21 rather than 19. The known ^{16}O:^{18}O isotope ratio (500:1) and the quadrupole transmission, $T(\text{m/z } 21) = 0.7$ is used to calculate m/z 19 raw signal, $i(\text{m/z } 19)$, i.e. $i(\text{m/z } 19) = i(\text{m/z } 21) \times 500/0.7$. Pure N_2 (PEAK scientific NM32L nitrogen generator) was sampled, with the stated dew point of -40℃ and typical room temperature of 20℃, the relative humidity would be ∼1% [124].

2.2.2 Inlet system and drift tube

The inlet system and drift tube is shown in figure 2.9. In brief, two branching T-junctions (J1 & J2, fig 2.9) step the input gas flow down into the drift tube. The drift tube itself is constructed using alternating stainless steel and PTFE rings. The metal rings are electrically connected to each other through a resistor chain, to enable a potential difference (V_d) across the ends of the tube. The primary ions from the ion source enter the drift tube and are mixed with the sample flow in a venturi-like inlet. The mixture then traverses the drift tube into the detection region.

To minimise memory effects and surface adsorption of the sample, PTFE gas lines and fittings are used [128,129]. The drift tube and ∼1 m long, 1/8 in diameter inlet line are independently temperature controlled (40–180 ℃) to reduce condensation and water clustering. The pressure between the inlet line and the drift tube is reduced by two T-pieces (J1 & J2, fig 2.9) that remove portions of the total inlet flow. The first of these T-pieces is connected through a needle valve (N1) to the membrane pump, achieving a constant negative pressure through the inlet line. The second T-piece is connected to the membrane pump via a pressure controller (Bronkhorst EL-PRESS) to indirectly regulate the final sample flow into the drift tube. The junctions are connected using a series of capillary tubes (C1–C3) to trap dust and particulate matter, to mitigate damage to the turbopumps and reduce interferences in the drift tube. A separate bypass inlet is also used to supply dry air, to reduce the humidity of the gas that passes through the membrane pump.

Similar to swarm experiments, the sample is used as a buffer while the primary ions traverse the drift tube. The drift tube pressure is monitored using a capacitance manometer gauge and kept close to 2 mbar. This ensures that the ions undergo many collisions with the buffer molecules. If it is energetically favourable, the buffer molecules are chemically ionised (by H_3O^+, see eq. (2.1)) and/or ionised through charge exchange (by NO^+ or O_2^+). The amount of time ions have to react in the drift tube is

$$t = l_d/v_d$$

where v_d is the ion drift velocity, itself a function of the applied electric field and ion mobility (see appendix B) and $l_d = 9.3$ cm is the length of the drift tube.

The critical parameter in the drift tube is the reduced electric field, E/N. The drift tube pressure, temperature and potential difference across the drift tube defines the resulting E/N. Several studies have looked at the impact on water clusters, sample fragmentation and sensitivity with changing E/N [122, 130, 131]. The mean centre of mass kinetic energy, $\langle \mathrm{KE_{CM}} \rangle$ between the ions and neutrals in the drift tube can be derived by an expression by Wannier [132–134],

$$\langle \mathrm{KE_{CM}} \rangle = \frac{(m_i + m_b)m_n}{2(m_i + m_n)} v_d^2 + \frac{3}{2} k_B T_d \tag{2.13}$$

where m_i, m_b and m_n is the mass of the reactant ion, buffer gas and the reactant neutral. This shows how the drift tube temperature (T_d) and drift velocity (v_d) has on the average kinetic energy of the ions in the drift tube. Depending upon the E/N ratio used in the drift tube, delicate product ions can undergo energetic collisions with the ions and break up. Known as a branching ratio, the ratio of the initial product ion into other products has also been measured and investigated experimentally [131, 135, 136].

In general, a low E/N reduces the ion drift velocity, thus the average kinetic energy (eq. (2.13)) of the collisions in the drift tube is decreased. The product ions therefore fragment less, resulting in higher sensitivity, at the loss of greater water clustering and a longer response time (because of the reduced ion velocity). For high E/N, the ion drift velocity increases, decreasing the reaction time and giving a shorter response time. There is also the benefit of less water clustering, however there is more sample fragmentation, making interpretation of the resulting measurements harder.

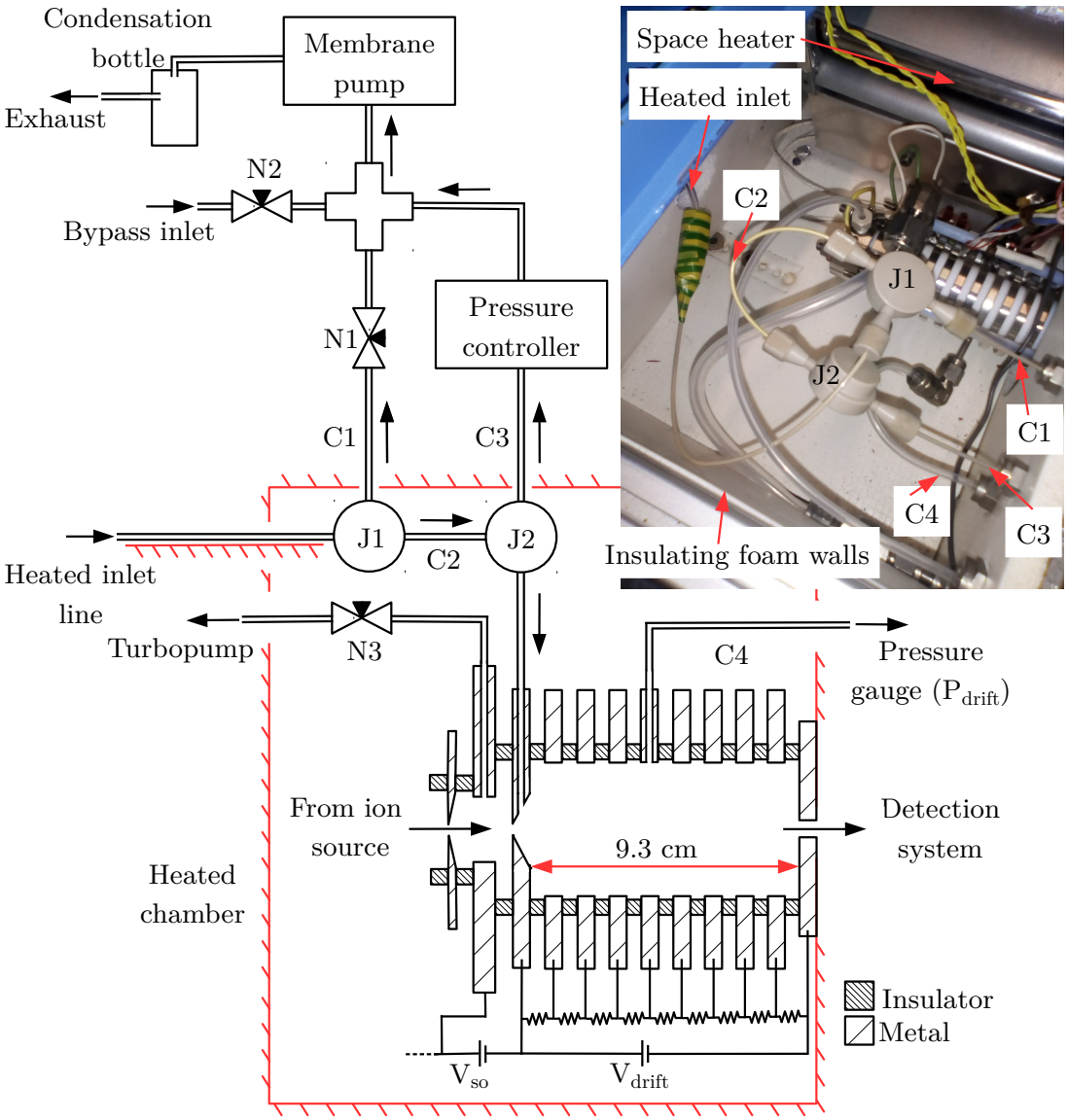

Figure 2.9: Schematic and photograph of the inlet sampling system and PTR-MS drift tube. N1 = inlet needle valve, N2 = bypass needle valve, N3 = ion source/drift tube needle valve. C1, C2 and C3 are all capillaries used to sequentially decrease the pressure to the drift tube and to stop some particulate matter. The temperature of the heated chamber and inlet line are controlled independently. The black arrows indicate the direction of gas flow.

The typically desired E/N is in the range 120–140 Td [76]. To have a sufficient number of collisions in the drift tube, the required pressure is p_d ∼1.9–2.1 mbar, usually at 60℃. To calculate the number density in the drift tube, (N) the following equation can be used [77],

$$N = \frac{N_A}{V_m}\frac{p_d T_0}{p_0 T_d} \tag{2.14}$$

where $N_A = 6.022 \times 10^{23}$ mol^{-1}, $V_m = 22414$ cm^3 mol^{-1}, $T_0 = 273$ K and $p_0 = 1013.25$ hPa. This avoids measuring the drift-tube volume directly, which can vary between instruments. p_d and T_d is the pressure and temperature of the drift tube respectively. Thus by using eq. (2.14), $N = 4.12$–4.56×10^{22} m^{-3}. The voltage across the 9.3 cm long drift tube is usually set between $V_d = 500$–600 V, giving an electric field of 5376–6451 Vm^{-1}. A range of E/N 117–156 Td (see appendix B for more details) is possible.

As previously mentioned, this reaction will only take place if the proton affinity of R is greater than water (see table 2.2). Assuming $[RH^+] \ll [H_3O^+] \approx [H_3O^+]_0 = \text{constant}$,

$$[RH^+] = [H_3O^+]_0(1 - e^{k[R]t}) \approx [H_3O^+]_0[R]kt \tag{2.15}$$

where t is the reaction time in the drift tube. Thus there is a linearity limit wherein $[H_3O^+] \approx [H_3O^+]_0$, i.e. when $k[R]t$ is small. In a practical sense, this means when [R] is small enough that it makes little change to $[H_3O^+]$.

To calculate the concentration of R (in ppbv), the following equation can be used,

$$[R] = \frac{i(RH^+)}{i(H_3O^+)}\frac{T(H_3O^+)}{T(RH^+)}\frac{1}{kt}\frac{10^9}{N} \tag{2.16}$$

where $i(x)$ and $T(x)$ is the measured counts per second and effective quadrupole transmission of x.

The proton transfer reaction rate k is the order of $\sim 2 \times 10^{-9}$ cm^{3}s^{-1}. Its determination and calculation is a whole field of study in itself, thus only pertinent details will be discussed here. Briefly, for polar molecules, the reaction rate can be determined using the trajectory calculations by Su and Chesnavich [137], otherwise for non-polar molecules, Langevin theory

can be used. The reaction rate has also been measured directly using selected ion flow tube (SIFT) for a large range of different molecules [138, 139].

Base	Proton affinity (kJ/mol)	Reaction rate, k (10^{-9} cm^3s^{-1})
Helium	178[c]	[a]
Argon	371[c]	[a]
O_2	422[c]	[a]
N_2	495[c]	[a]
CO_2	548[c]	[a]
Ethane	601[c]	[a]
Water	697[c]	[b]
Benzene	759[c]	1.97[d]
Toluene	784[d]	2.12[d], 2.0[f]
Ethanol	788[c]	2.7[e]
1-Propanol	798[c]	2.7[e]
Isoprene	826[d]	1.94[d], 2.0[f]
Diethyl ether	838[c]	2.4[g]

Table 2.2: Proton affinity of a range of substances. A substance with a proton affinity greater than or equal to water can be detected using PTR-MS.[a] the reaction is not energetically favourable.[b] water clustering is possible, i.e. $H_3O^+ \cdot nH_2O$. [c] From Jolly (1984) [140], [d] from Zhao et al. (2004) [141], [e] from Spanel et al. (1997) [138],[f] from Spanel et al. (1998)a [142], [g] from Spanel et al. (1998)b [139].

2.2.3 Ion detection

To detect the products from the drift tube, a secondary electron multiplier (SEM) is used via a quadrupole mass filter (see fig. 2.10). Once the ions leave the drift tube, a series of ion lenses are used to focus the ions into the linear quadrupole mass filter. A turbopump is also attached to the ion lens region to reduce the pressure between the drift tube and quadrupole/SEM.

This is important for two reasons - a) reactions between ions and molecules are assumed to cease in the quadrupole and SEM and b) transmission through the quadrupole would otherwise be negatively impacted through ion-neutral collisions.

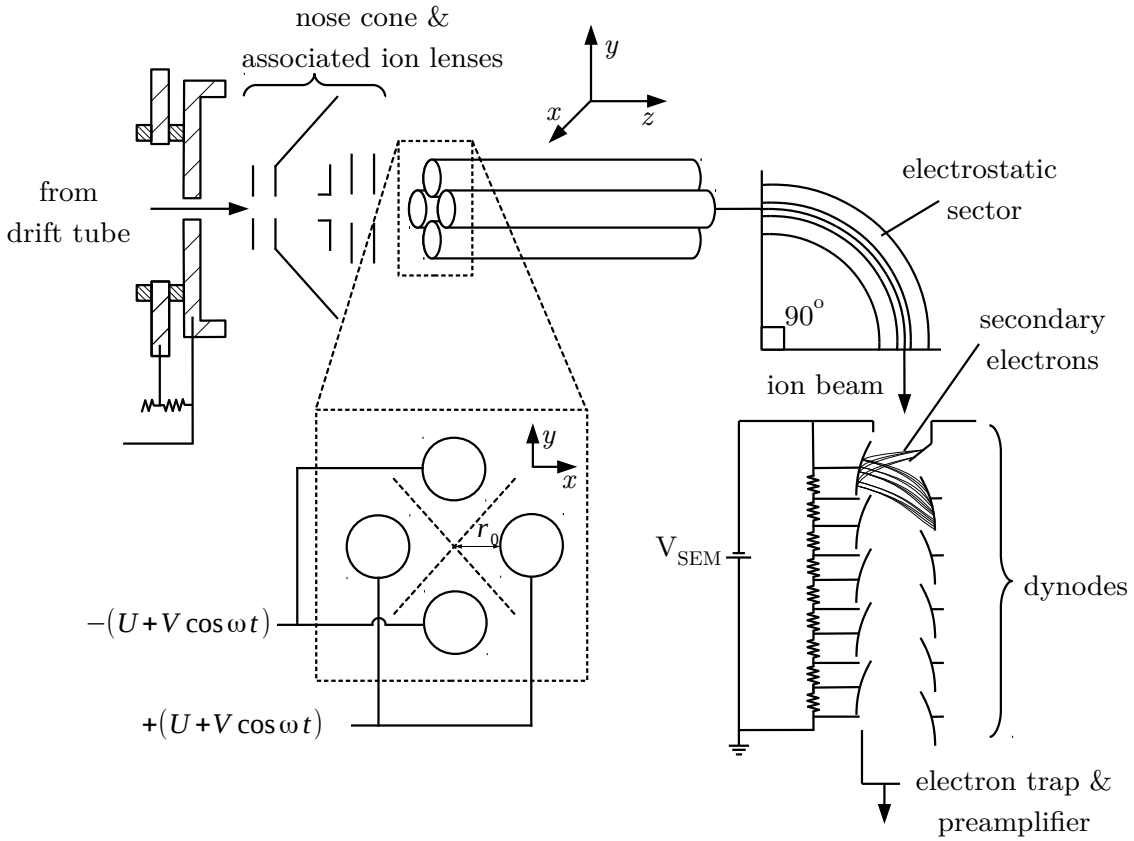

Figure 2.10: PTR-MS detection system schematic.

The quadrupole mass filter itself consists of four electrically connected hyperbolically or cylindrically shaped metal rods (extending into the z-axis) arranged into a square (in the xy-plane). An AC voltage (of amplitude V and frequency ω) and DC offset (U) across the rods creates a time varying electrical potential, $\Phi(t)$ defined by eq. (2.17) in the region between the rods as the ions travel through [143];

$$\Phi(t) = U + V\cos\omega t \tag{2.17}$$

The time varying electrical quadrupole field created by this potential is chosen such that

only one m/z ratio has a stable helical trajectory through the field. The system can be modelled by a series of Mathieu functions; eqs. (2.18) and (2.19) [144],

$$\frac{d^2x}{d\tau^2} + (a_x + 2q_x \cos 2\tau)x = 0 \tag{2.18}$$

$$\frac{d^2y}{d\tau^2} + (a_y + 2q_y \cos 2\tau)y = 0 \tag{2.19}$$

where

$$a_x = -a_y = \frac{4ZeU}{m_i r_0^2 \omega^2}, \quad q_x = -q_y = \frac{2ZeV}{m_i r_0^2 \omega^2}, \quad \text{and} \quad \tau = \frac{\omega t}{2}$$

Ze and m_i is the ion charge and mass and r_0 is the distance between the midpoint and the rods. By changing V and the ratio of U/V a certain m/z can be chosen. The energy of the ions entering the quadrupole are assumed to be approximately equal, and the ion velocity through the quadrupole is assumed to be uniform. In reality, due to the mass dependence of the mobility of the different ions, the ions do not traverse the quadrupole at the same speed. Also, assuming the ions have the same kinetic energy as they enter the quadrupole, the lighter ions have a greater velocity, changing their relative counts per second. The ions in unstable trajectories and neutrals will eventually impact the walls or quadrupole rods themselves and be removed by the vacuum system.

The shape of the rods, ratio of rod diameter to spacing and mobility of the ions through the filter gives a characteristic transmission through the filter (see fig. 2.11). Due to this, any slight movement of the rods can cause changes in the effective transmission, therefore the transmission curve should be re-measured every time the PTR-MS is transported.

After travelling through the quadrupole, the ions reach the SEM. The secondary electron multiplier uses a series of dynodes of a low work function metal to amplify the signal from the product ions. As a product ion hits the first dynode, depending on the energy of the ion and the work function of the dynode surface, a number of secondary electrons are liberated from the surface. Because of the electrical potential between the dynodes, the secondary electrons are accelerated to the second dynode, creating further secondary electrons. This process is repeated several times, resulting in a measurable current.

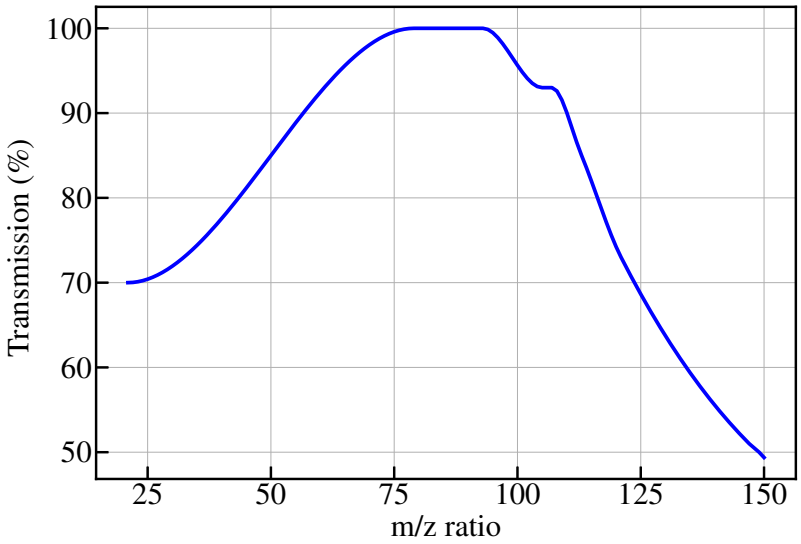

Figure 2.11: Quadrupole transmission curve. An arbitrary function is used for correcting the different mobilities of the ions through the quadrupole.

The SEM is placed 90° from the axis of the quadrupole to minimise stray light and undesired particles entering and hitting the SEM, that would otherwise cause noise. Over time, the dynode surfaces oxidise, increasing the work function and thus decreasing the number of available secondary electrons. To optimise the SEM, the SEM voltage was varied (see fig. 2.12) and the primary ion counts per second were measured, without amplifying the noise (shown with m/z 25). From fig. 2.12, the optimal detector voltage was 2305 V.

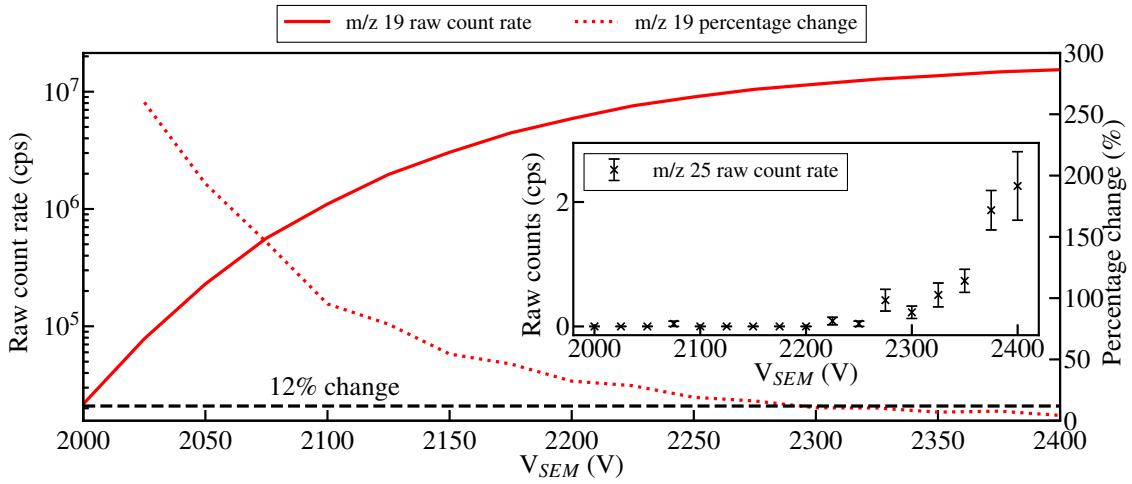

Figure 2.12: Measured raw counts per second and percentage change ($\frac{y_{(n+1)}-y_n}{y_n} \times 100$) of the primary ions under variation of the SEM detector voltage. The inset shows the mean and standard error of the mean of m/z 25 (dark counts). The horizontal line at 12% shows the optimal level for the detector (MasCom SEM). The chosen detector voltage was 2305 V.

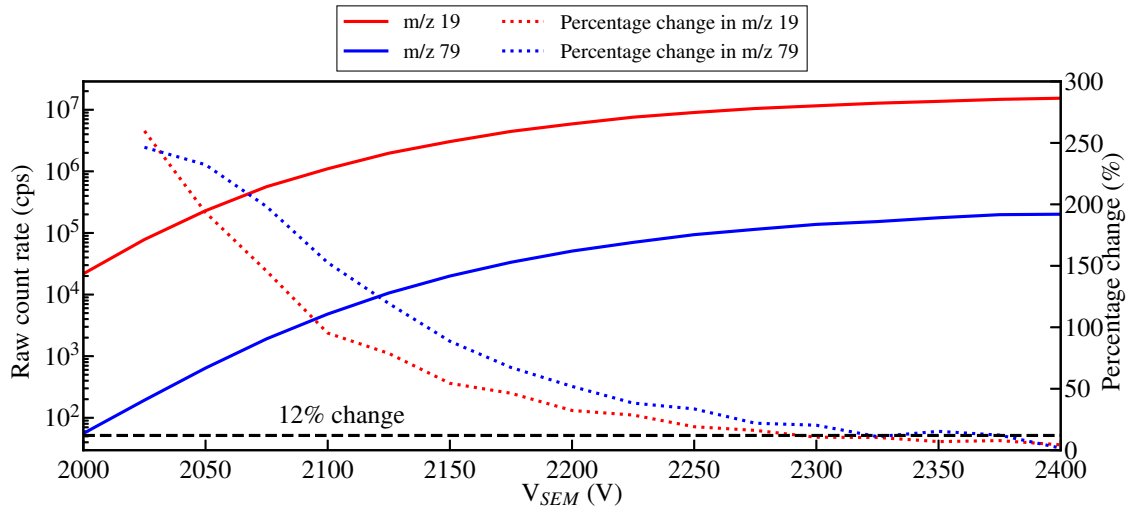

Figure 2.13: Raw count rate and percentage change of m/z 19 and 79 under variation of the SEM detector voltage. A constant 1 sccm flow from a prepared gas standard of ~1.2 ppth benzene in 1 slm air (from a Kaiser DC 1.5 E compressor) was sampled from the gas reactor.

2.3 Measurement calibration

To calibrate the measurements taken using the mass spectrometer, a series of controlled experiments were done using prepared gas standards (section 2.1.5). In these experiments, a small controlled flow from a prepared gas standard was mixed with a large flow of N_2 (from a PEAK scientific NM32L nitrogen generator) in the gas reactor. The flows were then changed to achieve different concentrations that were then sampled using the mass spectrometer. The mass flow controllers themselves were also calibrated (section 2.1.4), with a maximum error of ±5%. Along with the error of the partial pressure of the prepared gas standard of ±5%, the error of the concentration was ∼7%.

To characterise the response from the mass spectrometer, the limit of detection and quantification, linear range and sensitivity is discussed. The limit of detection and quantification is defined in the guidelines by MacDougall et al [145]. The gross analyte signal in this case is the product ion raw count per second normalised to $10^6 \times i(\mathrm{m19})$, i.e. $[\mathrm{RH}^+]_{ncps}$. Similar to the definition of de Gouw et al., Ammann et al. and Sinha et al. [83, 85, 146]:

$$[RH^+]_{ncps} = \frac{10^6 \times i(\mathrm{RH}^+)}{500 \times i(\mathrm{m21})} \frac{T(m21)}{T(\mathrm{RH}^+)} \tag{2.20}$$

The sensitivity is defined as the ratio of the normalised counts per second and the concentration (calculated using the flow rates and partial pressure of the compounds in the canister). Where possible, the measured normalised signal is converted to the concentration (in ppbv) using the measured sensitivity values. The limit of detection (LOD) and limit of quantification (LOQ) is defined as

$$LOD = S_b + 3\sigma \quad LOQ = S_b + 6\sigma$$

where σ, the standard deviation of the sample, is given by

$$\sigma = \sqrt{\frac{\sum_{i=1}^{n}(x_i - \bar{x})^2}{n-1}}$$

where n is the size of the sample, $\bar{x}$ is the mean of the sample and x_i are the individual values of the sample. The linearity limit of PTR-MS is approximately 10ppmv; this is related

to the approximation made that $[H_3O^+]$ doesn't change through the drift tube.

Shown in figure 2.14, the normalised signal intensity in time (calculated using eq. (2.20)) of m/z 69 is an example of one of these calibration runs. In the experiment, the flow of a canister of 77 ppb isoprene was increased between blanks in even 5 min steps.

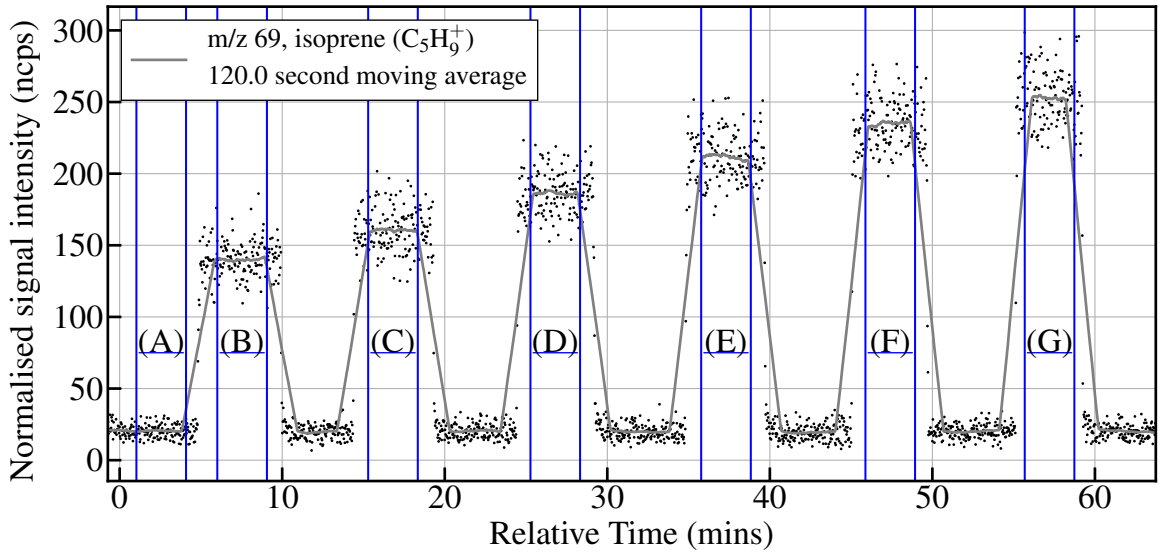

Figure 2.14: Normalised counts per second of m/z 69 under variation of dilution of a canister of 77 ppb isoprene to establish the linear response of the PTR-MS. The mean, standard deviation and standard error of the mean for each indicated region (A), (B), (C), ... is shown in table 2.3 and figure 2.16. The E/N used here was ∼144 Td, there are 66 measurement cycles per 120 s.

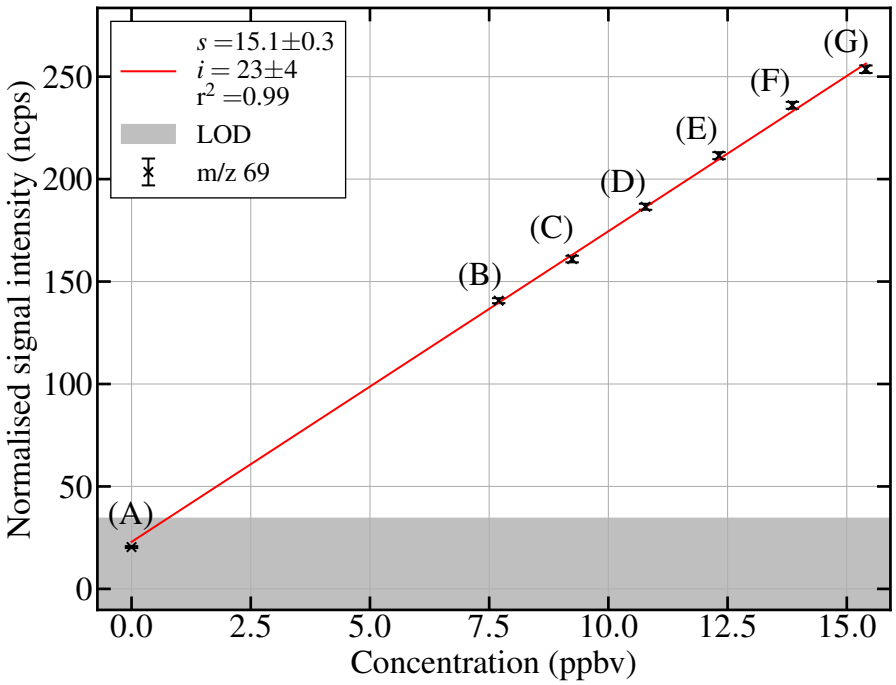

Figure 2.15: Normalised counts per second versus concentration from the data slices from figure 2.14, and the calculated concentration using the flow rates and canister concentration. The error bars correspond to the standard error of the mean. Details of the linear fit are shown in the legend, s is the slope and i the intercept. The limit of detection (LOD) is also shown.

To visualise the measurement error from the PTR-MS, the regions in fig. 2.14 are plotted as histograms (see fig. 2.16). The equivalent gaussian noise profile shows how after many cycles the probability density of the measured signal intensity approaches the continuous distribution. This is also shown in the relative change of the standard error (see fig. 2.17).

As is shown in figure 2.17, it took approximately 2–3 mins, using 7 channels for any additional measurements to make little change to the measured standard error. In most cases in this work, the time it took for the external experiment to stabilise took much longer than the PTR-MS measurements.

Table 2.3: Statistical information for the isoprene calibration shown in fig. 2.14. The sample size of each region consists of 100 measurements.

Label	Mean, $\bar{x}$ (ncps)	Standard deviation, σ (ncps)	Standard error of the mean, $\sigma_{\bar{x}}$ (ncps)
(A)	20.4	4.69	0.50
(B)	141	12.3	1.2
(C)	161	16.0	1.6
(D)	186	14.6	1.5
(E)	211	17.0	1.7
(F)	236	16.9	1.7
(G)	254	18.2	1.8

Over the course of this work, several different VOC were used (made up into Restek canisters - see section 2.1.5). The result of the calibrations, similar to the one done with isoprene, is shown in fig. 2.18, with the corresponding statistical information in table 2.4.

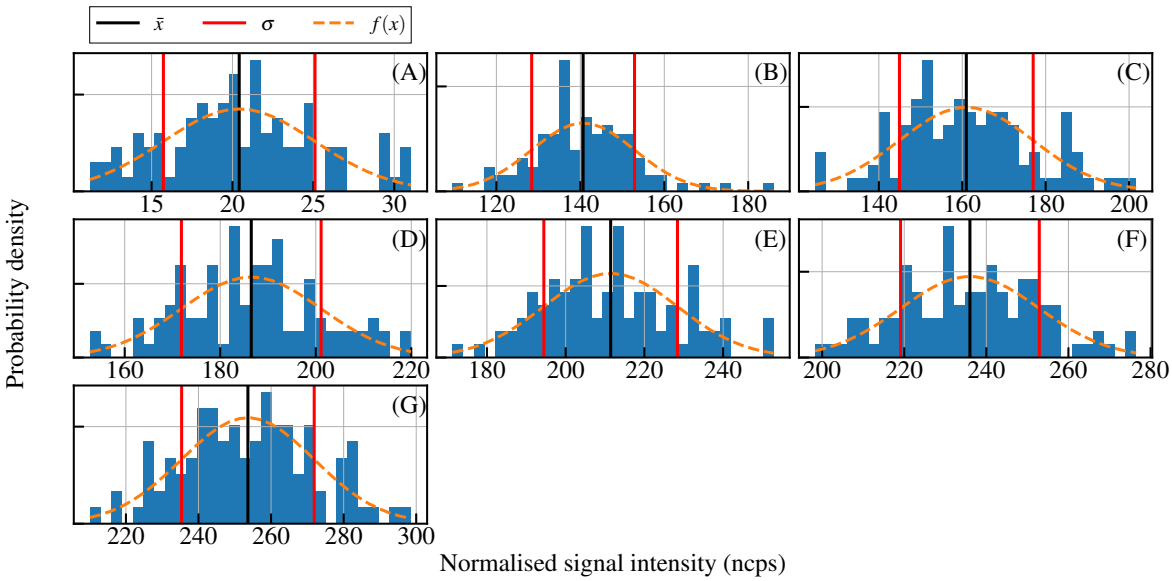

Figure 2.16: Spread of the data for the 6 data slices as taken from figure 2.14, the dashed orange line is fitted assuming a Gaussian noise distribution. Relevant statistical parameters are shown in table 2.3.

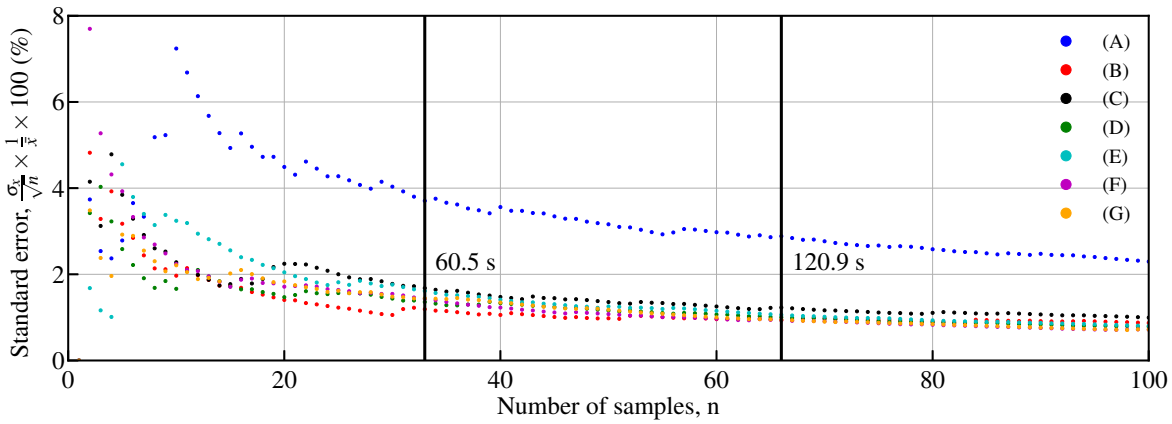

Figure 2.17: Standard error of the mean under variation of the number of samples. In this case a total of 8 channels were chosen with a 200 ms dwell time each.

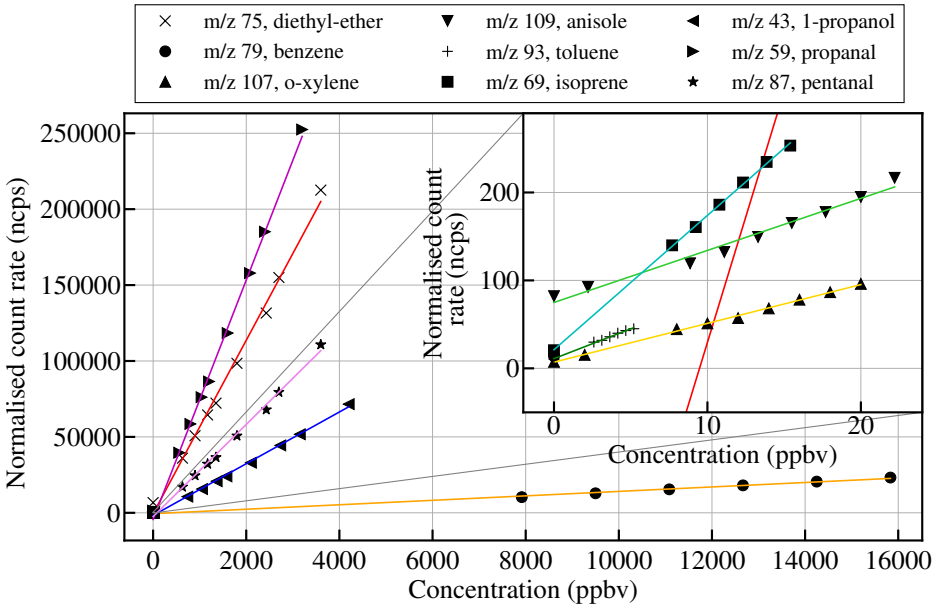

Figure 2.18: PTR-MS calibration curves for various compounds.

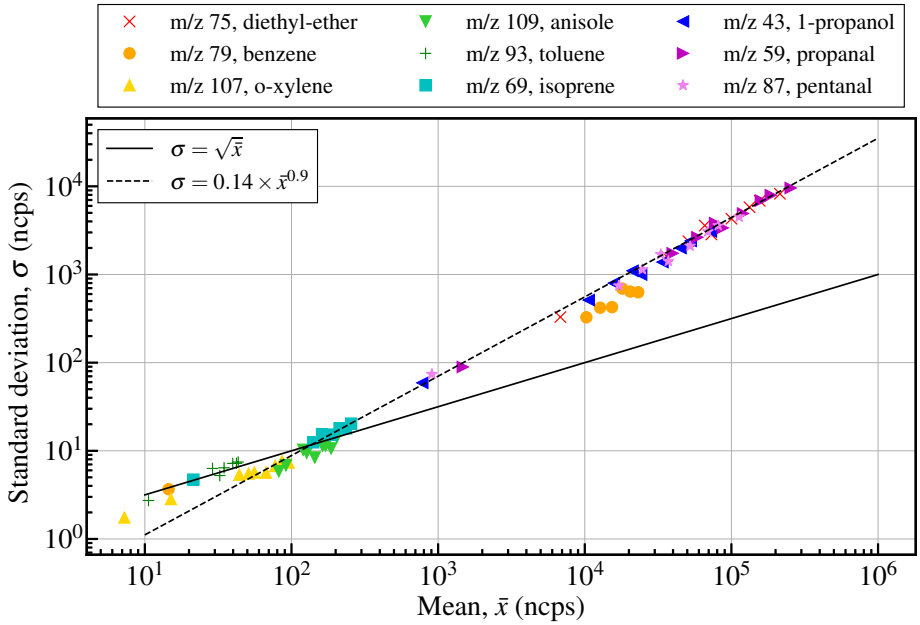

Figure 2.19: Standard deviation (σ) versus the mean of 50 measurements, corresponding to the calibration curves in fig. 2.18. The theoretical minimum Poissonian counting error ($\sigma = \sqrt{\bar{x}}$) and an arbitrary best fit is shown.

Table 2.4: PTR-MS sensitivity in cps/ppbv with the corresponding compound mass and the resulting mass used by the quadrupole in brackets.

Compound	Molecular mass (amu, quadrupole m/z)	Concentration in the calibration gas (ppbv)	H_3O^+ sensitivity (ncps/ppbv)	$k_{H_3O^+}$ (10^{-9} cm^3s^{-1})	Ref.
isoprene, C_5H_8	68 (m/z 69)	77	15.1	2.0	[142]
diethyl-ether, $(C_2H_5)_2O$	74 (m/z 75)	18×10^3	62	2.4	[139]
benzene, C_6H_6	78 (m/z 79)	6.333×10^6	1.63	2.0	[141, 142]
toluene, C_7H_8	92 (m/z 93)	26	6.5	2.2	[142]
o-xylene, C_8H_10	106 (m/z 107)	220	4.5	2.4	[142]
anisole, C_7H_8O	108 (m/z 109)	244	6.4	2.7	[139]
1-propanol, C_3H_8O	60 (m/z 61, 43)	21×10^3	18 (m/z 43)	2.7	[138]
propanal, C_3H_6O	58 (m/z 59)	16×10^3	82	3.6	[147]
pentanal, $C_5H_{10}O$	86 (m/z 87, 69)	18×10^3	33 (m/z 87)	3.6	[147]

2.4 Summary

In this chapter, the experimental setup is introduced. The RF-driven, atmospheric pressure plasma source for generating atomic chlorine is described with the driving frequency (40.68 MHz), gas mixture (argon with small admixture of molecular chlorine gas) and electrode-electrode distance (1.2 mm) chosen to maximise the conversion of molecular chlorine into atomic chlorine while also minimising any potential chemical interferences.

The proton transfer reaction mass spectrometer used in this work is also described. The concentration of prepared gas standards using different volatile organic compounds was measured using the PTR-MS on leaving the novel gas reactor. Through these calibrations, the measurements taken using PTR-MS was verified. The calibration of the mass flow controllers used in this work is also presented.

Chapter 3

Global modelling of an argon plasma containing chlorine and literature review

This chapter describes the effort made to model the argon/chlorine plasma source described in the previous chapter. A description of the zero-dimensional, global plasma model and a review of the available data for modelling chlorine-containing plasma is given. Swarm parameters calculated using BOLSIG+ from the cross section used in this work and other published cross sections is compared with experimental data. Model predictions under variation in input power, total flow rate and input Cl_2 admixture are discussed.

3.1 Global plasma modelling

Global plasma models are generally regarded as the simplest computationally, and are used to investigate large, complex chemistries and simple plasma geometries fast [148]. In this work, the global model is used to investigate the production of atomic chlorine with variation in input power, flow rate and input molecular chlorine admixture. Using volume averaged properties, these models assume a homogeneous plasma where all spatial derivatives are zero.

The model used in this work is a zero-dimensional global model called Globalkin [149, 150]. Globalkin has been used to model similar plasma source geometries, with He/H_2O and He/O_2 mixtures [3]. Other similar global models have been used to study Ar/Cl_2 plasmas [29, 151–153]. Globalkin comprises a two-term Boltzmann and ordinary differential equation (ODE) solver for a given input plasma chemistry set (see appendix A) and geometry (see fig. 3.1). The two main equations that are solved relate to energy and mass conservation of the different plasma species.

Equation (3.1) describes mass continuity, i.e. the rate of change of species density n_i [3].

$$\frac{dn_i}{dt} = \frac{A}{V}\left(-\frac{D_i n_i \gamma_i}{\gamma_i \Lambda_D + \frac{4D_i}{v_{th,i}}} + \sum_j \frac{D_j n_j \gamma_j f_{ji}}{\gamma_j \Lambda_D + \frac{4D_j}{v_{th,j}}}\right) + S_i \tag{3.1}$$

The first term in brackets on the right hand side calculates the diffusion losses of species i to the walls, the second term in the brackets calculates the gain of species i by the sum of the other species ($\sum_j$) returning from the walls as species i. A/V is the surface-volume ratio of the plasma; the diffusion coefficient D_i is calculated using the Lennard-Jones parameter σ for neutral species or given by lookup tables (such as [154]) for charged species. S_i is the stoichiometric production/destruction term of species i through chemical reactions j [149];

$$S_i = \sum_j (a_{ij}^{RHS} - a_{ij}^{LHS}) k_j \prod_l N_l^{a_{ij}^{(LHS)}} \tag{3.2}$$

where a_{ij} is the stoichiometric coefficient of species i in reaction j on the left-hand (LHS) and right-hand side (RHS) of the reaction. k_j is the reaction rate of reaction j and the product is over the densities of all the species on the left-hand side.

Other parameters are defined as follows: γ_i is the fraction of species i that is lost to the walls (see table 3.2); f_{ji} is the fraction of species j that is lost to the walls and returns to the plasma bulk as species i; $v_{th,i}$ is the thermal velocity of species i. Because of the rectangular plasma geometry (fig. 3.2), the diffusion length Λ_D is calculated using eq. (3.3) [156],

$$\frac{1}{\Lambda_D^2} = \left(\frac{\pi}{l}\right)^2 + \left(\frac{\pi}{h}\right)^2 + \left(\frac{\pi}{w}\right)^2 \tag{3.3}$$

where l, h and w is the length, height and width of the plasma, i.e. $50{\times}0.5{\times}5$ mm^3, $\Rightarrow \Lambda_D = 0.158$ mm. Due to the discrete time steps and finite precision used by the ODE solver [155], strict mass conservation (and by extension, charge conservation) is sometimes violated.

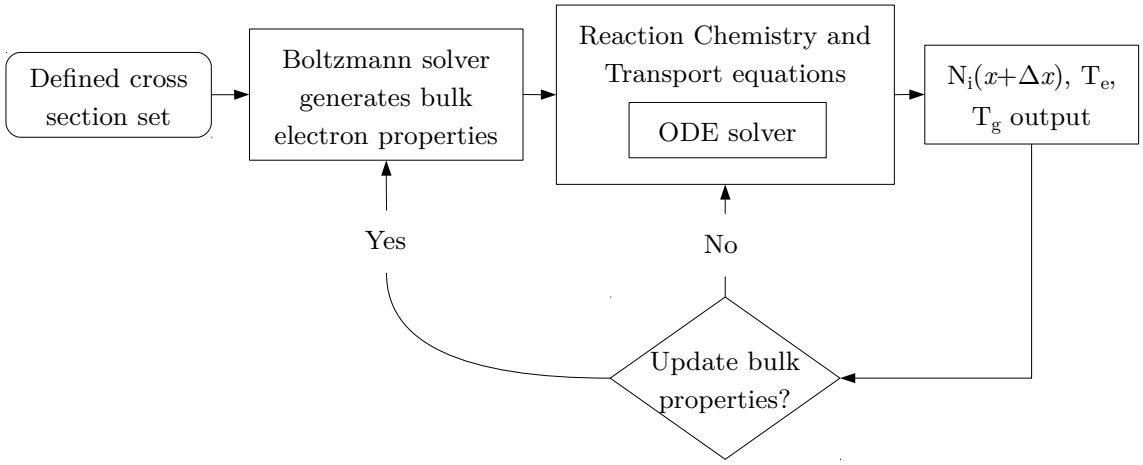

Figure 3.1: Globalkin workflow. Bulk electron transport and reaction coefficients are calculated from the user defined cross section set using an internal Boltzmann solver. These bulk electron reaction and transport coefficients are then used in eqs. (3.1), (3.4) and (3.5), with the resulting set of coupled ordinary differential equations (ODEs) integrated by the ODE solver [155].

Equations (3.4) and (3.5) calculate the rate of change of electron and background gas kinetic energy;

$$\frac{d}{dt}\left(\frac{3}{2}n_e k_B T_e\right) = \mathbf{J}\cdot\mathbf{E} - \sum_i \frac{3}{2}n_e\nu_{ei}\left(\frac{2m_e}{\overline{M_i}}\right)k_B(T_e - T_g) + \sum_j n_e k_j n_j \Delta\varepsilon_j \tag{3.4}$$

$$\begin{aligned}\frac{d}{dt}\left(\frac{3}{2}n_g c_p T_g\right) = P_{ion} + \sum_i \frac{3}{2}n_e\nu_{ei}\left(\frac{2m_e}{\overline{M_i}}\right)k_B(T_e - T_g)... \\ ... + \sum_i \Delta H_i k_i - \frac{\kappa}{\Lambda_D^2}(T_g - T_w)\end{aligned} \tag{3.5}$$

where **J** and **E** is the local current density and electric field, respectively. Equivalent to the applied power per unit volume, $\mathbf{J} \cdot \mathbf{E}$ corresponds to the ohmic/joule heating of the electrons. For the plug-flow case used here, the power deposition is defined as a function of position. Thus the power density in the model represents the time-averaged power deposition over many rf-cycles. As mentioned in the previous chapter, the power deposited in the plasma is not measured in this work. The power used here is similar to that measured using a similar plasma source, typically 30 W [114]. The second and third term on the right hand side of eq. (3.4) corresponds to the loss of energy due to elastic collisions with all the other species and gain of energy due to super-elastic and inelastic collisions. In eq. (3.5), P_{ion} is the power deposited by the ambipolar field into the ions. The second term corresponds to energy gain through elastic collisions of electrons with all other species. The third and fourth terms correspond to energy gain through the change in enthalpy, ΔH_i of reaction i and the conduction of heat to the walls.

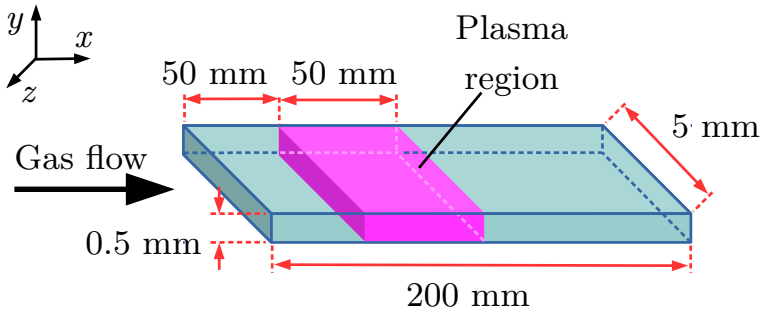

Figure 3.2: Geometry used in the model (not to scale). Assuming the whole system has reached steady-state, the temporal evolution of a gas slab is mapped onto a pseudo spatial dimension (i.e. the plasma channel, x-dimension) assuming a constant mass flux through the channel (plug flow).

ν_{ei} is the electron collision frequency with species i, m_e and $\overline{M_i}$ is the electron and mean molecular mass of the input gas mixture. T_e and T_g is the electron and gas temperature respectively. k_j is the inelastic reaction rate of electrons with species j, with $\Delta\varepsilon_j$ the change in electron energy after the collision. In eq. (3.5), c_p, κ and T_w is the specific heat, thermal

conductivity and wall temperature respectively.

Through assuming a constant mass flux, the zero-dimensional model is extruded into a pseudo 1-dimension;

$$\frac{dv_x}{dt} = -\frac{v_x}{\rho}\frac{d\rho}{dt} \tag{3.6}$$

where ρ is calculated using the instantaneous mean molecular weight. The flow velocity v_x is calculated using the equation

$$v_x = \frac{\phi}{A_{flow}}\frac{n_0}{n_g} \tag{3.7}$$

where ϕ is the flow rate (in sccm), A_{flow} is the cross sectional area of the flow, n_0 is the gas density at STP, i.e. 273.15 K at atmospheric pressure and n_g is the instantaneous gas density.

All experiments in this work use argon as the background gas with a small admixture ($\sim$1%) of molecular chlorine gas. The initial species densities in the model are defined as mole fractions; ground state argon is very close to 1 with ground state molecular chlorine making up the rest. The plasma generated species are given very small initial mole fractions of $\sim 10^{-20}$. The individual species tracked in the model are given in table 3.1.

3.2 PumpKin pathway analysis

To analyse the principal production and destruction reaction pathway for each species, a code by A. H. Markosyan called PumpKin [167] based on an algorithm by Lehmann [168] is used. As the code is described in detail elsewhere [167] only relevant details are discussed here. In brief, this code uses the output of a Globalkin run containing the list of reactions and the reaction rate of each reaction for each position in the run. Alongside this, a user defined input deck containing the species of interest, the time interval in the model output in which to run the analysis Δt, a species lifetime τ_{max} and reaction rate threshold k_{min} is used.

Species	Neutral	Positive	Negative
Ar	Ar, Ar*, Ar**	Ar^+	
Cl_2	$Cl_2(v = 0, 1, 2, 3)$, Cl_2*	Cl_2^+	
Cl	Cl, Cl*	Cl^+	Cl^-
Electrons			e

Table 3.1: Species tracked in the model. Ar* species includes the $1s_5$, $1s_4$, $1s_3$ and $1s_2$ states and Ar** species is the sum from higher forbidden and allowed states using cross sections from Tachibana [157]. The argon momentum transfer and ionisation from ground state cross sections are from Hayashi [158] and Rapp and Englander-Golden [159], respectively. The ionisation of Ar* and Ar** and step-wise excitation is taken from analogy with potassium [160, 161]. For discussion of the chosen Cl_2 cross section, see section 3.3. Cl_2* is the sum of the $^1\Sigma_u$ and $^1\Pi_u$ Rydberg states identified by Rescigno [162]. Cl* is the sum of 4s, 4p, 3d, 5p, 4d and 5d states from Ganas [163], with the Cl momentum transfer and ionisation cross sections the same as used by Rogoff et al. [164].

Initially, the analysis tool allocates each individual reaction to an individual reaction pathway. An effective lifetime τ_i for each species in the given time interval Δt is then calculated;

$$\tau_i = \frac{\bar{c}_i}{d_i}, \quad \bar{c}_i = \frac{1}{\Delta t} \cdot \int_0^{\Delta t} c_i(t)dt, \quad d_i = \tilde{d}_i + \sum_{\{l \,|\, m_{il}<0\}} |m_{il}| \cdot k_l \tag{3.8}$$

where $\bar{c}_i$ is the time-averaged concentration of species i and d_i is the total destruction rate of species i. $\tilde{d}_i$ is the sum of destruction rates slower than k_{min}, $|m_{il}|$ and k_l is the stoichiometry of species i and rate of reaction l respectively. Species with a lifetime longer than the user defined threshold τ_{max} are then neglected. This threshold allows for the separate investigation of short-lived and long-lived species. Of the remaining chemical species, those that are consumed by two or more significant reactions are chosen as 'branching points'. Starting with the branching point species with the shortest lifetime, the production and destruction pathways of this species are connected to each other, using the reaction rate threshold to

Species	γ	Return species	Ref.
Cl	0.02	$1/2Cl_2$	[21, 29]
Ar*	1.00	Ar	[165]
Ar**	1.00	Ar	[165]
$Cl_2(v)$	1.00	$Cl_2(v-1)$	[152, 166]
Cl*	1.00	Cl	[152]
Ar^+	1.00	Ar	*est.*
Cl_2^+	1.00	Cl_2	*est.*
Cl^+	1.00	Cl	*est.*
Cl^-	1.00	Cl	*est.*

Table 3.2: Wall sticking coefficients and returning species used in the model.

separate out reactions that are too slow (to avoid a large number of pathways). The impact of these slow reactions is taken into account in the calculation of the total destruction rate (see eq. (3.8)) and its effect checked at the end of the computation to ensure k_{min} was chosen correctly.

Pathways that contain other pathways (i.e. recycling of species/catalytic reactions) are also identified. The reactions in these sub-pathways are given a weighting (a positive natural number) to produce the correct net input & output species. Once this is done the process repeats with the next branching point species, until all the branching species have been analysed. Pumpkin then produces a list of the dominant production & destruction pathways (list of reactions) for the user chosen species.

3.3 Currently available data

Due to the difficulty of handling molecular chlorine, the available experimental data used for modelling chlorine-containing plasmas is more sparse than for relatively more inert molecular gases, such as N_2 or O_2. Even so, there have been several detailed reviews of the available data for modelling [169–171]. Several authors [164, 171–174] have suggested cross sections,

using a combination of the available experimental and theoretical data.

To help with the following discussion and review, the relevant electron-impact processes that occur with Cl_2 will be introduced. As mentioned in Hamilton et al. [175], the potential energy curves of Cl_2 are relatively easy to interpret, making Cl_2 a good test bed for more complex systems. Due to the electronic configuration of molecular chlorine, there are a number of low energy anti-bonding states (see fig. 3.3) that lead to dissociation and result in two ground state chlorine atoms.

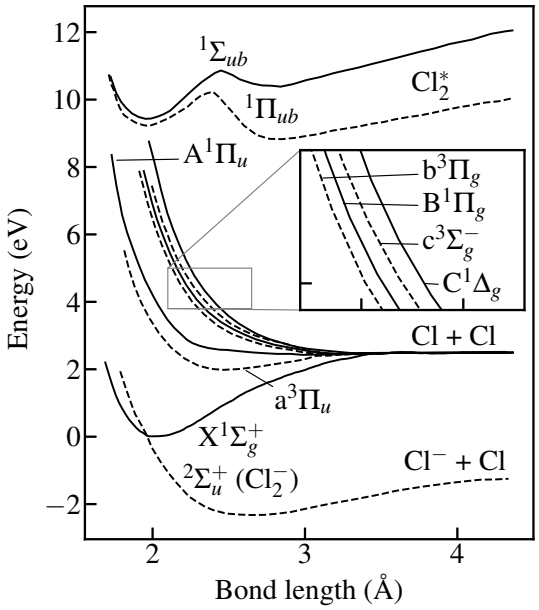

Figure 3.3: Molecular chlorine potential energy curves. Adapted from Peyerimhoff and Buenker [176]. In this work, electron impact excitation cross sections [174, 175] to $a^3\Pi_u$, $A^1\Pi_u$, $b^3\Pi_g$, $c^3\Sigma_g^-$ (identified as $1^3\Sigma_u^+$ in [176]), $B^1\Pi_g$, $C^1\Delta_g$, ($D^1\Sigma_g^+$, $e^3\Sigma_u^+$: not shown) states are assumed to spontaneously dissociate. The two Rydberg cross sections ($^1\Pi_{ub}$ and $^1\Sigma_{ub}$) calculated by Rescigno [162] are assumed to lead to Cl_2^*. The individual cross sections are used for calculation of the EEDF.

3.3.1 Molecular chlorine cross section review

For clarity, the following discussion is split into the available data for each electron-impact process. Starting with the cross section for momentum transfer (EMT) i.e. $Cl_2 + e^- \rightarrow Cl_2 + e^-$, it has been calculated by Rescigno, using the complex Kohn variational method [162]. Experimental measurements of the total electron scattering cross section have been taken by Gulley et al., Cooper et al. and Makochekanwa et al. [177–179]. In Rogoff et al. their chosen cross section was derived by iteratively changing an initial estimate until their calculated swarm parameters somewhat matched those measured by Bozin and Goodyear [164, 180]. Figure 3.4b) shows the comparison between the available cross section data for momentum transfer and the measured total electron scattering in Cl_2.

For each of the measured cross sections, a combination of an electron beam source, electrostatic lenses, collision cell and movable detector were used to measure the cross section. The stated error for each of the three measured cross sections was 8%, 20% and 4.5-6% for Gulley et al., Cooper et al. and Makochekanwa et al., respectively. The corresponding cross section in argon is also included in the figure to show the difference in agreement there is for such a well characterised and studied noble gas compared with Cl_2. Comparing the two figures it is clear that there is still some degree of disagreement over the exact cross section for this process in chlorine.

Electron impact vibrational excitation, (EVX) i.e. $Cl_2(v = n) + e^- \rightarrow Cl_2(v = n + 1) + e^-$ where n=0,1,2 has quite a large cross section, however it is the only cross section not to have been verified by experiment. This is evident in fig. 3.5a) as there is disagreement about the height, shape and threshold of the cross section. To begin with, Rogoff et al. assumed the initial cross section to have a shape similar to that of fluorine with a threshold of 0.069 eV [164]. The cross section was then iteratively altered to agree with the experimental swarm parameters [180]. Christophorou and Olthoff used a subtraction method to deduce the vibrational cross section, taking the sum of the other processes (dissociative attachment, ionisation, electronic excitation) away from the total elastic scattering cross section. Gregório and Pitchford used a similar technique, using the cross sections for the other processes to deduce a cross section for EVX. Ruf et al. is unique in that they used ab initio calculations

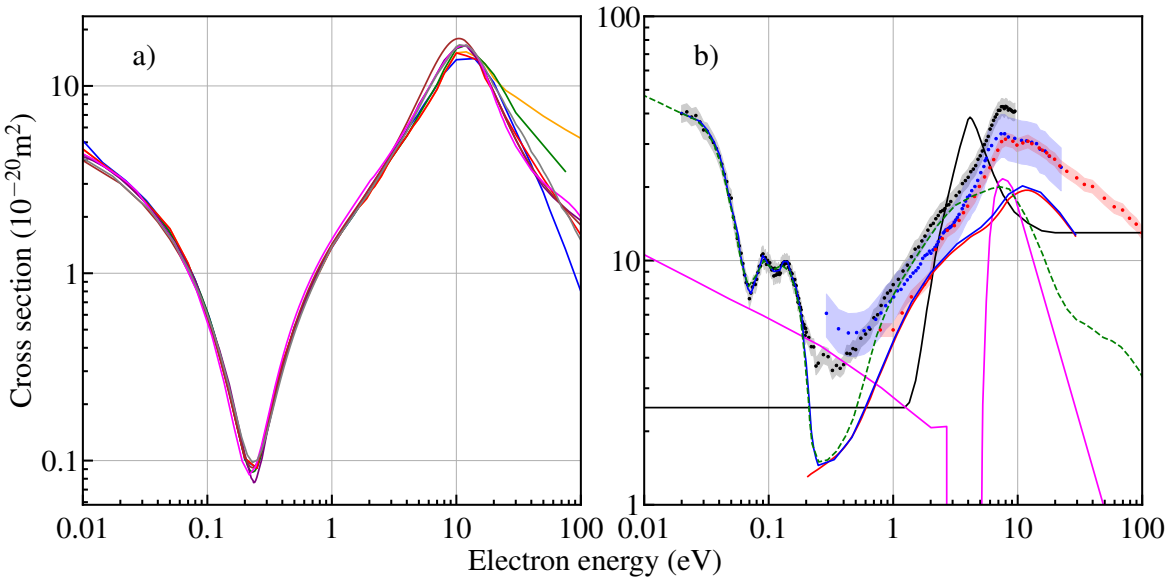

Figure 3.4: Comparison of momentum transfer (EMT) and measured total scattering cross section for a) argon [181] and b) Cl_2. For a), Puech (——) [182,183], Phelps (——) [184], Morgan (——) [185], IST-Lisbon (——) [186], Hayashi (——) [187], COP (——) [188], BSR (——) [189, 190] and Biagi 8.97 (——) [191]. For b) the measurements by Gulley (•) [177], Cooper (•) [178] and Makochekanwa (•) [179] are surrounded by a shaded region indicating the experimental error. The calculated results of Rogoff (——) [164], Rescigno (——) [162], Tuan (——) [172], Gregório (——) [173] and Kawaguchi (- - - - -) [174] are indicated by lines for ease of comparison.

to produce the cross section.

The dissociative attachment ($Cl_2 + e^- \rightarrow Cl^- + Cl$) cross section has been measured by Kurepa et al., Fabrikant et al. and Ruf et al. [192–194]. In Ruf et al. [192] they used laser photoelectron attachment to measure Cl^- formation (from dissociative electron attachment, EDA) from 0 to 195 meV. They compared the result of this experiment with results from semi empirical R matrix calculations to ensure their theoretical calculations were valid before extending those calculations to predict the cross section for EVX. Azria et al., Feketova et al. and Gope et al. have investigated and/or probed the negative ion states of Cl_2 using a technique called velocity slice imaging [195–197]. Due to the different shape and symmetry of

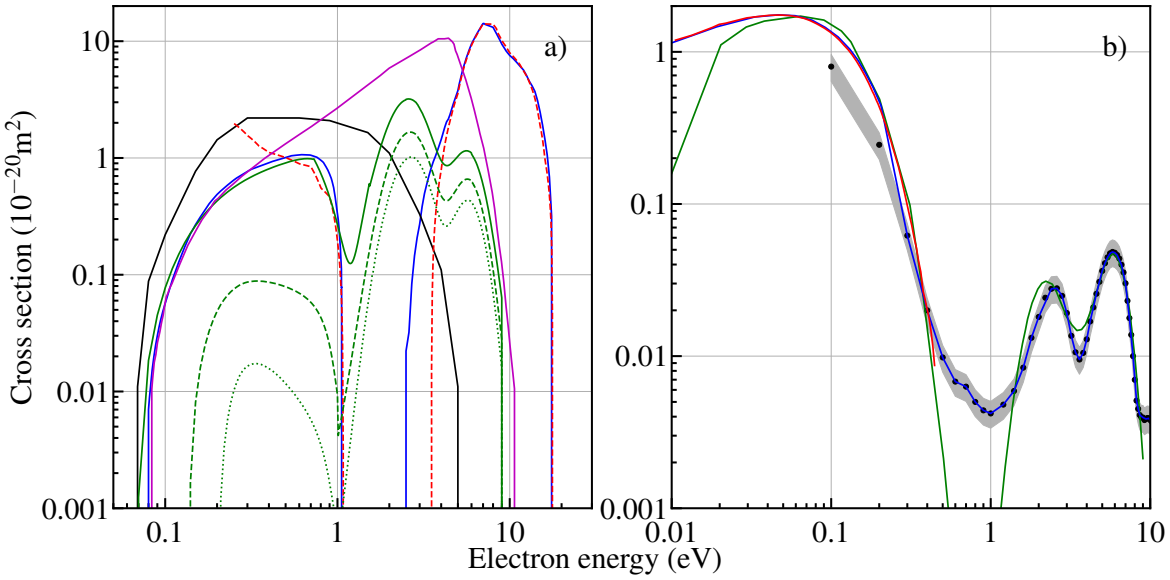

Figure 3.5: Comparison of a) calculated and derived cross section for electron impact vibrational excitation (EVX) of Cl_2 and b) measured and calculated dissociative electron attachment (EDA). In a); Rogoff (——) [164], Tuan (——) [172], Gregório (——) [173], Ruf ($v_o \rightarrow v_1$ ——, $v_o \rightarrow v_2$ - - - -, $v_o \rightarrow v_3$ ·····) [192], Christophorou (- - - -) [171]. For b); the measurements of Kurepa (•) [193] are surrounded by a shaded area indicating the experimental error, calculations by Ruf (——) [192] and Fabrikant (——) [194], as well as the review by Gregório (——) [173].

the anti-bonding orbitals, the products of EDA will have a characteristic angular distribution. This helps to distinguish what anionic states contribute to which peaks in the EDA cross section. For example, the two peaks at 2.5 eV and 5.6 eV in figure 3.5b) correspond to dissociation from the $^2\Pi_g$ and a mixture of $^2\Pi_u$ and $^2\Sigma_u^+$ states, respectively [192]. Looking at figure 3.5b) it is clear that the calculated and measured cross section agree, giving credence to the Ruf et al. EVX cross section in figure 3.5a).

For the electronic excitation of Cl_2, Figure 3.3 shows the early calculations of Peyerimhoff and Buenker of some low lying energy levels. As can be seen from the figure the lowest six levels are all anti-bonding, leading to dissociation. Measurements and calculations of the cross section for electron impact excitation leading to dissociation, EDS ($Cl_2 + e^- \rightarrow Cl +$

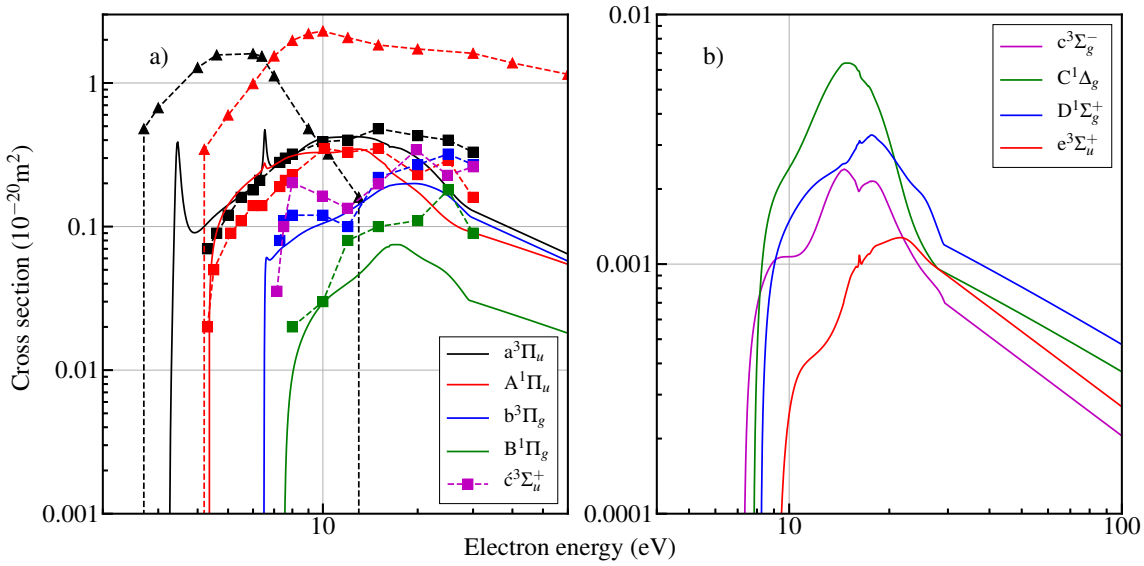

Figure 3.6: a) Comparison between sets of calculated cross sections for excitation into dissociative states (EDS) Hamilton [175](solid lines), Rescigno [162](dashed lines w/squares), and Rogoff [164] (dashed lines w/triangles). The cross section to $\acute{c}^3\Sigma_u^+$ identified by Rescigno [162] is included for comparison. b) Cross section to higher levels by Hamilton et al. [175].

$Cl + e^-$) have been done by Cosby et al. [198], Rescigno [162] and Hamilton et al. [175]. The results of recent R matrix calculations done by Hamilton et al. [175] to find the cross section to low-lying electronic states is shown in figure 3.7a). The cross section by Rogoff [164] to excited states $a^3\Pi_u$ & $A^1\Pi_u$ using data by Jureta et al. [199] is also given for comparison.

In fig. 3.7b), the sum of the calculated Hamilton cross section is compared to the measured data of Cosby [198] and the sum of Q_1 and Q_2 ($a^3\Pi_u + A^1\Pi_u$) cross sections of Rogoff [164]. As was mentioned in Hamilton et al. [175] it is perhaps not valid to compare these two datasets as the calculated values do not take into account the potential increase in the cross section due to vibrational excited Cl_2 that would have been present in the measurements of Cosby et al. [198]. The cross section used by Kawaguchi [174] is the Hamilton cross section multiplied by 2.5, this was done to increase the agreement with the measured swarm parameters of Gonzalez-Magana [200]. The cross section suggested by Tuan and Jeon [172] has a maximum of the same order of magnitude, however the shape and threshold is not in

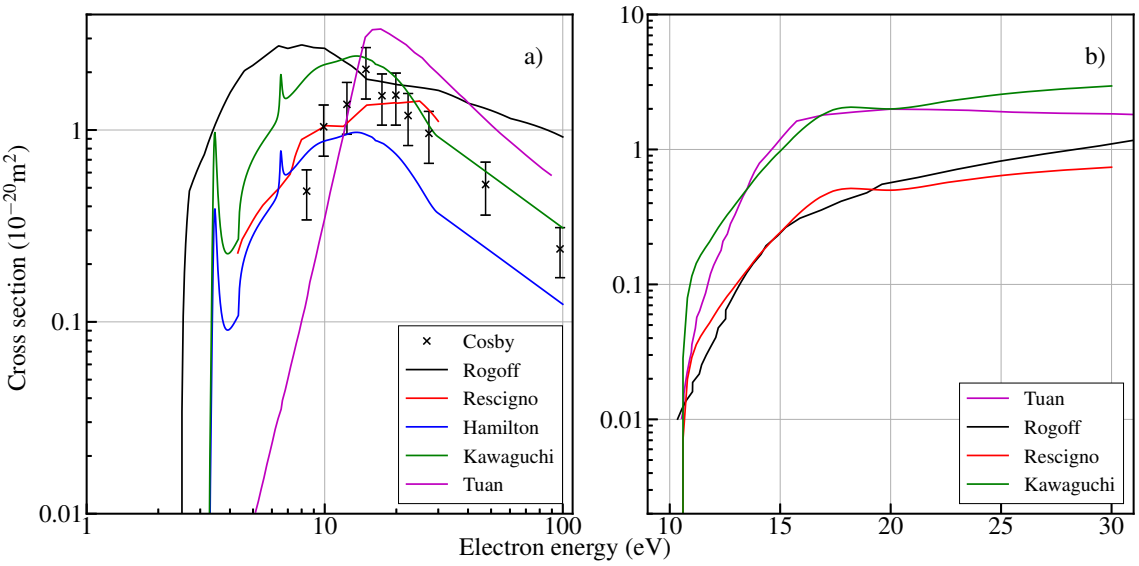

Figure 3.7: a) Comparison of the summed cross sections of figure 3.6. Rogoff [164], Kawaguchi [174], Rescigno [162], Hamilton [175] and Tuan [172], with the experimental data of Cosby [198]. b) summed excitation to Rydberg levels cross section (i.e. to levels $^1\Sigma_{ub} +^1 \Pi_{ub}$).

agreement with any of the previously calculated cross sections.

In fig. 3.7b) the cross section for excitation to two metastable Rydberg levels ($^1\Sigma_u$ and $^1\Pi_u$) is shown. Rogoff used the data of Spence et al. [201] for the basis of this cross section. The only other calculation of this cross section was done by Rescigno [162]. The cross section used by Kawaguchi (4×Rescigno) and Tuan et al is given for comparison.

The cross section for ionisation of molecular chlorine has been measured by many authors. For ease of comparison, only the most relevant cross sections are given in fig. 3.8. Figure 3.8 shows the most recent experimental data by Basner and Becker [41] of single ionisation, EIN$_1$ ($Cl_2 + e^- \rightarrow Cl_2^+ + 2e^-$), single dissociative ionisation, EIN$_2$ ($Cl_2 + e^- \rightarrow Cl^+ + Cl + 2e^-$), double ionisation, EIN$_3$ ($Cl_2 + e^- \rightarrow Cl_2^{++} + 3e^-$) and double dissociative ionisation, EIN$_4$ ($Cl_2 + e^- \rightarrow Cl^{++} + Cl + 3e^-$). The measured data for single ionisation and ion-ion production ($Cl_2 + e^- \rightarrow Cl^+ + Cl^- + e^-$) by Kurepa et al. is given as this data is used by Rogoff [164] and Christophorou [171]. The dashed green line shown is the Kawaguchi

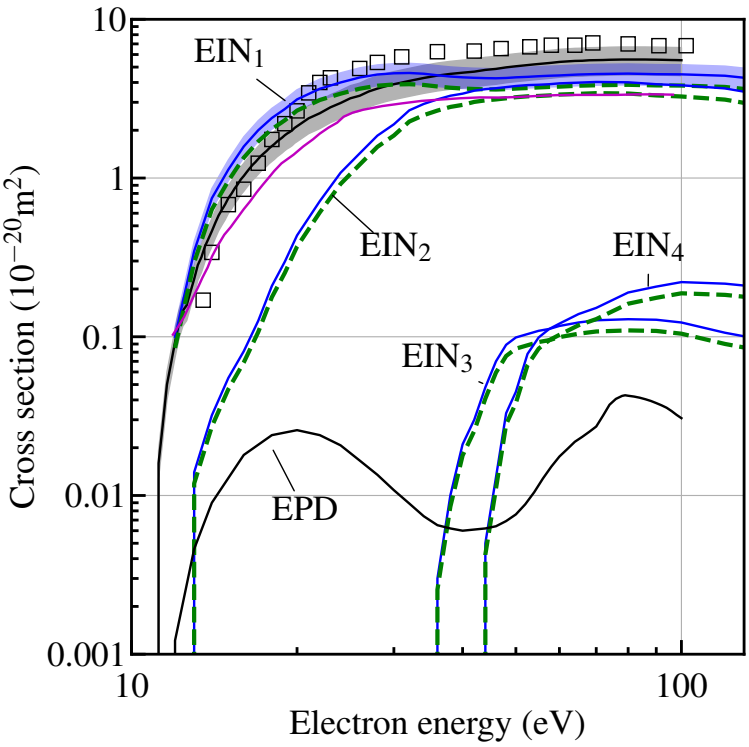

Figure 3.8: Comparison between single (EIN$_1$), dissociative (EIN$_2$), double (EIN$_3$) and dissociative double (EIN$_4$) ionisation and ion-ion production (polar dissociation, EPD). Stevie and Vasile (□), Kurepa (——), Basner and Becker (——), Tuan (——), Kawaguchi (- - - - -).

cross section, to have a better agreement with the net ionisation coefficient of Gonzalez-Magana [200] the ionisation cross section is multiplied by 0.85 (experimental error is 15%). An overview of the processes mentioned here are shown in table 3.3.

Table 3.3: Molecular chlorine reactions through electron impact.[a]n=0,1,2

Process	Reaction	Studies
Momentum transfer (EMT)	$Cl_2 + e^- \rightarrow Cl_2 + e^-$	[162, 164, 177–179]
Vibrational excitation (EVX)	$Cl_2(v = n)^a + e^- \rightarrow \ldots$ $\ldots Cl_2(v = n + 1) + e^-$	[164, 171, 173, 192]
Dissociative electron attachment (EDA)	$Cl_2 + e^- \rightarrow Cl + Cl^-$	[192–194]
Dissociation (EDS)	$Cl_2 + e^- \rightarrow Cl + Cl + e^-$	[162, 175]
Excitation (EEX)	$Cl_2 + e^- \rightarrow Cl_2^* + e^-$	[162]
Ion-ion production (EPD)	$Cl_2 + e^- \rightarrow Cl^+ + Cl^- + e^-$	[193]
Single ionisation (EIN1)	$Cl_2 + e^- \rightarrow Cl_2^+ + 2e^-$	[41, 202, 203]
Single dissociative ionisation (EIN2)	$Cl_2 + e^- \rightarrow Cl^+ + Cl + 2e^-$	[41]

3.3.2 Swarm parameters

As mentioned earlier with the case of Rogoff et al. [164], Tuan et al. [172] and Gregório et al. [173], experimentally measured swarm parameters have been used to evaluate complete cross section sets. Electron swarm parameters have been measured for a large array of different gas mixtures and pressures. The two main techniques for measuring swarm parameters are the pulsed Townsend (PT) and Steady-state Townsend (SST). As mentioned in [42, 204, 205], the number of experimental laboratories measuring swarm parameters has dropped in the last 50 years, thus verifying binary collision data has only become grown more difficult.

In this work, a new cross section based from the work by Kawaguchi et al. [174] has been developed. The focus on this cross section was the agreement with the effective ionisation coefficient $(\alpha - \eta)/\mathrm{N}$, where α and η are the Townsend ionization and attachment coefficients respectively, N is the number density. The new cross section is shown in figure 3.9, with Kawaguchi et al. and Gregório et al. [173, 174].

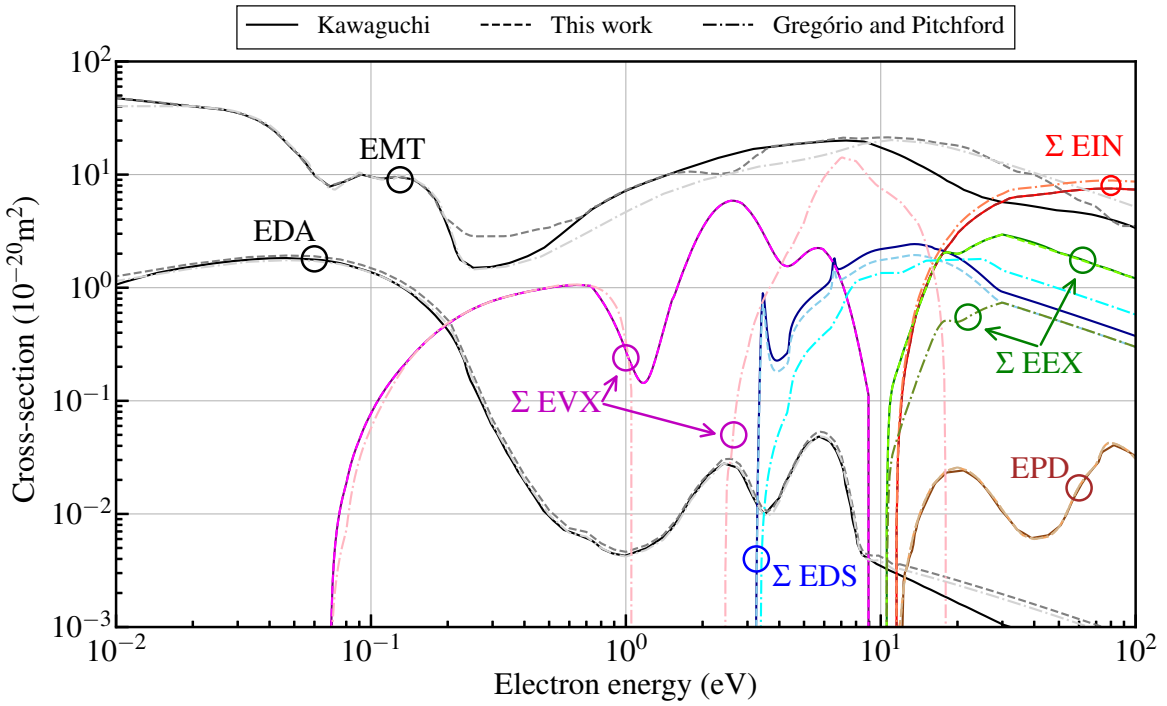

Figure 3.9: Comparison between the most recent cross section by Kawaguchi et al. [174], the cross section developed in this work and the cross section by Gregório and Pitchford [173]. The labels for each process correspond to those in table 3.3.

As shown in the figure above, the cross section for ionisation, vibrational excitation, excitation to Rydberg levels and polar dissociation (ion-ion production) for the cross section developed here is the same as used by Kawaguchi et al. [174]. To achieve a better agreement with the effective ionisation coefficient of González-Magaña et al. [200] (see fig. 3.12), the attachment cross section used by Gregório and Pitchford [173] was increased by 10%, within the stated relative error of Kurepa and Belic [193] (±20%). The electron impact excitation to dissociation cross section used the data of Hamilton et al. [175] however multiplied by 2 compared with ×2.5 as used by Kawaguchi et al. [174]. The change to the momentum transfer cross section used the total scattering cross section as measured by Gulley et al. [177]. To ensure that the change in the dissociation cross section does not result in an overestimated drift velocity, the momentum transfer cross section was altered such that the summed total

cross section compared well with the measured data of Gulley et al. [177].

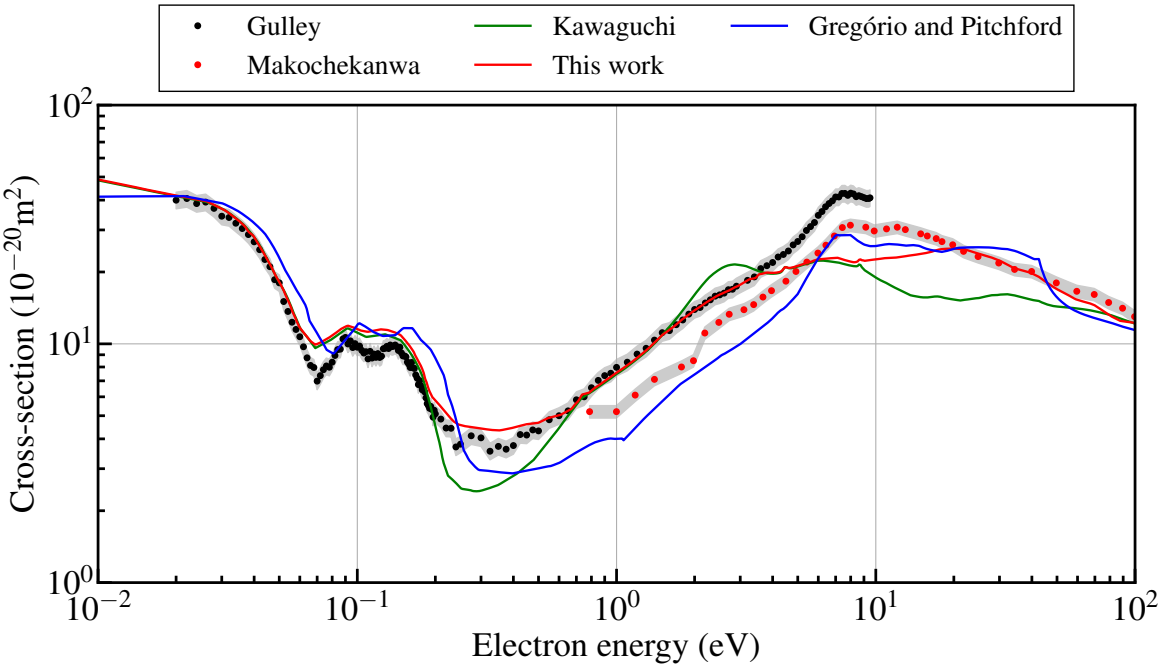

Figure 3.10: Comparison of the summed elastic and inelastic electron impact cross sections of Gregório and Pitchford [173], this work and Kawaguchi et al. [174] for molecular chlorine with experimental data of Gulley et al. [177] and Makochekanwa [179].

Shown in fig. 3.10, the cross section of Kawaguchi et al. [174] rarely exceeds the total scattering cross section by Gulley et al. [177]. As the Kawaguchi momentum transfer cross section uses the data by Gote et al. [206], the cross section above 10 eV decreases compared with Gregório et al. and this work.

To calculate the electron drift velocity using BOLSIG+, the given BOLSIG+ mobility (μN) is multiplied by the reduced electric field, i.e.

$$v_d = \mu \mathrm{N} \times \frac{\mathrm{E}}{\mathrm{N}}$$

As is shown in fig. 3.11, the cross section of Kawaguchi seems to agree the best over the whole range of E/N used by González-Magaña. Because of the high momentum transfer cross section (at high electron energy) of Gregório and Pitchford and this work, the electrons generally lose more energy per collision, resulting in a lower mobility and thus lower drift velocity.

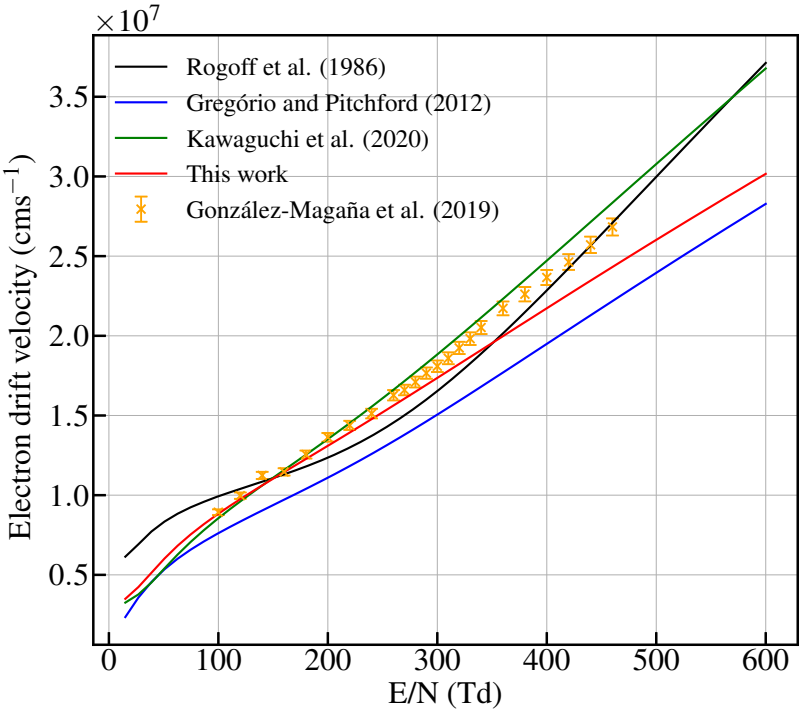

Figure 3.11: Electron drift velocity comparison between the experimental results of Gonzàlez-Magaña et al. [200] and calculations using BOLSIG+.

A was already mentioned, the newly developed cross section here focussed on having the best agreement with the effective ionization coefficient. As shown in fig. 3.12, the agreement is excellent between the Kawaguchi et al. [174], this work and the experimental data of González-Magaña et al. and Božin and Goodyear.

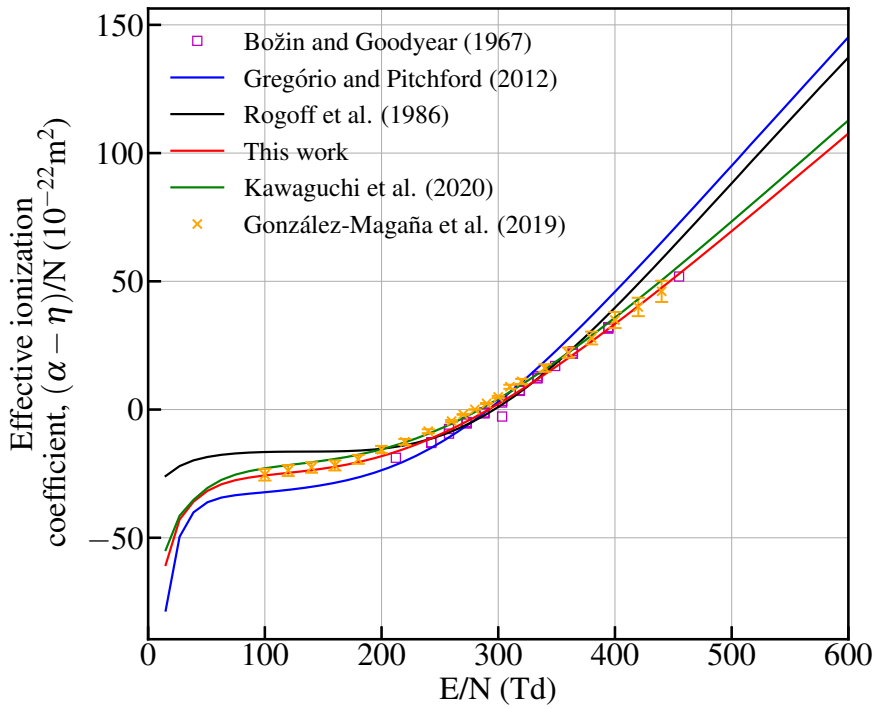

Figure 3.12: Comparison between measured (Božin and Goodyear [180], Gonzàlez-Magaña et al. [200]) and BOLSIG+ calculated cross sections [164, 173, 174].

This figure shows the impact of increasing the Hamilton excitation cross section and using a slightly reduced ionisation cross section. As the cross sections of Rogoff and Gregório use cross sections similar in size to the one by Rescigno the resulting ionisation rate will be artificially too high, resulting in an overestimated effective ionisation coefficient. Because of the relatively little difference between the measured values of the cross section developed here and the published cross section of Kawaguchi and the better agreement of the drift velocity with the Kawaguchi cross section, the Kawaguchi cross section for molecular chlorine was used for the subsequent modelling work.

3.3.3 Electron energy distribution function

The electron energy distribution function is calculated using BOLSIG+. As mentioned previously, the input cross section(s) has a large influence on the resulting EEDF and electron impact rate coefficients. This can be seen in fig. 3.13, with the variation of Cl_2/Ar for three complete cross sections.

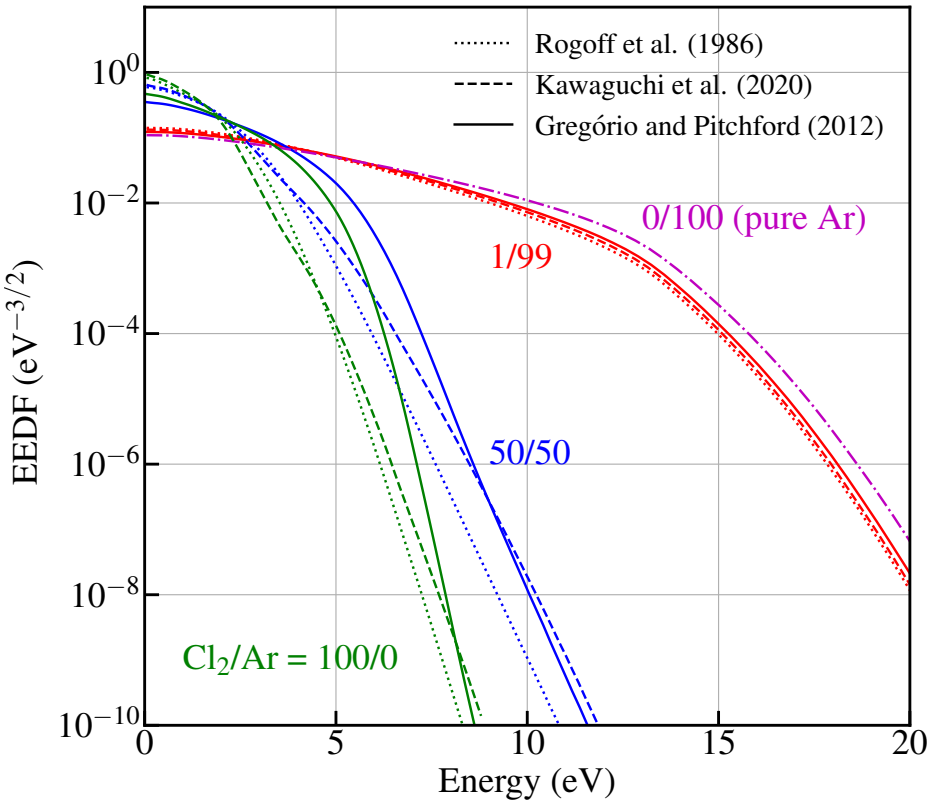

Figure 3.13: Comparison between the EEDF calculated using BOLSIG+ for different Cl_2/Ar mixtures using Rogoff et al., Gregório and Pitchford and Kawaguchi et al. Cl_2 and the argon cross section used in the model at the same reduced applied electric field of 20 Td. The mean electron energy for each of these cases is discussed in the text.

Starting with the 0/100 and 1/99 Cl_2/argon cases, there are many more high energy electrons ($\varepsilon > 10$ eV) than for the other cases. The reason for this is because argon only has high energy threshold (above 10 eV) ionisation and excitation to metastable state processes.

This means that the electrons are much less likely to lose energy in inelastic collisions with an argon atom. Because of the high concentration of argon in the 1/99 case, the small changes between each of the Cl_2 cross sections is not clear and the effect of argon dominates strongly.

Looking from the viewpoint of the 50/50 and 100% Cl_2 cases, it is clear the number of inelastic processes has a strong impact on the resulting EEDF. The slight differences between the cross sections is also much clearer in the 100% Cl_2 case. The mean electron energy of course will not be the same for each of these cases and shows an interesting trend. For the Rogoff, Gregório and Kawaguchi 100% Cl_2 cases, the mean electron energies are 1.279 eV, 1.869 eV and 1.146 eV, respectively [153]. Considering the cross sections for vibrational excitation and electronic excitation leading to dissociation (EDS) used between the Rogoff and Kawaguchi cases, it is not surprising their EEDFs are similar in shape and have similar mean electron energies. For the Gregório cross section uses a smaller EDS and EEX cross section, meaning that there will be more electrons in the 5 to 8 eV range, which is seen in fig. 3.13.

This is also seen with the electron energy loss coefficients fig. 3.14. At low E/N, only the low threshold inelastic collisions are accessible to the electrons. With the threshold of vibrational excitation (EVX) being a multiple of 0.069 eV and the threshold of EDS starting at 3.252 eV, the main energy loss will be through these two processes at low E/N (see fig. 3.14). As E/N increases, the number of accessible inelastic collisions will increase and due to the high cross section of EDS in the 5-8 eV range, the energy lost to these reactions overwhelmingly dominates. This is also seen in fig. 3.15 as the rate coefficient for the EVX and EDS processes are consistently the highest, with EDS slightly increasing with E/N. Something else to consider is the amount of energy the electron will lose with each type of collision - the electron will lose far more energy per EDS collision that each EVX one. Thus even through the EVX rate coefficient is high, the energy loss coefficient is still low.

As E/N increases above 100 Td, the rate coefficients of Cl_2 excitation to metastable states (EEX) and ionisation increase strongly. As the ionisation energy of Cl_2 is 11.49 eV compared to argon's 15.76 eV, and EEX thresholds are 10.54 eV and 11.60 eV for Cl_2 and argon respectively, the increase in the energy lost due to Cl_2 is due to the high cross section

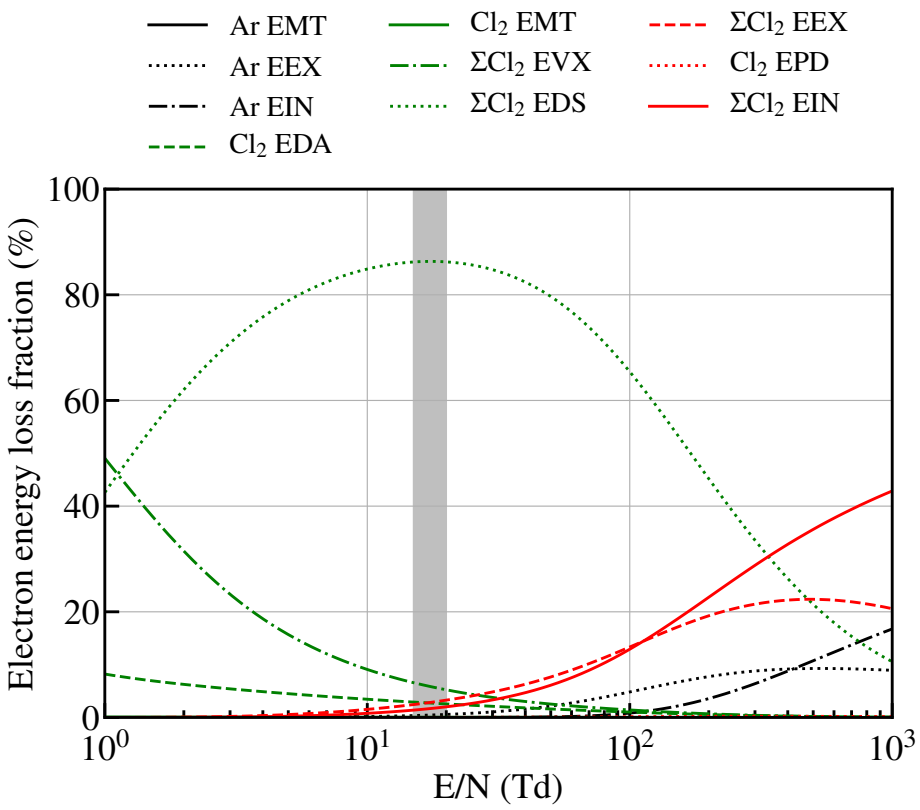

Figure 3.14: Electron energy loss fraction calculated using BOLSIG+ for a 1:99 Cl_2/argon mixture using the argon and chlorine cross sections used in the global model. The shaded area shows the E/N range accessable by the experiment.

for Cl_2 EIN. Even as the reaction rates for the processes are quite similar.

3.3.4 Reaction sets

As well as the set of cross sections used to model chlorine-containing plasmas, there are also a set of heavy-heavy particle reactions. In Globalkin, the arrhenius coefficients of reactions such as volume recombination of atomic chlorine;

$$\mathrm{Cl} + \mathrm{Cl} + \mathrm{M} \rightarrow \mathrm{Cl_2} + \mathrm{M}, \tag{3.9}$$

where M = Ar, Ar*, Ar**, Cl_2 ($v = 0, 1, 2, 3$), Cl, Cl*, are used. The heavy ions

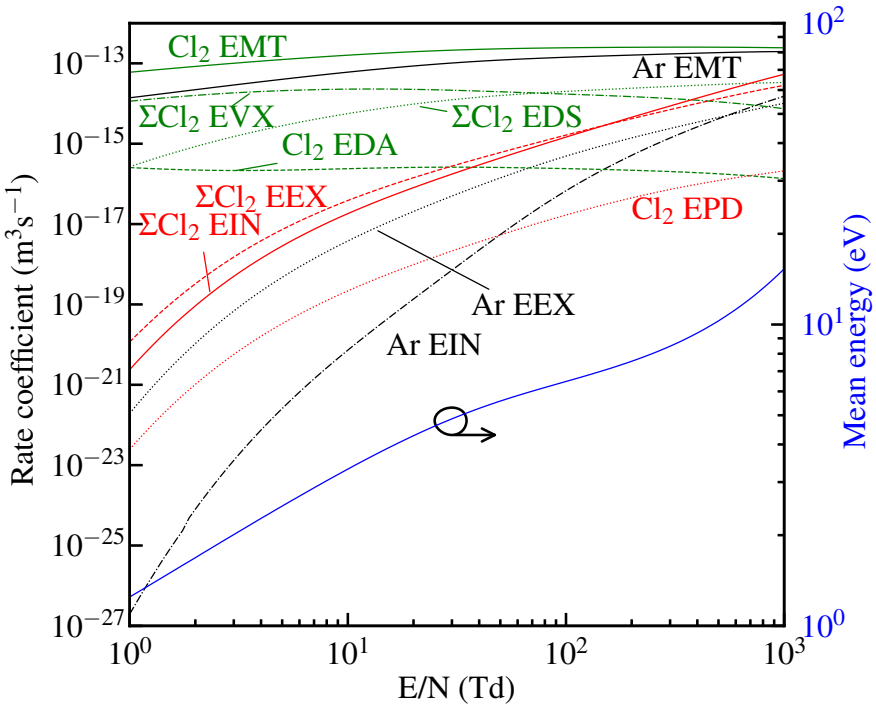

Figure 3.15: Electron impact rate coefficients calculated using BOLSIG+ for a 1:99 Cl_2/argon mixture using the same cross sections as used in the global model.

are assumed to have a maxwellian distribution, with the gas temperature calculated using equation 3.5. The rate coefficient k is calculated using

$$k = A(T/T_{ref})^n e^{-E_a/(k_B T)} \tag{3.10}$$

where A is a specific reaction-dependent pre-exponential factor, T is the absolute temperature (in Kelvin), T_{ref} usually is 298 K and $n = 0$ in the original arrhenius equation. This rate coefficient is then used in

$$-\frac{1}{2}\frac{\mathrm{d[Cl]}}{\mathrm{d}t} = \frac{\mathrm{d[Cl_2]}}{\mathrm{d}t} = k[\mathrm{Cl}]^2[\mathrm{M}] = \mathrm{R(cm^{-3}/s)} \tag{3.11}$$

To create a consistent set of reactions, the reaction sets of Tinck et al., Subramonium et al., Bassett et al. and Thorsteinsson et al. have been used as a basis [151, 153, 207, 208].

While all four papers consider chlorine/argon plasmas, they use a mixture of estimated and experimentally derived reaction coefficients. The rate coefficient for volume recombination used in this work is the one used by Subramonium et al. and Tinck et al. (1.28×10^{32} cm^6/s for atomic species and 5.4×10^{32} cm^6/s for molecular species). Another commonly quoted coefficient is by Ikezoe et al. [209].

Other important heavy-heavy reactions include ion-ion recombination, i.e.

$$A^+ + B^- \rightarrow A + B \tag{3.12}$$

where A = Cl_2, Ar, Cl and B is Cl. This reaction has been measured for Cl_2^+ by Church and Smith [210] (5.0×10^{-8} cm^3/s). The same reaction rate is assumed for the other possible positive ions. Charge exchange between a positive ion and neutral is also possible;

$$A^+ + B \rightarrow A + B^+ \tag{3.13}$$

For the possible combination of A and B, the following table shows the reaction rate.

Table 3.4: Charge exchange reaction rate coefficients (in cm^{3}s^{-1}). [a] Including Cl_2 $v = 0, 1, 2, 3$. [b] Atomic Cl's ionisation energy is greater than Cl_2. [c] Argon's IP is greater than Cl_2, Cl. [d] The produced ions are 75% (Cl^+ + Cl) and 25% Cl_2^+.

A↓ \B→	Cl_2 [a]	Cl	Ar
Cl_2	0.80×10^{-9} [208]	[b]	[c]
Cl	5.40×10^{-10} [208, 211]	1.00×10^{-9} [208]	[c]
Ar	7.6×10^{-10} [212][d]	2.00×10^{-10} [208]	5.66×10^{-10} [207, 208]

Quenching of Cl_2, Cl and argon excited states by the other species is also important to consider. The following equation shows the possible Penning ionization of species B,

$$A^* + B \rightarrow A + B^+ + e^- \tag{3.14}$$

This is especially relevant when considering metastable argon atoms colliding with ground state chlorine molecules. The quenching of metastable argon by atomic and molecular chlo-

rine has been measured by Gundel et al. [213]. The quenching of excited atomic and molecular chlorine by ground state argon, molecular chlorine and atomic chlorine by Fletcher and Husain [214, 215]. The rate coefficient for the quenching of Cl_2 vibrational levels by Cl and ground state Cl_2 is calculated using the method from Nina [216].

One of the first broadly used complete cross section sets was developed by Rogoff et al. [164]. In a joint experimental/theoretical paper, their global model was used to predict the time averaged power input per unit discharge length at the centre of a 1-1.5 torr, capacitively coupled, 13.56 MHz driven, pure Cl_2 discharge. This was done with a variation in pressure and input current, with measurements of the Cl_2 density using nine-pass absorption of 357 nm light. The ratio of Cl_2 to Cl measured in the discharge was used as input for calculating the rate coefficients of the electron impact collisions using a Boltzmann equation solver code written by Morgan [217, 218]. A complete Cl_2 cross section was proposed, using a mixture of directly measured experimental data and data from similar molecules (for example, electron impact ionisation and dissociative attachment data were taken from Kurepa and Belić [193] and vibrational excitation from F_2 [219]). Iteratively, swarm parameters calculated using the Boltzmann equation solver were compared with the experimentally measured swarm parameters from Bailey and Healey [220] and Božin and Goodyear [180]. While the threshold of each process was held fixed, the shape and magnitude of the cross sections were allowed to vary, focusing on the best agreement with the net ionisation coefficient. A more recent version by Tuan and Jeon [172] uses the swarm parameter data of Božin and Goodyear [180] to iterate and improve their suggested cross section. This process is shown in fig. 3.16.

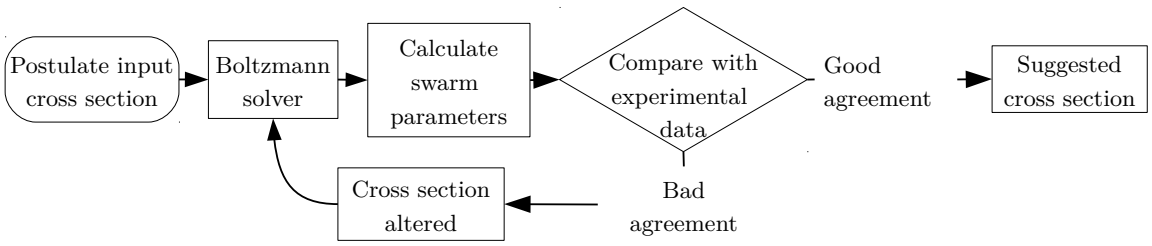

Figure 3.16: Flowchart from Rogoff [164].

Similarly, a complete cross section was suggested by Gregório and Pitchford [173] used

the same swarm parameters measured by Bailey and Healey [220] as well as those of Božin and Goodyear [180] to verify their suggested cross section. However, unlike Tuan and Jeon, they follow the method by Christophorou [171] to calculate the vibrational cross section. For this, the sum of the cross section for non-vibrational processes is subtracted from the total cross section. The remaining cross section is taken to be the cross section for electron impact vibrational excitation. For the cross sections that have measured experimental data, i.e. ionisation [41] and dissociative electron attachment [193] this data is used and not altered. To achieve a better agreement with the swarm parameter data, the cross section of EDS and EEX (measured by Cosby [198] and theoretical calculation by Rescigno [162]) is multiplied by 1.3. The reason for doing this instead of decreasing the ionisation cross section is because it also gives better agreement with the total measured electron scattering data of Gulley et al. [177].

Following on from this, using a more recent set of measured swarm parameters of Cl_2/N_2 mixtures by González-Magaña et al. [200], a new cross section has been suggested by Kawaguchi et al. [174]. The suggested cross section set by Kawaguchi et al. has many advantages - it incorporates the more recent calculations of electron impact electronic excitation to dissociation of Hamilton et al. [175] and the more recent set of swarm parameters [200] and stays within the experimental error of the other experimentally measured cross sections, similarly to Gregório et al. (see Table 3.5).

A global model developed by Bassett and Economou was used to predict important species densities and the self-sustaining electric field for a pure argon and a 95% argon/ 5% chlorine plasma in the range of 0.3 to 1 Torr [151]. The Cl_2 cross section from Rogoff et al. was chosen [164]. As was shown in the paper, the addition of even a few % of Cl_2 was enough to cause substantial changes to the resulting EEDF and rate coefficients for processes with high threshold energies (i.e. ionisation of ground state argon or excitation of ground state argon to the metastable state). They also show the impact of the additive gas to the destruction and production mechanisms of metastable argon. Before the addition of Cl_2 they predict the main production mechanisms of metastable argon to be from ground state excitation (53.5%) and quenching from higher states (36.9%) with the destruction

mechanism dominated by quenching to higher excited states (82.5%). After addition of Cl_2, the main production mechanism almost entirely comes from ground state excitation (99.8%) and destruction from quenching with chlorine (99.6%).

Another global model developed by Lee and Lieberman [221] compared Ar, O_2, Cl_2 and Ar/O_2 plasmas. For the Cl_2 case, they use the experimentally measured ionisation, dissociative attachment and dissociative ionisation cross section from Kurepa [193] and the calculated neutral dissociation cross section from Rescigno [162]. They show the effect the wall recombination coefficient γ_{Cl} has on the electronegativity (n_-/n_e) and degree of dissociation of Cl_2 for varying pressures. As γ_{Cl} was increased, the destruction rate of Cl increases and the production rate of Cl_2 increases. These two effects decreases the degree of dissociation. The increase in production of Cl_2 also has an effect on the electronegativity. As the rate of dissociative attachment will increase due to the higher production of Cl_2 and the destruction rate of Cl^- is unaffected by any change in γ_{Cl}, the electronegativity (n_-/n_e) increases with γ_{Cl}.

In the work by Corr et al. [21], the results of a 2D fluid model is compared to probe-based laser photodetachment (measuring the negative ion density, n_-), Langmuir probe (electron energy probability function, n_e, T_e. The positive ion density n_+ was calculated assuming quasineutrality, $n_+ = n_e + n_-$ with n_- measured using laser photodetachment) and laser induced fluoresence (n_{Cl}) measurements. In the paper they use the same reaction set as Lee and Lieberman [221], and mention how a lack of relevant coefficients and cross sections in the model may have resulted in an overestimation of the species densities and an underestimation in the energy loss of the electrons. Even with this discrepancy, there was good qualitative and quantitative agreement of the electronegativity (n_-/n_e) with varying power, pressure and Cl_2 concentration. For the agreement between the predicted and measured electron density, there was good qualitative agreement in the power, pressure and Cl_2 concentration trends. The predicted electron density was consistently overestimated.

Similarly to this, in work done by Despiau-Pujo et al. [29, 222] a 0D global model is used to model instabilities, neutral species densities, electron temperature and ion flux for an industry-relevant, 13.56 MHz, 1–20 kHz pulsed 5-20 mTorr pure chlorine ICP. In [29] a

previous model by Lieberman et al. [31] was used as a starting point, while the description of the inductive resistance of the plasma is updated to include separate magnetic and azimuthal electric field components. A Cl_2 chemistry set, based on that of Ashida et al. and Corr et al. [21, 22] was then also implemented and the time evolution of species densities and electron temperature of the turbulence is presented. In [222], the same model is used as a starting point and developed using the work by Thorsteinsson and Gudmundsson [153, 223] and used to model a 1–20 kHz pulsed, 5–20 mTorr pure Cl_2 and pure argon plasma. Experimentally, line-integrated absolute Cl_2 densities were measured using broadband UV absorption spectroscopy effectively 5 cm from the powered coils. Modulated beam mass spectroscopy (MBMS) was used to measure the relative argon and atomic chlorine density 13 cm below the powered coils. A capacitively coupled ion flux probe, at the same height as the MBMS orifice was also used. In the work, the additional plasma chemistry introduced by chlorine is shown by the value and rise/decay time of the ion flux with varying duty cycle. Compared to the pure argon case, where the duty cycle had very little impact on the ion flux, as the electron density decreases faster than the negative ion density, an ion-ion plasma forms approx 75 μs in the off-period. The duty cycle also effectively controls the Cl/Cl_2 ratio, as the timescale of Cl kinetics is longer than for the charged species.

In a series of papers by Thorsteinsson and Gudmundsson et al., a zero-dimensional global model is used to investigate a 1-100 mTorr pure Cl_2 and mixed argon/Cl_2 plasma under pulsed and continuous power [40, 153, 223, 224]. In [224], a detailed discussion of their choice of cross sections and rate coefficients is given, along with formulation and analysis of their chosen recombination coefficient, γ_{rec}. For their choice of γ_{rec}, they make a least squares fit from data by Guha [225] and Stafford [226]. They also use experimental data from [227] to calculate an input neutral gas temperature depending upon the pressure and input power. The experimental work of Corr [21] is compared with results from the model; similar to [21], there is some discrepancy in the low power regime (P_{abs} <100 W) of the electron density and electronegativity. However compared with the data from Donnelly and Malyshev, [17,228] the agreement between the model results and experimental data of n_{Cl} and n_e was very good. The atomic chlorine, electron density and electron temperature was also compared with

experimental data [17, 21, 229] with variation in pressure between 1–100 mTorr. It was seen that the electronegativity increased with pressure while the degree of dissociation decreased. The reason for this is similar to that seen by Lee and Liebermann [221]; as the pressure increases, the relative rate of Cl wall recombination to pump out increases, decreasing the degree of dissociation as wall recombination almost becomes a 'new' source of Cl_2. For the same reason the electronegativity increases, as the rate of dissociative attachment stays relatively constant, however the density of Cl_2 increases.

In the study of the Cl_2/Ar continuous power plasma by Thorsteinsson and Gudmundsson [153], they use a slightly more rigorous reaction set than in their previous work [224]. In [153] there was somewhat good qualitative agreement of the electronegativity trends from Corr [21] and degree of dissociation by Fuller [20] for varying argon/chlorine content. They found that the electron temperature generally increases with argon content and decreases with pressure, and that the degree of dissociation of Cl_2 increased with chlorine content and somewhat decreased with pressure. As seen previously [224], the electronegativity increased with pressure, however decreased slightly with argon content up to ∼80% argon, where the electronegativity drops much faster. They also studied the destruction mechanism of atomic chlorine with changing the surface/volume ratio of the discharge. They found that generally for large chambers, the primary loss of atomic chlorine was through ionisation whereas for smaller chambers the primary destruction mechanism was through pumping losses. For moderately-sized chambers, (radius, length ∼10 cm, S/V=0.6 cm^{-1}) wall recombination becomes the primary destruction mechanism.

In more recent work, Kemanenci et al. [152] used a global model to investigate the impact the wall recombination coefficient and external wall heating has on continuous and pulsed inductively coupled Cl_2 plasma. They use the same expression for the wall recombination coefficient as Thonsteinsson and Gudmundsson [224]. Similar to the work by Lee and Lieberman [221], they predict increasing electronegativity with wall recombination coefficient and pressure.

	Rogoff et al. [164]	Christophorou et al. [171]	Thorsteinsson et al. [224]	Gregorio et al. [173]	Kawaguchi et al. [174]
EMT	[a]	[162, 177]	[162,171,206,230]	[162, 177]	[162, 206]
EVX	[a]	[b]	[231]	[b]	[192]
EDA	[193]	[193]×1.3	[193]×1.3, [192]	[192, 193]	[192, 193][c]
EPD	[d]	[193]×1.3	[232]	[193]	[193]
EIN	[193]	[193, 203][e]	[41]	[41]	[41]×0.85
EEX	[a]	[f]	[g]	[162] ×1.3	[162]×4
EDS	[a]	[198]	[198]	[162,198] ×1.3	[175]×2.5

Table 3.5: Table showing the origin of the cross section for each of the processes for each published complete cross section. [a] estimated. [b] Calculated through subtraction of the total cross section by the other processes. [c] Below 0.2 eV the theoretical calculation of Ruf et al. [192] multiplied by 1.05 is used, above 0.2 eV the measurements of Kurepa et al. [193] is used. [d] Ion-ion production is put with EDA. [e] Mean of Kurepa [193] and Stevie [203] measurements. [f] Discussed but no cross section suggested. [g] Rydberg states are neglected in [224].

3.4 Wall reactions

The recombination coefficient, γ (also known as wall sticking coefficient or disappearance fraction) is an important model input parameter. As mentioned in section 3.3.4, several studies have attempted to measure this value for various experimental conditions and materials [17, 21, 233]. Figure 3.17 shows the change in electronegativity and atomic chlorine density in the plasma with varying γ_{Cl}.

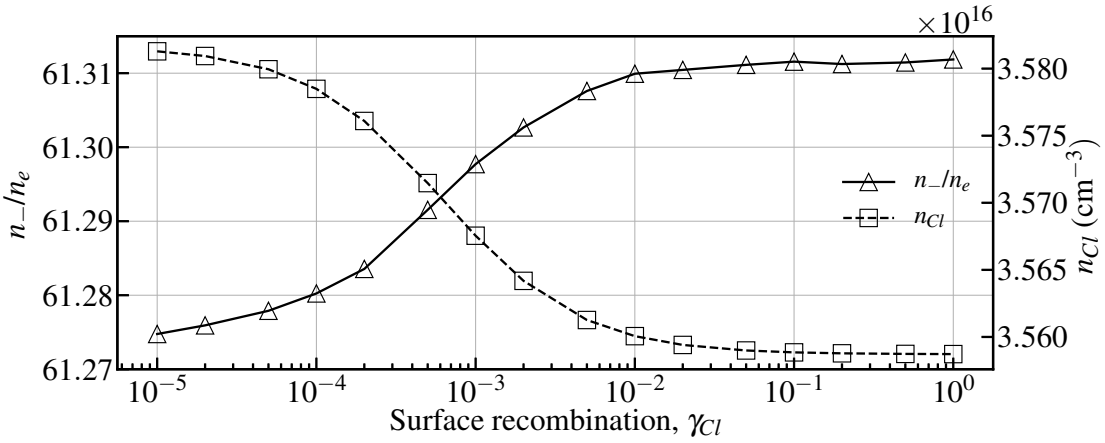

Figure 3.17: Electronegativity and atomic chlorine density in the plasma (7.5 cm along the plasma channel) under variation of γ_{Cl}. This is for a 1% Cl_2/Ar, 500 sccm 40 W power discharge. At atmospheric pressure, the main destruction mechanism of Cl is volume recombination, thus any variation in γ_{Cl} will make little change to n_{Cl_2}, and thus little change to the electronegativity.

3.5 Variation of input power

To the author's knowledge there are no other experiments that use molecular chlorine in an atmospheric pressure plasma, thus there is no other experimental data to benchmark the following simulation results. In the model used in this work, plug flow is assumed and the simulations are extruded in space, assuming the system is already in steady-state. Following on from this, figure 3.2 shows the modelled domain. The typical operating conditions are similar to the experiment, i.e. 5 cm long electrodes, 500 sccm total flow rate, 0.1–1.5% Cl_2 admixture (see chapter 2). The power is chosen to come on part-way through the simulation to ensure that erroneous or otherwise missing reactions are caught. It also gives clarity on whether features are numerical artefacts or true predictions. Typical input power deposition profiles are shown in figure 3.18.

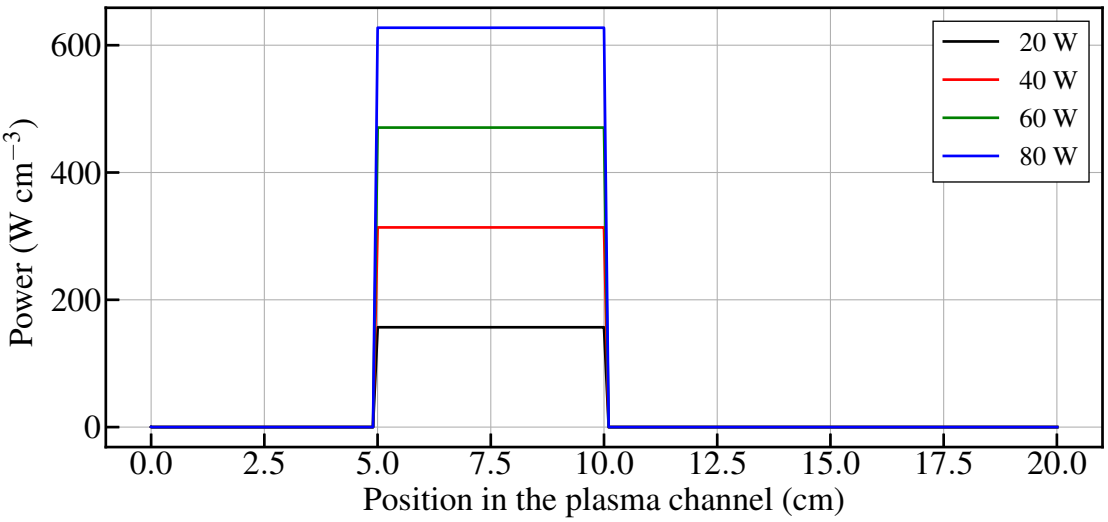

Figure 3.18: Power density deposition profile used in the global model. The volume of the plasma is (0.05×0.5×5) 0.125 cm^3.

The density of the chlorine and argon species included in the model, at different points in the plasma channel for the base case operating conditions is shown in figures 3.19 and 3.20.

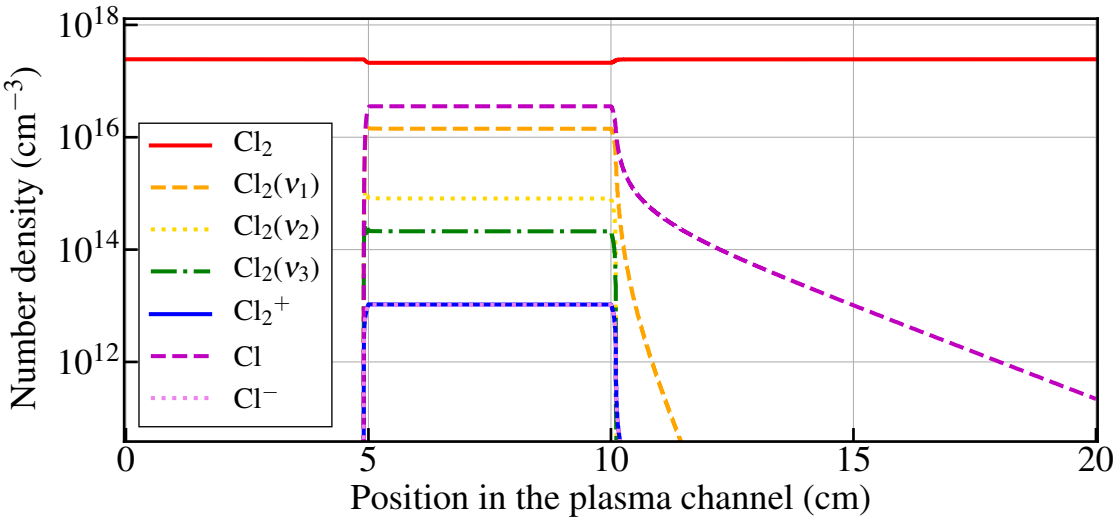

Figure 3.19: Number density of some chlorine species through the plasma channel. Operating conditions are: 40 W, 500 sccm total, 1 % Cl_2 in argon.

As is shown in figure 3.19, the densities of the plasma-generated species, i.e. $Cl_2(v_1)$, $Cl_2(v_2)$ etc have negligible densities ($<10^{11}$cm^{-3}) before reaching the plasma region. In the plasma region, the density of neutral ground state molecular chlorine decreases as the production of other species occurs. The density of molecular chlorine seems to be the highest, with the atomic Cl and the different vibrational states of Cl_2 following. The reason for this is the main production of Cl can be through dissociative electron attachment and through direct electron impact excitation into one of the low-lying anti-bonding states. Whereas the route for generating $Cl_2(v_n)$ is through direct electron impact, or V-V/V-T reactions that are generally slower than electron impact. The density of Cl^- and Cl_2^+ are almost the same through the plasma region. To maintain quasineutrality, the density of Cl_2^+ is slightly higher than Cl^-. At the end of the plasma region, the vibrationally excited and ionised species decay very fast through volume recombination, the density of Cl decays much slower.

In figure 3.20, the densities of some electronically excited and other charged species is shown. As all of these species are almost entirely electron-moderated, they only appear at substantial densities during the plasma. They appear at much lower densities than vibrationally excited Cl_2 and atomic Cl as the threshold energies for electronically excited Cl_2, Cl and Ar are much higher, i.e. ~ 10 eV. This logic is the same for the ionised species Cl^+ and Ar^+.

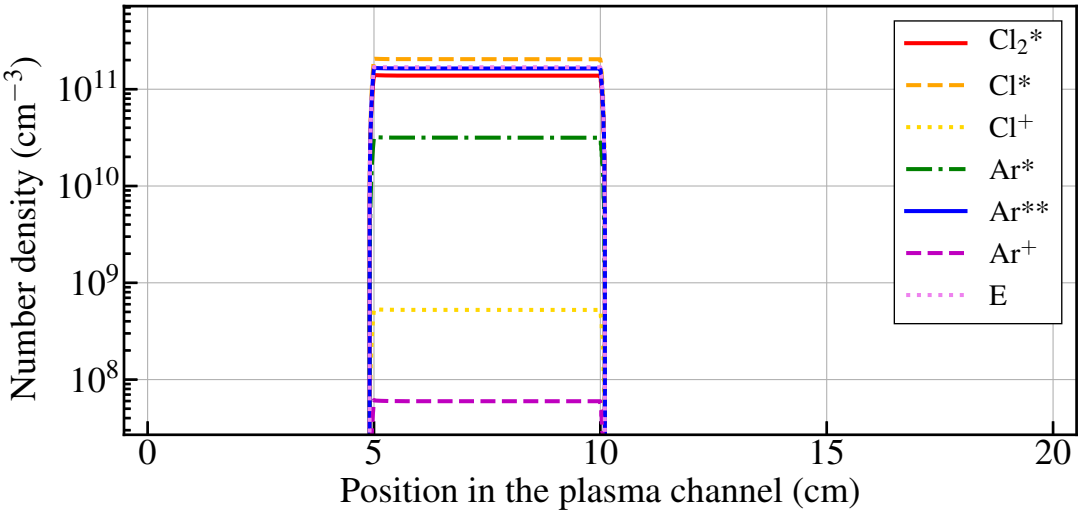

Figure 3.20: Number density of several species through the plasma channel. Operating conditions are same as in figure 3.19

Through increasing the time-averaged power deposited into the plasma (**J**·**E**), the electron density increases (see eq. (3.4)). Thus increasing the reaction rate of all electron-mediated processes. As shown in figures 3.21 and 3.22, the plasma density and the degree of dissociation increases through increasing the plasma power.

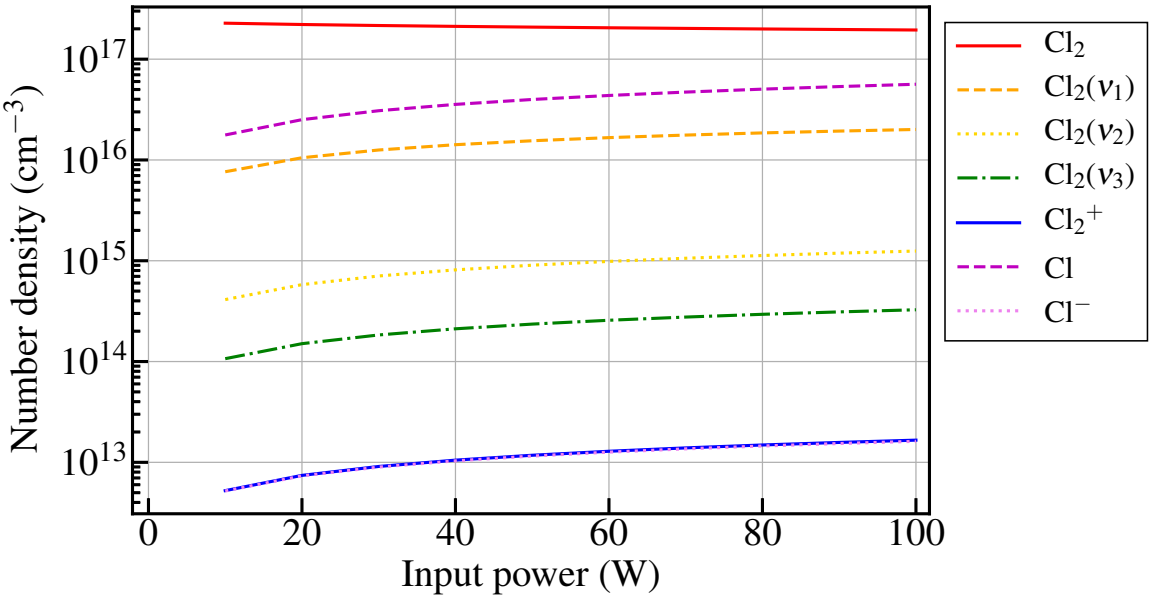

Figure 3.21: Number density of some chlorine species at 7.5 cm in the plasma channel versus input power. Other operating conditions are same as in figure 3.19

Another impact the power has is on the electronegativity. As the electron density increases, the electronegativity will decrease. The rate of dissociation to neutral chlorine atoms and rate of dissociative attachment will increase at a similar rate (see fig. 3.23), thus the dissociation degree will increase. The rate of dissociation and dissociative attachment will both increase because the electron temperature stays relatively constant, whereas the electron density increases.

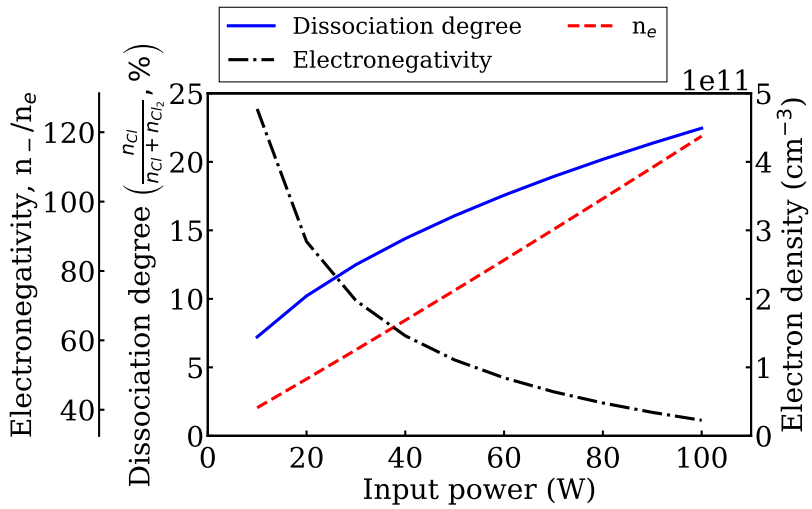

Figure 3.22: Dissociation degree, electron density and electronegativity versus input power at 7.5 cm in the plasma channel.

3.5.1 Pathway analysis I - Power variation

The destruction and production rates of Cl_2 is shown in figure 3.23. As is shown in fig. 3.15 the greatest electron-impact reaction rate for a 1% Cl_2 in Ar case around 15–20 Td that destroys ground state Cl_2 is vibrational excitation, then neutral-neutral dissociation. This is mirrored here as the rate of vibrational excitation to $Cl_2(v = 1, 2, 3)$ is greatest, followed by dissociation into neutral products.

The increase in both production and destruction rates is dependant upon the electron density. The electron temperature does not change as much over the variation in input power. The main production of ground state Cl_2 is from quenching of $Cl_2(v = 1)$ by argon and chlorine atoms and ground state Cl_2. Volume recombination of Cl atoms is the next highest contributor of ground state chlorine molecules with wall recombination of Cl atoms nearly two orders of magnitude lower.

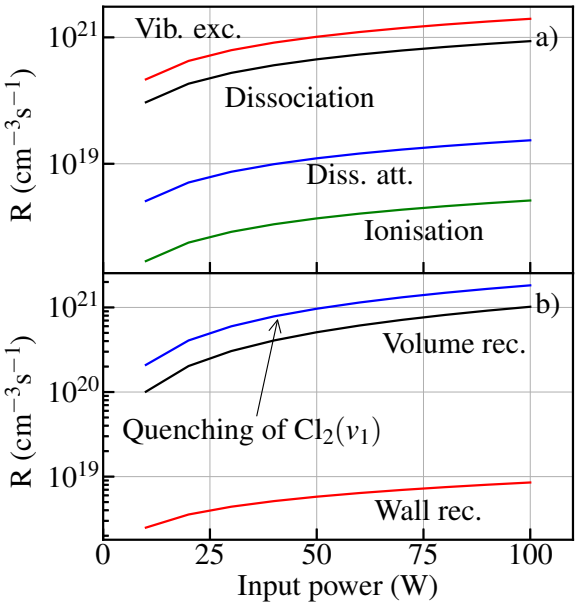

Figure 3.23: Absolute rates of a) destruction and b) production of Cl_2 ($v = 0$) with variation in plasma power. The other plasma parameters are 1% Cl_2 in Ar, 500 sccm total flow rate.

3.6 Variation of total flow rate

Through varying the total flow rate through the plasma source, the gas residence time changes. This becomes important when considering the main destruction mechanism of atomic chlorine - volume recombination. As is shown in figure 3.24, as the flow rate is increased, the decay of atomic chlorine leaving the plasma region decreases.

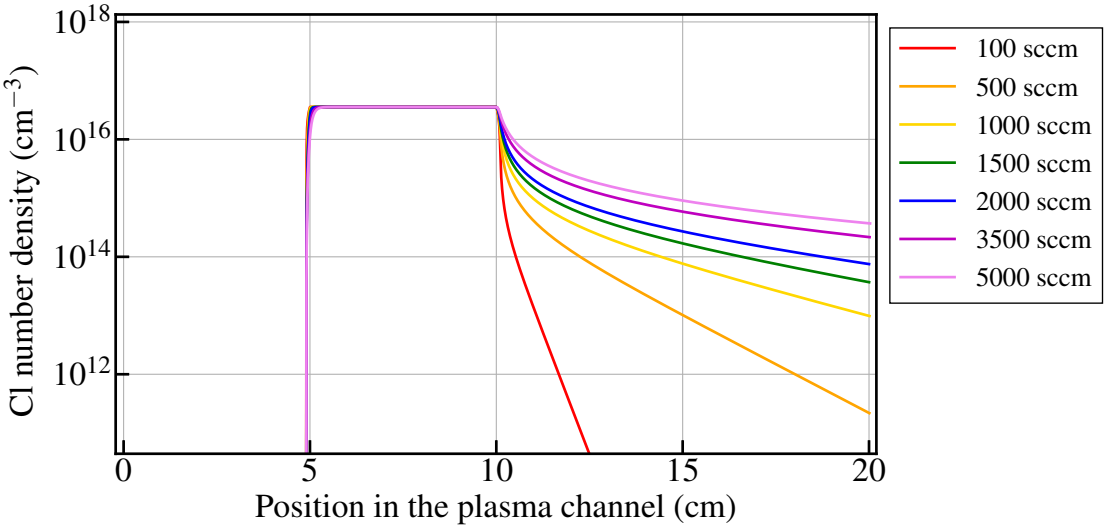

Figure 3.24: Atomic chlorine density through the plasma for varying flow rates. The operating conditions are: 40 W, 1% Cl_2 in argon.

From figure 3.24 the flow rate has little impact on the density of atomic chlorine in the plasma itself. As the production and destruction of Cl relies on the electron and argon density respectively, and as these are independent of the flow rate, the absolute density of atomic chlorine in the plasma stays relatively constant.

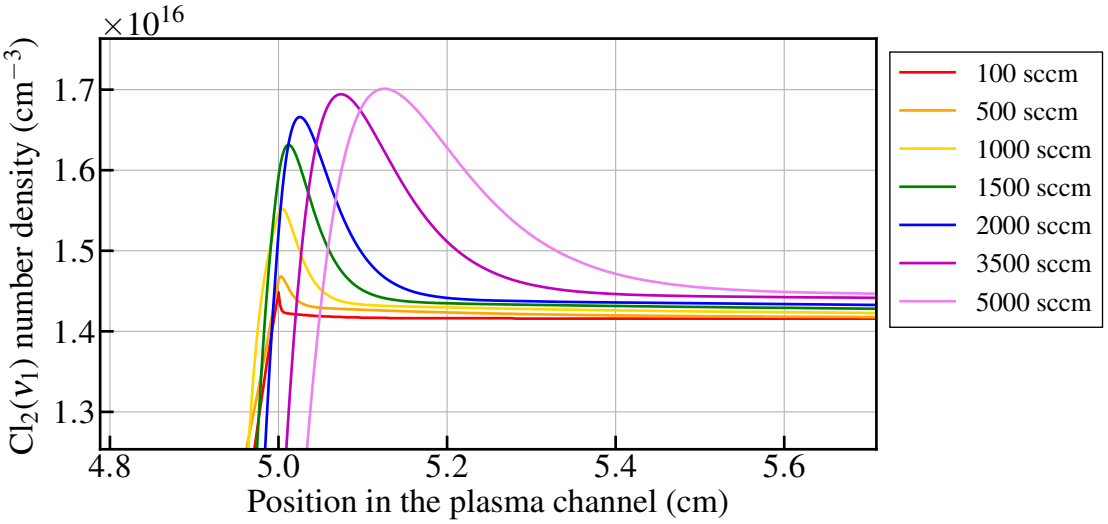

Figure 3.25: Vibrationally excited molecular chlorine density in the channel for varying flow rates. The operating conditions are the same as in figure 3.24.

Changing the residence time affects the evolution in space of the production of species in the plasma. As is shown in figures 3.25 and 3.26, the decay in time of $Cl_2(v_n)$ to Cl stays the same, however as the gas velocity is increased, this corresponds to a greater overshoot in $Cl_2(v_n)$, leading to slower build-up of atomic chlorine.

The decrease in the decay of Cl for increasing flow rate is seen in figure 3.27. In this figure, the atomic chlorine density 16 cm into the plasma channel is plotted, with the gas velocity and corresponding gas residence time in the plasma (5 cm $/V_{gas}$) versus flow rate. As the gas velocity increases, the residence time decreases and the atomic chlorine density increases.

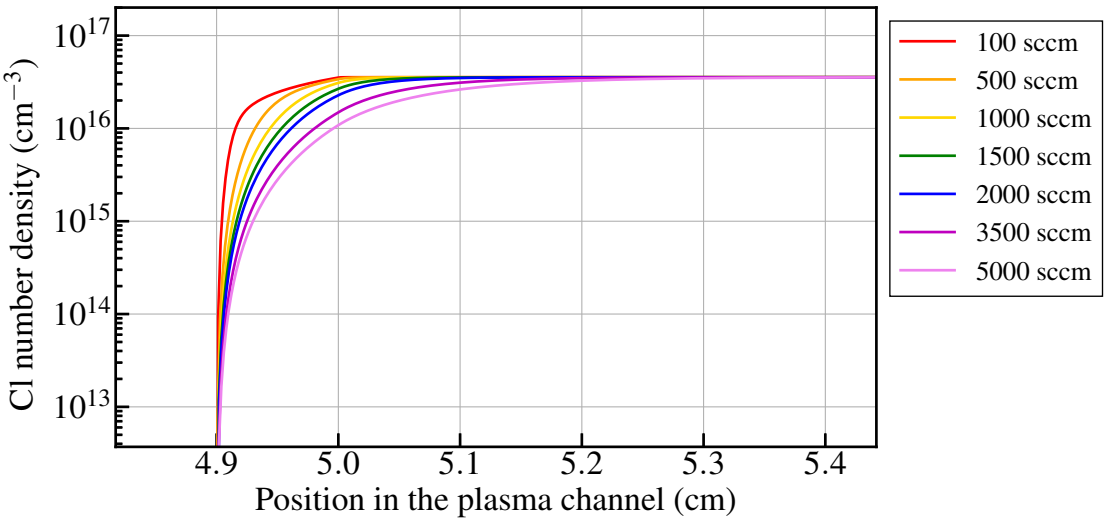

Figure 3.26: Atomic chlorine density in the channel for varying flow rates. The power deposition rise starts at 4.9 cm and reaches the maximum at 5 cm. The operating conditions are the same as in figure 3.24.

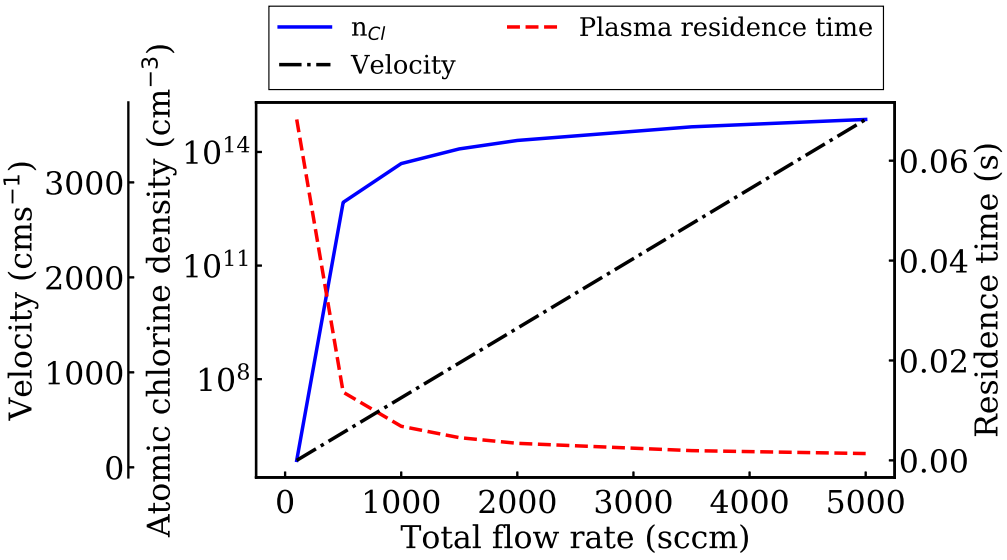

Figure 3.27: Gas velocity, atomic chlorine density at 16 cm in the plasma channel and residence time through the plasma versus flow rate

3.7 Variation of Cl_2 admixture

To investigate the impact of molecular chlorine admixture on the plasma chemistry and subsequent products in the effluent, the admixture is varied by 0.1–4.1%. This is roughly equivalent to the admixture range accessible in the experiment. Figure 3.28 shows the concentration of a few important chlorine species at 7.5 cm in the plasma channel. As can be seen in the figure, there is little change in the densities of the plasma-produced products with more than 1% Cl_2/argon.

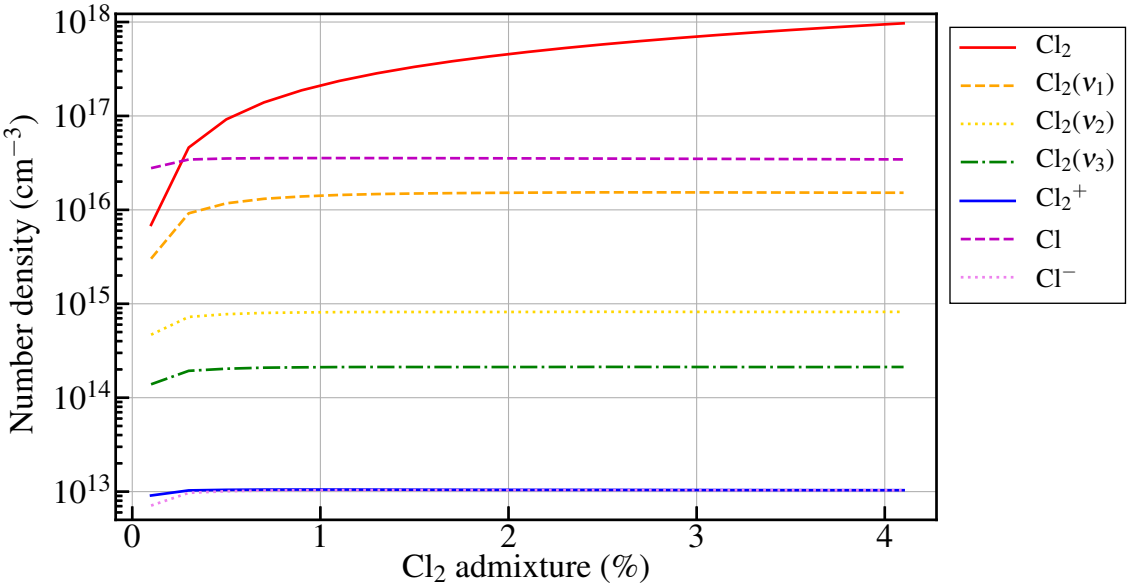

Figure 3.28: Number density of important chlorine species at 7.5 cm in the plasma channel versus input chlorine admixture. The other operating conditions are: 40 W, 500 sccm total flow rate.

The reason for the seemingly independent nature of the admixture on the species densities is due to several factors. One of these is the self-imposed limit on the electron density by the rate of dissociative attachment and ionisation. For the plasma to be self-sustaining, the rate of electron production (ionisation) must be at least equal to the rate of destruction (attachment). The effect of increasing the Cl_2 input increases the attachment rate, thus the electron and positive ion density decreases, while the electronegativity increases (see

figs. 3.29 and 3.30).

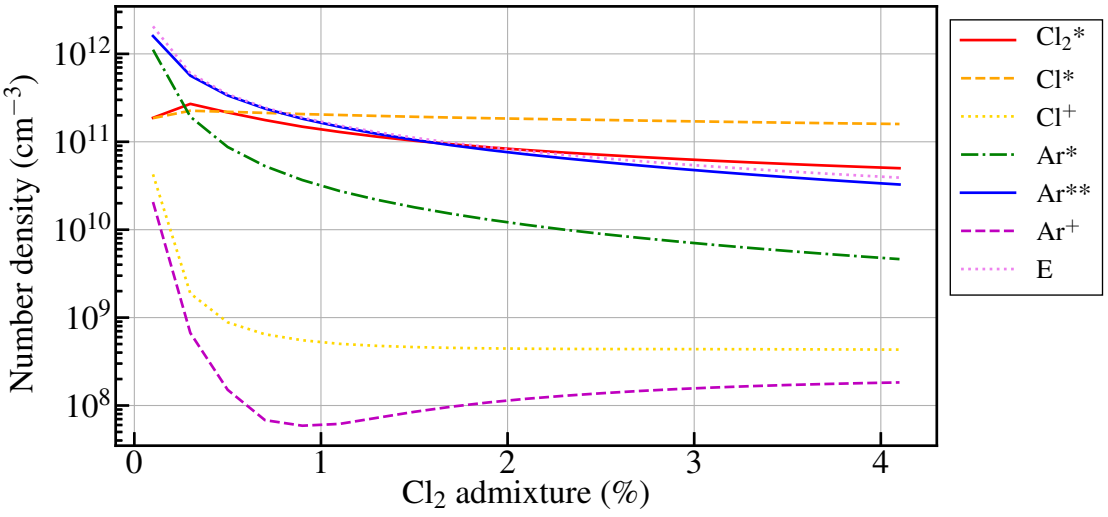

Figure 3.29: Species density at 7.5 cm in the plasma channel versus input chlorine admixture. The other operating conditions are the same as in figure 3.28.

Interesting in figure 3.29 is the minimum in Ar^+ at 0.9–1% Cl_2 admixture. The location of this minimum is the same as the maximum in Cl density (see figure 3.30). A possible reason for this could be that it is a point of minimum electron energy, thus the resulting rate argon ionisation rate coefficient would be minimised. From the figure above, the electron density monotonically decreases with increasing chlorine admixture, thus the density of Ar^+ is relatively independent of n_e.

As well as this, as is shown in figure 3.30, the electron temperature rapidly decreases between 0.1 to 1% input Cl_2. This has the effect of decreasing the rate of dissociation through excitation to an anti-bonding state, as well as electron impact excitation of argon and atomic chlorine.

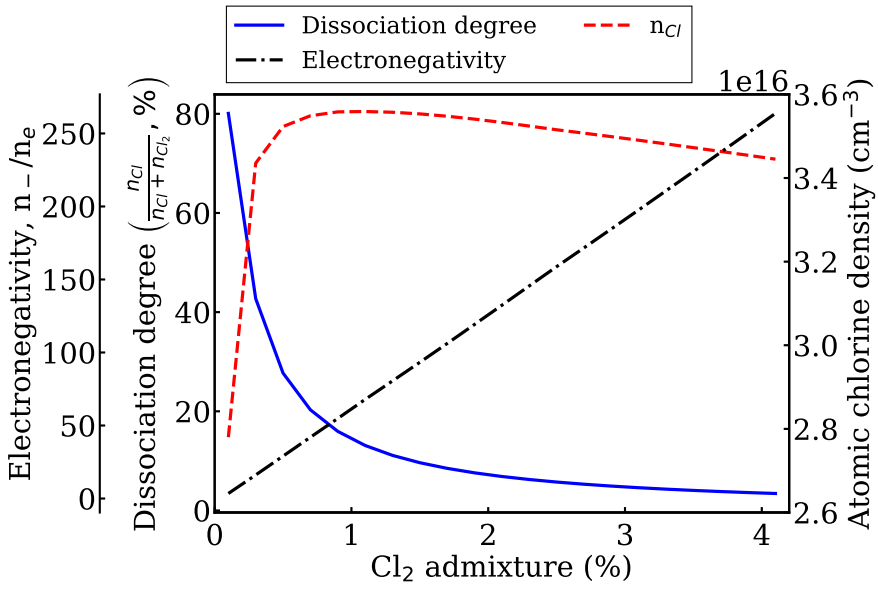

Figure 3.30: Electronegativity, dissociation degree and atomic chlorine density in the plasma for varying input chlorine admixture. The other operating conditions are the same as in figure 3.28.

3.7.1 Pathway analysis II - Admixture variation

As shown in the figure below, the production and destruction rates of ground state Cl_2 show some interesting features. As the total production rate of electrons is tied to the constant applied electric field ($\mathbf{J} \cdot \mathbf{E}$), as the chlorine content increases, the ionisation rate of Cl_2 increases. As was shown in the previous figure (fig. 3.30) the density of atomic chlorine reaches a maximum at ∼1% and then decreases slightly. This is also seen in the rates of dissociation to neutral products and dissociative attachment. With the increase of molecular chlorine the dissociation of chlorine moves from being dominated by neutral-neutral production to dissociative attachment. This is shown by the increase in electronegativity with chlorine admixture.

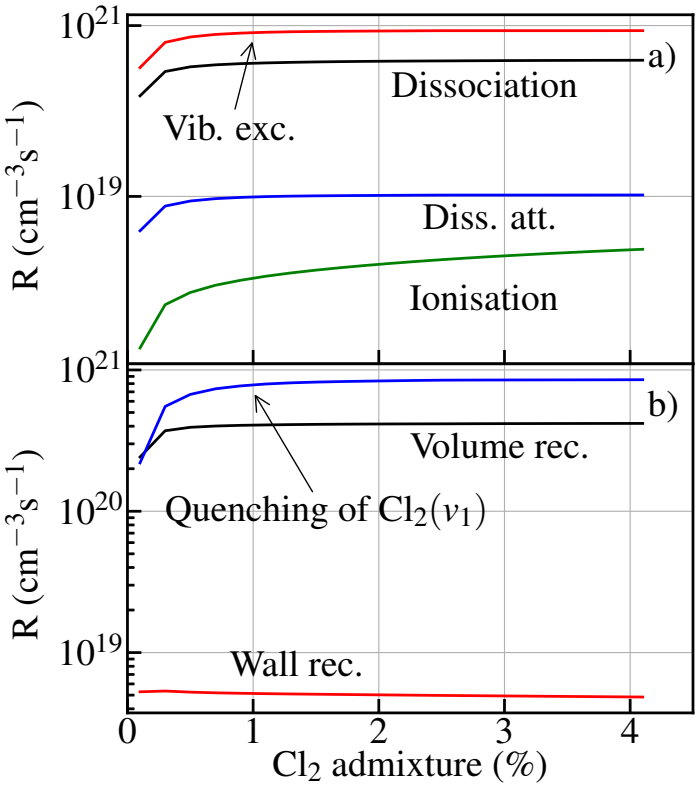

Figure 3.31: Absolute rates of a) destruction and b) production of Cl_2 ($v = 0$) with variation in input molecular chlorine admixture.

3.8 Summary

In summary, the zero dimensional model used to the simulate the argon/chlorine plasma introduced in the previous chapter is described. A review of cross section data for electron impact processes of ground state Cl_2 is also given with comparison between recently experimentally measured swarm parameters and swarm parameters calculated using BOLSIG+. The main electron driven processes are presented with reference to previous experimental work.

The densities of the various plasma-produced species are followed with variation in input power, flow rate and chlorine admixture. In general, the input power controls the electron density and thus the total plasma density. The flow rate influences the time evolution of the plasma species, however this model is a very idealised case and may not represent the actual gas flow in an experiment. Finally, the chlorine admixture controls the electronegativity and dissociation degree of Cl_2 in the plasma.

Chapter 4

Reference compound investigation and comparative reactivity method measurements

In this chapter, the reference compound was tested against a well-characterised VOC mix of known Cl-reactivity. Evidence from PTR-MS studies indicated that the plasma generated unwanted radical fragments. These were identified by optical emission spectroscopy to include N_2^* and highly reactive OH radicals. The concentration of OH was determined by quantitative detection of phenol following titration with benzene. Methods for reducing these chemical interferences in the effluent with regards to future reactivity measurements are discussed. Variation of chlorine admixture using the chosen reference compound is compared with results of the zero dimensional plasma model. A relative rate experiment using a mixture of benzene and diethyl-ether and Cl-reactivity measurements using mixtures of isoprene and toluene are also presented.

4.1 Choice of reference compound

For choosing the appropriate reference compound, the criteria defined by Sinha et al. [15] was used. In short, the reference should be: volatile (to be made into a gas standard), have a well established, competitive rate coefficient (in this case with Cl, comparable with other species in ambient air), be detectable (in this work, have good response on PTR-MS) and not be present at comparable concentrations in ambient air already.

A shortlist of four of the most likely candidates was made, these are included in the table below with the respective properties that make them a potential reference.

Table 4.1: Potential reference compound properties.
[a] reaction coefficient in $\times 10^{-10}$cm^3 molecule^{-1} s^{-1}.

Compound	Functional group	Molar mass (g mol^{-1})	k^a_{Cl}	$\frac{k_{Cl}}{k_{OH}}$	Vapour pressure (Torr at 20 ℃)	Ref.
1-propanol	alcohol	60.096	1.6	27.6	14.92	[101]
pentanal	aldehyde	86.134	2.3	9.3	26	[234, 235]
propanal	aldehyde	58.080	1.3	5.42	257.95	[101]
diethyl-ether	ether	74.123	2.5	18.9	439.98	[236, 237]

In the original OH-comparative reactivity method [15], Pyrrole, C_4H_5N was used as the reference compound. This has a well established reaction rate with OH and as the compound contains nitrogen, falls onto an odd mass after being protonated, making measurements and subsequent analysis simple with PTR-MS. In the case here, there are few measurements of Cl + amines and nitriles (NVOC), thus the reaction rate is not known. On the other hand, there are many more kinetic studies of oxygenated organics (OVOC) in reaction with Cl, thus many OVOC have well characterised Cl and OH kinetics. OVOCs are also readily available, respond well to PTR-MS and are (compared to NVOC) of low toxicity. Thus the decision was made to use an OVOC. Alkanes and alkenes are not possible options due to their proton affinity being too low to use PTR-MS.

The ideal reference compound should have a competitive reaction rate with Cl, but

not with other potential reactive products such as hydroxyl (OH), hydroperoxyl (HO_2) and organic peroxy radicals (RO_2, where R is any organic group). For example, after reaction with Cl, the reference compound RH will oxidise and produce RO_2 radicals:

$$Cl + RH \rightarrow R + HCl \tag{4.1}$$

$$R + O_2(+M) \rightarrow RO_2(+M) \tag{4.2}$$

Similarly, the reaction of OH with OVOC creates HO_2,

$$OH + RCH_2OH \rightarrow H_2O + RCHOH \tag{4.3}$$

$$RCHOH + O_2 \rightarrow HO_2 + RCHO \tag{4.4}$$

With the addition of water vapour in the sampled air mass it could be possible to create OH and HCl through surface reactions:

$$Cl_2 + 2H_2O + S \rightarrow 2HCl + 2OH + S \tag{4.5}$$

though this is quite speculative. Other established routes to OH formation from VOC degradation include:

$$HO_2 + NO \rightarrow OH + NO_2 \tag{4.6}$$

and

$$HO_2 + O_3 \rightarrow OH + 2O_2 \tag{4.7}$$

There exist several known routes from HO_2 to OH [50], but under the unusual composition of the reactor, surface moderated Cl_2 to OH conversion may be important. To compare the possible interference from OH, HO_2 and RO_2, the ratio of k_{Cl}/k_{OH} is included in the table. Ideally the compound with the largest ratio would experience the least amount of interference.

To investigate the impact molecular chlorine had on the PTR-MS measurements and decide on the reference compound, a gas standard containing the four potential compounds in N_2 was introduced into the reactor while flowing 0.21% molecular chlorine through the plasma source before, during and after igniting the plasma. The measured concentration of the 4 potential OVOC is shown in figure 4.1. The total reactivity of the mixture was 292 s^{-1}. Assuming only atomic chlorine was produced by the plasma, by the total depletion of the compounds with the plasma on, the concentration of atomic chlorine in the reactor was $(7.0\pm0.1)\times10^{11}$ cm^{-3}.

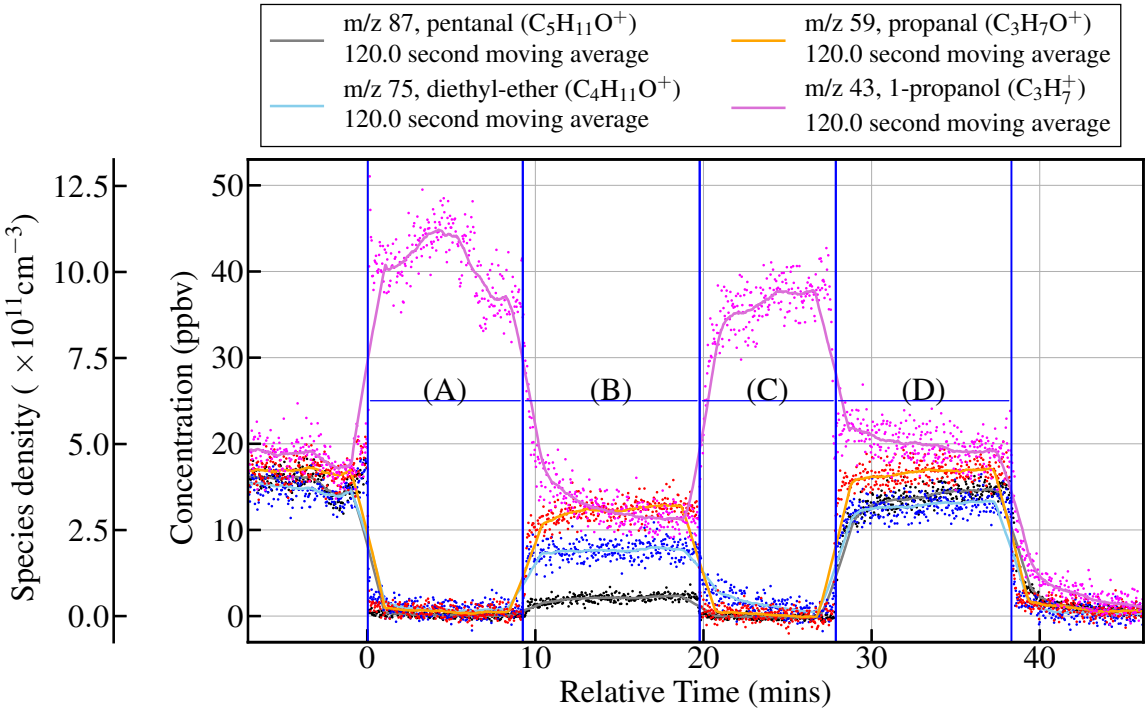

Figure 4.1: Interference on the PTR-MS measurements from relatively high molecular chlorine concentration. In the figure, regions (A) to (C) correspond to when 0.21% Cl_2 in argon was introduced to the reactor through the plasma source. Region (B) corresponds to the time when the plasma was on (40 W_f generator power). The flow of VOC into the reactor is constant up to $t = 39$ mins (the end of region (D)).

As explained in chapter 2, the power deposited in the plasma was not measured, thus

only the effective forward generator power is stated here.

As is shown in figure 4.1, the period of time while the plasma was off and chlorine was flowing correlate with unrealistic measurements from the PTR-MS. The measured concentration of diethyl-ether ($C_2H_5OC_2H_6^+$), pentanal ($C_5H_{11}O^+$) and propanal ($C_3H_7O^+$) seem to fall to zero whereas the concentration of 1-propanol ($C_3H_7^+$) increased. Reasons for this could be that the amount of Cl_2 entering the PTR-MS creates a large amount of other reactive species that then go on to oxidise the VOC inside the PTR-MS drift tube. The high concentration of Cl_2 could have also directly affected the detector causing spurious ion count rates. While the plasma is on the concentration of the 4 compounds seems to return to a more realistic level. It is difficult to determine exactly what has caused the increase in m/z 43 as the PTR-MS detects any positive ion of the same mass/charge ratio.

A different interesting feature was the loss of the four VOC while having the plasma ignited, but without any input Cl_2. As is shown in figure 4.2, once the plasma was on there was consistent depletion of all four compounds. This would suggest that the plasma produced other reactive species that would have caused the oxidation of the four VOC.

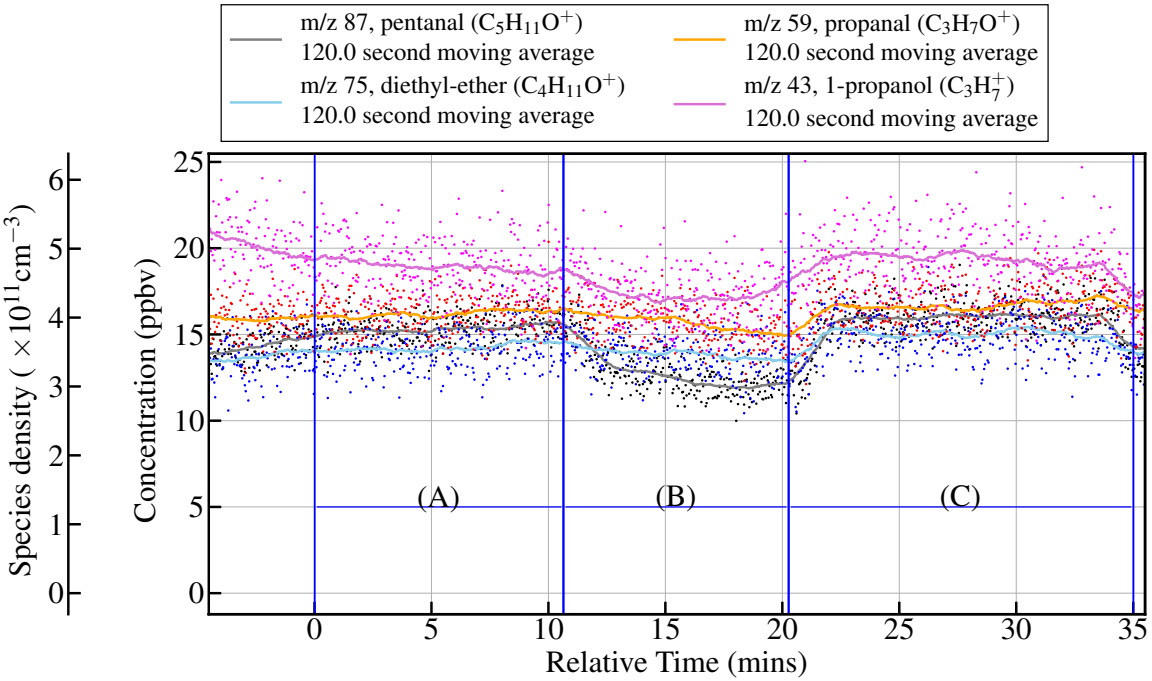

Figure 4.2: Evidence of interference from the plasma. In the figure, there is a constant flow of VOC mix into the reactor (waiting for the signal to stabilise before region A). The plasma is on (40 W_f, 1500 sccm argon, no Cl_2) during region (B). In total, the amount of lost VOC from the mixture correlates to 5.05 ppbv (1.26×10^{11} cm^{-3}).

In fig. 4.2, it seems that the propanal and diethyl-ether signal deplete on a much slower timescale than the pentanal and 1-propanol ones. In this experiment, the mixture of the four compounds was kept in a single canister. The compounds have a similar reaction rate with OH & have similar volatility. A possible reason for the difference in depletion is the majority of the propanal and diethyl-ether signals could be from water clusters, i.e. $H_3O^+ \cdot nH_2O$ (with different combinations of ^{16}O and ^{18}O) and not $C_3H_7O^+$ or $C_4H_{11}O^+$ from the PTR-

MS not being properly optimised. In fig. 4.1 and 4.2 the E/N used was 150 Td whereas for the later figures E/N = 161 Td. This would mean a possible underestimation of the lost VOC from the products of the plasma.

An attempt was made to use singularly-deuterated ethanol, C_2H_5OD for its odd mass when protonated. Unfortunately the PTR-MS could not resolve the masses between the deuterated and un-deuterated version. Because of the spurious increase in 1-propanol with and the next lowest ratio of k_{Cl}/k_{OH} diethyl ether was chosen as the reference compound.

4.2 Species identification using OES

To identify the additional reactive species in the plasma, optical emission spectroscopy was used (section 1.2.4). The ends of the fibre optics from the two different spectrometers were fixed facing the plasma (see fig. 4.3). To make simultaneous measurements, these were placed facing the same 'side' of the plasma, due to the proximity of the matchbox and clamp supporting the input plasma power cable. The UVA-UVB spectrometer was placed ∼2.5 cm along the plasma channel axis with the broadband spectrometer fixed another ∼1.6 cm along the channel.

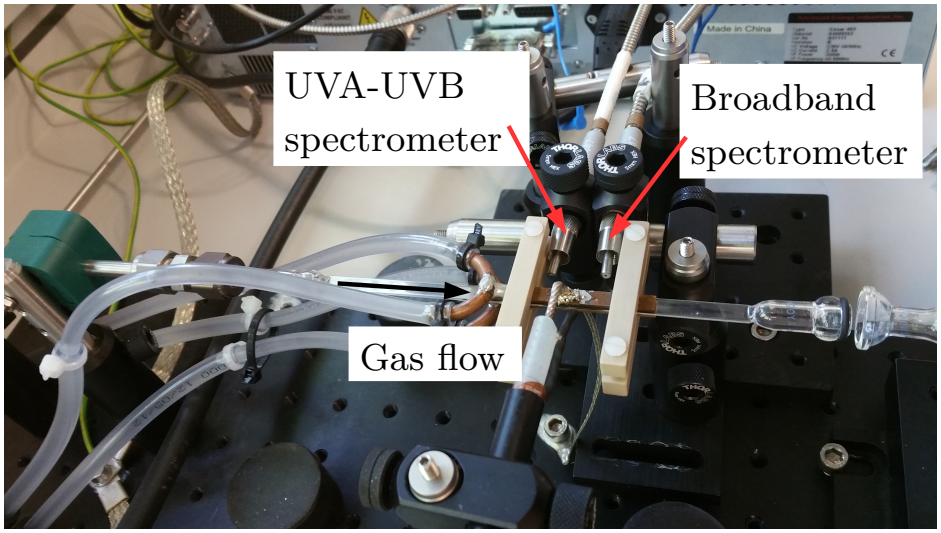

Figure 4.3: Photograph of the plasma source with the two USB spectrometers.

Due to the very shallow cone of emission (from the 0.5 mm ID height of the capillary) it was found that the plasma had to be ignited first to find the optimum height for the two fibre optics (as the two fibre optics were fixed at 90^{o} to the plasma channel axis). The fibre optics were placed close to the plasma to increase the signal to noise ratio and make it easier to find the optimal position. A similar experimental setup was used by Niemi et al. [238].

Emission from OH at 308 nm and N_2 molecular band at 336 nm and 357 nm was collected by a spectrometer covering the UVA and UVB bands (Ocean optics HR4C4859) with an optical range of 294.44 nm to 393.78 nm and 0.02 nm resolution. A broadband spectrometer (Ocean optics HR4C4667) with a 196.03–1119.76 nm optical range and resolution of ∼0.3 nm covered detail of the argon and oxygen lines. Examples of the emission collected is shown in figures 4.4, 4.6 and 4.12. For the OH and N_2 emission, a typical integration time of 0.9 s was used, with each measurement an average of 30 spectra, i.e. taking 27 s per point. For the broadband measurements, an integration time of 0.05 s, averaged over 30 spectra was typically used, giving 1.5 s.

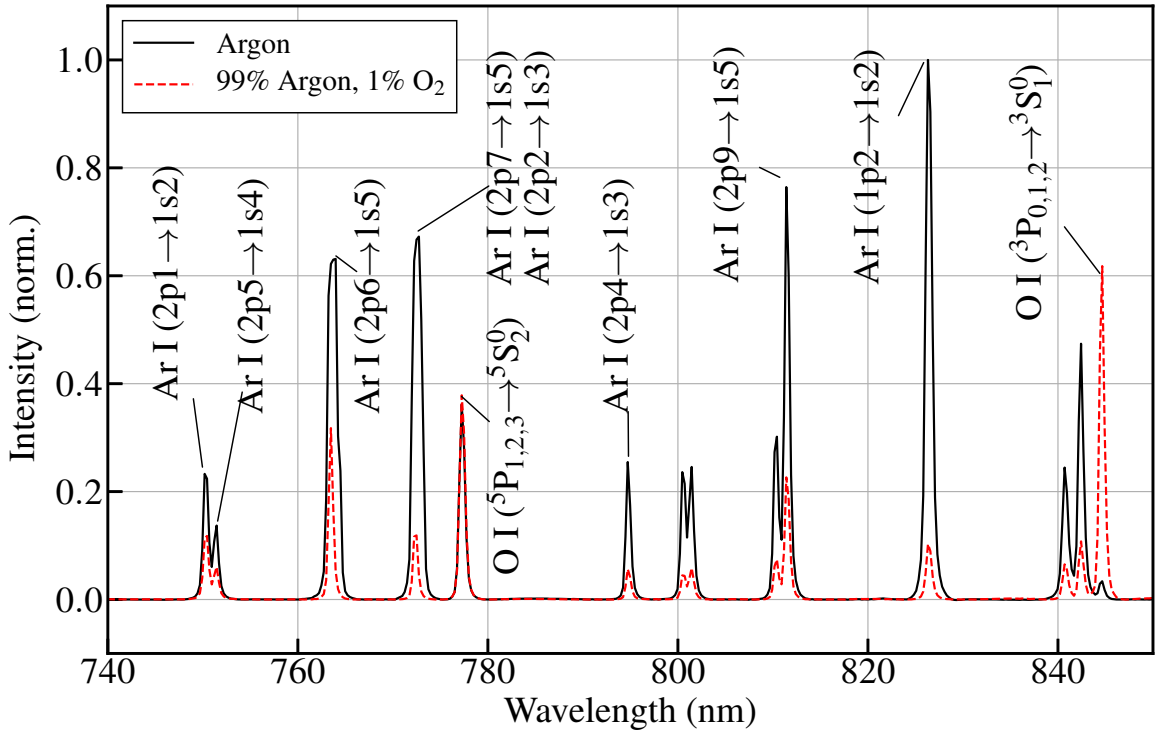

Figure 4.4: Close up of the measured argon and atomic oxygen emission. O-atom emission is clearly seen from the 844 nm and 777 nm triplet lines; due to impurities in the argon flow there is some O-atom emission present. Some of the high intensity argon lines are also labelled [238].

To measure the mean flushing time of the reactor and determine how long it takes to flush residual air in the reactor, the reactor was left open to ambient air overnight. The plasma source was then flushed with 400 sccm argon with no other gas flows into the reactor. The plasma was ignited soon after the argon flow was started to observe the emission from the air impurity in the argon plasma. The resulting measurement of NO^+ from the PTR-MS (another potential product from the residual ambient air) and absolute irradiance of the 308.92 nm OH line and 357.56 nm N_2 molecular band line is shown in figure 4.5.

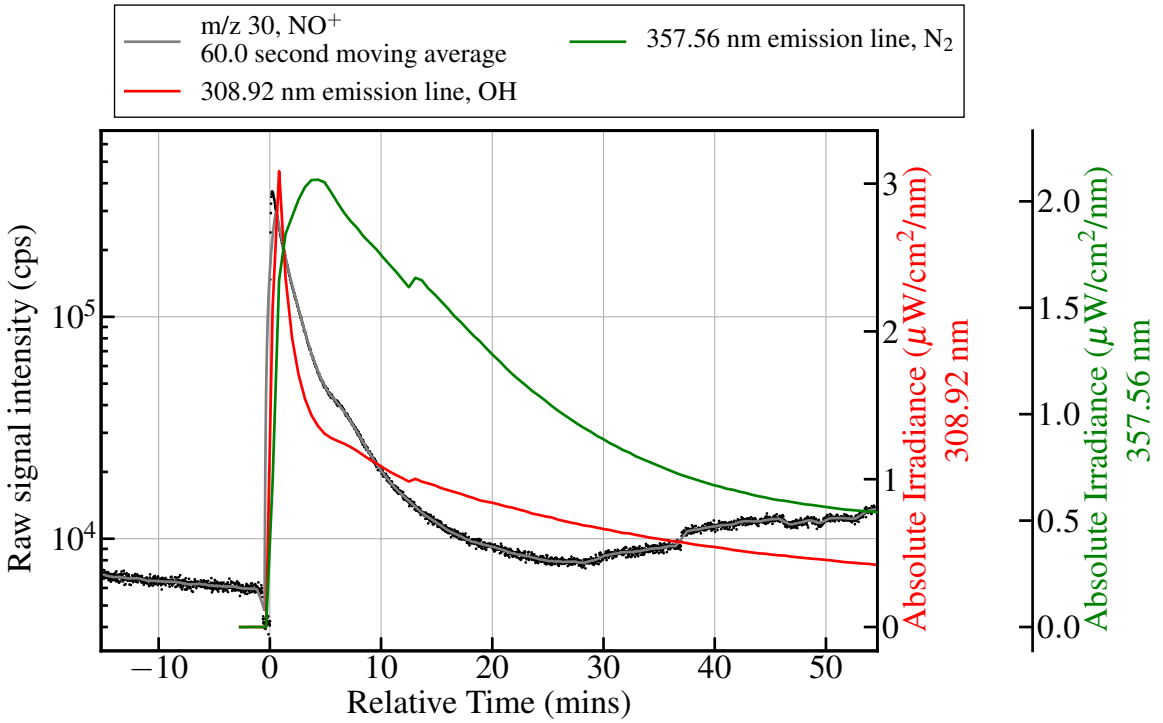

Figure 4.5: Timescale of flushing the plasma source (and gas reactor) with 400 sccm argon. After leaving the plasma source open to ambient air overnight, argon at 400 sccm is flushed through the plasma source into the gas reactor (started just before $t = 0$) and the plasma ignited (40 W_f) at $t = 0$. A flow of 200 sccm N_2 into the gas reactor was started at 37 mins.

In figure 4.5 there is evidence of OH and N_2 in the plasma, with potential NO also produced. It is also clear that the species have different mean flushing times through the plasma source and gas reactor. For example, the half-life of the OH emission seems to be ∼5 mins, whereas the N_2 molecular band emission takes ∼25 mins, about 5× longer.

Further detail of the spectra collected in this experiment is shown in figure 4.6. This figure shows a close up of the OH emission region (306–314 nm) for two different relative times in the flushing, showing the decrease in OH emission.

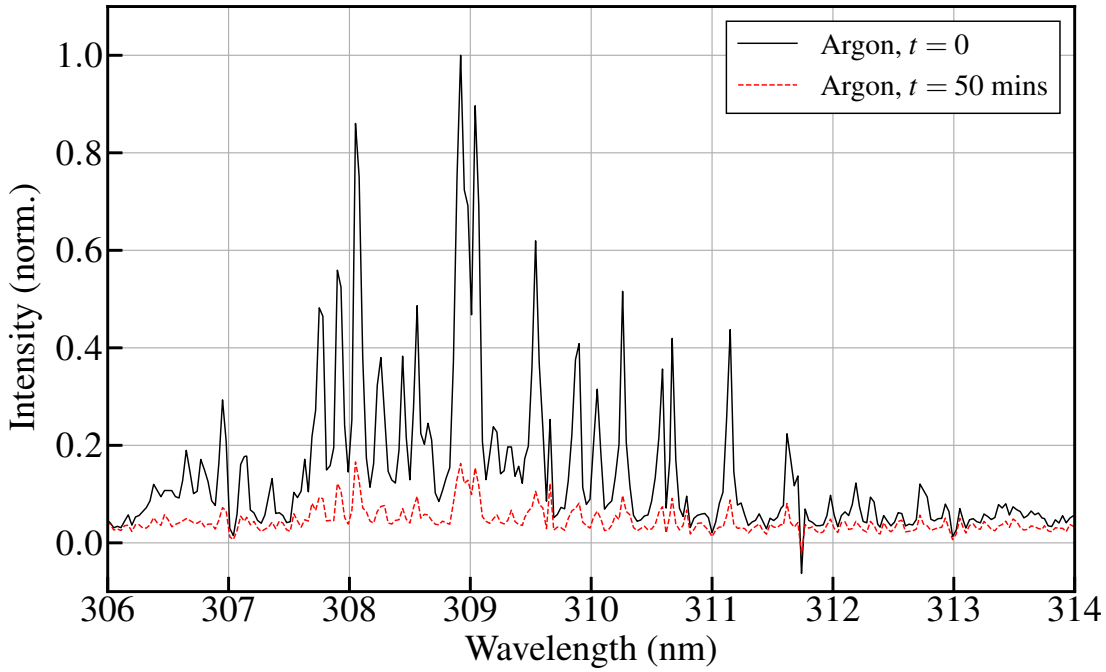

Figure 4.6: Dispersed fluorescence spectrum of OH emission ($A^2\Sigma^+ \rightarrow X^2\Pi, \Delta v = 0$) from the plasma recorded at $t = 0$ (black line) and $t = 50$ mins (dashed red line). The relative times correspond to figure 4.5.

4.3 Hydroxyl quantification

OH was identified by OES as an unwanted reactive component in the plasma effluent (see section 4.2). To quantify the OH density, several different gas mixtures were added. Benzene was used as an OH scrubber, rapidly converting OH to phenol (R4.8–R4.9) for detection by PTR-MS.

$$OH + C_6H_6\ (+M) \rightarrow HOC_6H_6\ (+M) \tag{4.8}$$

$$HOC_6H_6 + O_2 \rightarrow C_6H_5OH + HO_2 \tag{4.9}$$

Through monitoring the concentration of phenol as benzene was added to the plasma effluent, the density of OH was determined. To convert signal counts to absolute phenol concentrations, values from table 4.2 were used.

Table 4.2: OH scrubber compound properties. [a] reaction with Cl. [b] reaction with OH.

Compound	Functional group	Molar mass ($gmol^{-1}$)	k ($cm^3molecule^{-1}s^{-1}$)	Vapour pressure (Torr at 20°C)	Ref.
phenol	aromatic	94.113	[a] 1.93×10^{-10}, [b] 2.8×10^{-11}	0.4	[239][a] [240][b]
benzene	aromatic	78.114	[a] 1.3×10^{-16}, [b] 1.2×10^{-12}	95.3	[241][a] [240][b]

Shown in figure 4.7, the plasma was ignited at $t = 0$ mins (region (A), 40 W_f) then benzene was introduced into the reactor at $t \approx 6.5$ mins (region (B)). As benzene was introduced, the measured concentration of phenol (m/z 95) increased. As is also shown in figure 4.5, the absolute irradiance of OH decreased over time. As soon as the plasma was turned off (at $t \approx 24$ mins) the measured concentration of phenol rapidly decreased. The flow of benzene was unchanged, thus the concentration of benzene stayed relatively constant.

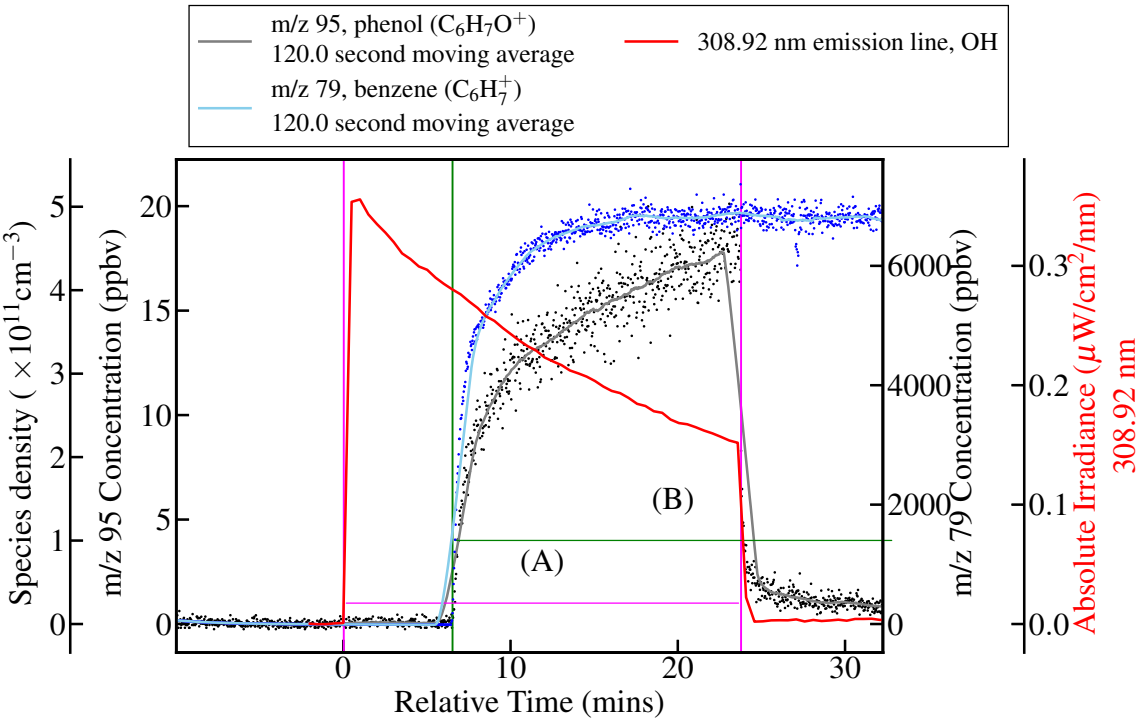

Figure 4.7: Evidence of phenol production (m/z 95) from OH + benzene reactions. An argon plasma was ignited at $t = 0$ mins (region (A), 40 W_f input plasma generator power) then benzene was introduced into the reactor at $t \approx 6.5$ mins (region (B)).

Alternatively, as shown in figure 4.8, the plasma was ignited after the addition of benzene.

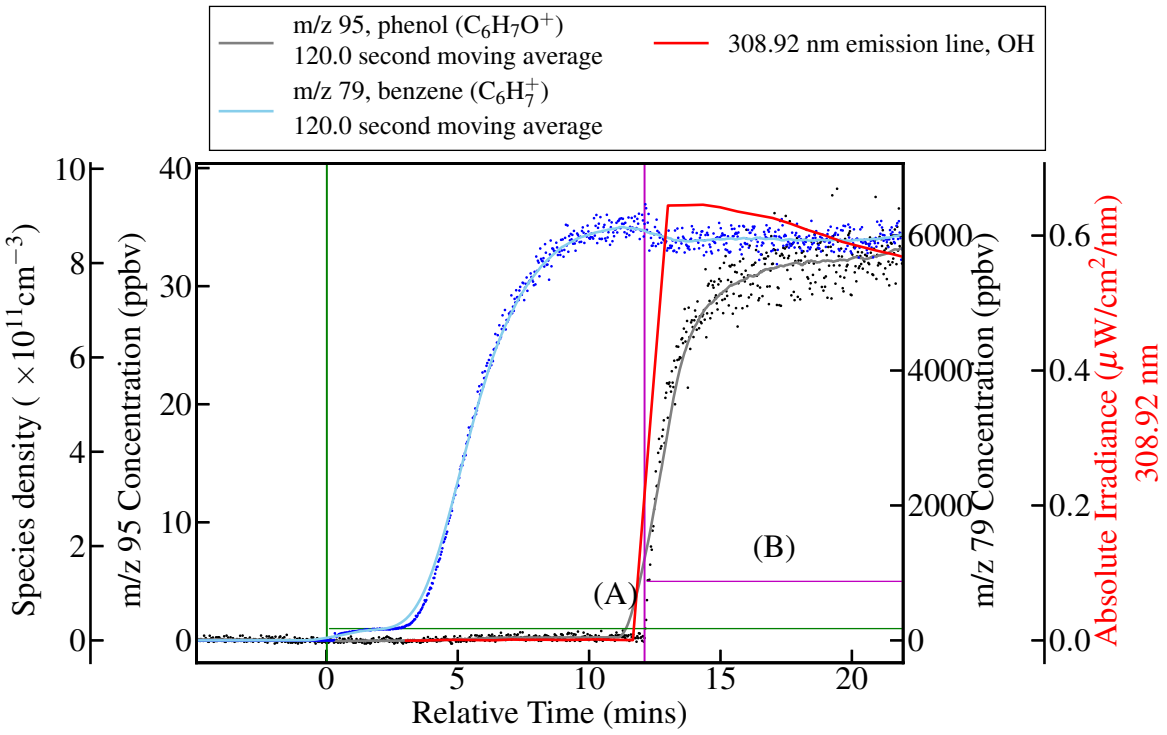

Figure 4.8: Production of phenol (m/z 95) after turning the plasma on. The regions (A) and (B) correspond to the times when benzene and the plasma (40 W_f plasma generator power) were on. Flow rates were 0.5 slm of each argon and zero air/benzene mix.

4.3.1 Hydroxyl mitigation

To mitigate the residual impurity in the argon flow, a few different methods were attempted. As previously mentioned, benzene is very effective at scrubbing OH due to its reaction rate with OH (1.2×10^{-12} cm^{3}molecule^{-1}s^{-1}) and substantially slow reaction with Cl (1.3×10^{-16} cm^{3}molecule^{-1}s^{-1}). However, due to the production of phenol, and phenol's rate of reaction with Cl (1.93×10^{-10} cm^{3}molecule^{-1}s^{-1}), this could interfere with the reaction of the reference compound and Cl in any subsequent reactivity measurements.

It was considered that an H_2O impurity was the likely source of OH. Therefore a dry ice and acetone cold trap (at 195.15 K, -78 °C) was placed in the argon line between the mass

flow controller and the plasma source. Because of the relatively high melting point of argon (83 K) liquid nitrogen (with a 77 K boiling point) could not be used. The result of using a cold trap are shown in figure 4.9.

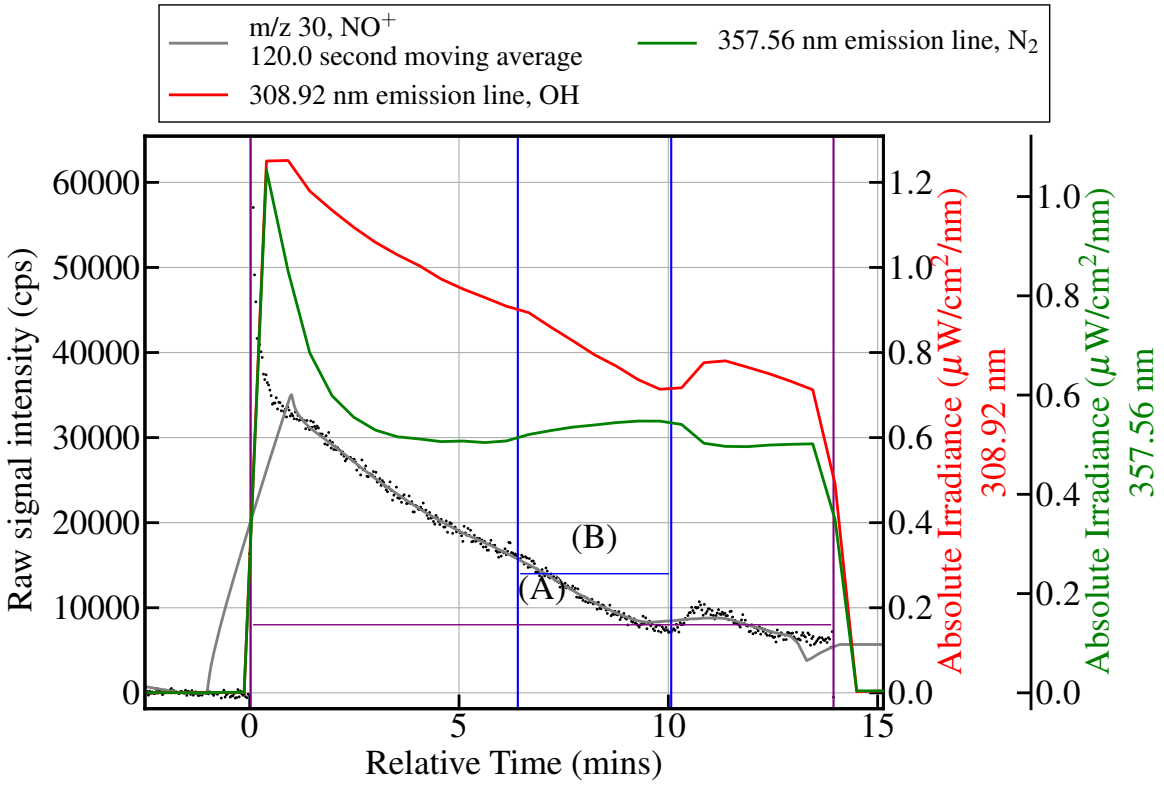

Figure 4.9: Impact of the acetone/CO_2 cold trap on OH and N_2 emission. The argon plasma (40 W_f) is on at t ≈2.5 mins (region a) with the trap on at t ≈9 to 12.5 mins. There is a sharper decrease in OH emission, with a slight increase in N_2 band emission, due to the decrease in H_2O.

As shown in the figure above, while the cold trap was attached to the argon line there is a steeper reduction in OH emission. This would suggest that residual H_2O in the input argon flow is freezing to the inner walls of the line. There is also a small relative increase in the 357 nm N_2 molecular band line, suggesting that the cold trap does not have an effect on the density of N_2 reaching the plasma. Another way of reducing the amount of humid air in the argon flow could be through using a molecular sieve. Other work into looking at

the impact of the material of the gas lines suggest that stainless steel is realistically the best option [118]. In the work here, stainless steel swagelok lines were used for all the input gas lines.

Further investigation of the humid air impurity included adding a small percentage (1-2%) of O_2 into the argon flow for the plasma. This is shown in figure 4.10.

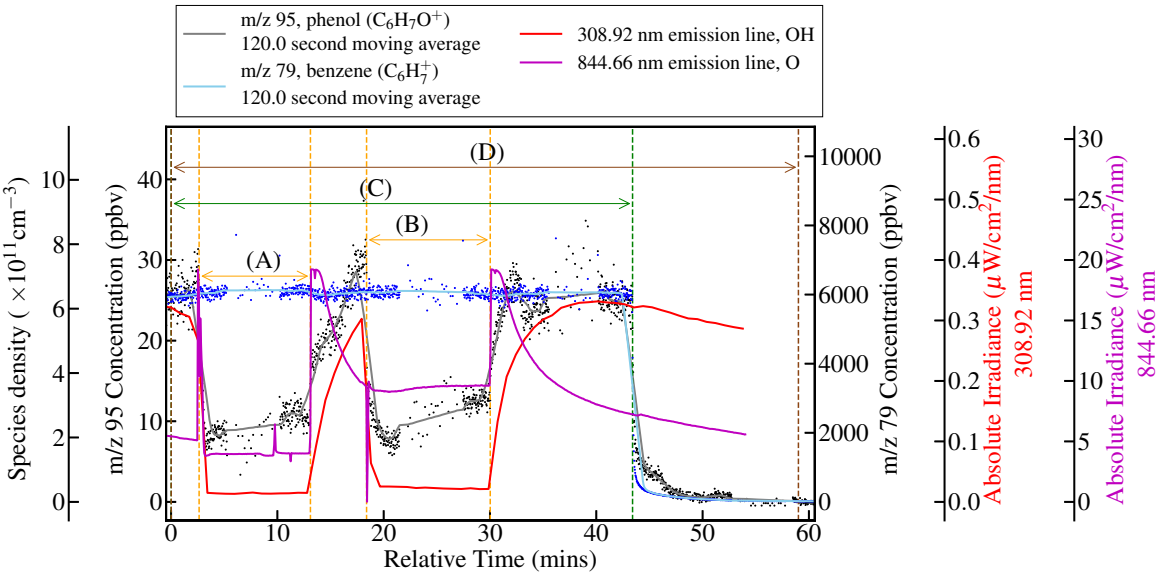

Figure 4.10: Investigation using O_2 in the input gas flow for the plasma. Benzene (m/z 95) was added in excess to the vessel, while the concentration of phenol (m/z 79) leaving the reactor was monitored. In this figure, regions (A) and (B) correspond to times when 2% and 1% O_2 was introduced to the input plasma gas flow. Regions (C) and (D) correspond to times when benzene and the plasma is on (40 W_f). The 308.92 nm OH line and 844.66 nm atomic oxygen triplet line is also monitored throughout.

As is seen in figure 4.10, the concentration of phenol and the OH emission line at 308 nm rapidly drops with the addition of O_2 to the plasma ($t \approx 3$ mins, $t \approx 19$ mins). Once the O_2 flow is stopped, the emission of the 844 nm atomic oxygen line seems to rapidly increase. The reason for this could be that as the O_2 concentration drops, the dissociation of O_2 increases, creating atomic O. This atomic oxygen will also slowly be removed, resulting in the observed steady decrease in 844 nm atomic oxygen emission. As the molecular and atomic oxygen is

flushed out of the plasma, the humid air impurity comes to dominate, resulting in more OH emission and an increase in the measured phenol concentration.

4.4 Chlorine admixture variation

To compare with the measurements from the zero dimensional global model, the concentration of Cl_2 in the gas mixture entering the plasma source was varied. A constant flow of diethyl-ether was introduced into the vessel, with the plasma power set at 40 W_f.

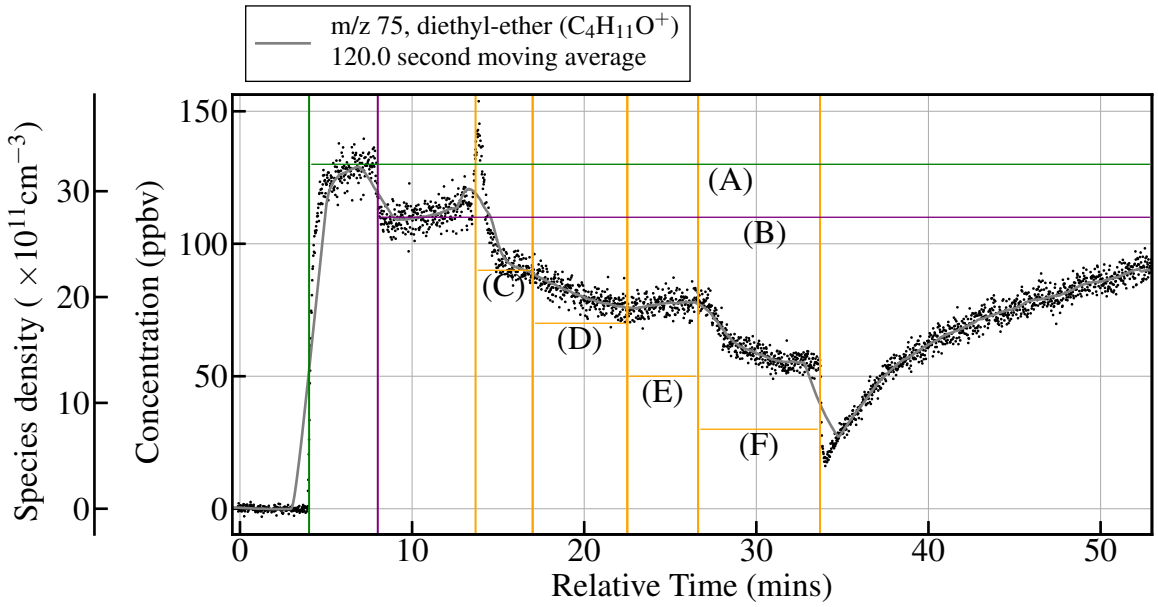

Figure 4.11: Evidence of depletion by OH and Cl radicals during an input Cl_2 admixture variation run. The regions indicated in the plot are: (A) 500 sccm of 126.6±0.5 ppb diethyl-ether in N_2, 1.5 slm argon (B) plasma on, 40 W_f, (C) 0.053% Cl_2 in argon into the plasma (D) 0.067% Cl_2 in argon into the plasma, (E) 0.053% Cl_2 in argon into the plasma, (F) 0.08% Cl_2 in argon into the plasma. The large recovery time of diethyl-ether after the Cl_2 is removed is most likely due to the plasma residence time of the humid air impurity.

As seen in the figure above, as the plasma is initially ignited at (B) there is a drop in the measured concentration of diethyl-ether. This is most likely due to the hydroxyl produced in the plasma. As the chlorine is introduced into the plasma there is a sharp

increase in measured diethyl-ether concentration. The reason for this is that many times with adding chlorine to the plasma, the impedance matching would have to be changed, thus the plasma would sometimes extinguish itself, before the correct matching point was found. The concentration of diethyl-ether then decreases again due to the production of atomic chlorine by the plasma. By subtracting the diethyl-ether concentration after chlorine is added from the concentration after the plasma is initially turned on, the atomic chlorine concentration could be determined.

What was also seen was an increase in N_2 molecular band emission as chlorine was added to the plasma. An example of the emission observed is shown in figure 4.12.

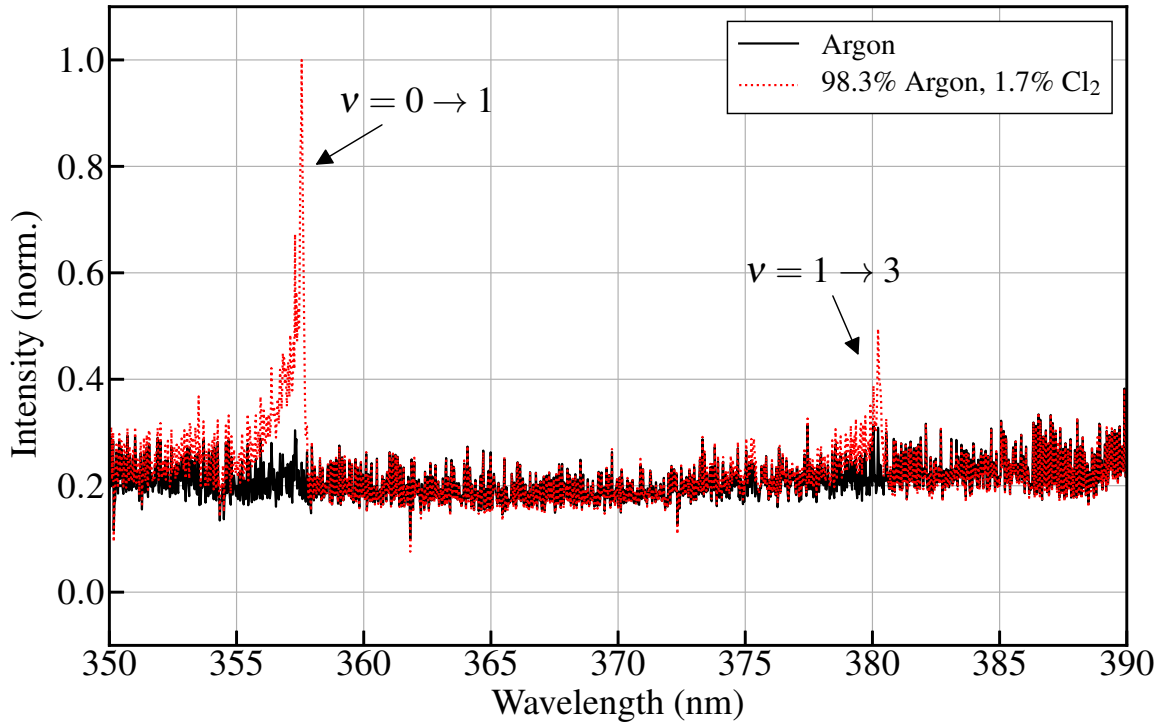

Figure 4.12: Close up of N_2 molecular band emission at 357 nm and 380 nm. Emission is from the N_2 ($C^3\Pi_u^+ \rightarrow B^3\Pi_g^+, \quad \nu' \rightarrow \nu''$) transition [238, 242].

To see how the results of the model compare with the experiment, the input chlorine admixture into the plasma was varied while flowing a constant concentration of diethyl-ether into the reactor. The measured depletion of diethyl-ether was plotted against two modelled

flow rate cases (fig. 4.13). In the experiment the total flow rate through the plasma was 500 sccm.

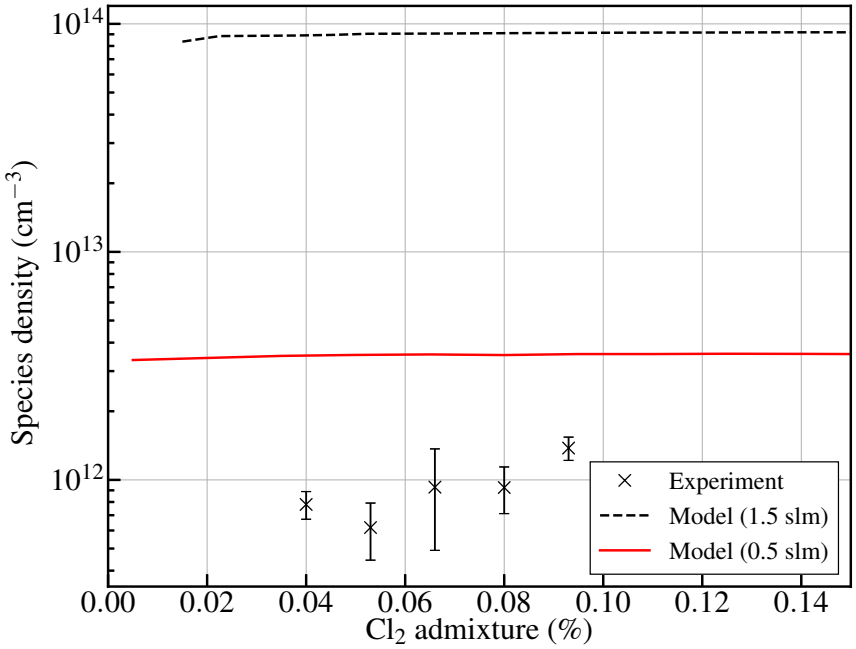

Figure 4.13: Comparison between the Cl density predicted by the model (see chapter 3) for two different total flow rates and that measured by the depletion of diethyl-ether using a total flow rate of 1.5 slm argon/chlorine and 0.5 slm diethyl-ether.

From the figure it was clear that there was a large quantitative difference between the model and the experimental results. Possible reasons for the discrepancy was the negative impact the humid air impurity had on the production and destruction rates of Cl_2 and Cl in the plasma. As was seen in the zero-dimensional modelling results, as the total flow rate was increased, the decay of Cl leaving the plasma decreased, resulting in a higher Cl density on leaving the plasma. However, as the COMSOL modelling indicated (section 2.1.3), as the flow rate is increased, there was insufficient mixing in the reactor, leading to incomplete reactions between Cl and the VOC.

4.5 Relative rate experiment

To test if the OH plasma by-product could be removed, benzene was used to scrub OH during a reactivity measurement. Differing amounts of diethyl-ether were added to the gas reactor while benzene was added in excess. Shown in figure 4.14, the measured OH emission drops consistently over the time of the experiment. With the addition of Cl_2 to the plasma there is an increased amount of m/z 30 (NO^+) and a reduction in the phenol and diethyl-ether concentration. The main problem with this experiment is that the reduction in phenol can not be explained by either the rapid Cl + phenol reaction, nor the slow Cl + benzene reactions. If there was the amount of Cl the reduction in phenol would suggest, there would be a much greater reduction in the measured diethyl-ether concentration.

Possible reasons for this could be that the impurity OH produced by the plasma is itself destroyed, reaction 4.10 producing HOCl and Cl. As the OH emission from the plasma seems to be relatively constant with addition of Cl_2, it follows that the OH produced from the plasma would also be relatively constant. With this reduction in OH, less phenol would be produced, i.e.

$$Cl_2 + OH \rightarrow HOCl + Cl \tag{4.10}$$

$$OH + C_6H_6 \rightarrow HOC_6H_6 \tag{4.11}$$

where $k_{R4.10} = 6.5 \times 10^{-14}$ $cm^3 molecule^{-1} s^{-1}$ [243]. The input 0.06% Cl_2 in argon is diluted by the zero air/benzene flow, thus $[Cl_2] \approx 7.5 \times 10^{15}$ cm^{-3}. The 12 ppm benzene flow is diluted by the argon/chlorine flow, thus $[C_6H_6] \approx 1.5 \times 10^{14}$ cm^{-3} and 5×10^{11} cm^{-3} [OH] from the density of phenol in the reactor;

$$[Cl_2][OH]k_{R4.10} = 2.4 \times 10^{14}\ cm^{-3} s^{-1} \tag{4.12}$$

and

$$[OH][C_6H_6]k_{R4.11} = 9 \times 10^{13}\ cm^{-3} s^{-1} \tag{4.13}$$

Thus, R4.10/R4.11 = 2.7

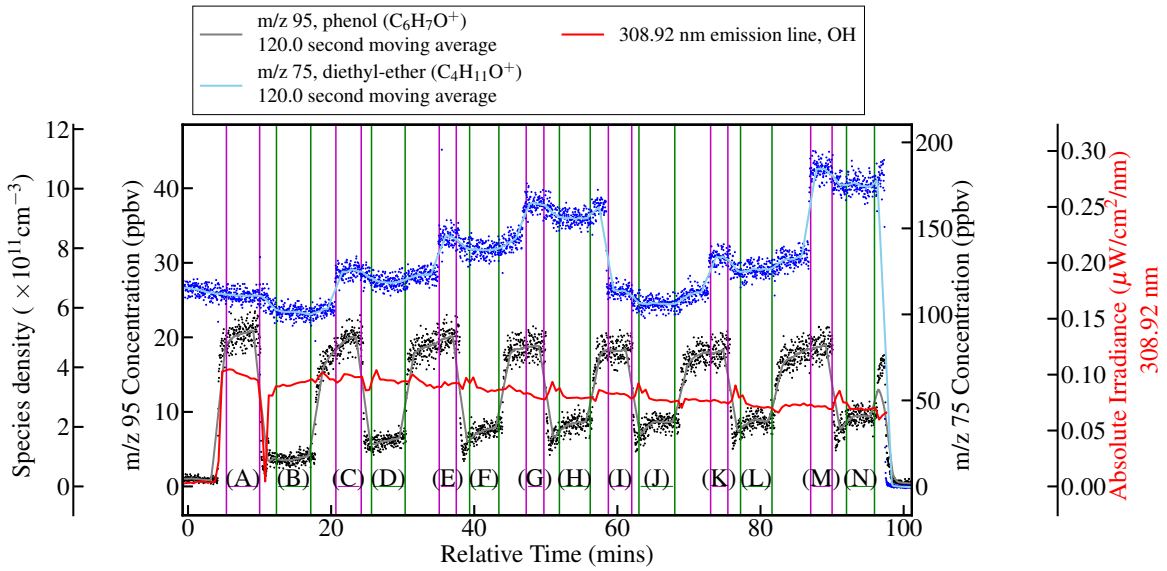

Figure 4.14: Relative rate experiment between phenol and diethyl ether. 500 sccm zero air with ≈12 ppm Benzene is introduced into the reactor for the whole duration of the experiment. The plasma is on from the beginning of region (A) to just after region (N) (seen by the measured OH emission). 0.06% chlorine is added to the 500 sccm argon plasma gas flow in the regions indicated in green, i.e. (B), (D), (F), (H), (J), (L), (N) with the regions in magenta ((A), (C), (E), (G), (I), (K), (M)) indicating the time waiting for diethyl ether to stabilise after changing its concentration into the reactor.

The reduction in diethyl-ether also seems to be relatively constant with addition of Cl_2 to the plasma. To see the impact the large amount of Cl_2 has on the measured concentrations of phenol and diethyl-ether a simulation using Kintecus [244] was done.

Kintecus is a chemical box model that focuses on large chemistry sets, similar in action to the ordinary differential solver used in Globalkin, it tracks the evolution in time of the various chemical species involved, given a user-created chemistry set (see table 4.3).

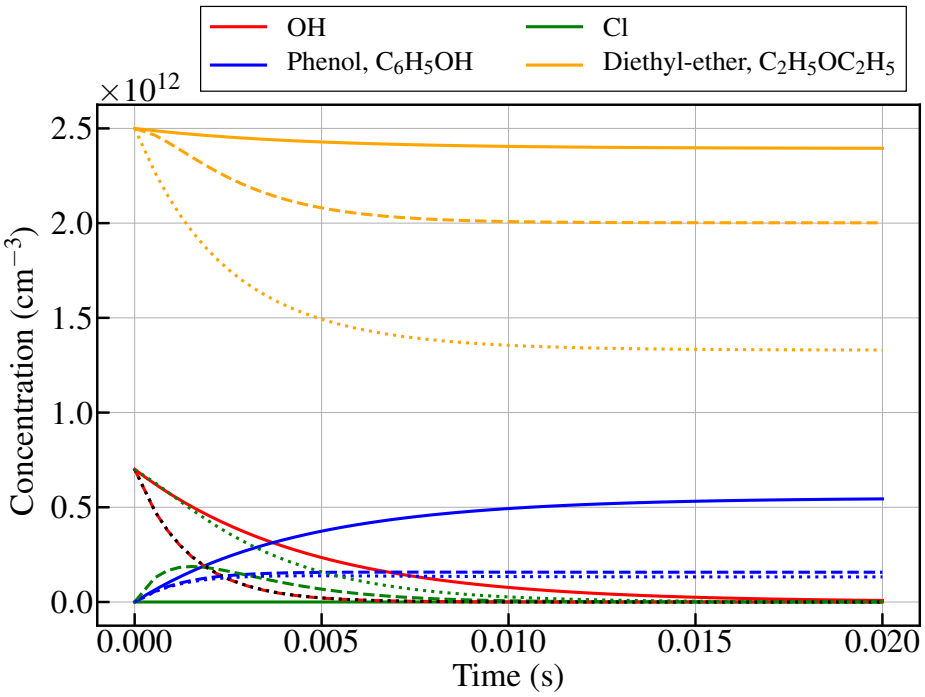

Figure 4.15: Simulation using Kintecus of the relative rate experiment shown in fig. 4.14. The solid line is the case with $[OH] = 7 \times 10^{11}$ cm^{-3} without any Cl_2 or Cl, dashed line for $[OH] = 7 \times 10^{11}$ cm^{-3}, $[Cl_2] = 7.5 \times 10^{15}$ cm^{-3} and dotted line for [OH]=[Cl] $= 7 \times 10^{11}$ cm^{-3} $[Cl_2] = 7.5 \times 10^{15}$ cm^{-3}. The black dotted line is [OH], this is used for clarity

As is shown in the figure above, the concentrations of an initial amount of OH, Cl and diethyl-ether are tracked. The initial concentration of phenol in each of these cases is 0, with the same amount of diethyl-ether (2.5×10^{12} cm^{-3}). The model is kept very basic with focus on the first-order reactions of the plasma-generated radicals and introduced VOC species. Initially, the plasma-produced OH can only react with the VOC present, eventually forming phenol and initiating the breakdown of diethyl-ether. As the relatively high concentration Cl_2 (0.06%) is added, some of the available OH is converted into HOCl and Cl that then

goes on to react with the available diethyl-ether; as there is less OH, less phenol is produced, therefore more of the diethyl-ether is depleted by the OH and Cl. In the final case, as the same amount of Cl as OH is added, this makes a large difference again to the diethyl-ether concentration, however little difference to the phenol concentration, as the same amount of OH is destroyed by the high concentration of Cl_2. Compared to the measurements using PTR-MS, other potential products from the plasma include atomic oxygen, hydrogen and nitrogen which may all cause decomposition of phenol. The system is not fully characterised thus the impact these other products has is not known. It is also not known if Cl_2 on the surfaces takes part in any of the chemistry in the reactor, potentially causing further depletion of phenol.

Table 4.3: Kintecus reactions, rate coefficients in $cm^3molecule^{-1}s^{-1}$.

Reaction	Rate coefficient	Ref.
$OH + C_6H_6 \rightarrow C_6H_5OH + HO_2$	1.2×10^{-12}	[245]
$OH + C_6H_5OH \rightarrow C_6H_5O + H_2O$	3.36×10^{-12}	[245]
$OH + C_2H_5OC_2H_5 \rightarrow DiethylRad + H_2O$	1.36×10^{-11}	[237]
$OH + Cl_2 \rightarrow HOCl + Cl$	6.5×10^{-14}	[243]
$Cl + C_6H_6 \rightarrow PhenylRad + HCl$	1.3×10^{-16}	[241]
$Cl + C_2H_5OC_2H_5 \rightarrow DiethylRad + HCl$	2.58×10^{-10}	[236]
$Cl + C_6H_5OH \rightarrow PhenolRad + HCl$	1.93×10^{-10}	[239]

4.6 Proxy air reactivity measurements

A mixture of 77 ppb isoprene and 26 ppb toluene was used as a proxy for a polluted air sample. These compounds were chosen to represent a mix of naturally-occurring (isoprene) and anthropogenic (toluene) pollutants. The OH and Cl kinetics of isoprene and toluene are well characterised, thus their reaction rates with OH and Cl are known (see table 4.4). The mixture is basic, with chemistry from other VOC, NO_2 and O_3 absent. To calculate the Cl-reactivity of the mixture, equation 4.14 was used;

$$R_{calc} = k_{\mathrm{a+Cl}}[\mathrm{a}] + k_{\mathrm{b+Cl}}[\mathrm{b}] + \ldots \tag{4.14}$$

Similarly to the comparative reactivity method by Sinha et al. [15], eq. (4.15) is used to measure the reactivity of a gas sample from the relative change in concentration of a reference compound, in this case, diethyl-ether;

$$R_{meas} = \left(\frac{[x]_C - [x]_B}{[x]_A - [x]_C} \right) k_x \cdot [x]_A \tag{4.15}$$

Table 4.4: Compounds used in the polluted air proxy. [a] reaction with Cl.
[b] reaction with OH.

Compound	Functional group	Molar mass ($gmol^{-1}$)	k ($cm^3 molecule^{-1} s^{-1}$)	Vapour pressure (Torr at 20℃)	Ref.
isoprene	diene	68.12	[a] 4.0×10^{-10}, [b] 1.0×10^{-10}	5.5	[a] [246] [b] [240]
toluene	aromatic	92.14	[a] 5.81×10^{-11}, [b] 5.6×10^{-12}	21	[a] [247] [b] [248]

The reactivity was varied between 10 to 40 s^{-1} using small flows of the isoprene and toluene mixture. In figure 4.16, regions (D), (F), (H), (J) the reactivity is 10.1, 20.2, 30.3, and 40.4 s^{-1}.

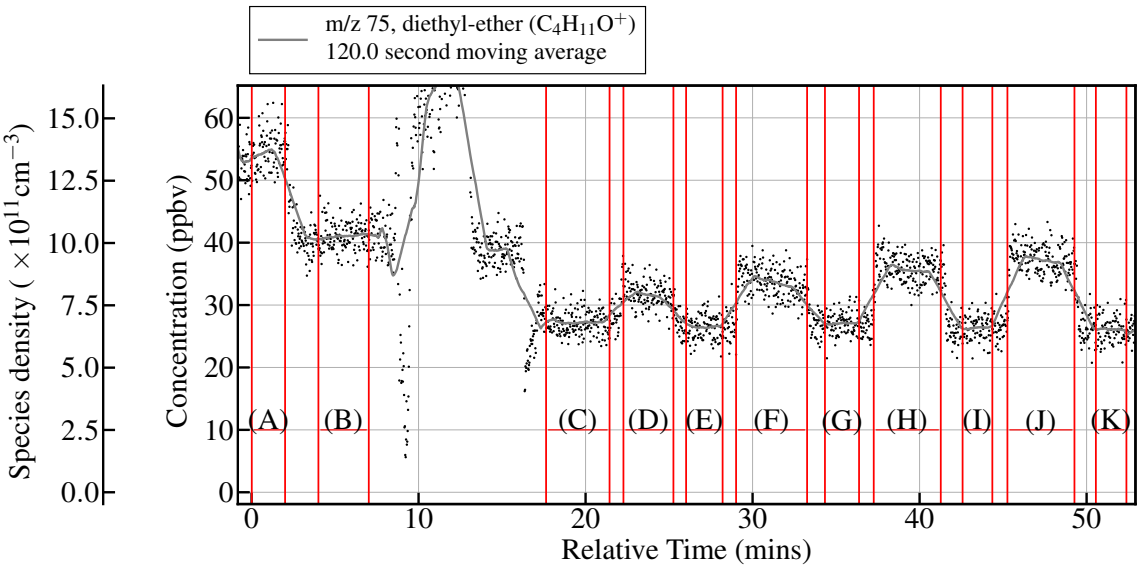

Figure 4.16: Measured concentration of the reference compound (diethyl ether) under variation of the proxy polluted air mixture (77 ppb isoprene, 26 ppb toluene). The plasma is ignited at the end of region (A) with chlorine added just before region (C). The regions (D), (F), (H) and (J) correspond to the times when increasing amounts of the proxy air mixture is added to the reference compound flow.

In figure 4.17 the reactivity was varied between 12–57 s^{-1}. The plasma was ignited at the end of region (A) with chlorine added to the plasma at the end of region (B). Regions (D), (F), (H), (J) and (L) correspond to increased additions of the toluene/isoprene mixture, and refer to reactivity of 12, 24, 35, 46 and 57 s^{-1}.

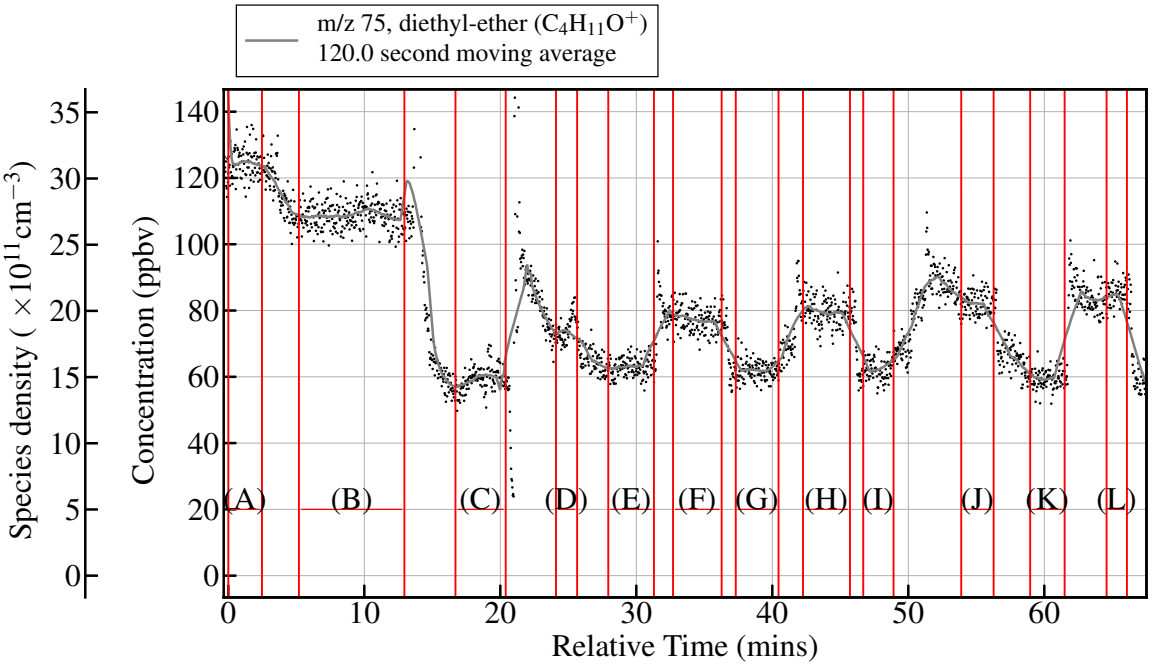

Figure 4.17: Measured concentration of the reference compound (diethyl ether) under variation of the proxy polluted air mixture (77 ppb isoprene, 26 ppb toluene). The plasma is ignited at the end of region (A) with chlorine added at the end of region (B). The regions (D), (F), (H), (J) and (L) correspond to the times when increasing amounts of the proxy air mixture is added to the reference compound flow.

The measured versus calculated reactivity from figures 4.16 and 4.17 is shown in the figure below.

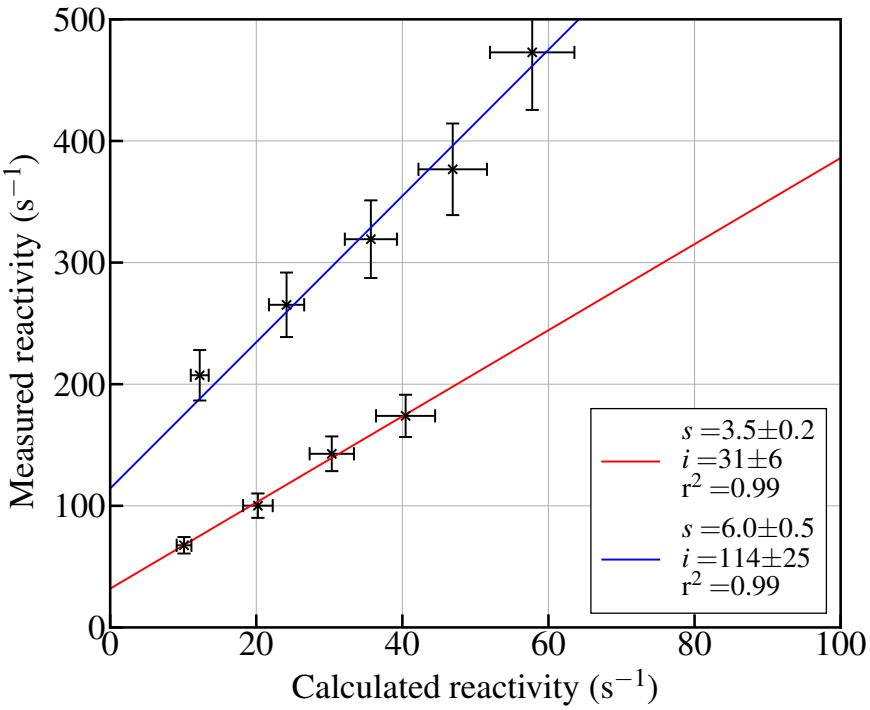

Figure 4.18: Measured (using eq. (4.15), and concentrations from figs. 4.16 and 4.17) versus calculated (using eq. (4.14)) reactivity. The terms in the caption correspond to the slope (s) and intercept (i) linear fit of the two sets of reactivity measurements.

As is shown in the figure above, the measured reactivity using the comparative reactivity method was several times larger than the reactivity calculated using the relevant flow rates, canister concentrations and reaction rates. From the relative rate experiment, the reason for the overestimated reactivity could be due to other reactive fragments (other than Cl) also reacting with the reference compound. Somewhat related is the assumption that the extra decay of the reference concentration seen as chlorine was added to the plasma was only due to plasma-generated Cl atoms. As was shown by the relative rate experiment, the high concentration of Cl_2 and OH generated by the plasma created further Cl. Also, as a zero-air generator was not used for this experiment, background methane (CH_4) could also be

present, causing the over-estimate in the reactivity. However, due to the relatively small rate coefficient ($k_{Cl+CH_4} = 1.0 \times 10^{-13} cm^3 molecule^{-1} s^{-1}$ [101]) there would have to be a large amount (∼20 ppm) to make a substantial difference. For the measured reactivity to equate the calculated reactivity, the concentration of the isoprene-toluene mixture would have to be ×5 the one used here. As the discrepancy changes with the concentration of isoprene and toluene, it is not clear if any change in the measured [Cl] or [diethyl-ether] would reduce the intercept. It may be possible that incomplete mixing or removal from the reactor has caused too much depletion causing the discrepancy.

It is important to note that the chemistry here was under-characterised, the products from the plasma are not fully known. We understand the plasma does affect the reference compound without Cl_2, however we do not know to what extent this is still true as chlorine was added to the plasma.

4.7 Summary

In summary, a well characterised mixture of four oxygenated volatile organic compounds was used to decide the reference compound for the Cl-reactivity method. During this investigation, it was discovered that the plasma creates reactive radical fragments that depleted the mixture of four OVOC. Optical emission spectroscopy identified OH and N_2^* emission from the plasma, indicating that the radical fragments could be caused by impurity humid air. Further investigation using benzene to scrub the plasma-produced OH produced phenol that was then used as part of relative rate experiment using diethyl-ether.

Finally, the Cl-reactivity of a well-characterised mixture of isoprene and toluene was attempted using diethyl-ether as the reference compound. From these measurements it was clear that the extra radical fragments produced from the plasma cause additional reactions with the reference compound causing an inflated reactivity measurement.

Chapter 5

Conclusion and future outlook

In conclusion, an atmospheric pressure, capacitively coupled plasma source containing chlorine has been built, characterised using OES and PTR-MS, applied to atmospheric chemistry and modelled for the first time. As the study of short-lived reactive species is an important aspect in both plasma science and atmospheric chemistry, there is no doubt that this overlap gives a window for more possible applications for low-temperature plasmas. The plasma source studied here has been shown to be highly effective in dissociation and production of atomic chlorine at atmospheric pressure. This is the first time such a plasma source has been used to produce atomic chlorine at atmospheric pressure.

In this work, a plasma source was used to create short-lived reactive species that were then probed using different volatile organic compounds. A proton transfer reaction mass spectrometer was used to monitor the resulting gas mixture. Through interference of the measured VOC concentration while having nothing added to the plasma, it was found through optical emission spectroscopy that OH and N_2^* was present in the plasma. Attempts were made to reduce the impurities entering the plasma, using an acetone/dry ice cold trap. The OH produced by the plasma was quantified by PTR-MS using measurements of phenol as OH was titrated by benzene. Measurement of the reactivity of a mixture of isoprene and toluene was attempted using the comparative reactivity method of Sinha et al. [15].

Unfortunately, the efficiency of the low-temperature plasma used in this work leads to its own downfall. As any small amount of contaminant that enters the plasma will be

dissociated, this creates a highly reactive mixture of different radical species. The argon gas purity used in this work, BOC N6.0 grade (99.9999%) means there is 1 ppmv of impurities. In relative rate experiments, the reagents have to react only with the target radical and nothing else. Very similar to a relative rate experiment, the comparative reactivity method has this same vulnerability. As the plasma generates other radicals from the 1 ppmv impurity, these all interfere with the desired chemistry. Increasing the input concentration of Cl_2 will not ease the problem, as the desired chlorine atom density in the reactor is 1×10^{12}cm^{-3}, already much less than the 1 ppmv impurity (1×10^{12}cm^{-3} $\approx$ 40 ppbv= 0.04 ppmv).

To minimise this interference, a molecular sieve to remove H_2O, O_2 and N_2 from the argon and argon/chlorine supply could be tested and measurements of OH repeated using benzene. On the other hand, the plasma in this work may be useful for generating OH radicals, as humid air is already the main impurity. OH reactivity measurements could be attempted by intentionally adding a water bubbler to the inlet argon flow. Other changes could include redesigning the gas reactor so the plasma source is at an offset angle to rule out any possible interference by UV plasma radiation. The gas mixture inlet could also be offset, to encourage better gas mixing in the reactor.

For the future development of any atomic chlorine competitive reactivity measurements, the experiment would need some adjustments to make its use in the field practical. Ways of doing this would include making the experimental system more robust to reduce the chance of the glass capillary breaking. By fixing the position of the heavy impedance matchbox and placing the plasma source and gas reactor glassware into a metal box using a carefully constructed inserts, the glassware could be made into a single piece and simplified. This could also reduce the distance between the plasma source and gas reactor, potentially increasing the amount of atomic chlorine that reaches the gas reactor. The cooling system for the plasma source could also be included in the box to reduce the number of ports. Ideally the only ports needed would be for the input gas sample and plasma gas mixture, output from the gas reactor to the PTR-MS, and electrical ports for the coaxial power cable and power for the closed cooling loop. The metal box would also double as RF shielding from the plasma source. For igniting the plasma, a metal mesh window on the side of the box or

a camera could be used. A pump and mass flow controller could also be added to the outlet of the gas reactor to ensure that none of the VOC mixtures diffuse into the plasma source.

Alternative ambient Cl-atom production methods could also be attempted. These include the photolysis of molecular chlorine itself or other precursors, such as phosgene, $COCl_2$ using UV lamps or the thermal decomposition of Cl_2. These methods use zero air as a carrier gas and could be more selective in creating Cl, thus a more pure stream of Cl atoms than the current argon + Cl_2 plasma method could be produced.

Further diagnostics of the plasma could also be done. These could include electrical measurements, i.e. measuring the voltage and current waveforms between the plasma source and matchbox to measure the power deposited in the plasma. Also, it may be possible to use an adapted plasma source to measure the atomic chlorine density in the immediate effluent of the plasma source using TALIF to verify the current measurements of Cl. It could also be of interest to measure the decay of argon metastables exiting the plasma, using tunable diode laser absorption spectroscopy [249]. Further modelling work could also be carried out with these measurements used to benchmark the model. It could also be interesting to add different VOC to the enclosure to mimic different operating conditions and measure the decay of different reactive species, i.e. OH, N, O and Cl. Through this technique, the energy and conversion efficiency of the plasma source could also be verified. The use of chlorine-containing plasmas can work for the generation of large atomic chlorine densities and may therefore find a role in atmospheric research where other atmospheric pressure sources of Cl are inefficient.

To measure Cl-atom density and reactivity in the atmosphere directly with current technology is a great challenge. As mentioned earlier (see sections 1.3.3 and 1.3.4), alternative methods to the comparative reactivity method would require laser induced fluorescence of Cl atoms in ambient air. This leads to the severe problem of O_2 and H_2O absorption overlap at similar wavelengths.

Glossary

Symbol/ Acronym	Name	Description
VOC	Volatile organic compound	A large class of organic compounds that are usually in the gas phase at standard conditions.
λ_{De}	Debye length	Characteristic electrostatic length scale in a plasma. Equal to $\left(\frac{\varepsilon_0 k_B T_e}{n_e e^2}\right)^{1/2}$.
ICP	Inductively coupled plasma	Plasma sustainment using the magnetic field produced by a time-varying current through a coil.
CCP	Capacitively coupled plasma	Plasma sustainment using the electric field produced between two conductive plates.
EEDF	Electron energy distribution function	Function describing the distribution of electron energy. Gas composition, pressure, power deposition-dependent.
ω_{pe}	Plasma frequency	Characteristic frequency, electron density-dependent; $\sqrt{\frac{e^2 n_e}{\varepsilon_0 m_e}}$
$\mathbf{F}$	Applied force vector	
$\mathbf{E}$	Applied electric field potential vector	

TALIF	Two-photon laser induced fluorescence	Active plasma diagnostic using two-photon absorption to measure absolute atomic species densities.
T_{eff}	Effective electron temperature	
N_A	Avogadro's constant	6.02214076×10^{23} mol^{-1}
V_m	Molar volume at 0℃, 1 atm	22414 cm^3 mol^{-1}
e	Elementary charge	$1.602176634\times10^{-19}$ C
ε_0	Vacuum permittivity	$8.854187812\times10^{-12}$ F m^{-1}
k_B	Boltzmann's constant	1.380649×10^{-23} J K^{-1}

Appendix A

Plasma reaction set

Table A.1: Electron impact reactions. [a] $n = 0, 1, 2, 3$. [b] $m = 0, 1, 2$. [c] The reverse super-elastic reaction is calculated using detailed balance. [d] The cross section for $Cl_2(v > 1)$ is generated by reducing the threshold by $v \times 0.069$ eV.

No.	Reaction	ε_{th}(eV)	Rate	Ref.	Note
EI1	$e^- + Cl_2(v = n) \rightarrow Cl_2(v = n) + e^-$	0.0	$f(\varepsilon)$	[174]	*a*
EI2	$e^- + Cl_2(v = n) \rightarrow Cl + Cl^-$	0.0	$f(\varepsilon)$	[174]	*a*
EI3	$e^- + Cl_2(v = m) \rightarrow Cl_2(v = m + 1) + e^-$	0.069	$f(\varepsilon)$	[174]	*bc*
EI4	$e^- + Cl_2(v = n) \rightarrow Cl_2(a^3\Pi_u) + e^- \rightarrow 2Cl + e^-$	3.252	$f(\varepsilon)$	[174]	*ad*
EI5	$e^- + Cl_2(v = n) \rightarrow Cl_2(A^1\Pi_u) + e^- \rightarrow 2Cl + e^-$	4.348	$f(\varepsilon)$	[174]	*ad*
EI6	$e^- + Cl_2(v = n) \rightarrow Cl_2(b^3\Pi_g) + e^- \rightarrow 2Cl + e^-$	6.498	$f(\varepsilon)$	[174]	*ad*
EI7	$e^- + Cl_2(v = n) \rightarrow Cl_2(c^3\Sigma_g^-) + e^- \rightarrow 2Cl + e^-$	7.257	$f(\varepsilon)$	[174]	*ad*
EI8	$e^- + Cl_2(v = n) \rightarrow Cl_2(B^1\Pi_g) + e^- \rightarrow 2Cl + e^-$	7.537	$f(\varepsilon)$	[174]	*ad*
EI9	$e^- + Cl_2(v = n) \rightarrow Cl_2(C^1\Delta_g) + e^- \rightarrow 2Cl + e^-$	7.790	$f(\varepsilon)$	[174]	*ad*
EI10	$e^- + Cl_2(v = n) \rightarrow Cl_2(D^1\Sigma_g^+) + e^- \rightarrow 2Cl + e^-$	8.228	$f(\varepsilon)$	[174]	*ad*
EI11	$e^- + Cl_2(v = n) \rightarrow Cl_2(e^3\Sigma_u^+) + e^- \rightarrow 2Cl + e^-$	9.219	$f(\varepsilon)$	[174]	*ad*
EI12	$e^- + Cl_2(v = n) \rightarrow Cl_2^*(\text{Rydberg } {}^1\Pi_u) + e^-$	10.54	$f(\varepsilon)$	[174]	*ad*
EI13	$e^- + Cl_2(v = n) \rightarrow Cl_2^*(\text{Rydberg } {}^1\Sigma_u) + e^-$	10.70	$f(\varepsilon)$	[174]	*ad*

EI14	$e^- + Cl_2(v = n) \rightarrow Cl^+ + Cl^-$	11.00	$f(\varepsilon)$	[193]	*ad*
EI15	$e^- + Cl_2(v = n) \rightarrow Cl_2^+ + 2e^-$	11.49	$f(\varepsilon)$	[174]	*ad*
EI16	$e^- + Cl_2(v = n) \rightarrow Cl^+ + Cl + 2e^-$	11.49	$f(\varepsilon)$	[174]	*ad*
EI17	$e^- + Cl_2(v = n) \rightarrow Cl_2^{2+} + 3e^-$	35.50	$f(\varepsilon)$	[174]	*ad*
EI18	$e^- + Cl_2(v = n) \rightarrow Cl^{2+} + Cl + 3e^-$	43.50	$f(\varepsilon)$	[174]	*ad*
EI19	$e^- + Cl_2^* \rightarrow Cl_2^* + e^-$	0.0	$f(\varepsilon)$	[174]	
EI20	$e^- + Cl_2^* \rightarrow Cl_2^+ + 2e^-$	0.79	$f(\varepsilon)$	[250]	
EI21	$e^- + Cl_2^+ \rightarrow 2Cl$	0.0	$f(\varepsilon)$	[251]	
EI22	$e^- + Cl \rightarrow Cl + e^-$	0.0	$f(\varepsilon)$	[252]	
EI23	$e^- + Cl \rightarrow Cl^*(4s) + e^-$	8.9	$f(\varepsilon)$	[163]	*c*
EI24	$e^- + Cl \rightarrow Cl^*(4p) + e^-$	10.4	$f(\varepsilon)$	[163]	*c*
EI25	$e^- + Cl \rightarrow Cl^*(3d) + e^-$	10.9	$f(\varepsilon)$	[163]	*c*
EI26	$e^- + Cl \rightarrow Cl^*(5p) + e^-$	11.8	$f(\varepsilon)$	[163]	*c*
EI27	$e^- + Cl \rightarrow Cl^*(4d) + e^-$	12.0	$f(\varepsilon)$	[163]	*c*
EI28	$e^- + Cl \rightarrow Cl^*(5d) + e^-$	12.4	$f(\varepsilon)$	[163]	*c*
EI29	$e^- + Cl \rightarrow Cl^+ + 2e^-$	12.99	$f(\varepsilon)$	[164]	
EI30	$e^- + Cl^* \rightarrow Cl^* + e^-$	0.0	$f(\varepsilon)$	[252]	
EI31	$e^- + Cl^* \rightarrow Cl^+ + e^-$	2.09	$f(\varepsilon)$	[250]	
EI32	$e^- + Cl^+ \rightarrow Cl^+ + e^-$	0.0	$f(\varepsilon)$	[252]	
EI33	$e^- + Cl^+ \rightarrow Cl$	0.0	$f(\varepsilon)$		
EI34	$e^- + Cl^- \rightarrow Cl^- + e^-$	0.0	$f(\varepsilon)$	[252]	
EI35	$e^- + Cl^- \rightarrow Cl + 2e^-$	3.613	$f(\varepsilon)$		
EI36	$e^- + Ar \rightarrow Ar + e^-$	0.0	$f(\varepsilon)$	[158]	
EI37	$e^- + Ar \rightarrow Ar^* + e^-$	11.6	$f(\varepsilon)$	[157]	*c*
EI38	$e^- + Ar \rightarrow Ar^{**} + e^-$	13.1	$f(\varepsilon)$	[157]	*c*
EI39	$e^- + Ar \rightarrow Ar^+ + e^-$	16.0	$f(\varepsilon)$	[159]	
EI40	$e^- + Ar^* \rightarrow Ar^* + e^-$	0.0	$f(\varepsilon)$	[158]	
EI41	$e^- + Ar^* \rightarrow Ar^{**} + e^-$	1.58	$f(\varepsilon)$	[161]	*c*

EI42	$e^- + Ar^* \rightarrow Ar^+ + e^-$	4.425	$f(\varepsilon)$	[160]
EI43	$e^- + Ar^{**} \rightarrow Ar^{**} + e^-$	0.0	$f(\varepsilon)$	[158]
EI44	$e^- + Ar^{**} \rightarrow Ar^+ + e^-$	2.9	$f(\varepsilon)$	[250]
EI45	$e^- + Ar^+ \rightarrow Ar^+ + e^-$	0.0	$f(\varepsilon)$	
EI46	$e^- + Ar^+ \rightarrow Ar$	0.0	$f(\varepsilon)$	
EI47	$e^- + Ar^+ \rightarrow Ar^*$	0.0	$f(\varepsilon)$	
EI48	$2e^- + Ar^+ \rightarrow Ar + e^-$	0.0	7×10^{-27}	[253]
EI49	$2e^- + Ar^+ \rightarrow Ar^* + e^-$	0.0	5×10^{-27}	[254]
EI50	$2e^- + Ar^+ \rightarrow Ar^{**} + e^-$	0.0	7.18×10^{-27}	[254]
EI51	$e^- + Ar^+ + Ar \rightarrow Ar^{**} + Ar$	0.0	7.18×10^{-27}	[254]

Table A.2: Ion-ion reactions.

No.	Reaction	Rate	Ref.	Note
II1	$Cl^+ + Cl^- \rightarrow 2Cl$	5×10^{-8}	[210]	
II2	$Cl_2^+ + Cl^- \rightarrow Cl_2 + Cl$	5×10^{-8}	[210]	
II3	$Cl_2^+ + Cl^- \rightarrow 3Cl$	5×10^{-8}	[210]	
II4	$Ar^+ + Cl^- \rightarrow Ar + Cl$	5×10^{-8}	[210]	

Table A.3: Ion-neutral reactions. $^a n = 0, 1, 2, 3$.

No.	Reaction	Rate	Ref.	Note
IN1	$Cl_2(v = n) + Cl^+ \rightarrow Cl_2^+ + Cl$	5.4×10^{-10}	[211]	
IN2	$Cl_2(v = n) + Cl_2^+ \rightarrow Cl_2^+ + Cl_2$	8×10^{-10}	[208]	^{a}
IN3	$Cl_2(v = n) + Ar^+ \rightarrow Cl_2^+ + Ar$	1.9×10^{-10}	[212]	^{a}
IN4	$Cl_2(v = n) + Ar^+ \rightarrow Cl + Cl^+ + Ar$	5.7×10^{-10}	[212]	^{a}
IN5	$Cl_2^* + Cl^+ \rightarrow Cl_2^+ + Cl$	5.4×10^{-10}	[211]	
IN6	$Cl_2^* + Cl_2^+ \rightarrow Cl_2^+ + Cl_2$	8×10^{-10}	[208]	^{a}

IN7	$Cl_2^* + Ar^+ \rightarrow Cl_2^+ + Ar$	1.9×10^{-10}	[212]	^{a}
IN8	$Cl_2^* + Ar^+ \rightarrow Cl + Cl^+ + Ar$	5.7×10^{-10}	[212]	^{a}
IN9	$Cl + Ar^+ \rightarrow Cl^+ + Ar$	2×10^{-10}	[208]	
IN10	$Cl + Cl^+ \rightarrow Cl^+ + Cl$	1×10^{-9}	[208]	
IN11	$Ar + Ar^+ \rightarrow Ar^+ + Ar$	5.7×10^{-10}	[208]	

Table A.4: Neutral-neutral reactions. $^a n = 0, 1, 2, 3$.

No.	Reaction	Rate	Ref.	Note
NN1	$Ar^* \rightarrow Ar$	1×10^5	[151]	
NN2	$Ar^{**} \rightarrow Ar$	1×10^5	[151]	
NN3	$Cl^* \rightarrow Cl$	1×10^5	[152]	
NN4	$Ar + Ar^* \rightarrow Ar + Ar$	2.1×10^{-15}	[151]	
NN5	$Ar + Ar^{**} \rightarrow Ar + Ar$	2.1×10^{-15}	[151]	
NN6	$Ar^{**} + Ar^{**} \rightarrow Ar^+ + Ar + e^-$	5×10^{-10}	[255]	
NN7	$Ar^* + Ar^{**} \rightarrow Ar^+ + Ar + e^-$	1.2×10^{-9}		
NN8	$Ar^* + Ar^* \rightarrow Ar^+ + Ar + e^-$	1×10^{-10}	[255]	
NN9	$Ar^* + Cl \rightarrow Cl^* + Ar$	1.8×10^{-11}	[213]	
NN10	$Ar^{**} + Cl \rightarrow Cl^* + Ar$	1.8×10^{-11}	[213]	
NN11	$Ar^* + Cl_2(v = n) \rightarrow Ar + Cl_2^+ + e^-$	2.2×10^{-10}	[213]	^{a}
NN12	$Ar^* + Cl_2(v = n) \rightarrow Ar + Cl^* + Cl$	1.1×10^{-10}	[213]	^{a}
NN13	$Ar^* + Cl_2(v = n) \rightarrow Ar + Cl_2^*$	1.8×10^{-11}	[213]	^{a}
NN14	$Ar^* + Cl_2^* \rightarrow Ar + Cl_2^+ + e^-$	2.2×10^{-10}	[213]	^{a}
NN15	$Ar^* + Cl_2(v = n) \rightarrow Ar + Cl^* + Cl$	1.1×10^{-10}	[213]	^{a}
NN16	$Ar^{**} + Cl_2(v = n) \rightarrow Ar + Cl_2^+ + e^-$	2.2×10^{-10}	[213]	^{a}
NN17	$Ar^{**} + Cl_2(v = n) \rightarrow Ar + Cl^* + Cl$	1.1×10^{-10}	[213]	^{a}
NN18	$Ar^{**} + Cl_2(v = n) \rightarrow Ar + Cl_2^*$	1.8×10^{-11}	[213]	^{a}
NN19	$Ar^{**} + Cl_2^* \rightarrow Ar + Cl_2^+ + e^-$	2.2×10^{-10}	[213]	^{a}

NN20	$Ar^{**} + Cl_2(v = n) \rightarrow Ar + Cl^* + Cl$	1.1×10^{-10}	[213]	^{a}
NN21	$Cl^* + Ar \rightarrow Cl + Ar$	1.1×10^{-12}	[215]	
NN22	$Cl^* + Cl_2 \rightarrow Cl + Cl_2$	4.5×10^{-11}	[214]	
NN23	$Cl + Cl_2(v = 1) \rightarrow Cl + Cl_2$	1.2×10^{-12}	Nina's thesis	
NN24	$Cl + Cl_2(v = 2) \rightarrow Cl + Cl_2(v = 1)$	1.2×10^{-11}	[216]	
NN25	$Cl + Cl_2(v = 3) \rightarrow Cl + Cl_2(v = 1)$	6.4×10^{-12}	[216]	
NN26	$Cl + Cl_2(v = 3) \rightarrow Cl + Cl_2(v = 2)$	1.4×10^{-11}	[216]	
NN27	$Cl_2 + Cl_2(v = 1) \rightarrow Cl_2 + Cl_2$	5.9×10^{-15}	[216]	
NN28	$Cl_2 + Cl_2(v = 2) \rightarrow Cl_2 + Cl_2(v = 1)$	1.17×10^{-14}	[216]	
NN29	$Cl_2 + Cl_2(v = 3) \rightarrow Cl_2 + Cl_2(v = 2)$	1.75×10^{-14}	[216]	
NN30	$Cl_2^* + Cl \rightarrow Cl_2 + Cl^*$	1×10^{-10}	*est.*	
NN31	$Cl_2^* + Cl_2^* \rightarrow Cl_2 + 2Cl$	1×10^{-10}	*est.*	
NN32	$Cl_2(v = n) + Cl_2^* \rightarrow Cl_2 + 2Cl$	1×10^{-10}	*est.*	^{a}
NN33	$Cl_2^* + Cl_2^* \rightarrow Cl_2^+ + Cl_2 + e^-$	1×10^{-10}	*est.*	
NN34	$Cl_2^* + Cl_2^* \rightarrow Cl_2 + Cl^* + Cl$	1×10^{-10}	*est.*	
NN35	$Ar + Cl + Cl \rightarrow Ar + Cl_2$	1.28×10^{-32}	[208]	
NN36	$Cl + Cl + Cl \rightarrow Cl + Cl_2$	1.28×10^{-32}	[208]	
NN37	$Cl_2(v = n) + Cl + Cl \rightarrow Cl_2 + Cl_2$	5.4×10^{-32}	[208]	^{a}
NN38	$Ar^* + Ar + Ar \rightarrow Ar + Ar + Ar$	1.1×10^{-32}	[151]	
NN39	$Ar^* * + Ar + Ar \rightarrow Ar + Ar + Ar$	1.1×10^{-32}	[151]	

Appendix B

PTR-MS concentration

The proton transfer reaction for the single compound R with rate k is

$H_3O^+ + R \xrightarrow{k} H_2O + RH^+$

however a gas sample may contain several compounds R_i with concentrations $[R_i]$. To calculate the total rate of change of $[H_3O^+]$ from the exit of the ion source to the end of the drift tube we can use the equation;

$$-\frac{d[H_3O^+]}{dt} = [H_3O^+]\sum_i [R_i]k_i \tag{B.1}$$

By integrating eq. (B.1) assuming $\sum_i [R_i]$ is constant on the timescale through the drift tube (between $t = 0$ and $t = t$), we can derive expressions for $\sum_i [R_i]k_i$ and $[H_3O^+]_t$,

$$\int_0^{\Delta t} \frac{1}{[H_3O^+]} d[H_3O^+] = -\sum_i [R_i]k_i \int_0^t dt$$

$$\ln[H_3O^+]_t - \ln[H_3O^+]_0 = -t\sum_i [R_i]k_i$$

$$\sum_i [R_i]k_i = -\frac{1}{t}\ln\left(\frac{[H_3O^+]_t}{[H_3O^+]_0}\right) \tag{B.2}$$

$$[H_3O^+]_t = [H_3O^+]_0 \exp\left(-t\sum_i [R_i]k_i\right) \tag{B.3}$$

We also assume that the loss of $[H_3O^+]$ is through reaction with $\sum_i[R_i]$, i.e.

$$\sum_i [R_i H^+] = [H_3O^+]_0 - [H_3O^+]_t \tag{B.4}$$

substituting in $[H_3O^+]_t$ from eq. (B.3)

$$\sum_i [R_i H^+] = [H_3O^+]_0 \left(1 - \exp\left(-t \sum_i [R_i] k_i\right)\right) \tag{B.5}$$

The rate equation for a single compound R_a is

$$\frac{d[R_a H^+]}{dt} = k_a [R_a][H_3O^+]_t \tag{B.6}$$

substituting in $[H_3O^+]_t$ from eq. (B.3) into eq. (B.6),

$$\frac{d[R_a H^+]}{dt} = k_a [R_a][H_3O^+]_0 \exp\left(-t \sum_i [R_i] k_i\right) \tag{B.7}$$

after integrating eq. (B.7),

$$[R_a H^+] = \frac{k_a [R_a]}{\sum_i [R_i] k_i} [H_3O^+]_0 \left(1 - \exp\left(-t \sum_i [R_i] k_i\right)\right) \tag{B.8}$$

substituting in $\sum_i [R_i] k_i$ from eq. (B.2) into eq. (B.8),

$$[R_a H^+] = -\frac{k_a t [R_a][H_3O^+]_0}{\ln([H_3O^+]_t / [H_3O^+]_0)} \left(1 - \exp\left(-t \sum_i [R_i] k_i\right)\right) \tag{B.9}$$

substituting in $[H_3O^+]_0 \left(1 - \exp\left(-t \sum_i [R_i] k_i\right)\right)$ from eq. (B.5) and rearranging for $[R_a]$,

$$[R_a] = \frac{[R_a H^+]}{\sum_i [R_i H^+]} \frac{1}{k_a t} \ln\left(\frac{[H_3O]_0}{[H_3O]_t}\right) \tag{B.10}$$

substituting for $[H_3O]_0$ from eq. (B.4),

$$[R_a] = \frac{[R_a H^+]}{\sum_i [R_i H^+]} \frac{1}{k_a t} \ln\left(1 + \frac{\sum_i [R_i H^+]}{[H_3O]_t}\right) \tag{B.11}$$

The natural logarithm can be approximated using the Maclaurin series, i.e. $\ln(1+x) = x - \frac{x^2}{2} + \frac{x^3}{3} + ...$ for $|x| < 1$. Because $\frac{\sum_i [R_i H^+]}{[H_3O]_t} \ll 1$ the non-linear terms are neglected, thus eq. (B.11) can be simplified to

$$[R_a] = \frac{1}{k_a t} \frac{[R_a H^+]}{[H_3O]_t}$$

Concentration $[x]$ is directly proportional to raw signal $i(x)$ by the transmission efficiency T_x, i.e. $i(x) = [x]T_x$. Also to calculate the volume mixing ratio in ppbv, 10^9 is divided by N the number of particles in the drift tube;

$$[R_a] = \frac{1}{k_a t} \frac{i(R_a H^+)}{i(H_3O_t)} \frac{T_{H_3O_t}}{T_{R_a H^+}} \frac{10^9}{N} \tag{B.12}$$

N is calculated using

$$N = \frac{N_A}{V_m} \frac{T_0 p_d}{T_d p_0} \tag{B.13}$$

where $N_A = 6.022 \times 10^{23}$ mol^{-1} and $V_m = 22414$ cm^3/mol is the Avogadro constant and molar volume of gas at STP, i.e. $T_0 = 273.15$ K and $p_0 = 1013.25$ mbar respectively. T_d and p_d is the temperature and pressure in the drift tube respectively.

The reaction time t is calculated using

$$t = l/v_d$$

where l and v_d is the drift tube length (9.3 cm) and ion drift velocity respectively. The ion drift velocity can be calculated using

$$v_d = \mu \times E = \mu \times \frac{U_d}{l}$$

where μ is the ion mobility, E is the electric field across the drift tube and U_{drift} is the potential across the drift tube. The ion mobility can be calculated by

$$\mu = \mu_0 \times \frac{T_d}{T_0} \times \frac{p_0}{p_d}$$

where the reduced mobility, $\mu_0 = 2.8$ cm^2/Vs [256]. Thus the reaction time can be calculated using

$$t = \frac{l^2}{\mu_0 U_d} \frac{T_0 p_d}{T_d p_0} \tag{B.14}$$

After substituting eqs. (B.13) and (B.14) into eq. (B.12),

$$[R_a](\text{ppbv}) = \frac{10^9}{k_a} \frac{i(R_a H^+)}{i(H_3O_t)} \frac{T_{H_3O_t}}{T_{R_a H^+}} \frac{\mu_0 U_d}{l^2} \frac{T_d^2 p_0^2}{T_0^2 p_d^2} \frac{V_m}{N_A}$$

List of References

[1] I. Adamovich, S. D. Baalrud, A. Bogaerts, P. J. Bruggeman, M. Cappelli, V. Colombo, U. Czarnetzki, U. Ebert, J. G. Eden, P. Favia, D. B. Graves, S. Hamaguchi, G. Hieftje, M. Hori, I. D. Kaganovich, U. Kortshagen, M. J. Kushner, N. J. Mason, S. Mazouffre, S. Mededovic Thagard, H.-R. Metelmann, A. Mizuno, E. Moreau, A. B. Murphy, B. A. Niemira, G. S. Oehrlein, Z. Lj. Petrovic, L. C. Pitchford, Y.-K. Pu, S. Rauf, O. Sakai, S. Samukawa, S. Starikovskaia, J. Tennyson, K. Terashima, M. M. Turner, M. C. M. van de Sanden, and A. Vardelle. The 2017 Plasma Roadmap: Low temperature plasma science and technology. *Journal of Physics D: Applied Physics*, 50(32):323001, 2017.

[2] Y. Gorbanev, D. O'Connell, and V. Chechik. Non-Thermal Plasma in Contact with Water: The Origin of Species. *Chemistry–A European Journal*, 22(10):3496, 2016.

[3] S. Schröter, A. Wijaikhum, A. R. Gibson, A. West, H. L. Davies, N. Minesi, J. Dedrick, E. Wagenaars, N. De Oliveira, L. Nahon, M. J. Kushner, J.-P. Booth, K. Niemi, T. Gans, and D. O'Connell. Chemical kinetics in an atmospheric pressure helium plasma containing humidity. *Physical Chemistry Chemical Physics*, 20(37):24263, 2018.

[4] G. S. Oehrlein, D. Metzler, and C. Li. Atomic Layer Etching at the Tipping Point: An Overview. *ECS Journal of Solid State Science and Technology*, 4(6):N5041, 2015.

[5] E. W. McDaniel and W. L. Nighan. *Gas Lasers: Applied Atomic Collision Physics*, volume 3. Academic Press, 2017.

[6] A. K. Baker, C. Sauvage, U. R. Thorenz, P. Van Velthoven, D. E. Oram, A. Zahn, C. A. M. Brenninkmeijer, and J. Williams. Evidence for strong, widespread chlorine radical chemistry associated with pollution outflow from continental Asia. *Scientific Reports*, 6(1):1, 2016.

[7] B. J. Finlayson-Pitts. The Tropospheric Chemistry of Sea Salt: A Molecular-Level View of the Chemistry of NaCl and NaBr. *Chemical Reviews*, 103(12):4801, 2003.

[8] R. Atkinson, D. L. Baulch, R. A. Cox, R. F. Hampson Jr, J. A. Kerr, M. J. Rossi, and J. Troe. Evaluated Kinetic and Photochemical Data for Atmospheric Chemistry: Supplement VIII, Halogen Species Evaluation for Atmospheric Chemistry. *Journal of Physical and Chemical Reference Data*, 29(2):167, 2000.

[9] S. P. Sander, R. R. Friedl, J. R. Barker, D. M. Golden, M. J. Kurylo, P. H. Wine, J. Abbatt, J. B. Burkholder, C. E. Kolb, G. K. Moortgat, and R. E. Huie. Chemical Kinetics and Photochemical Data for Use in Atmospheric Studies, Evaluation Number 14. *JPL Publication*, 2003.

[10] J. Stutz, R. Ackermann, J. D. Fast, and L. Barrie. Atmospheric reactive chlorine and bromine at the Great Salt Lake, Utah. *Geophysical Research Letters*, 29(10):18, 2002.

[11] A. A. P. Pszenny, E. V. Fischer, R. S. Russo, B. C. Sive, and R. K. Varner. Estimates of Cl atom concentrations and hydrocarbon kinetic reactivity in surface air at Appledore Island, Maine (USA), during International Consortium for Atmospheric Research on Transport and Transformation/Chemistry of Halogens at the Isles of Shoals. *Journal of Geophysical Research: Atmospheres*, 112(D10), 2007.

[12] C. B. Faxon and D. T. Allen. Chlorine chemistry in urban atmospheres: a review. *Environmental Chemistry*, 10(3):221, 2013.

[13] J. A. Thornton, J. P. Kercher, T. P. Riedel, N. L. Wagner, J. Cozic, J. S. Holloway, W. P. Dubé, G. M. Wolfe, P. K. Quinn, A. M. Middlebrook, B. Alexander, and S. S. Brown. A large atomic chlorine source inferred from mid-continental reactive nitrogen chemistry. *Nature*, 464(7286):271, 2010.

[14] Ø. Svanes, R. J. Bertelsen, S. H. L. Lygre, A. E. Carsin, J. M. Antó, B. Forsberg, J. M. García-García, J. A. Gullón, J. Heinrich, M. Holm, M. Kogevinas, I. Urrutia, B. Leynaert, J. M. Moratalla, N. L. Moual, T. Lytras, D. Norbäck, D. Nowak, M. Olivieri, I. Pin, N. Probst-Hensch, V. Schlünssen, T. Sigsgaard, T. D. Skorge, S. Villani, D. Jarvis, J. P. Zock, and C. Svanes. Cleaning at home and at work in relation to lung function decline and airway obstruction. *American Journal of Respiratory and Critical Care Medicine*, 197(9):1157, 2018.

[15] V. Sinha, J. Williams, J. N. Crowley, and J. Lelieveld. The Comparative Reactivity Method - a new tool to measure total OH Reactivity in ambient air. *Atmospheric Chemistry and Physics*, 8(8):2213, 2008.

[16] J. T. Shaw. *Multivariate relative rate measurements of reactions between volatile organic compounds (VOCs) and atmospheric radicals.* Ph.D. thesis, University of York, 2018.

[17] M. V. Malyshev and V. M. Donnelly. Diagnostics of inductively coupled chlorine plasmas: Measurement of Cl_2 and Cl number densities. *Journal of Applied Physics*, 88(11):6207, 2000.

[18] D. Marinov, M. Foucher, E. Campbell, M. Brouard, P. Chabert, and J.-P. Booth. High sensitivity ultra-broad-band absorption spectroscopy of inductively coupled chlorine plasma. *Plasma Sources Science and Technology*, 25(3):035019, 2016.

[19] F. Neuilly, J.-P. Booth, and L. Vallier. Chlorine dissociation fraction in an inductively coupled plasma measured by ultraviolet absorption spectroscopy. *Journal of Vacuum Science & Technology A: Vacuum, Surfaces, and Films*, 20(1):225, 2002.

[20] N. C. M. Fuller, I. P. Herman, and V. M. Donnelly. Optical actinometry of Cl_2, Cl, Cl^+, and Ar^+ densities in inductively coupled Cl_2–Ar plasmas. *Journal of Applied Physics*, 90(7):3182, 2001.

[21] C. S. Corr, E. Despiau-Pujo, P. Chabert, W. G. Graham, F. G. Marro, and D. B. Graves. Comparison between fluid simulations and experiments in inductively coupled argon/chlorine plasmas. *Journal of Physics D: Applied Physics*, 41(18):185202, 2008.

[22] S. Ashida and M. A. Lieberman. Spatially Averaged (Global) Model of Time Modulated High Density Chlorine Plasmas. *Japanese Journal of Applied Physics*, 36(2R):854, 1997.

[23] G. S. Selwyn, L. D. Baston, and H. H. Sawin. Detection of Cl and chlorine-containing negative ions in rf plasmas by two-photon laser-induced fluorescence. *Applied Physics Letters*, 51(12):898, 1987.

[24] F. G. Marro and W. G. Graham. Atomic chlorine two-photon LIF characterization in a Cl_2 ICP plasma. *Plasma Sources Science and Technology*, 17(1):015007, 2007.

[25] J. P. Booth, Y. Azamoum, N. Sirse, and P. Chabert. Absolute atomic chlorine densities in a Cl_2 inductively coupled plasma determined by two-photon laser-induced fluorescence with a new calibration method. *Journal of Physics D: Applied Physics*, 45(19):195201, 2012.

[26] N. Sirse, J.-P. Booth, P. Chabert, A. Surzhykov, and P. Indelicato. Chlorine atom densities in the excited spin–orbit state measured by two-photon absorption laser-induced fluorescence in a chlorine inductively coupled plasma. *Journal of Physics D: Applied Physics*, 46(29):295203, 2013.

[27] C. S. Corr, P. G. Steen, and W. G. Graham. Temporal phenomena in inductively coupled chlorine and argon–chlorine discharges. *Applied Physics Letters*, 86(14):141503, 2005.

[28] F. Soberón, F. G. Marro, W. G. Graham, A. R. Ellingboe, and V. J. Law. Chlorine plasma system instabilities within an ICP tool driven at a frequency of 13.56 MHz. *Plasma Sources Science and Technology*, 15(2):193, 2006.

[29] E. Despiau-Pujo and P. Chabert. Global model of instabilities in low-pressure inductive chlorine discharges. *Plasma Sources Science and Technology*, 18(4):045028, 2009.

[30] C. S. Corr, P. G. Steen, and W. G. Graham. Instabilities in an inductively coupled oxygen plasma. *Plasma Sources Science and Technology*, 12(2):265, 2003.

[31] M. A. Lieberman, A. J. Lichtenberg, and A. M. Marakhtanov. Instabilities in low-pressure inductive discharges with attaching gases. *Applied Physics Letters*, 75(23):3617, 1999.

[32] F. F. Chen. *Introduction to Plasma Physics and Controlled Fusion*, volume 1. Springer, 1984.

[33] T. J. Boyd, T. J. M. Boyd, and J. J. Sanderson. *The Physics of Plasmas*. Cambridge University Press, 2003.

[34] Y. P. Raizer and J. E. Allen. *Gas discharge physics*, volume 2. Springer Berlin, 1997.

[35] J. Waskoenig, K. Niemi, N. Knake, L. M. Graham, S. Reuter, V. Schulz-Von Der Gathen, and T. Gans. Atomic oxygen formation in a radio-frequency driven micro-atmospheric pressure plasma jet. *Plasma Sources Science and Technology*, 19(4):045018, 2010.

[36] J. Golda, F. Kogelheide, P. Awakowicz, and V. Schulz-von der Gathen. Dissipated electrical power and electron density in an RF atmospheric pressure helium plasma jet. *Plasma Sources Science and Technology*, 28(9):095023, 2019.

[37] R. Massarczyk, P. Chu, C. Dugger, S. R. Elliott, K. Rielage, and W. Xu. Paschen's law studies in cold gases. *Journal of Instrumentation*, 12(06):P06019, 2017.

[38] G. J. M. Hagelaar and L. C. Pitchford. Solving the Boltzmann equation to obtain electron transport coefficients and rate coefficients for fluid models. *Plasma Sources Science and Technology*, 14(4):722, 2005.

[39] J. T. Gudmundsson. On the effect of the electron energy distribution on the plasma parameters of an argon discharge: a global (volume-averaged) model study. *Plasma Sources Science and Technology*, 10(1):76, 2001.

[40] J. T. Gudmundsson, A. T. Hjartarson, and E. G. Thorsteinsson. The influence of the electron energy distribution on the low pressure chlorine discharge. *Vacuum*, 86(7):808, 2012.

[41] R. Basner and K. Becker. Experimental absolute electron impact ionization cross-sections of Cl_2. *New Journal of Physics*, 6(1):118, 2004.

[42] Z. Lj. Petrović, S. Dujko, D. Marić, G. Malović, v. Nikitović, O. Šašić, J. Jovanović, V. Stojanović, and M. Radmilović-Rađenović. Measurement and interpretation of swarm parameters and their application in plasma modelling. *Journal of Physics D: Applied Physics*, 42(19):194002, 2009.

[43] J. Luque and D. R. Crosley. LIFBASE: Database and spectral simulation program (version 1.5). *SRI international report MP*, 99(009), 1999.

[44] A. M. Holloway and R. P. Wayne. *Atmospheric chemistry*. Royal Society of Chemistry, 2010.

[45] J. B. Burkholder, J. P. D. Abbatt, I. Barnes, J. M. Roberts, M. L. Melamed, M. Ammann, A. K. Bertram, C. D. Cappa, A. G. Carlton, L. J. Carpenter, J. N. Crowley, Y. Dubowski, C. George, D. E. Heard, H. Herrmann, F. N. Keutsch, J. H. Kroll, V. F. McNeill, N. L. Ng, S. A. Nizkorodov, J. J. Orlando, C. J. Percival, B. Picquet-Varrault, Y. Rudich, P. W. Seakins, J. D. Surratt, H. Tanimoto, J. A. Thornton, Z. Tong, G. S. Tyndall, A. Wahner, C. J. Weschler, K. R. Wilson, and P. J. Ziemann. The Essential Role for Laboratory Studies in Atmospheric Chemistry. *Environmental Science and Technology*, 2017.

[46] United States National Oceanic and Atmospheric Administration and United States Air Force. *US standard atmosphere, 1976*, volume 76. National Oceanic and Atmospheric Administration, 1976.

[47] P. Muller. Glossary of terms used in physical organic chemistry (IUPAC Recommendations 1994). *Pure and Applied Chemistry*, 66(5):1077, 1994.

[48] R. Atkinson, J. Arey, and S. M. Aschmann. Atmospheric chemistry of alkanes: Review and recent developments. *Atmospheric Environment*, 42(23):5859, 2008.

[49] M. E. Jenkin, S. M. Saunders, and M. J. Pilling. The tropospheric degradation of volatile organic compounds: a protocol for mechanism development. *Atmospheric Environment*, 31(1):81, 1997.

[50] S. M. Saunders, M. E. Jenkin, R. G. Derwent, and M. J. Pilling. Protocol for the development of the Master Chemical Mechanism, MCM v3 (Part A): tropospheric degradation of non-aromatic volatile organic compounds. *Atmospheric Chemistry and Physics*, 3(1):161, 2003.

[51] National Research Council. *The Atmospheric Sciences: Entering the Twenty-First Century*. National Academies Press, 1998.

[52] P. Bousquet, P. Ciais, J. B. Miller, E. J. Dlugokencky, D. A. Hauglustaine, C. Prigent, G. R. Van der Werf, P. Peylin, E.-G. Brunke, C. Carouge, R. L. Langenfelds, J. Lathiére, F. Papa, M. Ramonet, M. Schmidt, L. P. Steele, S. C. Tyler, and J. White. Contribution of anthropogenic and natural sources to atmospheric methane variability. *Nature*, 443(7110):439, 2006.

[53] R. Watson, G. Machado, S. Fischer, and D. D. Davis. A temperature dependence kinetics study of the reactions of $Cl(^2P_{3/2})$ with O_3, CH_4, and H_2O_2. *The Journal of Chemical Physics*, 65(6):2126, 1976.

[54] A. R. Ravishankara and P. H. Wine. A laser flash photolysis-resonance fluorescence kinetics study of the reaction $Cl(^2P) + CH_4 \rightarrow CH_3 + HCl$. *The Journal of Chemical Physics*, 72(1):25, 1980.

[55] R. G. Manning and M. J. Kurylo. Flash Photolysis Resonance Fluorescence Investigation of the Temperature Dependencies of the Reactions of $Cl(^2P)$ Atoms with CH_4, CH_3Cl, CH_3F, CH_3F^*, and C_2H_6. *The Journal of Physical Chemistry*, 81(4):291, 1977.

[56] J. J. Wang and L. F. Keyser. Kinetics of the Cl (^2P_J) + CH_4 Reaction: Effects of Secondary Chemistry below 300 K. *The Journal of Physical Chemistry A*, 103(37):7460, 1999.

[57] G. L. Vaghjiani and A. R. Ravishankara. New measurement of the rate coefficient for the reaction of OH with methane. *Nature*, 350(6317):406, 1991.

[58] B. J. Finlayson-Pitts, M. J. Ezell, T. M. Jayaweera, H. N. Berko, and C. C. Lai. Kinetics of the reactions of OH with methyl chloroform and methane: Implications for global tropospheric OH and the methane budget. *Geophysical Research Letters*, 19(13):1371, 1992.

[59] T. Gierczak, R. K. Talukdar, S. C. Herndon, G. L. Vaghjiani, and A. R. Ravishankara. Rate Coefficients for the Reactions of Hydroxyl Radicals with Methane and Deuterated Methanes. *The Journal of Physical Chemistry A*, 101(17):3125, 1997.

[60] J. Lelieveld, S. Gromov, A. Pozzer, and D. Taraborrelli. Global tropospheric hydroxyl distribution, budget and reactivity. *Atmospheric Chemistry and Physics*, 16(19):12477, 2016.

[61] J. V. Michael and J. H. Lee. Selected rate constants for H, O, N, and Cl atoms with substrates at room temperatures. *Chemical Physics Letters*, 51(2):303, 1977.

[62] P. Beichert, L. Wingen, J. Lee, R. Vogt, M. J. Ezell, M. Ragains, R. Neavyn, and B. J. Finlayson-Pitts. Rate Constants for the Reactions of Chlorine Atoms with Some Simple Alkanes at 298 K: Measurement of a Self-Consistent Set Using Both Absolute and Relative Rate Methods. *The Journal of Physical Chemistry*, 99(35):13156, 1995.

[63] R. S. Lewis, S. P. Sander, S. Wagner, and R. T. Watson. Temperature-dependent rate constants for the reaction of ground-state chlorine with simple alkanes. *The Journal of Physical Chemistry*, 84(16):2009, 1980.

[64] A. Mellouki. Kinetic studies of Cl atom reactions with series of alkanes using the pulsed laser photolysis-resonance fluorescence method. *Journal de Chimie Physique et de Physico-Chimie Biologique*, 95(3):513, 1998.

[65] Y. Matsumi, K. Izumi, V. Skorokhodov, M. Kawasaki, and N. Tanaka. Reaction and Quenching of $Cl(^2P_J)$ Atoms in Collisions with Methane and Deuterated Methanes. *The Journal of Physical Chemistry A*, 101(7):1216, 1997.

[66] E. W. Kaiser and T. J. Wallington. Kinetics of the Reactions of Chlorine Atoms with C_2H_4 (k_1) and C_2H_2 (k_2): A Determination of $\Delta H_{f,298}$ for C_2H_3. *The Journal of Physical Chemistry*, 100(10):4111, 1996.

[67] R. T. Watson. Rate constants for reactions of ClO_x of atmospheric interest. *Journal of Physical and Chemical Reference Data*, 6(3):871, 1977.

[68] H.-P. Dorn, U. Brandenburger, T. Brauers, and M. Hausmann. A New In Situ Laser Long-Path Absorption Instrument for the Measurement of Tropospheric OH Radicals. *Journal of the Atmospheric Sciences*, 52(19):3373, 1995.

[69] D. Pöhler, L. Vogel, U. Frieß, and U. Platt. Observation of halogen species in the Amundsen Gulf, Arctic, by active long-path differential optical absorption spectroscopy. *Proceedings of the National Academy of Sciences*, 107(15):6582, 2010.

[70] T. M. Hard, R. J. O'Brien, C. Y. Chan, and A. A. Mehrabzadeh. Tropospheric Free Radical Determination by Fluorescence Assay with Gas Expansion. *Environmental Science & Technology*, 18(10):768, 1984.

[71] D. E. Heard. Atmospheric Field Measurements of the Hydroxyl Radical using Laser-Induced Fluorescence Spectroscopy. *Annual Review of Physical Chemistry*, 57:191, 2006.

[72] D. Creasey, P. Halford-Maw, D. Heard, M. Pilling, and B. Whitaker. Implementation and initial deployment of a field instrument for measurement of OH and HO_2 in the troposphere by laser-induced fluorescence. *Journal of the Chemical Society, Faraday Transactions*, 93(16):2907, 1997.

[73] I. C. Faloona, D. Tan, R. L. Lesher, N. L. Hazen, C. L. Frame, J. B. Simpas, H. Harder, M. Martinez, P. Di Carlo, X. Ren, and W. H. Brune. A Laser-induced Fluorescence Instrument for Detecting Tropospheric OH and HO_2: Characteristics and Calibration. *Journal of Atmospheric Chemistry*, 47(2):139, 2004.

[74] S. Dusanter, D. Vimal, and P. S. Stevens. Measuring tropospheric OH and HO_2 by laser-induced fluorescence at low pressure. A comparison of calibration techniques. *Atmospheric Chemistry and Physics*, 8:321, 2008.

[75] H. Berresheim, T. Elste, C. Plass-Dülmer, F. L. Eiseleb, and D. J. Tannerb. Chemical ionization mass spectrometer for long-term measurements of atmospheric OH and H_2SO_4. *International Journal of Mass Spectrometry*, 202(1-3):91, 2000.

[76] W. Lindinger, A. Hansel, and A. Jordan. On-line monitoring of volatile organic compounds at pptv levels by means of proton-transfer-reaction mass spectrometry (PTR-MS) medical applications, food control and environmental research. *International Journal of Mass Spectrometry and Ion Processes*, 173(3):191, 1998.

[77] R. Holzinger, J. Williams, F. Herrmann, J. Lelieveld, N. M. Donahue, and T. Röckmann. Aerosol analysis using a Thermal-Desorption Proton-Transfer-Reaction Mass Spectrometer (TD-PTR-MS): a new approach to study processing of organic aerosols. *Atmospheric Chemistry and Physics*, 10(5):2257, 2010.

[78] M. Graus, M. Müller, and A. Hansel. High Resolution PTR-TOF: Quantification and Formula Confirmation of VOC in Real Time. *Journal of the American Society for Mass Spectrometry*, 21(6):1037, 2010.

[79] D. Smith and P. Španěl. Selected ion flow tube mass spectrometry (SIFT-MS) for on-line trace gas analysis. *Mass Spectrometry Reviews*, 24(5):661, 2005.

[80] F. Brilli, B. Gioli, P. Ciccioli, D. Zona, F. Loreto, I. A. Janssens, and R. Ceulemans. Proton Transfer Reaction Time-of-Flight Mass Spectrometric (PTR-TOF-MS) determination of volatile organic compounds (VOCs) emitted from a biomass fire developed under stable nocturnal conditions. *Atmospheric Environment*, 97:54, 2014.

[81] P. R. Veres, P. Faber, F. Drewnick, J. Lelieveld, and J. Williams. Anthropogenic sources of VOC in a football stadium: Assessing human emissions in the atmosphere. *Atmospheric Environment*, 77:1052, 2013.

[82] J. Williams, C. Stönner, J. Wicker, N. Krauter, B. Derstroff, E. Bourtsoukidis, T. Klüpfel, and S. Kramer. Cinema audiences reproducibly vary the chemical composition of air during films, by broadcasting scene specific emissions on breath. *Scientific Reports*, 6:25464, 2016.

[83] J. A. de Gouw, P. D. Goldan, C. Warneke, W. C. Kuster, J. M. Roberts, M. Marchewka, S. B. Bertman, A. A. P. Pszenny, and W. C. Keene. Validation of proton transfer reaction-mass spectrometry (PTR-MS) measurements of gas-phase organic compounds in the atmosphere during the New England Air Quality Study (NEAQS) in 2002. *Journal of Geophysical Research: Atmospheres*, 108(D21), 2003.

[84] T. Karl, A. Guenther, R. J. Yokelson, J. Greenberg, M. Potosnak, D. R. Blake, and P. Artaxo. The tropical forest and fire emissions experiment: Emission, chemistry, and transport of biogenic volatile organic compounds in the lower atmosphere over Amazonia. *Journal of Geophysical Research: Atmospheres*, 112(D18), 2007.

[85] V. Sinha, V. Kumar, and C. Sarkar. Chemical composition of pre-monsoon air in the Indo-Gangetic Plain measured using a new air quality facility and PTR-MS: high surface ozone and strong influence of biomass burning. *Atmospheric Chemistry and Physics*, 14(12):5921, 2014.

[86] R. S. Blake, P. S. Monks, and A. M. Ellis. Proton-Transfer Reaction Mass Spectrometry. *Chemical Reviews*, 109(3):861, 2009.

[87] D. J. Creasey, G. E. Evans, D. E. Heard, and J. D. Lee. Measurements of OH and HO_2 concentrations in the Southern Ocean marine boundary layer. *Journal of Geophysical Research: Atmospheres*, 108(D15), 2003.

[88] R. Sommariva, A.-L. Haggerstone, L. J. Carpenter, N. Carslaw, D. J. Creasey, D. E. Heard, J. D. Lee, A. C. Lewis, M. J. Pilling, and J. Zádor. OH and HO_2 chemistry in clean marine air during SOAPEX-2. *Atmospheric Chemistry and Physics Discussions*, 2004.

[89] D. E. Heard, L. J. Carpenter, D. J. Creasey, J. R. Hopkins, J. D. Lee, A. C. Lewis, M. J. Pilling, P. W. Seakins, N. Carslaw, and K. M. Emmerson. High levels of the hydroxyl radical in the winter urban troposphere. *Geophysical Research Letters*, 31(18), 2004.

[90] I. Bey, D. J. Jacob, R. M. Yantosca, J. A. Logan, B. D. Field, A. M. Fiore, Q. Li, H. Y. Liu, L. J. Mickley, and M. G. Schultz. Global modeling of tropospheric chemistry with assimilated meteorology: Model description and evaluation. *Journal of Geophysical Research: Atmospheres*, 106(D19):23073, 2001.

[91] J. A. Logan, M. J. Prather, S. C. Wofsy, and M. B. McElroy. Tropospheric chemistry: A global perspective. *Journal of Geophysical Research: Oceans*, 86(C8):7210, 1981.

[92] C. Dolgorouky, V. Gros, R. Sarda-Esteve, V. Sinha, J. Williams, N. Marchand, S. Sauvage, L. Poulain, J. Sciare, and B. Bonsang. Total OH reactivity measurements in Paris during the 2010 MEGAPOLI winter campaign. *Atmospheric Chemistry and Physics*, 12(20):9593, 2012.

[93] V. Sinha, J. Williams, J. Lelieveld, T. M. Ruuskanen, M. K. Kajos, J. Patokoski, H. Hellen, H. Hakola, D. Mogensen, M. Boy, and J. Rinne. OH Reactivity Measurements within a Boreal Forest: Evidence for Unknown Reactive Emissions. *Environmental Science and Technology*, 44(17):6614, 2010.

[94] V. Sinha, J. Williams, J. M. Diesch, F. Drewnick, M. Martinez, H. Harder, E. Regelin, D. Kubistin, H. Bozem, Hosaynali-Beygi, Z. H. Fischer, M. D. Andres-Hernandez, D. Kartal, J. A. Adame, and J. Lelieveld. Constraints on instantaneous ozone production rates and regimes during DOMINO derived using in-situ OH reactivity measurements. *Atmospheric Chemistry and Physics*, 12(15):7269, 2012.

[95] D. J. Creasey, D. E. Heard, and J. D. Lee. OH and HO_2 measurements in a forested region of north-western Greece. *Atmospheric Environment*, 35(27):4713, 2001.

[96] A. Hofzumahaus, U. Aschmutat, M. Hessling, F. Holland, and D. H. Ehhalt. The measurement of tropospheric OH radicals by laser-induced fluorescence spectroscopy during the POPCORN field campaign. *Geophysical Research Letters*, 23(18):2541, 1996.

[97] S. Dusanter, D. Vimal, P. S. Stevens, R. Volkamer, and L. T. Molina. Measurements of OH and HO_2 concentrations during the MCMA-2006 field campaign-Part 1: Deployment of the Indiana University laser-induced fluorescence. *Atmospheric Chemistry and Physics*, 9:1665, 2009.

[98] W. H. Brune, P. S. Stevens, and J. H. Mather. Measuring OH and HO_2 in the Troposphere by Laser-Induced Fluorescence at Low Pressure. *Journal of the Atmospheric Sciences*, 52(19):3328, 1995.

[99] R. Atkinson and J. Arey. Atmospheric Degradation of Volatile Organic Compounds. *Chemical Reviews*, 103(12):4605, 2003.

[100] R. Atkinson. Kinetics and Mechanisms of the Gas-Phase Reactions of the Hydroxyl Radical with Organic Compounds under Atmospheric Conditions. *Chemical Reviews*, 86(1):69, 1986.

[101] R. Atkinson, D. L. Baulch, R. A. Cox, J. N. Crowley, R. F. Hampson, R. G. Hynes, M. E. Jenkin, M. J. Rossi, and J. Troe. Evaluated kinetic and photochemical data for atmospheric chemistry: Volume II – gas phase reactions of organic species. *Atmospheric Chemistry and Physics*, 6(11):3625, 2006.

[102] S. Kim, D. Sanchez, M. Wang, R. Seco, D. Jeong, S. Hughes, B. Barletta, D. R. Blake, J. Jung, D. Kim, G. Lee, M. Lee, J. Ahn, S.-D. Lee, G. Cho, M.-Y. Sung, Y.-H. Lee, D. B. Kim, Y. Kim, J.-H. Woo, D. Jo, R. Park, J.-H. Park, Y.-D. Hongg, and J.-H. Hongg. OH reactivity in urban and suburban regions in Seoul, South Korea an East Asian megacity in a rapid transition. *Faraday Discussions*, 189:231, 2016.

[103] T. A. Kovacs, W. H. Brune, H. Harder, M. Martinez, J. B. Simpas, G. J. Frost, E. Williams, T. Jobson, C. Stroud, V. Young, A. Fried, and B. Wert. Direct measurements of urban OH reactivity during Nashville SOS in summer 1999. *Journal of Environmental Monitoring*, 5(1):68, 2003.

[104] M. J. Molina and F. S. Rowland. Stratospheric sink for chlorofluoromethanes: chlorine atom-catalysed destruction of ozone. *Nature*, 249(5460):810, 1974.

[105] B. J. Finlayson-Pitts, M. J. Ezell, and J. N. Pitts. Formation of chemically active chlorine compounds by reactions of atmospheric NaCl particles with gaseous N_2O_5 and $ClONO_2$. *Nature*, 337(6204):241, 1989.

[106] J. W. Fitzgerald. Marine aerosols: A review. *Atmospheric Environment. Part A. General Topics*, 25(3-4):533, 1991.

[107] K. A. Rahn, R. D. Borys, and R. A. Duce. Tropospheric halogen gases: Inorganic and organic components. *Science*, 192(4239):549, 1976.

[108] R. J. Cicerone. Halogens in the Atmosphere. *Reviews of Geophysics*, 19(1):123, 1981.

[109] B. J. Finlayson-Pitts and J. N. Pitts. Tropospheric Air Pollution: Ozone, Airborne Toxics, Polycyclic Aromatic Hydrocarbons, and Particles. *Science*, 276(5315):1045, 1997.

[110] G. J. Phillips, M. J. Tang, J. Thieser, B. Brickwedde, G. Schuster, B. Bohn, J. Lelieveld, and J. N. Crowley. Significant concentrations of nitryl chloride observed in rural continental Europe associated with the influence of sea salt chloride and anthropogenic emissions. *Geophysical Research Letters*, 39(10), 2012.

[111] P. P. Bemand and M. A. A. Clyne. Atomic Resonance Fluorescence Spectrometry for Rate Constants of Rapid Bimolecular Reactions. Part 4. Chlorine Atom Fluorescence $4s^{2,4}$P–$3p^5$ ^{2}P. *Journal of the Chemical Society, Faraday Transactions 2: Molecular and Chemical Physics*, 71:1132, 1975.

[112] W. R. Simpson, S. S. Brown, A. Saiz-Lopez, J. A. Thornton, and R. von Glasow. Tropospheric halogen chemistry: Sources, cycling, and impacts. *Chemical Reviews*, 115(10):4035, 2015.

[113] A. West. *Optical and Electrical Diagnosis of Atmospheric Pressure Plasma Jets*. Ph.D. thesis, University of York, 2016.

[114] A. Foote. *Converting Carbon Dioxide into Value Added Chemicals via Low Temperature Atmospheric Pressure Plasmas*. Ph.D. thesis, University of York, 2018.

[115] R. Brandenburg. Dielectric barrier discharges: progress on plasma sources and on the understanding of regimes and single filaments. *Plasma Sources Science and Technology*, 26(5):053001, 2017.

[116] J. Golda, J. Held, B. Redeker, M. Konkowski, P. Beijer, A. Sobota, G. Kroesen, N. Braithwaite, S. Reuter, M. M. Turner, T. Gans, D. OConnell, and V. Schulz-von der Gathen. Concepts and characteristics of the 'COST Reference Microplasma Jet'. *Journal of Physics D: Applied Physics*, 49(8):084003, 2016.

[117] F. Riedel, J. Golda, J. Held, H. Davis, M. van der Woude, K. Niemi, T. Gans, V. Schulz-von der Gathen, and D. O'Connell. Reproducibility of 'COST reference microplasma jets'. *Plasma Sources Science and Technology*, 2020.

[118] S. Große-Kreul, S. Hübner, S. Schneider, A. von Keudell, and J. Benedikt. Methods of gas purification and effect on the ion composition in an RF atmospheric pressure plasma jet investigated by mass spectrometry. *EPJ Techniques and Instrumentation*, 3(1):6, 2016.

[119] R. F. Hansen, M. Blocquet, C. Schoemaecker, T. Léonardis, N. Locoge, C. Fittschen, B. Hanoune, P. S. Stevens, V. Sinha, and S. Dusanter. Intercomparison of the comparative reactivity method (CRM) and pump-probe technique for measuring total OH reactivity in an urban environment. *Atmospheric Measurement Techniques*, 8(10):4243, 2015.

[120] A. Hansel, A. Jordan, R. Holzinger, P. Prazeller, W. Vogel, and W. Lindinger. Proton transfer reaction mass spectrometry: on-line trace gas analysis at the ppb level. *International Journal of Mass Spectrometry and Ion Processes*, 149:609, 1995.

[121] R. Taipale, T. M. Ruuskanen, J. Rinne, M. K. Kajos, H. Hakola, T. Pohja, and M. Kulmala. Quantitative long-term measurements of VOC concentrations by PTR-MS - measurement, calibration, and volume mixing ratio calculation methods. *Atmospheric Chemistry and Physics Discussions*, 2008.

[122] J. de Gouw, C. Warneke, T. Karl, G. Eerdekens, C. van der Veen, and R. Fall. Sensitivity and specificity of atmospheric trace gas detection by proton-transfer-reaction mass spectrometry. *International Journal of Mass Spectrometry*, 223:365, 2003.

[123] B. Yuan, A. R. Koss, C. Warneke, M. Coggon, K. Sekimoto, and J. A. de Gouw. Proton-transfer-reaction mass spectrometry: applications in atmospheric sciences. *Chemical Reviews*, 117(21):13187, 2017.

[124] J. de Gouw and C. Warneke. Measurements of volatile organic compounds in the earth's atmosphere using proton-transfer-reaction mass spectrometry. *Mass Spectrometry Reviews*, 26(2):223, 2007.

[125] W. Lindinger. Reaction-Rate Constants in Steady-State Hollow-Cathode Discharges: Ar + H_2O Reactions. *Physical Review A*, 7(1):328, 1973.

[126] F. Howorka, W. Lindinger, and R. N. Varney. Reaction rate constants in steady-state hollow cathode discharges: N_2 + H_2O reactions. *The Journal of Chemical Physics*, 61(3):1180, 1974.

[127] F. Howorka, W. Lindinger, and M. Pahl. Ion sampling from the negative glow plasma in a cylindrical hollow cathode. *International Journal of Mass Spectrometry and Ion Physics*, 12(1):67, 1973.

[128] M. Steinbacher, J. Dommen, C. Ammann, C. Spirig, A. Neftel, and A. S. H. Prevot. Performance characteristics of a proton-transfer-reaction mass spectrometer (PTR-MS) derived from laboratory and field measurements. *International Journal of Mass Spectrometry*, 239(2-3):117, 2004.

[129] J. A. Neuman, L. G. Huey, T. B. Ryerson, and D. W. Fahey. Study of Inlet Materials for Sampling Atmospheric Nitric Acid. *Environmental Science & Technology*, 33(7):1133, 1999.

[130] C. Warneke, C. Van Der Veen, S. Luxembourg, J. A. De Gouw, and A. Kok. Measurements of benzene and toluene in ambient air using proton-transfer-reaction mass spectrometry: calibration, humidity dependence, and field intercomparison. *International Journal of Mass Spectrometry*, 207(3):167, 2001.

[131] A. Tani, S. Hayward, and C. N. Hewitt. Measurement of monoterpenes and related compounds by proton transfer reaction-mass spectrometry (PTR-MS). *International Journal of Mass Spectrometry*, 223:561, 2003.

[132] G. H. Wannier. Motion of Gaseous Ions in Strong Electric Fields. *The Bell System Technical Journal*, 32(1):170, 1953.

[133] A. A. Viggiano and R. A. Morris. Rotational and Vibrational Energy Effects on Ion-Molecule Reactivity as Studied by the VT-SIFDT Technique. *The Journal of Physical Chemistry*, 100(50):19227, 1996.

[134] A. A. Viggiano, R. A. Morris, F. Dale, J. F. Paulson, K. Giles, D. Smith, and T. Su. Kinetic energy, temperature, and derived rotational temperature dependences for the reactions of $Kr^+(^2P_{3/2})$ and Ar^+ with HCl. *The Journal of Chemical Physics*, 93(2):1149, 1990.

[135] A. Jordan, S. Haidacher, G. Hanel, E. Hartungen, J. Herbig, L. Märk, R. Schottkowsky, H. Seehauser, P. Sulzer, and T. D. Märk. An online ultra-high sensitivity Proton-transfer-reaction mass-spectrometer combined with switchable reagent ion capability (PTR+SRI-MS). *International Journal of Mass Spectrometry*, 286(1):32, 2009.

[136] C. N. Hewitt, S. Hayward, and A. Tani. The application of proton transfer reaction-mass spectrometry (PTR-MS) to the monitoring and analysis of volatile organic compounds in the atmosphere. *Journal of Environmental Monitoring*, 5(1):1, 2003.

[137] T. Su and W. J. Chesnavich. Parametrization of the ion–polar molecule collision rate constant by trajectory calculations. *The Journal of Chemical Physics*, 76(10):5183, 1982.

[138] P. Španěl and D. Smith. SIFT studies of the reactions of H_3O^+, NO^+ and O_2^+ with a series of alcohols. *International Journal of Mass Spectrometry and Ion Processes*, 167:375, 1997.

[139] P. Španěl and D. Smith. SIFT studies of the reactions of H_3O^+, NO^+ and O_2^+ with several ethers. *International Journal of Mass Spectrometry and Ion Processes*, 172(3):239, 1998.

[140] W. L. Jolly. *Modern Inorganic Chemistry*. McGraw-Hill College, 1984.

[141] J. Zhao and R. Zhang. Proton transfer reaction rate constants between hydronium ion (H_3O^+) and volatile organic compounds. *Atmospheric Environment*, 38(14):2177, 2004.

[142] P. Španěl and D. Smith. Selected ion flow tube studies of the reactions of H_3O^+, NO^+ and O_2^+ with several aromatic and aliphatic hydrocarbons. *International Journal of Mass Spectrometry*, 181(1-3):1, 1998.

[143] J. H. Gross. *Mass Spectrometry: A Textbook*. Springer Science & Business Media, 2006.

[144] É. Mathieu. Mémoire sur le mouvement vibratoire d'une membrane de forme elliptique (Memoire on the vibratory movement of an elliptical membrane). *Journal de mathématiques pures et appliquées*, 13:137, 1868.

[145] D. MacDougall and W. B. Crummett. Guidelines for Data Acquisition and Data Quality Evaluation in Environmental Chemistry. *Analytical Chemistry*, 52(14):2242, 1980.

[146] C. Ammann, C. Spirig, A. Neftel, M. Steinbacher, M. Komenda, and A. Schaub. Application of PTR-MS for measurements of biogenic VOC in a deciduous forest. *International Journal of Mass Spectrometry*, 239(2-3):87, 2004.

[147] P. Španěl, Y. Ji, and D. Smith. SIFT studies of the reactions of H_3O^+, NO^+ and O_2^+ with a series of aldehydes and ketones. *International Journal of Mass Spectrometry and Ion Processes*, 165:25, 1997.

[148] A. Hurlbatt, A. R. Gibson, S. Schröter, J. Bredin, A. P. S. Foote, P. Grondein, D. O'Connell, and T. Gans. Concepts, Capabilities, and Limitations of Global Models: A Review. *Plasma Processes and Polymers*, 14(1-2):1600138, 2017.

[149] A. M. Lietz and M. J. Kushner. Air plasma treatment of liquid covered tissue: long timescale chemistry. *Journal of Physics D: Applied Physics*, 49(42):425204, 2016.

[150] D. S. Stafford and M. J. Kushner. $O_2(^1\Delta)$ production in He/O_2 mixtures in flowing low pressure plasmas. *Journal of Applied Physics*, 96(5):2451, 2004.

[151] N. L. Bassett and D. J. Economou. Effect of Cl_2 additions to an argon glow discharge. *Journal of Applied Physics*, 75(4):1931, 1994.

[152] E. Kemaneci, E. Carbone, J.-P. Booth, W. Graef, J. van Dijk, and G. Kroesen. Global (volume-averaged) model of inductively coupled chlorine plasma: Influence of Cl wall recombination and external heating on continuous and pulse-modulated plasmas. *Plasma Sources Science and Technology*, 23(4):045002, 2014.

[153] E. G. Thorsteinsson and J. T. Gudmundsson. A global (volume averaged) model of a Cl_2/Ar discharge: I. Continuous power. *Journal of Physics D: Applied Physics*, 43(11):115201, 2010.

[154] H. W. Ellis, R. Y. Pai, E. W. McDaniel, E. A. Mason, and L. A. Viehland. Transport Properties of Gaseous Ions over a Wide Energy Range. *Atomic Data and Nuclear Data Tables*, 17(3):177, 1976.

[155] P. N. Brown, G. D. Byrne, and A. C. Hindmarsh. VODE, A Variable-Coefficient ODE Solver. *SIAM Journal on Scientific and Statistical Computing*, 10(5):1038, 1989.

[156] J. R. Roth. Industrial Plasma Engineering, 1995.

[157] K. Tachibana. Excitation of the $1s_5$, $1s_4$, $1s_3$, and $1s_2$ levels of argon by low-energy electrons. *Physical Review A*, 34(2):1007, 1986.

[158] M. Hayashi. Report of the Institute of Plasma Physics, No. IPPJ-AM-19. Technical report, Nagoya University, 1981.

[159] D. Rapp and P. Englander-Golden. Total cross sections for ionization and attachment in gases by electron impact. I. Positive ionization. *The Journal of Chemical Physics*, 43(5):1464, 1965.

[160] R. H. McFarland and J. D. Kinney. Absolute cross sections of lithium and other alkali metal atoms for ionization by electrons. *Physical Review*, 137(4A):A1058, 1965.

[161] I. P. Zapesochnyi, L. L. Shimon, and A. K. Soshnikov. Effective Excitation Cross Sections of Alkali Metal Atoms Colliding with Slow Electrons. II. Potassium. *Optics and Spectroscopy*, 19:480, 1965.

[162] T. N. Rescigno. Low-energy electron-collision processes in molecular chlorine. *Physical Review A*, 50(2):1382, 1994.

[163] P. S. Ganas. Electron impact excitation cross sections for chlorine. *Journal of Applied Physics*, 63(2):277, 1988.

[164] G. L. Rogoff, J. M. Kramer, and R. B. Piejak. A Model for the Bulk Plasma in an RF Chlorne Discharge. *IEEE Transactions on Plasma Science*, 14(2):103, 1986.

[165] J. T. Gudmundsson and E. G. Thorsteinsson. Oxygen discharges diluted with argon: dissociation processes. *Plasma Sources Science and Technology*, 16(2):399, 2007.

[166] E. G. Thorsteinsson and J. T. Gudmundsson. The low pressure Cl_2/O_2 discharge and the role of ClO. *Plasma Sources Science and Technology*, 19(5):055008, 2010.

[167] A. H. Markosyan, A. Luque, F. J. Gordillo-Vázquez, and U. Ebert. Pumpkin: A tool to find principal pathways in plasma chemical models. *Computer Physics Communications*, 185(10):2697, 2014.

[168] R. Lehmann. An Algorithm for the Determination of All Significant Pathways in Chemical Reaction Systems. *Journal of Atmospheric Chemistry*, 47(1):45, 2004.

[169] J. W. Gallagher, E. C. Beaty, J. Dutton, and L. C. Pitchford. An Annotated Compilation and Appraisal of Electron Swarm Data in Electronegative Gases. *Journal of Physical and Chemical Reference Data*, 12(1):109, 1983.

[170] W. L. Morgan. A Critical Evaluation of Low-Energy Electron Impact Cross Sections for Plasma Processing Modeling. I: Cl_2, F_2, and HCl. *Plasma Chemistry and Plasma Processing*, 12(4):449, 1992.

[171] L. G. Christophorou and J. K. Olthoff. Electron Interactions With Cl_2. *Journal of Physical and Chemical Reference Data*, 28(1):131, 1999.

[172] D. Anh Tuan and B.-H. Jeon. Electron Collision Cross Sections for the Cl_2 Molecule from Electron Transport Coefficients. *Journal of the Physical Society of Japan*, 80(8):084301, 2011.

[173] J. Gregório and L. C. Pitchford. Updated compilation of electron–Cl_2 scattering cross sections. *Plasma Sources Science and Technology*, 21(3):032002, 2012.

[174] S. Kawaguchi, K. Takahashi, and K. Satoh. Electron collision cross section set of Cl_2 gas and electron transport analysis in Cl_2 gas and Cl_2/N_2 mixtures. *Japanese Journal of Applied Physics*, 59(SH):SHHA09, 2020.

[175] J. Hamilton, J. Tennyson, J. P. Booth, T. Gans, and A. R. Gibson. Calculated electron impact dissociation cross sections for molecular chlorine (Cl_2). *Plasma Sources Science and Technology*, 2018.

[176] S. D. Peyerimhoff and R. J. Buenker. Electronically excited and ionized states of the chlorine molecule. *Chemical Physics*, 57(3):279, 1981.

[177] R. J. Gulley, T. A. Field, W. A. Steer, N. J. Mason, S. L. Lunt, J. P. Ziesel, and D. Field. Very low energy electron collisions with molecular chlorine. *Journal of Physics B: Atomic, Molecular and Optical Physics*, 31(13):2971, 1998.

[178] G. D. Cooper, J. E. Sanabia, J. H. Moore, J. K. Olthoff, and L. G. Christophorou. Total electron scattering cross section for Cl_2. *Journal of Chemical Physics*, 110(1):682, 1999.

[179] C. Makochekanwa, H. Kawate, O. Sueoka, and M. Kimura. Total cross section measurement for electron scattering from chlorine molecules in the energy region from 0.8 to 600 eV. *Journal of Physics B: Atomic, Molecular and Optical Physics*, 36(9):1673, 2003.

[180] S. E. Božin and C. C. Goodyear. Measurements of ionization and attachment coefficients in chlorine. *British Journal of Applied Physics*, 18(1):49, 1967.

[181] L. C. Pitchford, L. L. Alves, K. Bartschat, S. F. Biagi, M. C. Bordage, A. V. Phelps, C. M. Ferreira, G. J. M. Hagelaar, W. L. Morgan, S. Pancheshnyi, V. Puech, A. Stauffer, and O. Zatsarinny. Comparisons of sets of electron–neutral scattering cross sections and swarm parameters in noble gases: I. Argon. *Journal of Physics D: Applied Physics*, 46(33):334001, 2013.

[182] V. Puech and L. Torchin. Collision cross sections and electron swarm parameters in argon. *Journal of Physics D: Applied Physics*, 19(12):2309, 1986.

[183] Puech database, www.lxcat.net, retrieved on June 6, 2020.

[184] Phelps database, www.lxcat.net, retrieved on June 6, 2020.

[185] Morgan database, www.lxcat.net, retrieved on June 6, 2020.

[186] L. L. Alves, The IST-Lisbon database on LXCat, www.lxcat.net, retrieved on June 6, 2020.

[187] M. Hayashi. Bibliography of electron and photon cross sections with atoms and molecules published in the 20th century. Argon. Technical report, National Institute for Fusion Science, 2003.

[188] R. P. McEachran and A. D. Stauffer. Momentum transfer cross sections for the heavy noble gases. *The European Physical Journal D*, 68(6):153, 2014.

[189] M. Allan, O. Zatsarinny, and K. Bartschat. Near-threshold absolute angle-differential cross sections for electron-impact excitation of argon and xenon. *Physical Review A*, 74(3):030701, 2006.

[190] O. Zatsarinny and K. Bartschat. B-spline Breit–Pauli R-matrix calculations for electron collisions with argon atoms. *Journal of Physics B: Atomic, Molecular and Optical Physics*, 37(23):4693, 2004.

[191] S. F. Biagi, MagBoltz v8.97 database, www.lxcat.net, retrieved on June 6, 2020.

[192] M. W. Ruf, S. Barsotti, M. Braun, H. Hotop, and I. I. Fabrikant. Dissociative attachment and vibrational excitation in low-energy electron collisions with chlorine molecules. *Journal of Physics B: Atomic, Molecular and Optical Physics*, 37(1):41, 2003.

[193] M. Kurepa and D. Belic. Electron-chlorine molecule total ionisation and electron attachment cross sections. *Journal of Physics B: Atomic and Molecular Physics*, 11(21):3719, 1978.

[194] I. I. Fabrikant, T. Leininger, and F. X. Gadéa. Low-energy dissociative electron attachment to Cl_2 molecules. *Journal of Physics B: Atomic, Molecular and Optical Physics*, 33(21):4575, 2000.

[195] R. Azria, R. Abouaf, and D. Teillet-Billy. Symmetry of Cl_2-resonant states formed in dissociative electron attachment reaction on Cl_2. *Journal of Physics B: Atomic and Molecular Physics*, 15(16):L569, 1982.

[196] L. Feketeova, D. J. Skalny, G. Hanel, B. Gstir, M. Francis, and T. D. Märk. Production of Cl^- via dissociative electron attachment to Cl_2. *International Journal of Mass Spectrometry*, 223:661, 2003.

[197] K. Gope, V. S. Prabhudesai, N. J. Mason, and E. Krishnakumar. Probing the resonant states of Cl_2 using velocity slice imaging. *Journal of Physics B: Atomic, Molecular and Optical Physics*, 49(1):015201, 2015.

[198] P. C. Cosby and H. Helm. Wright Laboratory Report. Technical report, WL-TR-93-2004, Wright Patterson AFB, OH 45433-7650, 1992.

[199] J. Jureta, S. Cvejanović, M. Kurepa, and D. Cvejanović. Threshold electron impact excitation of Cl_2. *Zeitschrift für Physik A Atoms and Nuclei*, 304(2):143, 1982.

[200] O. González-Magaña and J. de Urquijo. Measurement of electron swarm coefficients in chlorine and its mixtures with nitrogen. *Plasma Sources Science and Technology*, 27(6):06LT02, 2018.

[201] D. Spence, R. H. Huebner, H. Tanaka, M. A. Dillon, and R.-G. Wang. Electronic structure of Cl_2 from 5 to 15 eV by electron energy loss spectroscopy. *The Journal of Chemical Physics*, 80(7):2989, 1984.

[202] R. E. Center and A. Mandl. Ionization Cross Sections of F_2 and Cl_2 by Electron Impact. *Journal of Chemical Physics*, 57(10):4104, 1972.

[203] F. A. Stevie and M. J. Vasile. Electron impact ionization cross sections of F_2 and Cl_2. *Journal of Chemical Physics*, 74(9):5106, 1981.

[204] Z. Lj. Petrović, M. Šuvakov, Ž. Nikitović, S. Dujko, O. Šašić, J. Jovanović, G. Malović, and V. Stojanović. Kinetic phenomena in charged particle transport in gases, swarm parameters and cross section data. *Plasma Sources Science and Technology*, 16(1):S1, 2007.

[205] Z. Lj. Petrović, D. Marić, M. Savić, S. Marjanović, S. Dujko, and G. Malović. Using Swarm Models as an Exact Representation of Ionized Gases. *Plasma Processes and Polymers*, 14(1-2):1600124, 2017.

[206] M. Gote and H. Ehrhardt. Rotational excitation of diatomic molecules at intermediate energies: absolute differential state-to-state transition cross sections for electron scattering from N_2, Cl_2, CO and HCl. *Journal of Physics B: Atomic, Molecular and Optical Physics*, 28(17):3957, 1995.

[207] S. Tinck, W. Boullart, and A. Bogaerts. Simulation of an Ar/Cl_2 inductively coupled plasma: study of the effect of bias, power and pressure and comparison with experiments. *Journal of Physics D: Applied Physics*, 41(6):065207, 2008.

[208] P. Subramonium and M. J. Kushner. Two-dimensional modeling of long-term transients in inductively coupled plasmas using moderate computational parallelism. II. Ar/Cl_2 pulsed plasmas. *Journal of Vacuum Science & Technology A: Vacuum, Surfaces, and Films*, 20(2):325, 2002.

[209] Y. Ikezoe, S. Matsuoka, and M. Takebe. *Gas phase ion-molecule reaction rate constants through 1986*. Ion Reaction Research Group of the Mass Spectroscopy Society of Japan, 1987.

[210] M. J. Church and D. Smith. Ionic recombination of atomic and molecular ions in flowing afterglow plasmas. *Journal of Physics D: Applied Physics*, 11(16):2199, 1978.

[211] P. Španěl, M. Tichỳ, and D. Smith. The reactions of positive and negative halogen ions with Cl_2 and Br_2. *The Journal of Chemical Physics*, 98(11):8660, 1993.

[212] P. Španěl, M. Tichỳ, and D. Smith. SIFT studies of the reactions of rare gas atomic ions with Cl_2 and Br_2. *International Journal of Mass Spectrometry and Ion Processes*, 129:155, 1993.

[213] L. A. Gundel, D. W. Setser, M. A. A. Clyne, J. A. Coxon, and W. Nip. Rate constants for specific product channels from metastable Ar ($^3P_{2,0}$) reactions and spectrometer calibration in the vacuum ultraviolet. *The Journal of Chemical Physics*, 64(11):4390, 1976.

[214] I. S. Fletcher and D. Husain. The collisional behaviour of Cl [$3p^5(^2P_{1/2})$] by time-resolved attenuation of atomic resonance radiation in the vacuum ultraviolet. *Chemical Physics Letters*, 49(3):516, 1977.

[215] I. S. Fletcher and D. Husain. Collisional quenching of Cl [$3p^5(^2P_{1/2})$] by noble gases. *Journal of the Chemical Society, Faraday Transactions 2: Molecular and Chemical Physics*, 74:203, 1978.

[216] D. R. Nina. *Modelling Chlorine Plasmas*. Master's thesis, IST Lisbon, University of Lisbon, 2016.

[217] W. L. Morgan. *"ELENDIF": A Computer Program that Solves the Boltzmann Equation for a Partially Ionized Gas*. University of Colorado, 1979.

[218] W. L. Morgan and B. M. Penetrante. ELENDIF: A time-dependent Boltzmann solver for partially ionized plasmas. *Computer Physics Communications*, 58(1-2):127, 1990.

[219] M. Hayashi and T. Nimura. Calculation of electron swarm parameters in fluorine. *Journal of Applied Physics*, 54(9):4879, 1983.

[220] V. A. Bailey and R. H. Healey. LVII. The Behaviour of Electrons in Chlorine. *The London, Edinburgh, and Dublin Philosophical Magazine and Journal of Science*, 19(128):725, 1935.

[221] C. Lee and M. A. Lieberman. Global model of Ar, O_2, Cl_2, and Ar/O_2 high-density plasma discharges. *Journal of Vacuum Science & Technology A: Vacuum, Surfaces, and Films*, 13(2):368, 1995.

[222] E. Despiau-Pujo, M. Brihoum, P. Bodart, M. Darnon, and G. Cunge. Pulsed Cl_2/Ar inductively coupled plasma processing: 0D model versus experiments. *Journal of Physics D: Applied Physics*, 47(45):455201, 2014.

[223] E. G. Thorsteinsson and J. T. Gudmundsson. A global (volume averaged) model of a Cl_2/Ar discharge: II. Pulsed power modulation. *Journal of Physics D: Applied Physics*, 43(11):115202, 2010.

[224] E. G. Thorsteinsson and J. T. Gudmundsson. A global (volume averaged) model of a chlorine discharge. *Plasma Sources Science and Technology*, 19(1):015001, 2009.

[225] J. Guha, V. M. Donnelly, and Y.-K. Pu. Mass and Auger electron spectroscopy studies of the interactions of atomic and molecular chlorine on a plasma reactor wall. *Journal of Applied Physics*, 103(1):013306, 2008.

[226] L. Stafford, R. Khare, J. Guha, V. M. Donnelly, J.-S. Poirier, and J. Margot. Recombination of chlorine atoms on plasma-conditioned stainless steel surfaces in the presence of adsorbed Cl_2. *Journal of Physics D: Applied Physics*, 42(5):055206, 2009.

[227] V. M. Donnelly and M. V. Malyshev. Diagnostics of inductively coupled chlorine plasmas: Measurements of the neutral gas temperature. *Applied Physics Letters*, 77(16):2467, 2000.

[228] M. V. Malyshev and V. M. Donnelly. Diagnostics of inductively coupled chlorine plasmas: Measurement of electron and total positive ion densities. *Journal of Applied Physics*, 90(3):1130, 2001.

[229] A. M. Efremov, G.-H. Kim, J.-G. Kim, and C.-I. Kim. Self-consistent global model for inductively coupled Cl_2 plasma: Comparison with experimental data and application for the etch process analysis. *Thin Solid Films*, 515(13):5395, 2007.

[230] E. G. Thorsteinsson, A. T. Hjartarson, and J. T. Gudmundsson. The rate coefficients for the collisional energy loss of the chlorine discharge. Technical report, 2008.

[231] P. Kolorenč and J. Horáček. Dissociative electron attachment and vibrational excitation of the chlorine molecule. *Physical Review A*, 74(6):062703, 2006.

[232] A. P. Golovitskii. Temperature Dependence of an Electron Attachment to Chlorine Molecules. *Technical Physics*, 45(5):532, 2000.

[233] G. Cunge, N. Sadeghi, and R. Ramos. Influence of the reactor wall composition on radicals' densities and total pressure in Cl_2 inductively coupled plasmas: I. Without silicon etching. *Journal of Applied Physics*, 102(9):093304, 2007.

[234] E. Iwasaki, T. Nakayama, Y. Matsumi, K. Takahashi, T. J. Wallington, M. D. Hurley, and E. W. Kaiser. Kinetics and Mechanism of the Reaction of Chlorine Atoms with n-Pentanal. *The Journal of Physical Chemistry A*, 112(8):1741, 2008.

[235] J. Albaladejo, B. Ballesteros, E. Jiménez, P. Martín, and E. Martínez. A PLP–LIF kinetic study of the atmospheric reactivity of a series of C4–C7 saturated and unsaturated aliphatic aldehydes with OH. *Atmospheric Environment*, 36(20):3231, 2002.

[236] P. McLoughlin, R. Kane, and I. Shanahan. A relative rate study of the reaction of chlorine atoms (Cl) and hydroxyl radicals (OH) with a series of ethers. *International Journal of Chemical Kinetics*, 25(3):137, 1993.

[237] A. Mellouki, S. Teton, and G. Le Bras. Kinetics of OH radical reactions with a series of ethers. *International Journal of Chemical Kinetics*, 27(8):791, 1995.

[238] K. Niemi, S. Reuter, L. M. Graham, J. Waskoenig, N. Knake, V. Schulz-Von Der Gathen, and T. Gans. Diagnostic based modelling of radio-frequency driven atmospheric pressure plasmas. *Journal of Physics D: Applied Physics*, 43(12):124006, 2010.

[239] M. E. Jenkin, M. D. Hurley, and T. J. Wallington. Investigation of the Radical Product Channel of the $CH_3OCH_2O_2$ + HO_2 Reaction in the Gas Phase. *The Journal of Physical Chemistry A*, 114(1):408, 2010.

[240] R. Atkinson, D. L. Baulch, R. A. Cox, J. N. Crowley, R. F. Hampson, R. G. Hynes, M. E. Jenkin, M. J. Rossi, and J. Troe. Evaluated kinetic and photochemical data for atmospheric chemistry: Volume I – gas phase reactions of O_x, HO_x, NO_x and SO_x species. *Atmospheric Chemistry and Physics*, 4(6):1461, 2004.

[241] O. Sokolov, M. D. Hurley, T. J. Wallington, E. W. Kaiser, J. Platz, O. J. Nielsen, F. Berho, M.-T. Rayez, and R. Lesclaux. Kinetics and Mechanism of the Gas-Phase Reaction of Cl Atoms with Benzene. *The Journal of Physical Chemistry A*, 102(52):10671, 1998.

[242] A. Sarani, A. Y. Nikiforov, and C. Leys. Atmospheric pressure plasma jet in Ar and Ar/H_2O mixtures: Optical emission spectroscopy and temperature measurements. *Physics of Plasmas*, 17(6):063504, 2010.

[243] R. Atkinson, D. L. Baulch, R. A. Cox, J. N. Crowley, R. F. Hampson, R. G. Hynes, M. E. Jenkin, M. J. Rossi, and J. Troe. Evaluated kinetic and photochemical data for atmospheric chemistry: Volume III - reactions of inorganic halogens. 2006.

[244] J. C. Ianni. A comparison of the Bader-Deuflhard and the Cash-Karp Runge-Kutta integrators for the GRI-MECH 3.0 model based on the chemical kinetics code Kintecus. pages 1368–1372, 2003.

[245] A. Mellouki, M. Ammann, R. A. Cox, J. N. Crowley, H. Herrmann, M. E. Jenkin, V. F. McNeill, J. Troe, and T. J. Wallington. Evaluated kinetic and photochemical data for atmospheric chemistry: Volume VIII–gas phase reactions of organic species with four, or more, carbon atoms (C_4). *Atmospheric Chemistry and Physics Discussions*, pages 1–22, 2020.

[246] I. Suh and R. Zhang. Kinetic studies of isoprene reactions initiated by chlorine atom. *The Journal of Physical Chemistry A*, 104(28):6590, 2000.

[247] Task Group on Atmospheric Chemical Kinetic Data Evaluation, http://iupac.pole-ether.fr/, retrieved on Sep 8, 2020.

[248] M. Bartels, J. Edelbüttel-Einhaus, and K. Hoyermann. The reactions of benzyl radicals with hydrogen atoms, oxygen atoms, and molecular oxygen using EI/REMPI mass spectrometry. In *Symposium (International) on Combustion*, volume 22, pages 1041–1051. Elsevier, 1989.

[249] H. T. Do, V. Sushkov, and R. Hippler. Tunable diode laser absorption spectroscopy of argon metastable atoms in Ar/C_2H_2 dusty plasmas. *New Journal of Physics*, 11(3):033020, 2009.

[250] L. Vriens. Calculation of absolute ionisation cross sections of He, He*, He^+, Ne, Ne*, Ne^+, Ar, Ar*, Hg and Hg*. *Physics Letters*, 8(4):260, 1964.

[251] J. Brian and A. Mitchell. The dissociative recombination of molecular ions. *Physics Reports*, 186(5):215, 1990.

[252] Y. Wang, O. Zatsarinny, K. Bartschat, and J.-P. Booth. Fine-structure-resolved electron collisions from chlorine atoms in the $(3p^5)^2P^0_{3/2}$ and $(3p^5)^2P^0_{1/2}$ states. *Physical Review A*, 87(2):022703, 2013.

[253] A. Bogaerts and R. Gijbels. Role of Ar^{2+} and Ar_2^+ ions in a direct current argon glow discharge: A numerical description. *Journal of Applied Physics*, 86(8):4124, 1999.

[254] A. Bogaerts, R. Gijbels, and G. P. Jackson. Modeling of a millisecond pulsed glow discharge: Investigation of the afterpeak. *Journal of Analytical Atomic Spectrometry*, 18(6):533, 2003.

[255] D. J. Eckstrom, H. H. Nakano, D. C. Lorents, T. Rothem, J. A. Betts, M. E. Lainhart, K. J. Triebes, and D. A. Dakin. Characteristics of electron-beam-excited Kr_2^* at low pressures as a vacuum ultraviolet source. *Journal of Applied Physics*, 64(4):1691, 1988.

[256] I. Dotan, D. L. Albritton, W. Lindinger, and M. Pahl. Mobilities of CO_2^+, N_2H^+, H_3O^+, $H_3O^+{\cdot}H_2O$, and $H_3O^+{\cdot}(H_2O)_2$ ions in N_2. *The Journal of Chemical Physics*, 65(11):5028, 1976.